UNIVERSITY OF Southampton

University of Southampton Research Repository

Copyright © and Moral Rights for this thesis and, where applicable, any accompanying data are retained by the author and/or other copyright owners. A copy can be downloaded for personal non-commercial research or study, without prior permission or charge. This thesis and the accompanying data cannot be reproduced or quoted extensively from without first obtaining permission in writing from the copyright holder/s. The content of the thesis and accompanying research data (where applicable) must not be changed in any way or sold commercially in any format or medium without the formal permission of the copyright holder/s.

When referring to this thesis and any accompanying data, full bibliographic details must be given, e.g.

Thesis: Author (Year of Submission) "Full thesis title", University of Southampton, name of the University Faculty or School or Department, PhD Thesis, pagination.

Data: Author (Year) Title. URI [dataset]

Investigating dynamics in biomolecular solids by solid-state NMR

Jai Balachandra

Faculty of Engineering and Physical Sciences

SCHOOL OF CHEMISTRY

May 2021

University of Southampton

Abstract

Faculty of Engineering and Physical Sciences

School of Chemistry

Thesis for the degree of Doctor of Philosophy

by

Jai Balachandra

Solid-state nuclear magnetic resonance (ssNMR) is a powerful non-destructive tool in the analysis of structural and dynamic properties of a variety of complex biomolecules. The vast majority of ssNMR measurements are conducted on spin-½ nuclei, such as ^{13}C and ^{15}N, with the aid of isotopic enrichment. In this thesis we have used ^{14}N and ^{13}C at natural abundance levels to study the structure and dynamics of small molecules with the view to developing these as tools with which to investigate pharmaceuticals and other biomolecular systems.

Nitrogen-14 is an element ubiquitous in a vast number of APIs (active pharmaceutical ingredients), though due to the large quadrupole coupling, detection of the naturally abundant (>99%) NMR active isotope ^{14}N poses a multitude of challenges. However, the presence of this large anisotropic interaction can be advantageous as it offers a wealth of information on the conformation and dynamics in molecular systems. This thesis focuses on exploiting the quadrupolar interaction to glean valuable insight on (1) the dynamics in a family of quaternary ammonium salts (acetylcholine salts) and (2) the influence of the membrane protein Fk-1 on the phospholipid (POPC) bilayer. Through the study of the ^{14}N lineshape and relaxation as function of temperature, we have been able to probe the dynamics revealing that such measurements can provide valuable insights into how crystal packing and polymorphism can influence the properties of these pharmacologically important sites.

We have complemented these ^{14}N studies with natural abundance CP-MAS ^{13}C experiments, studying the influence of temperature range on the lineshape of quaternary ammonium groups. By applying *ab initio* quantum mechanical calculations to newly derived crystal structures, we have been able to model the chemical exchange processes that lead to complex ^{13}C lineshapes to further characterise the dynamics of this important pharmacophore.

In an expansion of these studies, we have used ^{14}N MAS-NMR to study the interaction of phosphatidylcholine headgroups with integral membrane proteins. Employing variable temperature studies, we have been able to use ^{14}N NMR and complementary ^{2}H NMR of deuterated lipids chains to investigate how integral membrane proteins interact and perturb the structure and phase behaviour of the lipid bilayer.

Table of Contents

Research Thesis: Declaration of Authorship

Print name:	JAI BALACHANDRA

Title of thesis:	Investigating dynamics in biomolecular solids by solid-state NMR

I declare that this thesis and the work presented in it are my own and has been generated by me as the result of my own original research.

I confirm that:

1. This work was done wholly or mainly while in candidature for a research degree at this University;
2. Where any part of this thesis has previously been submitted for a degree or any other qualification at this University or any other institution, this has been clearly stated;
3. Where I have consulted the published work of others, this is always clearly attributed;
4. Where I have quoted from the work of others, the source is always given. With the exception of such quotations, this thesis is entirely my own work;
5. I have acknowledged all main sources of help;
6. Where the thesis is based on work done by myself jointly with others, I have made clear exactly what was done by others and what I have contributed myself;
7. None of this work has been published before submission Parts of this work have been published as:

Signature:		Date:	28/09/2020

Acknowledgements

I would, first of all, like to give the biggest thanks to my supervisor Phil Williamson who took me under his wing like a much taller, better dressed Yoda; it's nothing short of magic what we have managed to do in two years and it's not an understatement to say it would have been impossible without his guidance. Speaking of magic, I'm not going to pretend to understand how Phil manages to successfully fix something where I have failed by doing the exact same thing. Either way, he has shown me what dedication and willpower can get you and I very much appreciate all the help he has given me. I would also like to thank my other supervisor Marcel Utz for believing in me and helping me find a way to enjoy doing my PhD. I'd like to thank Malcolm Levitt for lending an ear about any issues I had early on, including some music theory – our guitar jam session was pretty epic.

A thanks is also needed for the whole of the MagRes crew, specifically Maria Concistre and Marina Carravetta, who taught me many things in my first year and was always there when I struggled, including the long, arduous trips to Warwick University.

I have made many friends over the course of my PhD, and I can't leave out my favourite MATLAB wizard Steven Worswick, who for some reason only thinks in matrices now. Also, George Bacanu, whose infectious enthusiasm for NMR left me smiling at times when I didn't want to. A big thanks to Graham Saunders whose unexpected kindness during the final part of write-up boosted my spirits massively (in form of chocolate bourbons). I can't mention friends without mentioning my best friend Reece, who convinced me not to give up on multiple occasions and sat through my rants.

I would like to acknowledge the School of Chemistry and the School of Biological Sciences at the University of Southampton. Additionally, I acknowledge the use of the IRIDIS High Performance Computing Facility, and associated support services at the University of Southampton, in the completion of this work. I would also like to thank Professor Simon Cole and Wilma for their collaboration on the XRD analysis of my salts and getting the XRD results to me so quick!

Finally, a huge thank you to my family: my parents for their unwavering belief in me even if they had no idea what I was doing, my younger sister who cheered me on and my brother-in-law for all the free lifts with no complaints. The biggest of all to my older sister, without whom I wouldn't be where I am. I would also like to take the opportunity to welcome the newest part of our family, my nephew, Theeran, whose face cheered me up to no end during these times of isolation.

Definitions and Abbreviations

µg	Microgram
µs	Microsecond
Å	Ångström
acetylcholine	ACh
API	Active Pharmaceutical Ingredient
BFGS	Broyden–Fletcher–Goldfarb–Shanno
CP	Cross-Polarization
CP-MAS	Cross-Polarization Magic Angle Spinning
C_Q	Quadrupolar coupling constant
CSA	Chemical Shift Anisotropy
CST	Chemical Shielding Tensor
DSC	Differential Scanning Calorimetry
EFG	Electric field gradient
ER	Endoplasmic Reticulum
eV	Electronvolt
FID	Free Induction Decay
Fk-1	Fukutin-1-Transmembrane Domain
GHz	Gigahertz
GIPAW	Gauge Including Projector Augmented Wave
GTO	Gaussian Type Orbital
HB	Herzfeld-Berger

Hz	……	Hertz
IR	……	Infrared
K	……	Kelvin
kHz	……	Kilohertz
L/P	……	Lipid/Protein
LF	……	Laboratory Frame
MAS	……	Magic Angle Spinning
MHz	……	Megahertz
mm	……	Millimetre
ms	……	Millisecond
NMR	……	Nuclear Magnetic Resonance
ns	……	Nanosecond
PAF	……	Principal Axis Frame
POPC	……	1-palmitoyl-2-oleoyl-glycero-3-phosphocholine
ppm	……	parts per million
QM	……	Quantum mechanics
rd	……	Interpulse delay
RF	……	Radiofrequency
s	……	Second
SPINAL	……	Small Phase Incremental Alternation
ssNMR	……	Solid-state NMR
STO	……	Slater type orbitals
T	……	Temperature

T_1	……	Spin-lattice relaxation time
$T_{1\rho}$	……	Spin-lattice relaxation time in the rotating frame
T_2	……	Spin-spin relaxation time
T_m	……	Phase transition temperature
TMD	……	Transmembrane domain
VT	……	Variable temperature
XRD	……	X-ray powder diffraction

Chapter 1 Introduction

Nuclear Magnetic Resonance (NMR) is a widely-used method for the analysis of structures and interactions of organic, inorganic and biomolecules and has become a powerful method for the structural elucidation of large biomolecules such as nucleic acids and proteins. Solution state NMR has been adopted as a fundamental technique due to the high resolution spectra that can be obtained as a result of the rapid molecular tumbling of molecules in the sample, which in turn averages out the direction-dependent components to zero, leaving one with spectra dominated by isotropic chemical shifts. This has led to solution state NMR becoming a core spectroscopic technique in structural biology, along with X-ray crystallography, for the elucidation of structures in large biomolecules, as well as any dynamics present in the system.

In cases, however, where working with samples in the liquid state is unfeasible, for example, large molecules such as proteins and amino acids which exhibit slow rates of anisotropic tumbling and in the pharmaceutical sector where drugs are formulated in the solid-state, solid-state NMR (ssNMR) has become a useful and common practice. In ssNMR, many of the interactions a nucleus experiences in an external magnetic field are orientation dependent with respect to the external magnetic field. Since there is no intrinsic molecular tumbling, these orientation dependent interactions, or anisotropic interactions, in the sample are not averaged out resulting in broad signals in the spectra with a reduced resolution. However, these broad features in the spectra offer a wealth of information on the structure and dynamics present in the system; these anisotropic interactions can also be averaged via mechanical rotation of the sample via a technique called Magic Angle Spinning, which will be explored later.

Solid-state NMR typically exploits spin-½ nuclei which are easily studied as they lack a nuclear quadrupolar interaction, an anisotropic interaction unique to nuclei with spin >½, which interact with the electric field gradients (EFG) as well as the external magnetic field. This interaction is frequently large (typically larger than the amplitudes of radiofrequency pulses) and significant challenges arise when investigating quadrupolar nuclei. Solid-state NMR methods tend to utilise spin-½ nuclei, such as ^{1}H, ^{13}C and ^{15}N, in order to avoid the problematic quadrupolar interaction. One of the most frequently investigated elements is nitrogen, especially in the pharmaceutical sector as it is ubiquitous in drugs and active pharmaceutical ingredients (APIs). For this reason, isotopically enriched samples are typically used as they lack the nuclear quadrupolar interaction. The natural abundance of this particular spin ½ isotope, however, is low (0.4%) compared to the other NMR active isotope, the quadrupolar nucleus ^{14}N (99.6%); the issue also arises when labelling samples as it is generally time consuming, expensive and in certain cases, not possible [3].

For this reason, I wish to investigate the potential of using quadrupolar nuclei as tool for studying the dynamics in quaternary ammonium groups, an important pharmacophore ubiquitous in pharmaceuticals. A family of acetylcholine (ACh) salts were chosen as model systems to investigate the dynamics since they are predicted to have small C_Q as a result of symmetry at the quaternary ammonium site as well as motions which average the anisotropic interactions. In conjunction with the quadrupolar study, I implemented Cross-polarization methods and paired with chemical exchange simulations on the nuclei, ^{13}C, in order to model the motion as well as glean insight into the timescales of motions present at the quaternary ammonium site. This paved the way to investigations into larger systems, specifically the phospholipid POPC and the membrane protein Fukutin-1, which play a vital role in eukaryotic cells, by exploiting the quadrupolar nuclei ^{14}N and ^{2}H. This provides us with a clearer understanding of the dynamics present in the lipid bilayer (deuterated acyl chains) and the phospholipid choline headgroup which, analogous to the ACh salts, contains a quaternary ammonium group.

1.1 Introduction to NMR

The following section is an introduction to the general theory on the interactions that occur at the nucleus in a static external magnetic field. This chapter is adapted from Spin Dynamics by Malcolm Levitt [4], Solid-State NMR Spectroscopy Principles and Applications by Melinda Duer [5] and Deuterium magnetic resonance: theory and application to lipid membranes by Joachim Seelig [6].

We begin by defining the wavefunction (which describes the state of a system) for a nuclear spin system where all the interactions are independent of time, which is the solution of the time-independent Schrödinger equation (Equation 1.1):

Equation 1.1

$$\hat{H}\Psi = E\Psi$$

where $\hat{H}$ is the Hamiltonian, the energy operator for the system and E is the energy of the system. In NMR experiments, the majority of interactions that influence a spin system are time-dependent and so the time-dependent Schrödinger equation (Equation 1.2) where a time-dependent interaction is given by the time-dependent Hamiltonian:

Equation 1.2

$$\hat{H}(t)\Psi(t) = i\hbar\frac{\partial\Psi(t)}{\partial t}$$

1.2 The NMR Hamiltonians

In solid-state NMR, the spectra obtained are typically broad due to the effects of strong anisotropic interactions, making even protons difficult to detect to the same standard as liquid state NMR, for which these interactions are averaged as a result of rapid molecular tumbling. The interactions in the solid state are expressed as the following nuclear spin Hamiltonians in an NMR experiment (Equation 1.3):

Equation 1.3

$$\hat{H} = \hat{H}_z + \hat{H}_J + \hat{H}_D + \hat{H}_{CS} + \hat{H}_Q$$

The total Hamiltonian, $\hat{H}$, is a sum of the Hamiltonians which describe the NMR interactions; the terms $\hat{H}_z$, $\hat{H}_J$, $\hat{H}_D$, $\hat{H}_{CS}$ and $\hat{H}_Q$ correspond to the Zeeman, J-coupling, dipole-dipole, chemical shift and quadrupolar interaction, respectively. In most cases, the high-field approximation is assumed and the Zeeman interaction is much greater than the other NMR interactions. These interactions reflect the local physical and chemical environment of the nucleus under investigation enabling one to obtain a wealth of information on the structure and dynamics of the system. The interactions

depend on the orientation of the nucleus (and the molecule) with respect to the external magnetic field, B_0 making them anisotropic by nature; subsequently, the Hamiltonian of J-coupling, dipole-dipole, chemical shift and quadrupole can be expressed as a 2nd rank tensor, the components of which depend on the orientation of the nucleus and its chemical and physical environment. From these 2nd rank tensors, we can obtain useful parameters such as the isotropic component, the anisotropy and the asymmetry parameter; we do this by decomposition of the 2nd rank tensor into spherical tensors [7] of various ranks and changing the reference frame of the tensors from the Laboratory Frame to the Principle Axis Frame which provides us with the diagonal form of the tensors which we can exploit. As we will see later in the chapter, the anisotropic interactions possess an orientation dependent term $3cos^2\beta-1$ which is of significance (Section 1.4). The following sections provide a general overview of the important interactions which influence and give rise to our signals in the NMR spectrum.

1.2.1 Zeeman Hamiltonian

Nuclei in an external magnetic field, B_0, experience the Zeeman interaction, the interaction between the spin and the external magnetic field, which effectively removes the intrinsic degeneracy of the nuclear spin levels, allowing one to observe the NMR phenomenon. For a nucleus with spin I, the number of nuclear spin levels is $2I + 1$, ranging from $-I$ to $+I$.

In the case of ½ spin nuclei, the energy levels are split into 2 states: ± ½ with the + ½ state (α) decreasing in energy and – ½ state (β) increasing in energy as the strength of the magnetic field increases. The spin Hamiltonian for the Zeeman Hamiltonian ($\widehat{H}_z$), is given in Equation 1.4:

Equation 1.4

$$\widehat{H}_z = -\gamma B_0 \hat{I}_z$$

where $\hat{I}_z$ is the angular momentum operator for the z-component, ω_0 is the Larmor frequency which is equal to the term '$-\gamma B_0$', and γ is the gyromagnetic ratio of the nucleus.

1.2.2 J-coupling Hamiltonian

The energy of through-bond J-coupling between two nuclei is represented by $\widehat{H}_J$, the full form of the J-coupling Hamiltonian (Equation 1.5):

Equation 1.5

$$\widehat{H}_{jk}^{J.full} = 2\pi \hat{\boldsymbol{I}}_j . \boldsymbol{J}_{jk} . \hat{\boldsymbol{I}}_k$$

The Hamiltonian is shown for two spins 'j' and 'k'. '***J***' is the J-coupling tensor, which is dependent on molecular orientation and '$\hat{\boldsymbol{I}}_i$' is a vector form of the angular momentum operators along the *xyz*-direction for spins '*i*'. The full form therefore contains all the components of the J-coupling tensor. In isotropic liquids where the molecules undergo rapid tumbling, the J-coupling is averaged to a scalar (Equation 1.6):

Equation 1.6

$$J_{iso} = \frac{1}{3}\left(J_{xx} + J_{yy} + J_{zz}\right)$$

1.2.3 Chemical Shift Hamiltonian

The chemical shift Hamiltonian is denoted as $\widehat{H}_{CS}$, which represents the interaction between the external magnetic field and the nuclear spins via the electronic environment. The B_0 field induces an electronic current in the electron clouds which then generates a magnetic field which is called the induced field (B_i); the nuclear spins experience a total field, which is the sum of the induced field (generated by the electrons which effectively shield the nucleus) and the external field, and therefore may change the resonance frequency. The total magnetic field, B_{loc}, felt by the nuclear spins in given in Equation 1.7:

Equation 1.7

$$B_{loc} = B_0 + B_i$$

Since the shielding property associated with the nucleus depends on the orientation of the molecule within the external field B_0, it must be defined by a second rank tensor, which describes the variation in the size of the shielding w.r.t to orientation. The shielding tensor (Equation 1.8), $\boldsymbol{\sigma}$, is therefore represented by a 3x3 matrix:

Equation 1.8

$$\boldsymbol{\sigma} = \begin{pmatrix} \sigma_{xx} & \sigma_{xy} & \sigma_{xz} \\ \sigma_{yx} & \sigma_{yy} & \sigma_{yz} \\ \sigma_{zx} & \sigma_{zy} & \sigma_{zz} \end{pmatrix}$$

In the Laboratory frame, where B_0 is parallel with the *z*-axis, the total magnetic field, B_{loc}, at a nucleus is given in Equation 1.9:

Equation 1.9

$$B_{loc} = \boldsymbol{\sigma}^{lab}.B_0$$

Converting the axis frame from the Laboratory Frame to the Principle Axis Frame (PAF), allows for the diagonalization of the shielding tensor so we obtain the principal values of the shielding tensor; the orientation of the PAF is fixed with respect to the molecule containing the nucleus. In the case of an axially symmetric tensor, the principal values are such that $\sigma_{xx}^{PAF} = \sigma_{yy}^{PAF} \neq \sigma_{zz}^{PAF}$, and the tensor takes an symmetric ellipsoidal form. When the tensor is non-axial, the ellipsoid is asymmetric so $\sigma_{xx}^{PAF} \neq \sigma_{yy}^{PAF} \neq \sigma_{zz}^{PAF}$. Using the principal values of the shielding tensor, one can express the isotropic value (σ_{iso}), the anisotropic value (Δ) and the asymmetry parameter (η) as follows:

Equation 1.10

$$\sigma_{iso} = \frac{1}{3}(\sigma_{xx}^{PAF} + \sigma_{yy}^{PAF} + \sigma_{zz}^{PAF})$$

$$\Delta = \sigma_{zz}^{PAF} - \sigma_{iso}$$

$$\eta = (\frac{\sigma_{xx}^{PAF} - \sigma_{yy}^{PAF}}{\Delta})$$

In the case where the applied field is along the *z*-axis (for instance, in the presence of a static external field B_0), the Hamiltonian for the chemical shielding interaction is shown in Equation 1.11:

Equation 1.11

$$\hat{H}_{CS} = -\gamma\hbar\hat{I}_z\sigma_{zz}^{LAB}B_0$$

The chemical shifts, δ, observed in the solid-state NMR spectrum are related to the chemical shift tensor via Equation 1.12:

Equation 1.12

$$\delta = \sigma_{iso} + \frac{1}{2}\Delta_{CS}\{3cos^2\theta - 1 + \eta_{CS}sin^2\theta cos2\varphi\}$$

where Δ_{CS} is the anisotropic chemical shift and η_{CS} is the asymmetry parameter.

1.2.4 Dipolar Hamiltonian

Dipolar coupling is represented by the Hamiltonian, $\hat{H}_D$, and is the through-space coupling between two spins via the magnetic fields generated by the nuclei. It is a traceless tensor meaning there is no isotropic component. The full dipolar coupling Hamiltonian is calculated via Equation 1.13 and Equation 1.14:

Equation 1.13

$$\hat{H}_{jk}^{DD.full} = -b_{jk}\left(3\left(\hat{\boldsymbol{I}}_j.\boldsymbol{e}_{jk}\right)\left(\hat{\boldsymbol{I}}_k.\boldsymbol{e}_{jk}\right)\right) - \hat{\boldsymbol{I}}_j.\hat{\boldsymbol{I}}_k$$

Equation 1.14

$$b_{jk} = \left(\frac{\mu_0}{4\pi}\right)\frac{\hbar\gamma_j\gamma_k}{r_{jk}^3}$$

$\boldsymbol{e}_{jk}$ describes the line joining the centres of the two nuclei as a vector. The dipolar constant 'b_{jk}' is strongly dependent (and therefore, the dipole interaction itself) on the spin-spin distance 'r^{-3}' and the gyromagnetic ratio 'γ' of each spin (*j, k*). 'μ_0' is the magnetic constant; the dipole-dipole Hamiltonian can be treated analogous to the chemical shift anisotropy, where the orientation dependence is accounted for.

1.2.5 Quadrupolar Hamiltonian

The quadrupolar Hamiltonian, Equation 1.15, is the interaction between the non-spherical charge distribution in the nucleus (nuclear electric quadrupole moment) and the electric field gradient (EFG) (which is generated by electron clouds around the nucleus) and is only present in nuclei with spin >½:

Equation 1.15

$$\hat{\mathrm{H}}_Q = \left(\frac{eQ}{2I(2I-1)\hbar}\right)\hat{\boldsymbol{I}}.\boldsymbol{V}.\hat{\boldsymbol{I}}$$

where 'I' is the spin, 'e' is the elementary charge, '$\hat{\boldsymbol{I}}$' is the nuclear spin vector and 'Q' is the nuclear quadrupole moment which interacts with a second rank tensor for the EFG, '$\boldsymbol{V}$'.

The quadrupolar interaction tensor (EFG tensor) is a 3x3 matrix which takes the following form (Equation 1.16) in the principle Axis Frame (PAF):

Equation 1.16

$$V_{PAS} = \begin{pmatrix} V_{xx} & 0 & 0 \\ 0 & V_{yy} & 0 \\ 0 & 0 & V_{zz} \end{pmatrix}$$

The 2nd rank tensor for the quadrupolar interaction can be parameterised with the following equations (Equation 1.17, Equation 1.18 and Equation 1.19):

Equation 1.17

$$\delta_{iso} = \frac{1}{3}\left(V_{xx} + V_{yy} + V_{zz}\right) = 0$$

Equation 1.18

$$\delta = V_{zz} - V_{iso} = eq = V_{zz}$$

Equation 1.19

$$\eta = \frac{V_{xx} - V_{yy}}{V_{zz}}$$

Where δ_{iso} is the isotropic component 'η' is the asymmetry parameter; as V_{zz} is the largest field gradient ($|V_{zz}| \geq |V_{xx}| \geq |V_{yy}|$), the asymmetry parameter can be defined as $|0| \leq \eta \leq |1|$. The field gradient, '$eq = V_{zz}$', will be discussed later in this chapter using equations to provide context.

The quadrupolar interaction is anisotropic, therefore, the resonance peaks after excitation depend on the orientation of the 2nd rank tensor with respect to the external field. To calculate the resonance peaks, the tensor in the PAF must be rotated to the Laboratory Frame (LF). This is carried out by rotating about two Euler angles 'α' and 'β' consecutively, where α is the angle of rotation about the *z*-axis of the PAF in the *xy*-plane and β is the angle of rotation about the new *y*-axis to specify a new *z*-axis.

Accordingly, the position of the energy levels is dependent on the orientation of the molecule.

Under the influence of an external magnetic field, B_0 , the formerly degenerate energy levels split due to the Zeeman interaction, giving rise to $2I + 1$ non-degenerate energy levels termed '*m*' (the projection quantum number). For a *I* = 1 nucleus, such as ^{14}N, the energy levels split into $m = -1, 0, +1$. Where the Zeeman interaction is the largest internal interaction, we work in the Zeeman basis; this is called the 'high-field approximation':

Equation 1.20

$$E_m = -\gamma . B_0(m) + \frac{eQ}{4I(2I-1)}\left(\frac{3cos^2(\beta)-1}{2} + \frac{1}{2}\eta \sin^2\beta \, cos2\alpha\right)[3m^2 - I(I+1)]$$

Equation 1.21, Equation 1.22 and Equation 1.23 show the energy levels for each value of '*m*' which for a spin-1 nucleus such as ^{14}N gives $m = -1, 0$ and $+1$ states where *e*, *Q* and *I* are defined from the quadrupolar Hamiltonian (Equation 1.15). The previously introduced parameters, α, β and η, are present, showing the orientation dependence of the quadrupolar energy levels:

Equation 1.21

$$E_{-1} = \gamma . B_0 + \frac{1}{4}eQ.\left(\frac{3cos^2(\beta)-1}{2} + \frac{1}{2}\eta \sin^2\beta \, cos2\alpha\right)$$

Equation 1.22

$$E_0 = -\frac{1}{2}eQ.\left(\frac{3cos^2(\beta)-1}{2} + \frac{1}{2}\eta \sin^2\beta \, cos2\alpha\right)$$

Equation 1.23

$$E_{+1} = -\gamma . B_0 + \frac{1}{4}eQ.\left(\frac{3cos^2(\beta)-1}{2} + \frac{1}{2}\eta \sin^2\beta \, cos2\alpha\right)$$

Figure 1.1 illustrates the effect of the Zeeman and quadrupolar interactions on the degenerate energy level.

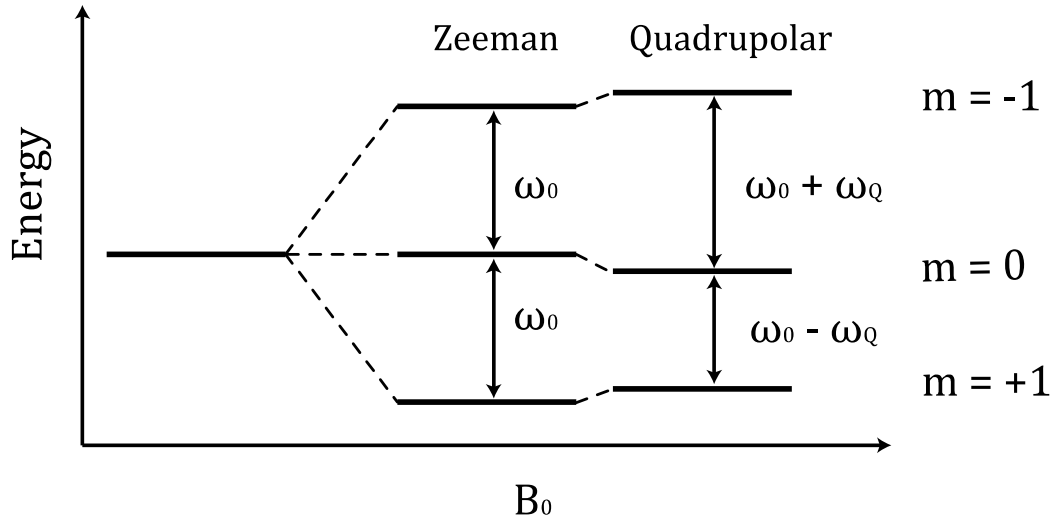

Figure 1.1: Figure showing the splitting of energy levels under the effect of the Zeeman interaction and the perturbation effect of the quadrupolar interaction.

From Figure 1.1, we can see that there are two allowed transitions (transition which change m by ± 1); these two resonance energies are then defined by Equation 1.24 and Equation 1.25:

Equation 1.24

$$E_{-1} - E_0 = \gamma . B_0 + \frac{3}{4} eQ . \left(\frac{3cos^2(\beta) - 1}{2} + \frac{1}{2} \eta \sin^2 \beta \, cos2\alpha \right)$$

Equation 1.25

$$E_0 - E_{+1} = \gamma . B_0 - \frac{3}{4} eQ . \left(\frac{3cos^2(\beta) - 1}{2} + \frac{1}{2} \eta \sin^2 \beta \, cos2\alpha \right)$$

The quadrupole splitting (the frequency between the two resonance lines in the spectrum) can be written as Δv_Q which is equal to $(E_{-1} - E_0) - (E_0 - E_{+1})$; this is shown in :

Equation 1.26, and simplified further in

Equation 1.27:

Equation 1.26

$$\Delta v_Q = \left(+ \frac{3}{4} eQ . \left(\frac{3cos^2(\beta) - 1}{2} + \frac{1}{2} \eta \sin^2 \beta \, cos2\alpha \right) \right) - \left(- \frac{3}{4} eQ . \left(\frac{3cos^2(\beta) - 1}{2} + \frac{1}{2} \eta \sin^2 \beta \, cos2\alpha \right) \right)$$

Equation 1.27

$$\Delta v_Q = \frac{3}{2}.\frac{eQ}{h}.\left(\frac{3cos^2(\beta)-1}{2}+\frac{1}{2}\eta\sin^2\beta\, cos2\alpha\right)$$

For the case where the *z*-axis of the PAF of the EFG tensor is parallel to the B_0 field and the tensor is axially symmetric, the η term becomes 0 and when $\beta = 0$, the $\frac{3cos^2(\beta)-1}{2}$ term is equal to 1. The $eq = V_{zz}$ is then multiplied by the $\frac{eQ}{h}$ term. This is demonstrated in Equation 1.28:

Equation 1.28

$$\Delta v_Q(B_0 \parallel z) = \frac{3}{2}.\frac{eQ}{h}.\left(\frac{3cos^2(\beta)-1}{2}+\frac{1}{2}\eta\sin^2\beta\, cos2\alpha\right) = \frac{3}{2}.\frac{eQ}{h}.eq = \frac{3}{2}.\frac{e^2qQ}{h}$$

Using Equation 1.28, one can obtain any orientation of the crystal by inserting the orientation dependent terms once more, so that the general equation for the quadrupolar splitting is given by Equation 1.29:

Equation 1.29

$$\Delta v_Q = \frac{3}{2}.\frac{e^2qQ}{h}.\left(\frac{3\cos^2\beta-1}{2}+\frac{1}{2}\eta\sin^2\beta\, cos2\alpha\right)$$

When the tensor is axially symmetric (i.e. when $\eta = 0$), the quadrupolar splitting is given by Equation 1.30:

Equation 1.30

$$\Delta v_Q = \frac{3}{2}.\frac{e^2qQ}{h}.\frac{1}{2}(3\cos^2\beta-1)$$

Equation 1.31

$$\frac{e^2qQ}{h} = C_Q$$

The value $\frac{e^2qQ}{h}$ (shown in Equation 1.31) is called the '*static quadrupolar coupling constant*' (C_Q) and can be obtained by fitting experimentally obtained data via simulations.

1.3 Influence of Dynamics

The process in which a spin system reaches the initial state at thermal equilibrium after excitation is called relaxation. This happens via interactions between the spin system and its molecular environment.

There are two main types of relaxation: spin-Lattice and spin-spin relaxation. Spin-lattice (longitudinal relaxation) focuses on the spin population regaining their Boltzmann distribution values (spin relaxing back along the z-axis, parallel to the B_0 field). Spin-spin (transverse relaxation) focuses on the decay of coherences in the transverse plane. Spin-lattice relaxation time in the rotating frame, $T_{1\rho}$, can also be measured, from which we can probe the low-frequency motional processes in a system. Measurement of all these relaxation times can offer insight into the dynamics of molecules.

1.3.1 T_1 Relaxation

T_1 relaxation, spin-lattice relaxation, is an anisotropic process (under the influence of an external magnetic field) which occurs due to fluctuations in the magnetic field felt by the spin as a result of thermal motion in the molecular system. In the absence of this process, the nuclear spin would maintain a constant angle of precession at the Larmor frequency indefinitely; however, processes take place causing the spin to deviate from this constant angle. The precessional motion is affected by the fluctuations such that the angle between the nuclear magnetization of the spins and the B_0 field changes over time. The timescale for this motion is typically nanoseconds (10^9 s^{-1}) [5]. The resulting effect is the relaxation of the spin to the longitudinal axis, typically occurring a period of seconds. This process has an exponential dependence on time, depending on a time constant T_1. Molecular motions, such as rotation of quaternary ammonium groups occur on the timescale of 10^6–10^9 s^{-1} [1]. The T_1 depends on the nucleus, spin interactions and the system, as well as parameters such as temperature and physical state of the sample and generally the most efficient relaxation occurs when the Larmor frequency matches the frequency of the motion.

After excitation, in the simple case where we consider the magnetic field fluctuating in only one direction, eg. B_x, the individual spins in the system will all experience the same field, though the fluctuating transverse field in the x-axis (B_x) which drives the relaxation process, changes over time. As the fluctuating field has positive and negative values, the overall B_x field averages to zero. In order to define the magnitude of the B_x field, the value is squared, i.e. B_x^2. The rate of fluctuation can be defined by using the autocorrelation function, which allows one to compare the fluctuating field for spin at time 'τ' and '$t + \tau$' and is equal to the product of the two time points (Equation 1.32).

Equation 1.32

$$\mathbb{G}(\tau) = \langle B_x(t)B_x(t+\tau)\rangle \neq 0$$

Where the time between 't' and '$t+\tau$', is the time interval 'τ'. When a field fluctuation is rapid, the auto correlation function decays rapidly, w.r.t 'τ'. This means when τ is 0, the $\mathbb{G}(0) = \langle B_x(t)B_x(t)\rangle$ which is $\langle B_x^2\rangle$. When τ is large, $\mathbb{G}(\tau)$ is close to zero and when τ is small, $\mathbb{G}(\tau)$ is large. The autocorrelation function is often written as an exponential decay of $\frac{\tau}{\tau_C}$, where τ_C is the correlation time of the fluctuations.

The correlation time (τ_C) is small when fluctuations are rapid and large when fluctuations are slow. Heating and cooling a system will decrease and increase the correlation time, respectively. Fast fluctuations have short correlation times and produce broad spectral density function and vice versa. The spectral density function is defined as twice the Fourier transform of the autocorrelation function, $\mathbb{G}$, and depends on the correlation time and the frequency; this frequency may be a sum of frequencies if the interaction is between heteronuclear spins, for example, dipole-dipole.[8] The relationship between lineshape and the correlation function can be explained by looking at normalised spectral density functions (Equation 1.33), $\mathcal{J}$: where ω is the frequency of interest.

Equation 1.33

$$\mathcal{J}(\omega) = \frac{\tau_C}{1+\omega^2\tau_C^2}$$

The spin-lattice relaxation time constant is expressed by Equation 1.34, which utilises the spectral density function.

Equation 1.34

$$T_1^{-1} = \gamma^2\langle B_x^2\rangle \frac{\tau_C}{1+\omega^0\tau_C^2}$$

We can see that the T_1 is dependent on the correlation time, the Larmor frequency and the gyromagnetic ratio. The spectral density function will always be a small value, but also a function of the Larmor frequency (and therefore the external magnetic field). The T_1 minimum (when the relaxation is most efficient) occurs when the correlation time is inverse to the Larmor frequency; this means that one can check the consistency of T_1 data by changing magnetic fields and observing the scaling factor.

A typical process for obtaining T_1 values is the saturation recovery pulse program; a sample placed in a magnetic field will result in the spin system reaching a state of thermal equilibrium. A train of radio frequency pulses can be applied to the sample to equilibrate the spins between the different

energy levels. Following this, the magnetization is allowed the recover towards thermal equilibrium for a time τ, after which the extent of recovery is monitored.

1.3.1.1 Dipole and Quadrupole T_1 Relaxation

As seen above in Section 1.3.1, the general equation for T_1 relaxation consists of 2 main components: the amplitude of the square of the fluctuating transverse field ($\langle B_x^2 \rangle$) and the spectral density functions corresponding to the fluctuating field. The spectral densities depend on the correlation time, τ_C, which can be influenced via heating or cooling of the sample; in the case of cooling, the fluctuation rates slow which increases correlation times resulting in a narrow spectral density function. The T_1 times, therefore, depend largely on the strength of the anisotropic interaction and the behaviour of the spectral density functions.

The equations for dipole[4] and quadrupole T_1 relaxation[9] (respectively, Equation 1.35 and Equation 1.36) in terms of spectral densities are as follows:

Equation 1.35

$$T_1^{-1} = \frac{3}{10} . {b_{jk}}^2 . \{\mathcal{J}(\omega^0) + 4\mathcal{J}(2\omega^0)\}$$

Equation 1.36

$$T_1^{-1} = \frac{3\pi^2}{2} . (C_Q)^2 . \{\mathcal{J}(\omega^0) + 4\mathcal{J}(2\omega^0)\}$$

Where b_{jk} and C_Q are the dipole-dipole and quadrupolar coupling constants, respectively (shown in Equation 1.14 and Equation 1.31).

Though the equations shown above have identical spectral densities, the behaviour of these spectral densities vary depending on the size of the fluctuations in the magnetic field and the correlation times of the motion. T_1 relaxation in liquids is dominated by stochastic molecular tumbling which results in random fluctuations in the field. In solid-state, however, these fluctuations are dependent on the motional model or the geometry of the motion and not all orientations and distances can be sampled. This is discussed further in context of the ACh salts in Section 3.1.1.2.

1.3.2 T_2 Relaxation

The T_2 relaxation process describes the decay of coherences of spins after excitation. Inducing coherence in the *xy*-plane by applying a radiofrequency pulse allows one to carry out NMR measurements; this magnetization, which is perpendicular to the external B_0 field, is called transverse magnetization [10].

After a $\frac{\pi}{2}$ pulse is applied, the individual spins precess at the Larmor frequency about the external magnetic field, resulting in a net magnetization which decays as a function of time. This free induction decay (FID) is due to fluctuations in the magnetic field felt by each individual spin; this results in a loss of coherence of the precessing nuclear spins. T_2 values, or spin-spin lattice relaxation, are typically less than the T_1 values as spins cannot obtain the initial *z*-magnetization without loss of magnetization in the *xy*-plane [11].

The T_2 relaxation can be observed by applying a spin echo pulse sequence. This experiment refocuses the out-of-phase nuclear spins (after the initial $\frac{\pi}{2}$ pulse) using a π pulse. This generates an echo if the time intervals (after the $\frac{\pi}{2}$ pulse and the π pulse) *t* and *2t*, are equal. By changing this parameter, one can obtain information on the T_2 of the system. In some cases, such as liquid state NMR measurements, the rapid Brownian movement results in short correlation times which promotes sharp resonances[12] from which the T_2 can be obtained by measuring the linewidths in the spectrum (in the absence of inhomogeneous broadening).

For quadrupolar nuclei, the π pulse is replaced with a $\frac{\pi}{2}$ and can be investigated by varying the intervals *t* and *2t* and observing the lineshapes. Measurement of transverse relaxation also offers insight into motions which occur on the timescale of micro- to milliseconds.

1.3.3 $T_{1\rho}$ Relaxation

Another approach for probing motions on the micro- to millisecond timescale is by measuring spin lattice relaxation in the transverse field. We can observe the low-frequency motional processes in a system by arraying the strength of the RF fields and measuring $T_{1\rho}$ relaxation times; this can provide us with information unobtainable via study of the aforementioned relaxation mechanisms.

$T_{1\rho}$ relaxation is more sensitive to slow fluctuations occurring in the Hz to kHz, allowing for the observation of internal motions. Since the magnetization is quantized along the RF field instead of the external magnetic field, the energy levels are split by values ranging in the kHz; this circumvents any issues that may arise due to the coherent effects (typically homonuclear dipole-dipole interaction) in the spin system [13-14].

Two of the main interactions which influence the $T_{1\rho}$ relaxation are the dipolar interaction and chemical exchange processes. The $T_{1\rho}$ values obtained are for the high gamma nuclei, in this case ^{1}H, as the extent of polarization transfer is limited by $T_{1\rho}$.

One method of investigating the $T_{1\rho}$ values is by using Cross-polarization (CP, discussed in Section 1.4.5) which utilises the high sensitivity of abundant, high gamma nuclei (^{1}H) to overcome the low sensitivity of dilute nuclei with low gyromagnetic ratio, such as ^{13}C, in solid-state NMR. Two parameters can be obtained by performing these experiments; the time constant T_{HC} and $T_{1\rho}$, which respectively represent the increase in spin magnetization (T_{HC}) before the signal begins to decay due to the spin locked proton magnetization ($T_{1\rho}$).

Both these parameters are sensitive to the dynamic processes in kHz range (µs - ms) and investigating the spectral intensities of the carbon sites as a function of contact time can provide valuable insight on the timescales of motion that are being observed. [5, 15]

Equation 1.37

$$I(tc) = I(0)e^{\frac{-tc}{T_{1\rho}}} \times \left(1 - e^{-tc\left(\frac{1}{T_{HC}} - \frac{1}{T_{1\rho}}\right)}\right)$$

Equation 1.37 describes the relationship between T_{HC} and $T_{1\rho}$, where 'tc' is the contact time. Figure 1.2 is a simulated build-up curve to highlight the differences in profile between a site which exhibits a large $T_{1\rho}$ value and small $T_{1\rho}$.

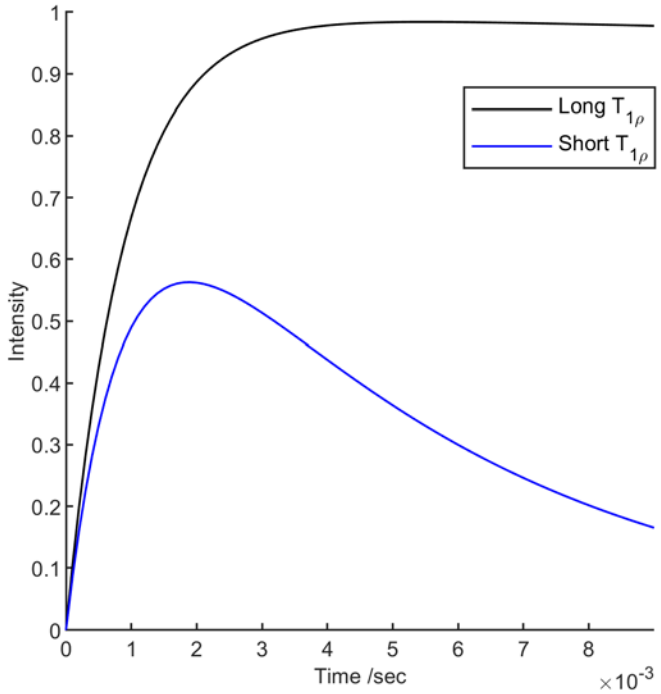

Figure 1.2: Plot showing simulation of CP build-up curves for a site with long $T_{1\rho}$ (black), and a site with short $T_{1\rho}$ (blue)

1.3.4 Chemical Exchange

Chemical exchange is a motional process in the micro- to millisecond timescale where a nucleus exchanges between two or more conformations, and thus environments; a relevant example is shown in Figure 1.3 in the case of the N-methyl carbons in the ACh salts studied.

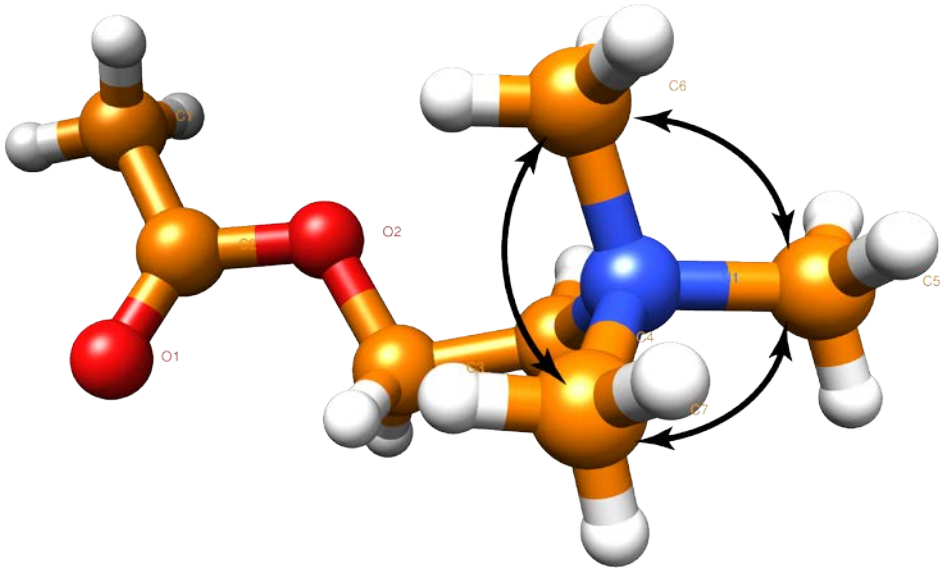

Figure 1.3: The chemical exchange phenomenon shown for the methyl carbons belonging to the quaternary ammonium group in a family of ACh salts

When the motions are in the range of typical NMR spectral frequencies (tens of kHz), these internal dynamics can be observed in the spectral lineshape. For instance, in the case of a two-site chemical exchange, sufficiently slow motions can produce two distinct chemical environments which appear on the spectrum as two distinct peaks. The rate of exchange (k_{ex}), and thus the motions, can be classed under three main motional timescales: Slow, Intermediate and Fast. These motions are categorised relative to the strength of the NMR interactions (Δv) present: $k_{ex} \ll |\Delta v|$, $k_{ex} \approx |\Delta v|$ and $k_{ex} \gg |\Delta v|$. Both the interaction frequency and the motional process share the same units, /seconds [16-17].

Since chemical exchange involves the evolution of the site populations and coherences, we treat the density matrix in Liouville space for convenience. This produces the density matrix as a vector which contains all possible observable of the system. The Liouville-von Neumann equation then governs the time evolution of the observables, shown in Equation 1.38 [18]:

Equation 1.38

$$\frac{d}{dt}\rho = -i\mathbf{L}\rho$$

Where $\mathbf{L}$ is the Liouville superoperator [16], represented as a matrix in Liouville space and ρ represents the density matrix. We obtain the time-domain solution for the density matrix by adding

the time component 't' and the exchange terms, $\boldsymbol{K_{ij}}$, which represents coherence leaving site i for site j; this is shown in Equation 1.39 [18]:

Equation 1.39

$$\frac{d}{dt}\rho = (-i\mathbf{L} - \boldsymbol{K})\rho$$

The chemical exchange and relaxation processes are also represented in matrix form and are widely described for two-site exchange with well formalized solutions. In the case of the systems we are studying in this thesis, a three-site model is more appropriate as the exchange occurs between the three carbons pertaining to the quaternary ammonium group; the equation of motion for three-site exchange is shown in Equation 1.40:

Equation 1.40

$$\frac{d}{dt}\begin{pmatrix}\rho_1\\ \rho_2\\ \rho_3\end{pmatrix} = \begin{pmatrix}-i\mathbf{L}_1 - \mathbf{K}_{12} & 0 & \mathbf{K}_{31}\\ \mathbf{K}_{12} & -i\mathbf{L}_2 - \mathbf{K}_{23} & 0\\ 0 & \mathbf{K}_{23} & -i\mathbf{L}_3 - \mathbf{K}_{31}\end{pmatrix}\begin{pmatrix}\rho_1\\ \rho_2\\ \rho_3\end{pmatrix}$$

In the case of MAS (Magic Angle Spinning) the Hamiltonian is time dependent due to the rotation of the anisotropic interaction under MAS. Numerical methods have been developed that permit the evolution of the density matrix to be calculated. These calculations are included in the simulation package *SPINACH* [19], and we have used these to simulate 3 site exchange broadening under MAS. These simulations use a Fokker Planck formalism where the time dependency and spherical averaging are eliminated at the expense of describing the system in a larger spin space.[20] We can use these exchange simulations to investigate the motional regimes the N-methyl carbons undergo in each ACh salt. By comparing them to the ^{13}C lineshapes in Section 4.4, we can assign the motional regimes as slow, intermediate or fast exchange.

In the slow exchange regime, $k_{ex} \ll |\Delta v|$, distinct resonances from each conformational state can be seen exhibiting the corresponding chemical shifts, intensities and linewidths. This occurs due to insufficiently fast interconversion between the sites resulting in separate signals for which the intensities reflect the population of the states.

When the dynamic process is on a timescale comparable to the interaction strength, $k_{ex} \approx |\Delta v|$, the exchange process leads to broadening of the peaks. If the exchange process is in the slow-to-intermediate regime ($k_{ex} \leq |\Delta v|$, the individual signals would be broadened by the exchange. If this motional process, $k_{ex} \geq |\Delta v|$, becomes faster (fast-to-intermediate) we would see the individual resonances disappear and become a single resonance; this single resonance is the population-weighted-average of the magnetically inequivalent states. In the intermediate motion regime, interferences between various time-dependent processes can be observed in a MAS SS-NMR experiment; for instance, Magic Angle Spinning (kHz), RF fields (kHz) and dynamic processes

(µs). Motions occurring on a timescale comparable to the spread of the chemical shift (~ kHz) have the potential to influence the lineshapes observed, a property referred to as chemical exchange, where jumps between sites within the molecule result in a jump in the resonance frequency during the course of the FID.

In the fast motional regime, $k_{ex} \gg |\Delta v|$, a single signal is observed at a population-weighted chemical shift. This arises due to the rapid interconversion of the sites and the averaging of the NMR parameters over the states. The NMR peak which would typically reflect the broadening nature of anisotropic interactions will instead show a narrower lineshape since motions are sufficiently rapid and the interactions have been averaged out. [21-23]

In order to model this exchange process to assess how such motions will affect the NMR lineshape, we must accurately define the relevant NMR parameters (shown in Chapter 2). This will help determine which factors within the molecular solid influence these dynamic processes.

1.4 NMR Methods in Thesis

1.4.1 Magic Angle Spinning (MAS)

Solid-state NMR experiments can be carried out under magic angle spinning (MAS) which partially averages the line broadening caused by anisotropic interactions in the system. When the sample is spun at 54.74°, interactions such as quadrupole terms, chemical shift anisotropies (CSA) and heteronuclear dipolar coupling are averaged (Figure 1.4) [4, 24-25].

At intermediate spinning speeds when the rotation frequency is less than that of the targeted anisotropic interaction, families of sidebands (spaced at the spinning frequency) appear that characterise the size and shape of the interaction; the intensity is focused into the sidebands resulting in significant improvements in signal-to-noise.

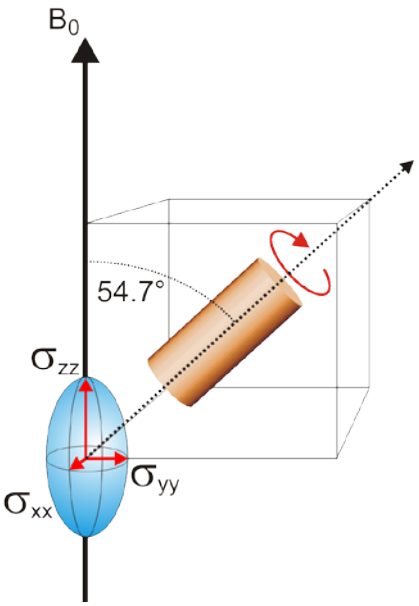

Figure 1.4: MAS is carried out at 54.74° - the different components of the tensor are projected evenly along the B_0 field.

The term $3cos^2\beta-1$ is the orientation dependent term in anisotropic interactions. When Equation 1.41 is satisfied, and the spinning frequency is larger than the interaction, the coupling is essentially equal to zero [24, 26].

Equation 1.41

$$\langle 3cos^2\theta - 1\rangle = \frac{1}{2}(3cos^2\theta_R - 1)(3cos^2\beta - 1)$$

Where 'θ_R' is the angle between the spinning axis and the external field and 'β' is the angle between the *z*-axis of the interaction tensor (in PAF) and θ_R. In a powdered sample, β takes on values for all possible orientations of the tensor, whereas θ_R is fixed by the experimenter.

From Equation 1.41, it is shown that when θ_R=54.74 the $(3cos^2\theta_R - 1)$ becomes 0. The overall anisotropic interaction, therefore, also becomes 0 [26].

Figure 1.5 illustrates the effect of MAS on a static deuterium lineshape (Figure 1.5A) at spinning frequencies 1 kHz (Figure 1.5B) and 2 kHz (Figure 1.5C). We can see that the sidebands are spaced at the respective spinning frequencies, as mentioned above.

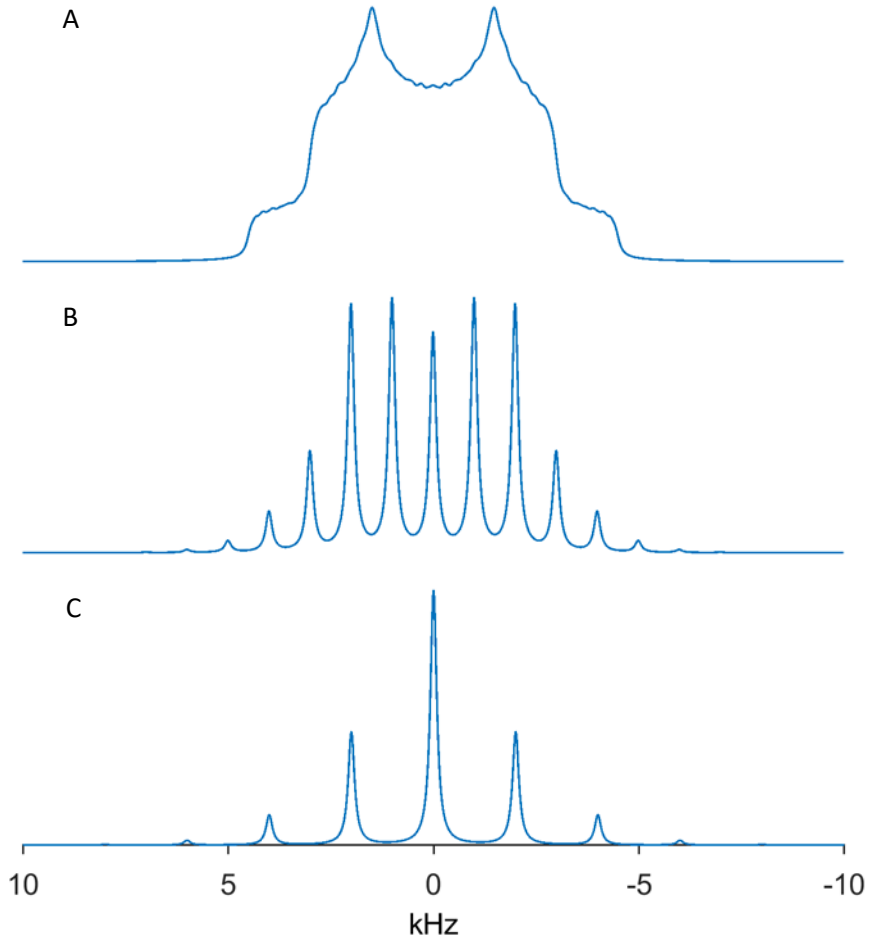

Figure 1.5: Lineshapes are simulated for a ^{2}H nucleus with a C_Q of 0.3 MHz, showing static lineshape (A), lineshape with 1 kHz MAS frequency (B) and lineshape with 2 kHz MAS frequency (C).

1.4.2 Direct Acquisition

NMR experiments on the ACh salts (Chapter 3) and the lipid and lipid-protein mixtures (Chapter 5) were performed on an Agilent DDR2 spectrometer operating at 14.1 T (Larmor frequency of 43.4 MHz for ^{14}N) equipped with a 3.2 mm triple resonance MAS probe tuned in double resonance mode, spinning at 10 kHz.

The RF amplitudes were calibrated on crystalline ammonium chloride and the ^{14}N spectra are referenced to crystalline ammonium chloride with a single reference at 35.9 ppm [27]. The ^{14}N NMR measurements were conducted using a direct acquisition pulse sequence (Figure 1.6) using 3 µs 90° pulses with an inter-pulse delay (rd) of 8 µs and the recycle delay was set to 0.5 s. The ^{14}N spectra shown are typically a result of 8K acquisitions. The datasets were zero-filled to 16,384 points and the FID was left shifted by 50 points to reach the top of the rotary echo. Line broadening of 300 Hz was used to process all ^{14}N spectra.

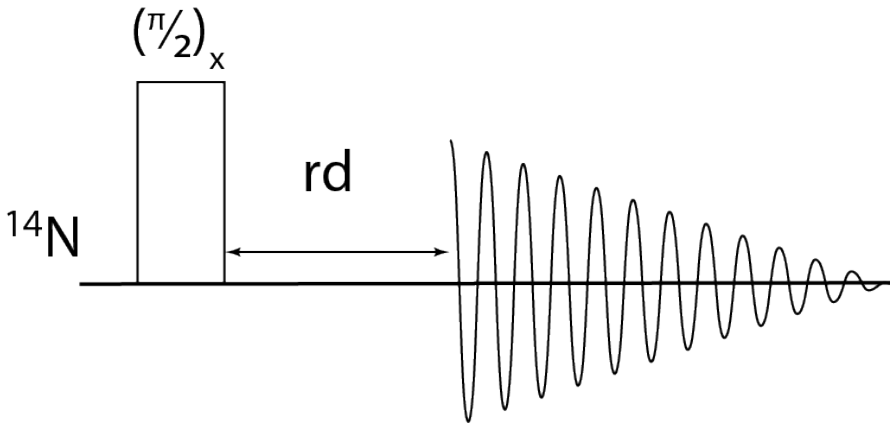

Figure 1.6: Direct acquisition pulse sequence

1.4.3 Heteronuclear Proton Decoupling

Due to the presence of strong homonuclear dipolar coupling in nuclei with low gyromagnetic ratios (such as ^{13}C and ^{14}N), the observed resonances are broad and exhibit a reduction in sensitivity [28]. These are typically larger than the moderate MAS frequencies employed and are, thus, not completely averaged. In order to counter the relatively poor resolution in solid-state spectra of low gamma nuclei (arising from the strong dipolar couplings from the protons), heteronuclear decoupling schemes are implemented during the measurement of the FID, suppressing the spin diffusion of the protons. Multiple schemes for the decoupling of protons exist such as TPPM [29], XiX [30] and *SPINAL* [31]; we have implemented the *SPINAL* decoupling technique for the CP pulse program discussed in Section 1.4.5.

1.4.4 Quadrupolar Echo

Deuterium NMR spectra of the lipid and lipid-protein mixtures were acquired on an Agilent DDR2 spectrometer operating at 14.1 T (Larmor frequency of 92.1 MHz for ^{2}H) equipped with a 3.2 mm triple resonance MAS probe tuned in double resonance mode. Anisotropic interactions such as quadrupolar couplings give rise to broad lines which have rapidly decaying FIDs. The acquisition of such signals is made challenging due to 'probe-ringing', which leads to artefacts, particularly in the baseline, when acquisitions are made directly after the pulse. By applying a solid echo pulse sequence where the dispersing transverse magnetization is refocused, a delay can be introduced between the last pulse and the start of the FID. This allows the acquisition of spectra without significant distortions, albeit at the loss of some signal and potential changes in lineshape due to the T_2 relaxation.

The solid echo pulse sequence is shown in Figure 1.7. The magnetization, initially along the *z*-axis, is transferred to the *xy*-plane with a 90° pulse. This transverse magnetization dephases under the influence of the quadrupolar interaction during the first τ period. The second 90° pulse rotates the magnetization such that the previously dephasing components are refocused after a second τ period [5].

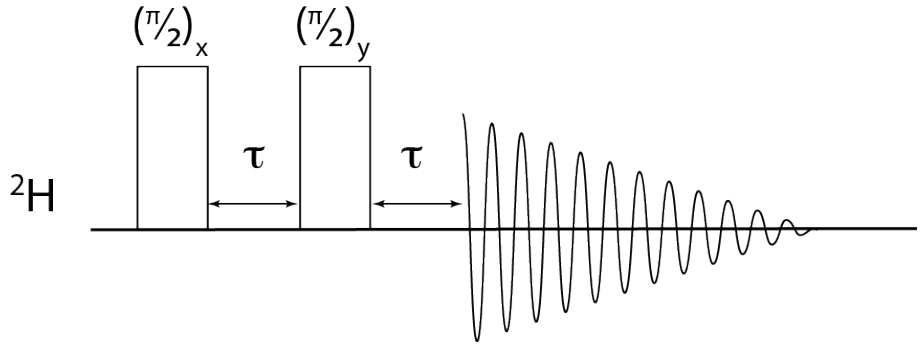

Figure 1.7: Solid Echo pulse sequence

The RF amplitudes were calibrated on liquid D_2O. The ^{2}H NMR measurements were conducted using a solid echo pulse sequence using 3 µs 90° pulses with 50 µs τ delay; the interpulse delay was chosen such that any ringing had subsided and the data could be acquired without baseline artefacts. The recycle delay was set to 0.5s and the deuterium spectra shown are typically a result of 16K acquisitions. The datasets were zero-filled to 4096 points and the FID was left shifted by 4 points to reach the top of the echo. Line broadening of 500 Hz was used to process all ^{2}H spectra. The second moment (M_2) for the ^{2}H spectra was calculated by quantifying the shape of the spectra (Equation 1.42), where ω is the frequency and $S(\omega)$ is the signal intensity at frequency ω:

Equation 1.42

$$M_2 = \frac{\int_0^\infty \omega^2 S(\omega) d\omega}{\int_0^\infty S(\omega) d\omega}$$

1.4.5 Cross-Polarization ($T_{1\rho}$)

In a standard NMR experiments where one wishes to observe dilute, low-gamma spins such as ^{13}C and ^{15}N, a number of problems arise. Firstly, the poor signal-to-noise ratio which is a result of the low abundance of these spins, and secondly, the long relaxation times which stem from the lack of strong homonuclear dipolar coupling (which typically drive the relaxation). Both issues can be solved by performing the well-known cross-polarization (CP) experiment. [24]

Since the dilute and abundant nuclei are in close proximity in many solids, they are coupled via the dipolar interaction which is exploited in CP NMR. CP utilises the heteronuclear dipolar interactions, and strength of the interaction relies on internuclear distances and mobility of the nuclei in the system observed. Given that molecular motions influence the efficiency of polarization transfer, we are able to monitor the molecular dynamics in solids by studying the connectivity between the coupled nuclei and thus the magnetization build-up of ^{13}C sites.

By introducing MAS to the system, we average the anisotropic interactions which give rise to the broad linewidths observed in typical solid-state spectra; the end result is a spectrum where the resonance condition is modulated producing a centreband signal and a series of spinning sidebands which appear at harmonics of the spinning frequency.[32] The CP-MAS pulse sequence shown in Figure 1.8, transfers magnetization from a high γ (^1H) nucleus to a low γ nucleus (^{13}C). During the CP step, the polarization is transferred by utilising the strong dipolar coupling present. Following excitation of the abundant protons by a $\frac{\pi}{2}$ pulse, spin lock pulses are applied to both the proton and low-gamma nuclei. Under these spin lock fields the magnetization is quantized in the B_1 field. By ensuring the two spin lock fields are matched, the so-called Hartmann-Hahn condition, magnetization can be transferred between two dipolar coupled nuclei. Under MAS this condition is modified to accommodate the effect of MAS, shown in Equation 1.43, where ω_H and ω_C are the respective nutation frequencies for the nuclear spins ^1H and ^{13}C, $n.\omega_r$ is the MAS frequency where typically $n = 1$ or 2 [5]:

Equation 1.43

$$\omega_H B_1 + n.\omega_r = \omega_C B_1$$

As discussed in Section 1.3.3, motions taking place in the kHz range can also be probed by measuring the magnetization build-up and decay time constants, respectively, T_{HC} and $T_{1\rho}$. This will provide us with insight on the timescales of motions (µs - ms) present in the sample.

NMR experiments on the ACh salts were performed on an Agilent DDR2 spectrometer operating at 14.1 T (Larmor frequencies of 150.9 MHz and 600 MHz for ^{13}C and ^1H, respectively) equipped with a 3.2 mm triple resonance MAS probe tuned in double resonance mode, spinning at 10 kHz.

For the experiments conducted in this chapter, the RF amplitudes were calibrated on adamantane and the ^{13}C spectra are referenced to adamantane with a single reference at 40.48 ppm. The protons were excited with a ^{1}H 90° pulses of 2.5 µs, and the ^{13}C spin-lock field set to 67 kHz and the proton RF amplitude matched experimental to obtain maximal signal. During acquisition, 100 kHz SPINAL decoupling [31] was used to supress the residual heteronuclear dipolar couplings to the protons which were not completely averaged by MAS. The pulse length and phase modulation (10°) was optimised to obtain optimal resolution with spin lock pulse lengths of 4000 µs, 500 µs, 4000 µs and 700 µs for ACh perchlorate, chloride, bromide and iodide, respectively. Prior to FT, all data was zero filled to 4096 points and had 70 Hz line broadening applied.

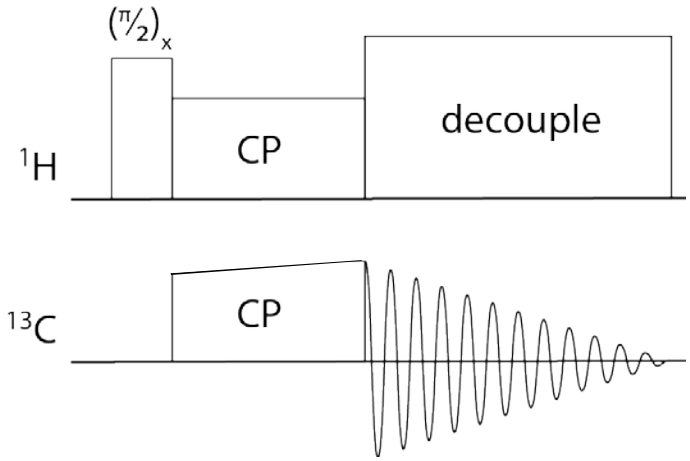

Figure 1.8: Cross polarization NMR pulse sequence with mixing times optimised for each salt: 4000 µs for ACh perchlorate and bromide, 500 µs for ACh chloride and 700 µs for ACh iodide.

1.4.6 Saturation Recovery Relaxation Experiments (T_1)

Longitudinal (T_1) relaxation measurements were made using a saturation recovery pulse sequence (Figure 1.9) rather than inversion recovery. Saturation recovery uses a train of pulses which saturates the entire spectrum, whilst the inversion recovery pulse sequence may struggle to invert. The ^{14}N spins were saturated by a train of 90° pulses (120 pulses, each 20 μs long) which saturates the energy levels such that the population of the spins are equal. Once saturated, the spins are allowed to relax for a period of time, τ, before the extent of relaxation is measured through the excitation with a last 90° pulse.

The 90° pulses were typically 5 μs. T_1 saturation recovery experiments were carried out for each salt over a range of temperatures (313 K – 238 K) to obtain insight on the dynamics and to ascertain the recycle delay.

RF amplitudes were once again calibrated on crystalline ammonium chloride and the ^{14}N spectra are referenced to crystalline ammonium chloride at 35.9 ppm [27]. Prior to FT the datasets were ACh perchlorate, chloride and bromide were zero-filled to 4096 and 8192 points for ACh iodide. The free induction decay (FID) was left shifted by 50 points to reach the top of the rotary echo and some 1st order phase manipulation was carried out. Line broadening of 500 Hz was used to process all ^{14}N spectra.

After processing the saturation curves, the sidebands were integrated and summed to provide the intensities. These intensities were then plotted as a function of relaxation time and fitted to Equation 1.44, where A_1 and A_2 reflect the amplitude of the signal and T_1 is the relaxation time constant:

Equation 1.44

$$M_z(t) = A_1 - A_2\left(1 - e^{\frac{-t}{T_1}}\right)$$

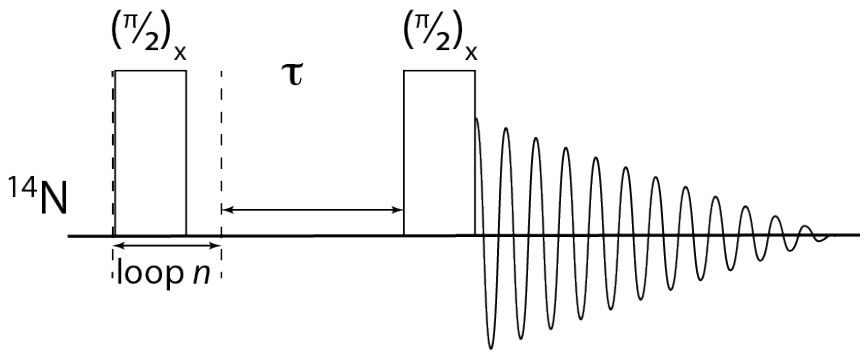

Figure 1.9: T_1 saturation recovery pulse sequence

1.5 Aims of Thesis

Solid state NMR has become a vital tool in structural biology for the structural and dynamic study of large biomolecules, such as proteins and nucleic acids. The highly abundant NMR active isotope ^{14}N, however, remains underutilized despite being prevalent in biological systems. This is largely due to the complications that arise when working with spin-1 quadrupolar nuclei with quadrupolar couplings typically on the MHz range [33]. This quadrupolar interaction, however, can provide us with useful insight into the molecular structure and is highly sensitive to relatively small changes in the local structure. This makes it a very useful reporter on the underlying dynamics in a system, without having to resort to isotope labelling. We can exploit natural abundance nitrogen-14 and carbon-13 to gain valuable insight into how crystal packing and polymorphism influences the dynamics of pharmacologically important sites.

The specific aims of this thesis are:

- To exploit the quadrupolar interaction of the ^{14}N to gain insight on the dynamics of a family of quaternary ammonium salts using MAS ssNMR.
- To complement the NMR measurements using CP-MAS NMR on natural abundance ^{13}C and conduct a series of simulations to postulate a model for the motions.
- To expand on these studies and use ^{14}N NMR in conjunction with ^{2}H NMR to investigate the interaction between membrane proteins and the lipid bilayer.

Chapter 2 Materials, Sample Characterisation and Calculation of NMR Parameters

2.1 Introduction

This chapter describes the characterisation of the acetylcholine salts (ACh) that have been studied in Chapters 3 and 4. Small molecular X-ray diffraction (XRD) was performed on each of the salts to provide context in which to interpret subsequent dynamics and relaxation studies. The high-resolution structures obtained allowed for the *ab initio* quantum mechanical (QM) calculations to be performed in *CASTEP* [34]. These calculations provided the static NMR observables, including chemical shielding anisotropy (CSA) and quadrupolar couplings (C_Q), used in numerical simulations that have proved important in the interpretation of the experimental spectra. A concise introduction to the diffraction methods and the QM calculations employed is provided together with the results of these studies.

2.1.1 X-ray Diffraction Crystallography

X-ray diffraction is a useful tool for the elucidation of the structures of crystalline materials. This is important since the physical and chemical properties of many pharmaceuticals are determined by the molecular structure and packing of the molecules in the solid-state.

Crystalline structures are characterized by a periodic arrangement of molecules in a 3D lattice. The simplest unit within this lattice is known as the unit cell which is repeated extensively in each dimension. The unit cell is defined by the three vectors *a*, *b* and *c* which characterise both the size and shape of the unit cell.[35] This means that the crystal can be assigned to one of seven crystal systems which provides insight into the packing and symmetry within [36] the crystallite. Each unit cell is typically composed of one or more asymmetric units; this is the smallest unit formed that can be repeated through symmetry-based operations and frequently represents a single copy of the molecule under study.[37] X-ray crystallography exploits the periodic properties of crystalline systems to provide information as to the size of the unit cell and the electron distribution within it.[38] This is possible as some of the X-rays passing through the sample are scattered when they interact with the electrons present.[39] Typically, this scattering will be from different atoms, resulting in interference and no coherent signal. However, as shown by Bragg, at particular orientations between the X-ray beam and the crystal, the scattering of X-rays from adjacent planes in the crystalline lattice ensures that the scattered beams constructively interfere resulting in the presence of a diffraction spot [40]. The position and intensity of this spot provide information on both the size of the unit cell and the electron density within it. By measuring a series of diffraction

patterns, where the orientation of the crystal is altered with respect to the incident X-ray beam, it is possible to reconstitute the distribution of the electron density within the unit cell, allowing a model of the structure to be refined [41].

This information becomes increasingly important as many solid-state drug substances exhibit polymorphism, where the crystalline polymorphs have the same chemical composition with differing internal crystal structures [42-44]. This can lead to differing chemical and physical properties. These differences in physical properties of drug substances in solid state have an important effect of the processing of drug substances into drug products [44].

2.1.2 *Ab initio* Calculation of NMR Parameters: *CASTEP*

The numerical simulation of NMR spectra for the analysis of exchange lineshapes and relaxation phenomena relies on knowledge of the interactions experienced by the nuclear spin (e.g. chemical shift, dipolar coupling, quadrupolar interaction) in the absence of any motional averaging. For small molecules such as ACh these are attainable from low temperature NMR studies. However, methods now exist that permit the calculation of these parameters in a computationally efficient way using *ab initio* quantum mechanical calculations. The principles underpinning these methods are described in brief below. The equations shown in this section are adapted from the following sources [34, 45-47].

Ab initio QM calculations allow the determination of all NMR observables and their relative orientations, including the chemical shielding anisotropy, J-coupling, dipolar coupling and the quadrupolar interaction. A number of *ab initio* methods have been developed for the calculation of NMR parameters including *CASTEP* (CAmbridge Serial Total Energy Package) [34], Gaussian [48] and Quantum Espresso [49].

The precision of these calculations of observables is, however, dependent on the accuracy of the computational model of the studied structure. By providing the electronic structure refinement with the high-resolution crystal structures determined here we can ensure fast convergence to an accurate structure for use in further calculations.

In this work we have employed *CASTEP* since it employs the use of planewave basis sets and is perfect for crystal systems which have small unit cells. The use of planewave basis sets allow for the user to control the accuracy of the calculation and the system is assumed to be periodic, allowing for intrinsic property of the unit cell to be utilised. The important parameters involved in a typical solid-state NMR calculation are explored further below.

2.1.2.1 Electronic Structure Calculation

The first step is to calculate the distribution of electrons around the nucleus and understand how they interact with the nuclear spin. To do this we take an iterative approach to minimise the total energy – under the Born-Oppenheimer approximation (the disparity in mass allows for the motions of electrons and nuclei to be separated) – varying the nuclear coordinates and solving the nonrelativistic, time-independent Schrodinger equation for the electronic structure. A system of electrons and nuclei can be described as (Equation 2.1):

Equation 2.1

$$\hat{H}(\boldsymbol{R})\Psi(r;\boldsymbol{R}) = E(\boldsymbol{R})\Psi(r;\boldsymbol{R})$$

The kinetic energy of the electrons is described by electronic Hamiltonian $\hat{H}(\boldsymbol{R})$ which depends on the nuclear position $\boldsymbol{R}$. $\Psi(r;\boldsymbol{R})$ is the many-body wave function describing the coordinates of the electrons 'r' and the nuclei '$\boldsymbol{R}$'. 'E' is the total energy of the system; NMR interaction tensors can be expressed as derivatives of 'E' and can, therefore, be defined by electronic structure calculations. [34, 46]

Samples of solid crystalline materials contain an unmeasurable number of electrons which make it almost impossible to run direct calculations on such systems. One must take advantage of the symmetry properties within the solids; a unit cell within the sample that can be subjected to periodic boundary conditions. This method reduces the number of atoms (and, therefore, the electrons) in the system into a more manageable number.

Bloch's theorem for single-particle wave functions demonstrates that particles in the system have quasi-periodic properties (Equation 2.2):

Equation 2.2

$$\Psi_{\boldsymbol{k}}^{n}(\boldsymbol{r}) = e^{i\boldsymbol{k}.\boldsymbol{r}}u_{\boldsymbol{k}}^{n}(\boldsymbol{r})$$

where $u_{\boldsymbol{k}}^{n}$ is a function periodic in the unit cell; $u_{\boldsymbol{k}}^{n}(\boldsymbol{r}) = u_{\boldsymbol{k}}^{n}(\boldsymbol{r}+\boldsymbol{R})$ and '$\boldsymbol{R}$' are the lattice vectors, $e^{i\boldsymbol{k}.\boldsymbol{r}}$ is the exponential describing the plane wave and propagates along the wavenumber k. The properties calculated are an average over all the values of k; the reciprocal unit cell (the Fourier transform of the lattice) contains only values of 'k' that are unique. In practise, the solutions to the Schrodinger equation change very gradually, therefore, one can take the sum over a grid of regular spaced k-points

2.1.2.2 Basis sets

In order to run simulations for an ensemble of particles, one must represent the electronic wave functions as a set of functions called the basis set. Typically, as the number of functions used is increased, the representation of the wave function becomes more accurate.

The method used in the following calculations is GIPAW (Gauge Including Projector Augmented Wave) [34], a technique using planewaves basis functions which is given in Equation 2.3 [46]:

Equation 2.3

$$\Psi_{\boldsymbol{k}}^{n}(\boldsymbol{r}) = \sum_{G} c_{k}^{n}(\boldsymbol{G})\, e^{i(\boldsymbol{k}+\boldsymbol{G}).\boldsymbol{r}}$$

The planewave functions naturally satisfy the periodic boundary conditions when '$\boldsymbol{G}$' are the reciprocal lattice vectors. Typical basis sets, e.g. GTO (Gaussian-type orbitals) [50] and STO (Slater-type orbitals) [51] resemble the molecular orbitals they represent; however, by using planewaves, calculations will use a considerably larger number of basis functions providing a greater degree of accuracy. Since this can be computationally expensive, the basis set is truncated and the sum of all wavefunctions is limited to a set of reciprocal lattice vectors bound within a sphere whose radius is defined by the cutoff energy, 'E_{cut}' (Equation 2.4):

Equation 2.4

$$\frac{1}{2}|\boldsymbol{k}+\boldsymbol{G}|^2 \leq E_{cut}$$

The basis set is, therefore, defined by the maximum kinetic energy; the ability to systematically control the cutoff energy, and hence, the convergence is a major advantage to the plane wave basis.

When calculating NMR parameters, using GTO and STO basis sets would require an extended description; however, in order to obtain the desired convergence with plane wave basis sets, one needs only to increase the E_{cut}.

The highest energy planewaves contribute to the wave functions closest to the nucleus, a region which typically does not take part in bonding; this means, in principle, the atomic species present determines the E_{cut} value required for convergence. Therefore, plane waves with small kinetic energy (low energy electron involved with bonding interactions) are more important than those with large kinetic energies.

2.1.2.3 Pseudopotentials

A disadvantage of planewave basis arises when one attempts to represent the core electrons, as this would increase the cutoff energy to very high values

This can be solved by assuming the "frozen core" approximation where the core electrons can be labelled as such and do not take part in bonding, remaining unchanged in any varying chemical environment; they can, therefore, be removed from any calculation, resulting in a reduced simulation time. The separating of the states into core and valence electrons is, however, not always clear-cut.

The pseudopotential method [46-47] works by replacing the strong Coulomb potential of the nucleus and the effects of the core electrons with an effective potential; this results in calculations where the non-valence electrons are eliminated, and the valence electrons are described by pseudo-wave functions.

2.1.2.4 NMR Calculations

In order to run NMR parameter calculations, one cannot disregard the core region as is done for the pseudopotential approximation.

However, it Is possible to obtain these NMR parameters by using a method based on pseudopotentials (Equation 2.5): a linear transformation (T) projects all valence pseudo wave functions, $|\widehat{\Psi}\rangle$, onto the corresponding wave functions $|\widehat{\Psi}\rangle = T|\widehat{\Psi}\rangle$:

Equation 2.5

$$T = 1 + \sum_{\boldsymbol{R},n} [|\varphi_{R,n}\rangle - |\hat{\varphi}_{\boldsymbol{R},n}\rangle]\langle\hat{\rho}_{\boldsymbol{R},n}|$$

$|\varphi_{R,n}\rangle$ and $|\hat{\varphi}_{\boldsymbol{R},n}\rangle$ are the all-electron and pseudo partial waves obtained from the atomic geometry calculations, $\langle\hat{\rho}_{\boldsymbol{R},n}|$ are a set of projectors. By using multiple projectors, the calculations can be made highly accurate as the atomic states establish a good basis for wave functions in the core region of the atom.

Using these methods, one can obtain accurate NMR parameters to run a series of simulations to aid comparison and analysis of experimental data in subsequent chapters (Chapter 3 and 0).

2.2 Materials and Methods

ACh perchlorate, chloride, bromide and iodide were purchased from *Sigma Aldrich*. These salts were used without purification for the NMR experiments (Figure 2.1).

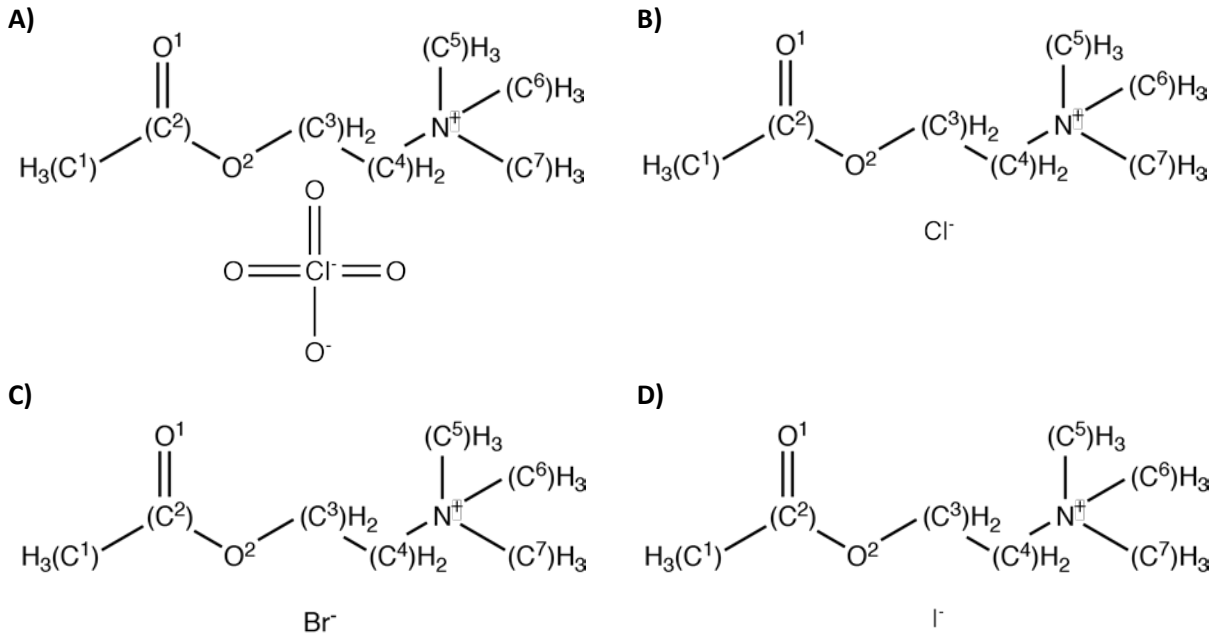

Figure 2.1: A figure showing chemical structures of ACh salts: (A) ACh perchlorate (B) ACh chloride (C) ACh bromide (D) ACh iodide

2.2.1 X-Ray structures

To accurately calculate the NMR observables, we determined new crystal structures for the four ACh salts under study in collaboration with (*Wilma Anyfanti and Prof Simon Coles*). Although there are earlier reports for the crystal structures of some of these salts [25, 52-53], fresh analyses were conducted which provided new detailed information about the crystal system that is required for the *ab initio* QM simulations.

2.2.1.1 ACh perchlorate

Colourless block-shaped crystals of ACh perchlorate were re-crystallized from methanol by slow evaporation. Mounted on a MITIGEN holder, data were collected using a ROS diffractometer operating at T = 100(2) K and a Rigaku FRE+ equipped with HF Varimax confocal mirrors and an AFC12 goniometer and HG Saturn 724+ detector diffractometer equipped with an Oxford Cryosystems low-temperature device. The experiments were run at different temperatures. In the latter, data were measured using profile data from ω-scans using MoKα radiation. In both experiments, the total number of runs and images was based on the strategy calculation from the program CrysAlisPro [54]. Data reduction, scaling and absorption corrections were performed using CrysAlisPro [54]. The structure was solved and the space group Pbca (61) determined by the ShelXS [55] structure solution program using Direct Methods and refined by Least Squares using version 2018/3 of ShelXL [56]. All non-hydrogen atoms were refined anisotropically. Hydrogen atom positions were calculated geometrically and refined using the riding model. There is a single molecule in the asymmetric unit. In other words: Z is 8 and Z' is 1.

2.2.1.2 ACh Chloride

A colourless needle-shaped crystal with dimensions 0.40×0.10×0.05 mm^3 was mounted on a MITIGEN holder. Data were collected using a DOT diffractometer equipped with an Oxford Cryosystems low-temperature device. The experiments were run at different temperatures. Data were measured using ω scans using CuKα radiation. The total number of runs and images was based on the strategy calculation from the program CrysAlisPro [54]). Data reduction, scaling and absorption corrections were performed using CrysAlisPro [54]. A multi-scan absorption correction was performed using CrysAlisPro 1.171.39.46b [54] using spherical harmonics as implemented in SCALE3 ABSPACK. The structure was solved and the space group $P2_12_12_1$ (19) determined by the ShelXT [55] structure solution program using Intrinsic Phasing and refined by Least Squares using version 2018/3 of ShelXL [56]. All non-hydrogen atoms were refined anisotropically. Hydrogen atom positions were calculated geometrically and refined using the riding model. There is a single molecule in the asymmetric unit (Z is 4 and Z' is 1).

2.2.1.3 ACh Bromide

A colourless block-shaped crystal with dimensions 0.10×0.09×0.06 mm^3 was mounted on a suitable support. Data were collected using a DOT diffractometer equipped with an Oxford Cryosystems low-temperature device. The experiments were run at different temperatures. Data were measured using ω scans using CuKα radiation. The total number of runs and images was based on the strategy calculation from the program CrysAlisPro [54]. Data reduction, scaling and absorption corrections were performed using CrysAlisPro [54]. A multi-scan absorption correction was performed using CrysAlisPro 1.171.39.46b [54] using spherical harmonics implemented in SCALE3 ABSPACK.The structure was solved and the space group $P2_1/n$ (14) determined by the ShelXT [55] structure solution program using Intrinsic Phasing and refined by Least Squares using version 2018/3 of ShelXL [56]. All non-hydrogen atoms were refined anisotropically. Hydrogen atom positions were calculated geometrically and refined using the riding model. There is a single molecule in the asymmetric unit (Z is 4 and Z' is 1).

2.2.1.4 ACh Iodide

Single colourless cut plate-shaped crystals of Ach iodide were recrystallized from methanol and ethanol as an antisolvent by vapour diffusion. A suitable crystal 0.24×0.15×0.02 mm^3 was selected and mounted on a MITIGEN holder on a DOT diffractometer. The crystal was kept at a steady T = 100(2) K during data collection. Data were measured using profile data from ω-scans using CuKα radiation. The total number of runs and images was based on the strategy calculation from the program CrysAlisPro [54]. Data reduction, scaling and absorption corrections were performed using CrysAlisPro [54]. A Gaussian absorption correction was performed using CrysAlisPro 1.171.39.46b [54]. The structure was solved and the space group *Pnna* (52) determined by the olex2.solve [57] structure solution program using Charge Flipping and refined by Least Squares using version 2018/3 of ShelXL [56]. All non-hydrogen atoms were refined anisotropically. Hydrogen atom positions were calculated geometrically and refined using the riding model. There are two molecules in the asymmetric unit and the value of Z' is 1.

In addition to the crystallographic studies, differential scanning calorimetry (DSC) studies were conducted on the family of ACh salts (powder, single crystal and ground single crystal) revealed an absence of any physical state changes as a function of temperature. This confirmed that the salts did not undergo any phase transitions or conformation changes.

2.2.2 *Ab initio* QM Simulations (*CASTEP*)

The chemical shielding anisotropy and electric field gradient/quadrupolar interaction for each of the ACh salts studied were calculated using *CASTEP*, which as described above, provides a fast efficient quantum mechanical method which uses planewave basis sets to compute numerous properties in periodic systems [34]. The simulations required ".cell" input files containing all information on the lattice structures for each salt. These were obtained by converting the raw ".cif" files (obtained via XRD) to ".cell" files using the program *cif2cell*. [58]

Geometry optimisation and NMR calculations were carried out using IRIDIS High Performance Computing Facility with dual 2.0 GHz Intel Skylake processor.

Geometry optimisation calculations were performed via pseudopotentials using the BFGS (Broyden–Fletcher–Goldfarb–Shanno)[34] optimisation method which finds the lowest energy structure and supports cell optimisation. The energy cutoff was optimised for each system after convergence was confirmed.

NMR calculations were performed using pseudopotentials and the GIPAW method. An ultrafine cutoff level proved to provide the most accurate values; since accurate NMR calculations were crucial for later chemical exchange simulations, a high cutoff value of 900 eV was chosen. The EFG tensor for each of the salts were also obtained from the *CASTEP* output, parameters necessary to simulate a series of ^{14}N MAS spectra, shown in Section 2.3.2.5, Figure 3.3.

CASTEP outputs contain data on the geometry (unit cell, atomic coordinates etc) and NMR parameters (NMR tensors and chemical shifts) which were then used for numerical calculations to model the chemical exchange process at the N-methyl sites in Section 4.4.

2.3 Results

2.3.1 XRD Results

2.3.1.1 Unit Cell

These studies have been performed in collaboration with Wilma Anyfanti and Prof Simon Coles.

The information for the unit cell obtained for each of the crystalline structures studied is shown below in Table 2.1; from the parameters obtained below it can be seen there are variances in properties between the 4 salts. ACh perchlorate, chloride and iodide salts exist in an orthorhombic unit cell with orthogonal axes. In contrast the ACh bromide which adopts a monoclinic unit cell with one axis tilted at 108.7°. ACh perchlorate, ACh chloride and ACh bromide each contain a single molecule of ACh per asymmetric units, whilst ACh iodide contains two. The R1 values measure the agreement between the X-ray diffraction data and the crystallographic model; typically, values are <10% and are considered good. The files containing information on the unit cells for each salt can be found in Appendix E.2.

Table 2.1: Table displaying XRD parameters obtained (Unit cell, space groups etc.)

Parameters	ACh Perchlorate	ACh Chloride	ACh Bromide	ACh Iodide
Unit Cell	Orthorhombic	Orthorhombic	Monoclinic	Orthorhombic
3D Space Group	Pbca	$P2_12_12_1$	$P2_1/n$	Pnna
a (Å)	11.9879	6.3078	7.0722	31.36
b (Å)	9.6418	9.9019	13.4495	11.499
c (Å)	19.3129	15.3171	10.9523	11.4925
β	/	/	108.7°	/
T (K)	100	100	100	100
R1	6.98%	2.20%	2.73%	6.60%
molecules in Asymmetric Unit Cell	1	1	1	2
molecules in the unit cell	8	4	4	16

2.3.1.2 Torsion Angles and Atomic Distances

A comparison of the structures of the ACh reveals some key differences in the chemical structure of the ACh salts. The torsion distances are discussed below; Figure 2.2 shows the backbone torsion angles explored with labelled atoms.

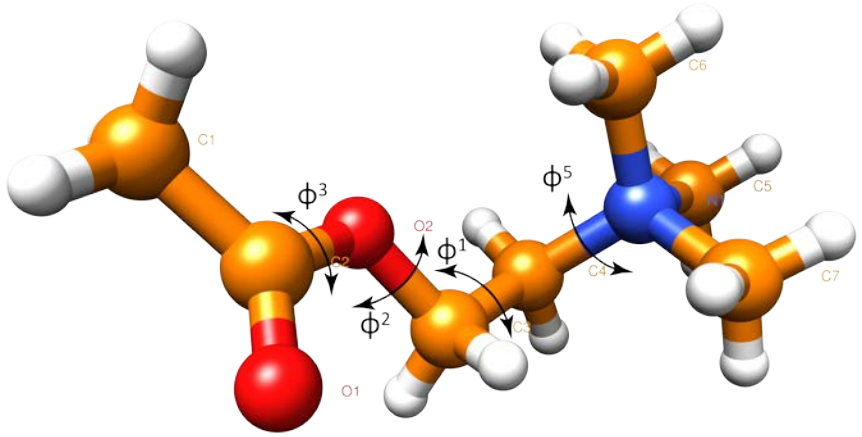

Figure 2.2. Structure of ACh chloride with the atoms labelled and backbone torsion angles measured, 'ϕ^N'.

Table 2.2: Table of torsion angles for ACh perchlorate, chloride, bromide and both molecules present in the unit cell of the iodide salt.

		Torsion Angle (°)			
ϕ^N	**Atoms**	**ACh perchlorate**	**ACh chloride**	**ACh bromide**	**ACh iodide**
ϕ^1	O^2-C^3-C^4-N^1	80.571	84.198	77.875	88.335/-87.609
ϕ^2	C^2-O^2-C^3-C^4	176.634	-169.884	76.013	81.203/-82.019
ϕ^3	C^3-O^2-C^2-O^1	-0.476	6.510	5.248	0.673/-0.248
ϕ^4	C^3-O^2-C^2-C^1	-179.663	-173.575	-171.944	-178.339/178.810
ϕ^5	C^5-N^1-C^4-C^3	61.936	170.849	-174.937	70.479/-70.799
ϕ^6	C^6-N^1-C^4-C^3	-60.124	-70.098	-56.130	-171.217/170.927
ϕ^7	C^7-N^1-C^4-C^3	178.661	52.789	66.844	-51.944/51.846

The torsion angles present in the 4 ACh salts is provided in Table 2.2, including both molecules present in the asymmetric unit cell for ACh iodide; as expected, the quaternary ammonium group angles indicated for $\phi^{5,6,7}$ show the quaternary carbon methyls to be ~120° from each other adopting a trigonal-planar conformation. All four salts indicate the nitrogen atom (N^1) to be *gauche* to the ether oxygen (O^2), a trait seen in past studies [25] for three of the salts (perchlorate, chloride and bromide) and now observed in the iodide salt.

Interestingly, the main backbone of the ACh molecules show some variation in torsion angles, specifically the plane containing atoms C^2 - O^2 - C^3 - C^4, (ϕ^2). Both ACh perchlorate and chloride

possess angles of 170° to 180°, whereas ACh bromide and iodide have torsion angles roughly ~80° indicating a difference in chemical structure to that of ACh perchlorate and chloride.

The torsion angles for both ACh bromide and iodide signify a folding of the structure causing the O^1 atom to be in closer proximity to the N-methyl carbons. This is reflected in the atomic distances measured, shown in Table 2.3. The distances between atoms C^5 and O^1 show lengths of 6.319 Å, 6.234 Å, 5.094 Å and 4.179 Å for ACh perchlorate, chloride, bromide and iodide respectively. This "folding" can also be seen in Figure 2.3C and D. The data presented reveals varying chemical structures for the four salts, with ACh perchlorate and chloride showing a high degree of similarity in both torsion angles and bond lengths; ACh bromide and iodide, however, show more unique values. This shows that within the unit cell, the counterion present can determine the conformation adopted by the ACh molecule influencing its packing, and potentially the dynamics present. The atomic distances shown in Table 2.3 for both ACh iodide molecules in the asymmetric unit cell differ by a maximum of ~0.02 Å.

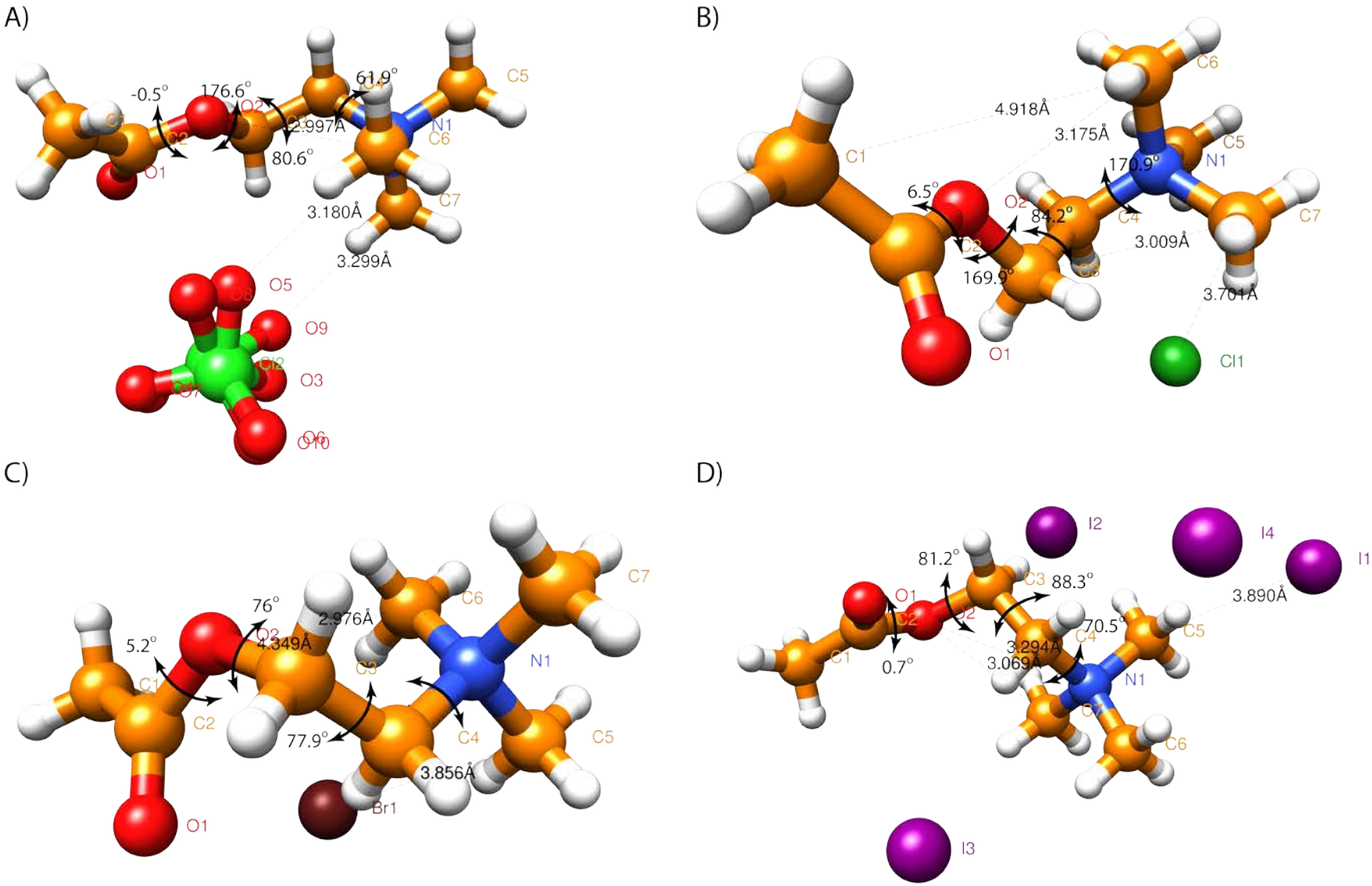

Figure 2.3: Figure displaying torsion angles φ1,2,3,5 and key atomic distances for ACh perchlorate C^6-O^2, O^5-C^6, O^9-C^7 (A), ACh chloride C^1-C^6, C^6-O^2, C^7-C^3, Cl^1-C^7 (B), ACh bromide C^6-C^1, C^6-O^2, Br^1-C^5 (C) and ACh iodide (one of the molecules in the asymmetric unit) C^7-O^2, C^7-C^1, C^5-O^2, I^1-C^5 (D)

As seen in Figure 2.3A, the perchlorate ion shows a static disorder such that two distinct conformations are seen, both displaying a tetrahedral arrangement. This is a feature typical of the perchlorate ions; variable temperature single crystal X-ray diffraction experiments detected the same trend in disorder at lower temperatures. This confirms it is a static type of disorder, with different counterion orientations present in different unit cells, and not dynamic and temperature dependent. The atomic distances measured between the perchlorate ion and the N-methyl carbons range between ~3 Å and ~5.5 Å. We know that the size of the halide counterion increases as we go further down the periodic table, meaning ACh chloride possesses the smallest counterion of the four salts, with atomic distances of ~3.5 Å to 6 Å between the counterion and the N-methyl carbons. ACh bromide and iodide exhibit distances between the counterion and the N-methyl carbons ranging ~3.8 Å and ~6 Å, with iodide having larger values (the distances between the counterion and C^6 are 3.8 Å and 5.7 Å for ACh bromide and iodide, respectively). Interestingly, the unit cell obtained from XRD for ACh iodide (Figure 2.4) revealed the presence of iodide counterions in special symmetry positions signifying that symmetry operations can be performed about the iodide ion and it will remain invariant.

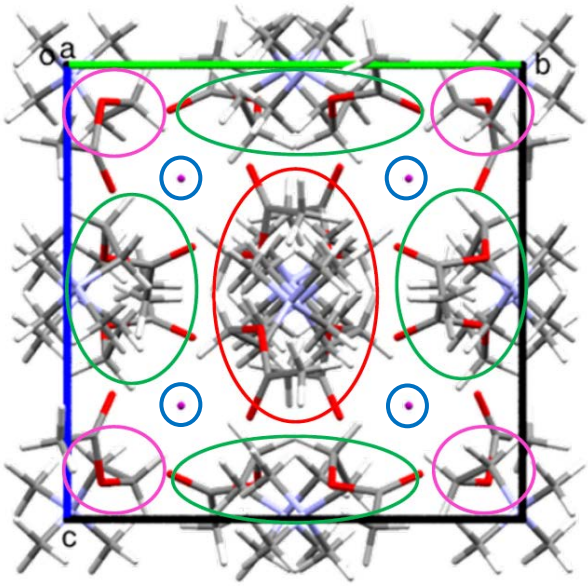

Figure 2.4: Figure displaying the unique unit cell for ACh iodide. 4 counterions are seen (blue circle), with one ACh molecule in the centre (red circle). Each green circle represents a ½ ACh molecule, and the magenta circles denote ¼ Ach molecules. The total sum of acetylholine molecules, therefore, is 4.

Table 2.3: Table displaying atomic distances between indicated atoms for ACh perchlorate, chloride, bromide and iodide (both molecules in the asymmetric unit).

Atoms		ACh ClO_4^- (Å)	ACh Cl (Å)	ACh Br (Å)	ACh I (Å)
C^6	O^1	4.921	4.860	4.508	5.242/5.256
C^6	O^2	2.997	3.175	2.976	4.462/4.458
C^6	C^1	4.752	4.918	4.349	6.088/6.094
C^6	C^3	3.046	3.168	3.033	3.826/3.831
C^6	C^4	2.477	2.497	2.499	2.433/2.436
C^7	O^1	5.164	4.786	5.447	4.775/4.768
C^7	O^2	3.934	3.902	4.008	3.069/3.054
C^7	C^1	6.033	5.934	6.095	4.786/4.772
C^7	C^3	3.049	3.009	3.115	2.957/2.955
C^7	C^4	2.470	2.495	2.485	2.478/2.476
C^5	O^1	6.319	6.234	5.094	5.523/5.533
C^5	O^2	4.448	4.553	4.434	4.179/4.173
C^5	C^1	6.640	6.766	5.857	6.392/6.391
C^5	C^3	3.185	3.822	3.826	3.145/3.150
C^5	C^4	2.416	2.421	2.419	2.488/2.488
N^1	C^1	5.379	5.428	4.980	5.259/5.257
N^1	O^1	4.943	4.795	4.363	4.513/4.518
N^1	O^2	3.185	3.250	3.202	3.294/3.285
N^1	C^3	2.557	2.573	2.569	2.562/2.562
Bond lengths between halide counterions (A^N) and N-methyl atoms					
A^1	C^7		3.701	5.686	6.035/6.031
A^1	C^6		5.404	3.853	5.757/5.743
A^1	C^5		3.768	3.856	3.890/3.878
A^1	N^1		4.753	4.197	5.350/5.339
Bond length between perchlorate atoms and N-methyl carbons					
C^6	O^5	3.180			
C^6	O^8	3.707			
C^6	O^9	3.728			
C^6	Cl^1	4.286			
C^6	Cl^2	4.306			
C^7	O^5	3.991			
C^7	O^9	3.299			
C^7	O^7	5.555			
C^7	Cl^1	4.566			
C^7	Cl^2	4.535			
Bond lengths between molecule #1 and counterion of molecule #2 (A^2 and N-methyl C)					
A^2	C^7		4.924	4.073	4.359/4.366
A^2	C^6		3.596	4.116	6.093/6.099
A^2	C^5		6.011	4.073	4.038/4.041
Bond lengths between molecule #1 and #2 (ClO_4^- and N-methyl C)					
O^7	C^5	4.203			
O^7	C^7	3.595			

2.3.2 *CASTEP* Calculations of NMR Parameters of Acetylcholine Salts

CASTEP calculations were performed on the newly derived crystal structures. The first step was the geometry optimization of the salts; this provided a structure with the lowest energy conformation which was then used to run NMR calculations. The energy minimizations typically converged after ~5 iterations and the deviation in atom positions from the crystal structure were less <0.5 Å. The outputs from the geometry optimization were then used to perform a series of NMR calculations. The NMR calculations produced outputs from which we obtained the chemical shift tensor (using the function written by Dr Ilya Kuprov, available in latest version of *SPINACH* [19]); in order to convert the values into ppm we performed a NMR calculation on the standard used in our measurements, adamantane, and applied the following conversion on the chemical shielding tensor (CST): $(CST \times (-1) + 175)$. The same conversion was applied to the chemical shift tensor for the ACh salts producing isotropic chemical shifts corresponding to each of the ^{13}C sites; the observed shifts showed good agreement with the experimental data. The distribution of calculated chemical shifts are visualised in Figure 2.5 as a ^{13}C spectrum. Note these simulated spectra (Figure 2.5) are the sum of Lorentzian peaks with artificial linebroadening of 70Hz at the appropriate chemical shifts and are presented to demonstrate the distribution of chemical shifts obtained. There are, however, small variations between the simulated and experimental chemical shifts with a maximum deviation of 7 ppm for the iodide salt occurring at the OCH_2 site. This peak is hidden in the experimental data due to the broad nature of the N-methyl peak, making it difficult to assign the site accurately. With the exception of deviations in the spectra due to motions, we speculate the differences that are observed in the calculations are comparable to the differences reported from other *ab initio* studies.[45] Table 2.4, Table 2.5, Table 2.6 and Table 2.7 display the experimental chemical shifts for each ACh salt, with calculated NMR parameters, including the isotropic chemical shifts, the CSA values and the Euler angles. Tables containing all *CASTEP* outputs are shown in Appendix C, with code to perform the CASTEP simulations in Appendix E.3, E.4.

2.3.2.1 ACh perchlorate

Table 2.4: Table of experimentally acquired chemical shifts and the simulated NMR parameters for ACh perchlorate, using CASTEP

Site	ACh perchlorate			
	Exp (ppm)	Sim (ppm)	CSA tensor	Euler angles (°)
C-methyl (C^1)	23	19.1193	[-10.0, 30.9, 36.7]	114.55, 19.02, 29.67
C=O (C^2)	175	179.8384	[272.6,116.5, 1.2]	101.71, 62.95, 43.52
O-CH_2 (C^3)	62	65.0781	[25.9, 81.8, 86.7]	4.78, 153.64, -146.76
N-CH_2 (C^4)	67	69.4441	[25.5, 85.8, 97.4]	5.69, 110.52, -8.05
N-methyl ($C^{5,6,7}$)	57	59.1386 54.3742 52.4345	[4.8, 76.1, 80.2] [1.3, 85.2, 90.1] [0.4, 72.9, 85.2]	-103.37, 51.05, -48.43 -3.20, 92.41, -114.97 118.72, 16.89, 87.14

2.3.2.2 ACh chloride

Table 2.5: Table of experimentally acquired chemical shifts and the simulated NMR parameters for ACh chloride, using CASTEP

Site	ACh chloride			
	Exp (ppm)	Sim (ppm)	CSA tensor	Euler angles (°)
C-methyl (C^1)	24	20.5698	[-8.2, 30.5, 39.4]	-143.76, 151.15, -149.13
C=O (C^2)	175	180.7738	[274.8, 116.1, 151.2]	152.92, 158.56, 131.08
O-CH_2 (C^3)	60	64.0163	[23.8, 79.5, 88.6]	3.19, 151.27, -137.53
N-CH_2 (C^4)	63	65.2097	[26.5, 76.9, 92.1]	116.11, 96.24, -37.20
N-methyl ($C^{5,6,7}$)	55	55.2757 54.3971 50.5475	[4.4, 77.3, 84] [6.3, 67.1, 78.1] [5.3, 77.4, 80.4]	45.37, 39.83, 78.78 -60.73, 32.92, -84.34 110.17, 90.84, -145.68

2.3.2.3 ACh bromide

Table 2.6: Table of experimentally acquired chemical shifts and the simulated NMR parameters for ACh bromide, using CASTEP

Site	ACh bromide			
	Exp (ppm)	Sim (ppm)	CSA tensor	Euler angles (°)
C-methyl (C^1)	22	20.5674	[-5.2, 30, 36.9]	60.60, 76.15, -13.99
C=O (C^2)	174	178.8254	[274.4, 115.2, 146.7]	99.95, 65.14, 159.81
O-CH_2 (C^3)	62	62.1987	[23.7, 62.9, 99.8]	158.32, 78.54, -19.92
N-CH_2 (C^4)	67	68.8126	[32.4, 81.8, 92.1]	89.48, 55.33, 89.48
N-methyl ($C^{5,6,7}$)	56	57.6849 54.2945 53.7728	[5.6, 80.9, 86.4] [5.9, 73.8, 83] [8.6, 74.6, 78]	-74.68, 58.15, -89.90 101.18, 57.80, 178.57 92.94, 58.20, 0.90

2.3.2.4 ACh iodide

Table 2.7: Table of experimentally acquired chemical shifts and the simulated NMR parameters for both molecules present in the asymmetric unit cell for ACh iodide, using CASTEP

Site	ACh iodide			
	Exp	Sim (ppm)	CSA tensor	Euler angles (°)
C-methyl (C^1)	22	21.9108/21.8693	[-7.76, 39.99, 33.50]/ [-7.78, 39.93, 33.45]	300.43, 73.98, 264.09/ 150.84, 145.73, 149.29
C=O (C^2)	175	179.9155/179.9083	[276.10, 148.74, 114.90]/ [276.08, 148.75, 114.88]	111.39, 76.14, 117.79/ 146.49, 25.50, 3.10
O-CH_2 (C^3)	~68	61.3167/61.3640	[22.85, 62.41, 98.68]/ [22.97, 62.33, 98.78]	112.72, 18.40, 96.01/ 277.54, 73.14, 239.69
N-CH_2 (C^4)	~68	71.3042/71.2468	[38.96, 95.01, 79.93]/ [38.85, 95, 79.88]	131.92, 92.50, 135.43/ 176.37, 42.46, 48.05
N-methyl ($C^{5,6,7}$)	58	58.0227/58.0282	[5.76, 88.01, 80.28]/ [5.41, 88.22, 80.44]	233.43, 104.08, 295.78/ 201.61, 38.86, 8.39
		55.6253/55.6021	[6.29, 84.31, 76.26]/ [6.37, 84.18, 76.24]	213.22, 85.01, 302.29/ 201.61, 38.86, 8.39
		53.5114/53.4281	[8.29, 78.18, 74.05]/ [8.10, 78.43, 73.74]	14.63, 130.01, 42.31/ 40.17, 77.79, 123.35

All four salts produced 3 individual resonances for the N-methyl carbons; this differs from the experimental data where the lines were broadened, and individual resonances were not present until reaching low temperatures. These significant differences between the experimental and calculated data is indicative of the chemical exchange process occurring at the site.

These quantum mechanical calculations provided the NMR parameters necessary to perform chemical exchange simulations. The Euler angles required were obtained from the *CASTEP* output. The *CASTEP* NMR calculation for ACh iodide produced two chemical shifts for the each of the carbon sites corresponding to the 2 molecules present in the asymmetric unit cell. Figure 2.5 shows the simulated spectra reflecting the distribution of chemical shifts with an artificial line broadening added. The variation in amplitude between the different sites observed in the ACh iodide spectrum (Figure 2.5D) arises from the overlap of the peaks pertaining to both molecules in the asymmetric unit. These are difficult to resolve since the difference between the isotropic shifts are small, ranging from 0.005 ppm (N-CH_3 site, C^5) and 0.057 ppm (N-CH_2, C^4).

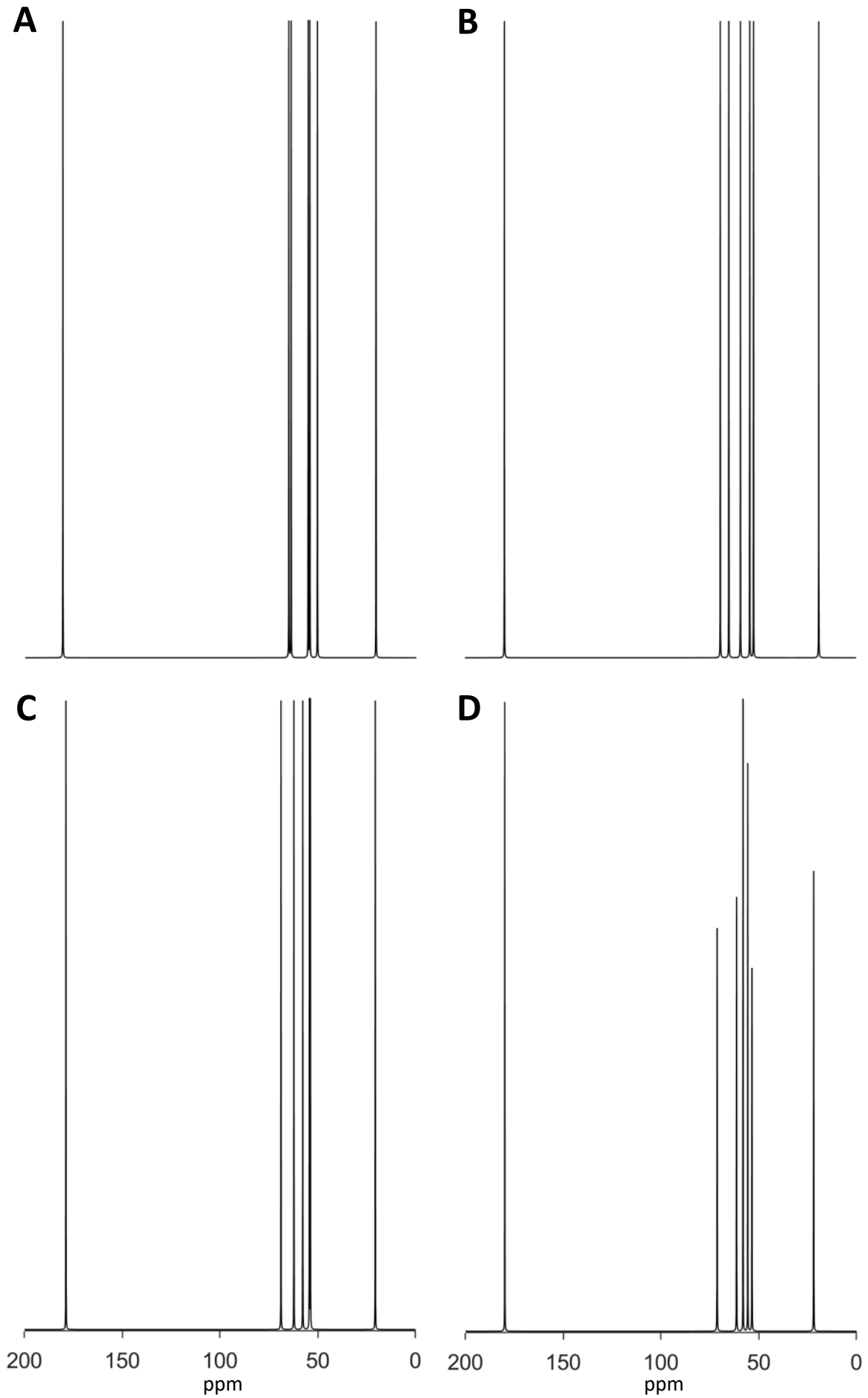

Figure 2.5: Synthetic spectra showing the distribution of isotropic chemical shifts obtained from CASTEP simulations for each of the acetylcholine salts studied. (A) ACh perchlorate (B) ACh chloride (C) ACh bromide (D) ACh iodide. The spectra were calculated in the time domain, with signals centred at each of the isotropic shifts and decaying with a value of 5 Hz. The data were zero filled to 132k points prior to fourier transform. All data plotted are normalised to the maximal intensity. Note J-coupling and all anisotropic interactions have been omitted and these spectra are shown purely to reflect the distribution of the isotripic chemical shifts.

2.3.2.5 Quadrupolar Calculations

In Chapter 3, we have investigated the effect of motion of the ^{14}N spectrum of the quaternary site within the ACh molecule and to aid in the interpretation of the spectra, the quadrupolar NMR parameters (C_Q, asymmetry parameter and the EFG tensors) for the nitrogen site were obtained from the static *CASTEP* calculation outputs.

As predicted, due to the high degree of symmetry present in the quaternary ammonium groups the ^{14}N quadrupolar coupling is relatively small, 10's kHz, compared to other ^{14}N sites [27, 59]. Due to the small size of the quadrupolar interactions, this indicates that the spectra can be studied using standard echo sequences in subsequent experimental chapters. Interestingly from the NMR parameters shown in Table 2.8, we can see that there is a vast different between the ACh salts, specifically the quadrupolar coupling constants. This indicates that the properties at the nitrogen site are different for the salts, irrespective of motion, suggesting that small differences in the molecular structure at the site can have large influences on the size of the quadrupolar interaction present at the quaternary ammonium site.

Table 2.8: Table of simulated quadrupolar NMR parameters for ACh bromide, using CASTEP

Site: ^{14}N	**ACh perchlorate**	**ACh chloride**	**ACh bromide**	**ACh iodide**
C_Q (kHz)	85.7	145.7	227.2	50.7
η	0.7581	0.2477	0.7044	0.5224
EFG tensor	0.0178 -0.0157 -0.0022	0.0303 -0.0189 -0.0114	0.0473 -0.0403 -0.0070	0.0105 -0.0080 -0.0025

2.4 Discussion

In this chapter, we show crystal structures determined via XRD for ACh perchlorate, chloride, bromide and iodide. Analysis of the torsion angles and atomic distances indicated that ACh perchlorate and chloride showed similar backbone structures, as do ACh bromide and iodide. The unit cells pertaining to each salt showed different values, with ACh iodide exhibiting the largest unit cell size with twice the number of molecules in the asymmetric unit cell.

Using the newly acquired crystal structures, a series of numerical static NMR calculations were performed using *CASTEP* in order to obtain NMR parameters necessary to carry out the chemical exchange simulations shown in Section 4.4: Chemical Exchange Lineshape Simulations. The static quadrupolar NMR parameters (C_Q, asymmetry parameter and EFG tensor) were also obtained to simulate the ^{14}N MAS lineshape shown in Section 3.3.1, which is indicative of a difference in symmetry and quadrupole interaction as well as other properties for each of the ACh salts at the quaternary ammonium ^{14}N site. A comparison between the ^{14}N simulations and the ^{14}N experimental data will be discussed in Chapter 3: Investigations into the Dynamics of Acetylcholine Salts by ^{14N} NMR.

Chapter 3 Investigations into the Dynamics of Acetylcholine Salts by ^{14}N NMR

3.1 Introduction

Acetylcholine is an important neurotransmitter, binding to two pharmacologically important receptors: the nicotinic acetylcholine receptor and the muscarinic acetylcholine receptors. These are important representatives of the ligand gated ion channel and G-protein coupled receptors families of protein, respectively. These receptors are the site of action of a wide range of drugs including anaesthetics and those used for the treatment of addiction, Alzheimer's [60-61] and Parkinson's Disease [62-63] and thus an understanding of their molecular pharmacology is of interest in the treatment of such conditions.

In the case of the nicotinic acetylcholine receptor, the ACh molecules diffuse across the neuromuscular junction and bind to the ACh receptors on the muscle fibres resulting in the opening of the ion channels.[64] This allows for the necessary ion exchanges to take place in various body parts, for instance, the central nervous system. In the muscarinic receptor the ACh binds to seven-transmembrane receptors are the most abundant of receptors and a conventional target for therapeutic drugs [65], and activates its complementary G-protein. A number of pharmacophores are involved in the binding of ACh to these receptors, but common to all is the interaction of the positively charged quaternary ammonium group with the ligand binding site through the formation of cation-pi interactions, shown in Figure 3.1.[2, 66]

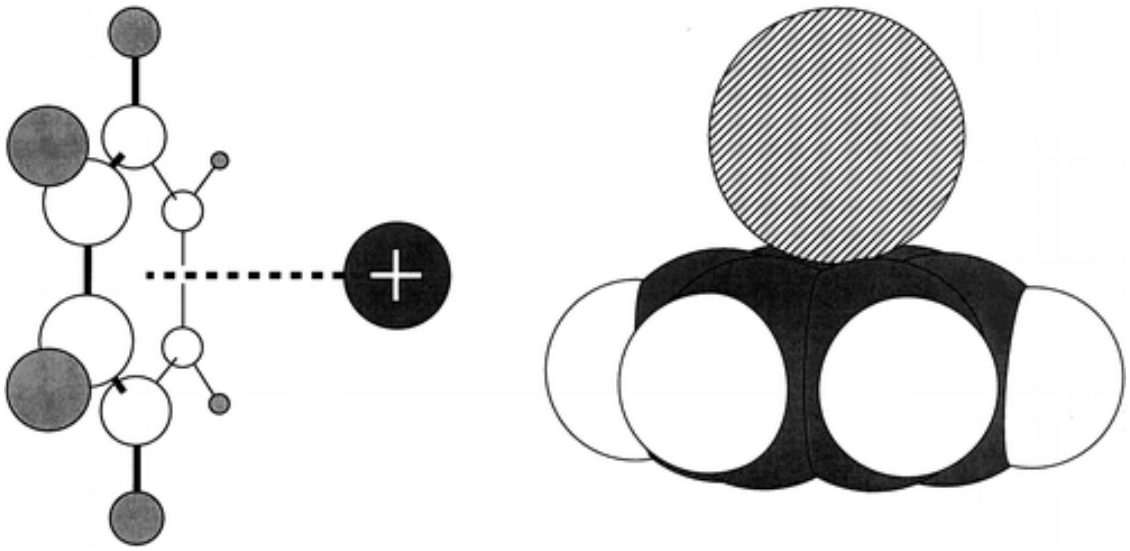

Figure 3.1: Schematic of the cation-pi interaction with generic cation (left) and space-filled model of cation-benzene complex. [2]

Indeed, the quaternary ammonium groups are becoming an important part in the medicinal chemists' palate of pharmacophores that can be utilized when designing new drugs. One mechanism for understanding how the quaternary ammonium group binds to receptors or packs in pharmaceuticals is the study of its dynamics, which are rich due to the high degree of symmetry.

The dynamics of ACh and the quaternary ammonium group is important as it will play a factor in the proficiency of the ligand binding [67]; these properties have previously been explored using solid-state NMR spectroscopy.[1, 68-69]

This chapter focuses on 4 ACh salts; ACh perchlorate, ACh chloride, ACh bromide and ACh iodide. These salts were characterised, and the molecular dynamics were explored by lineshape and spin-lattice relaxation analysis. Previous work on ACh salts show that the structure and dynamics of the salts can be explored by detecting ^{2}H, which was incorporated into the sample via isotopic labelling; the ^{2}H lineshapes varied over a range of temperatures for ACh perchlorate, chloride and bromide [1] (spectra shown in Figure 3.2).

Due to the well-characterised nature of these salts, we have used them to investigate the potential of ^{14}N NMR to study the conformation and dynamics of the systems; this would provide a means for studying the dynamics of the quaternary ammonium group without resorting to isotope labelling. The systems are particularly attractive to analyse via ^{14}N as they are predicted to have a small C_Q as a result of dynamics and symmetry. Sites, such as the quaternary ammonium group and tetramethylammonium groups [70-71] that possess a high degree of symmetry typically exhibit small anisotropic interactions.

In addition to the symmetry, previous static ^{2}H NMR studies[1], which probed the N-methyl groups' dynamics have indicated that in some salts, the quaternary ammonium group exhibits significant motion [71] about two axes of rotation that further scale the anisotropic interactions: 1) the rotation of the individual methyl groups (C_3 axis) and 2) the rotational motion of the entire quaternary ammonium group (C_3' axis) which averages the observed deuterium quadrupolar splitting, leading to narrower powder patterns (Figure 3.2). In this previous study, the molecular dynamics of ACh salts were explored by directly influencing these motions via cooling and heating of the sample. It was shown that the rotational motion of the ammonium group in ACh perchlorate (Figure 3.2C) has a lower energy barrier compared to the other two salts, ACh bromide and ACh chloride (Figure 3.2A and (Figure 3.2B). This is evident from the quadrupolar lineshape as the sample had to be cooled below 210 K in order to observe any large differences in the Pake pattern. ACh bromide, however, showed different lineshapes at each temperature, from high to low, indicative of a higher energy barrier. ACh chloride and ACh bromide showed a sharp central feature at 293 K, consistent with rotation about either the quaternary methyl carbons or the entire ammonium group. The presence of the central feature superimposed on the Pake pattern for ACh bromide (Figure 3.2A) is indicative

of motions entering the intermediate motional regime [1, 72-73]; however, at 293 K, the lineshape for ACh chloride is dominated by intermediate motions. For both ACh bromide and chloride, the central feature did not disappear until the temperature was lowered from 230 K to 190 K where an increase in the intensity of the powder lineshape was observed. This is indicative of intermediate motions giving rise to the previously seen lineshapes, being suppressed and the deuterium powder pattern at low temperatures governed by rapid rotation about either the quaternary ammonium group or the methyl groups, resulting in scaled quadrupolar coupling constant of 40 kHz (Figure 3.2A and Figure 3.2B at 170 K).

Interestingly, in contrast to the strong temperature dependence of ACh bromide and chloride, the ACh perchlorate ^{2}H spectra (Figure 3.2C) showed little variation until 210 K. Below 210 K, however, the appearance of a broad central intensity is observed, indicating that the motions of the quaternary ammonium group or the N-methyls are entering the intermediate motional regime.

In the following chapter, we analyse the ^{14}N MAS lineshapes and T_1 relaxation times for these ACh salts to provide insight on the dynamics occurring at the quaternary ammonium site. By applying a Herzfeld-Berger fit to the experimental lineshapes, we also obtain values for the quadrupolar coupling constants and the asymmetry parameters.

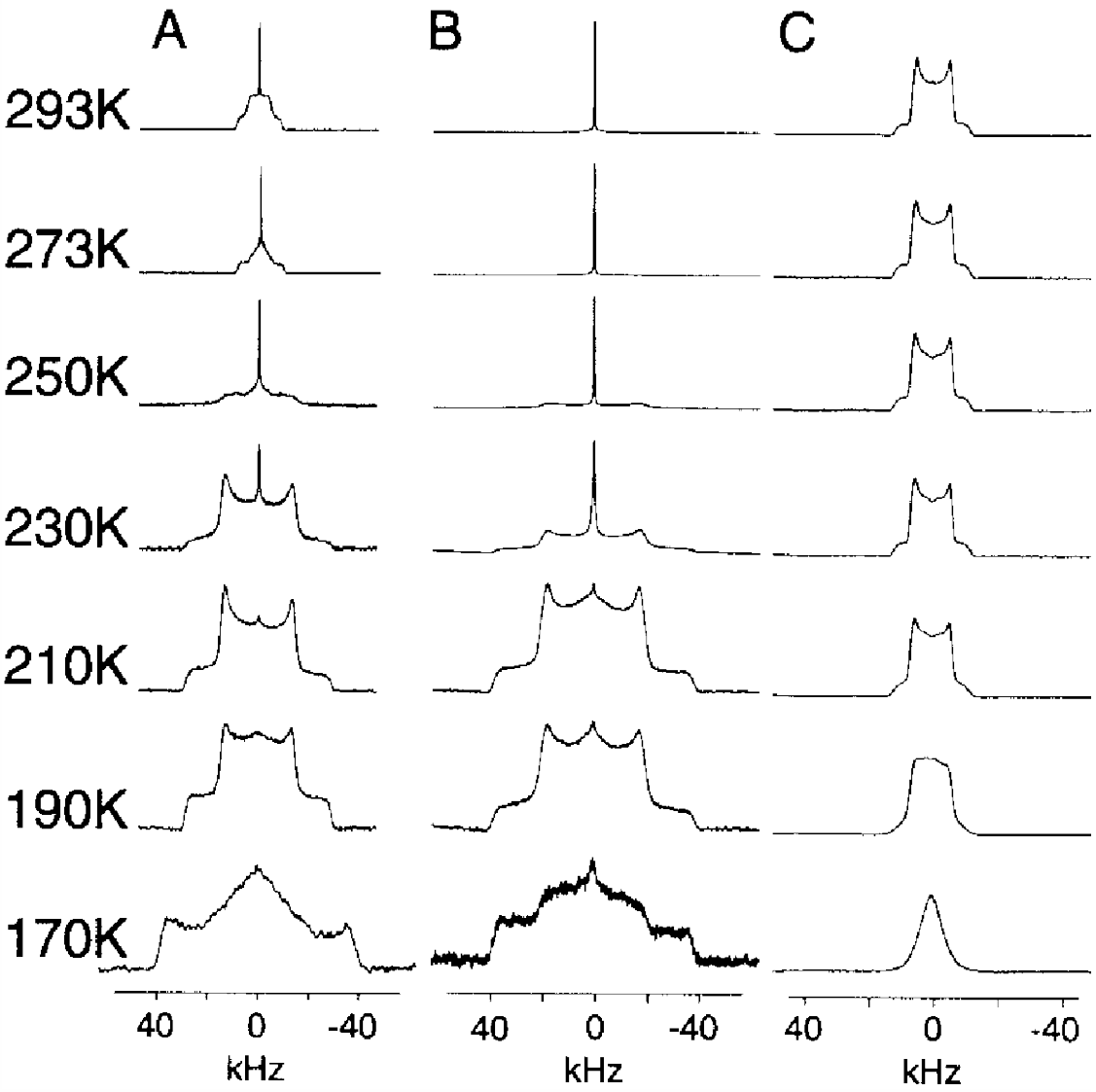

Figure 3.2: Deuterium VT NMR spectra of crystalline $N^+(CD_3)_3$-BAC bromide (A), $N^+(CD_3)_3$ ACh chloride (B) and $N^+(CD_3)_3$-ACh perchlorate (C). Data acquired at the temperatures indicated. [1]

3.1.1 Dynamics and Relaxation

The dynamics of the quaternary ammonium group is clearly of interest as it has been shown to exhibit reduced motion upon binding to a receptor. Further, dynamics in the molecular solid, can also report crystalline packing, and could therefore act as an excellent reporter for characterising formulated drugs. Here we use the different packing and dynamics previously observed for ACh salts to determine the feasibility of using the ^{14}N site to study the dynamics of the quaternary ammonium group. In the following chapter, we interpret and analyse the dynamics via lineshape and T_1 relaxation studies. The following section has been adapted from Solid-State NMR Studies of Molecular Motion by Melinda Duer [74].

3.1.1.1 Dynamics

Motion in molecular solids reflect the packing of groups within the crystalline lattice, data of interest when formulating pharmaceuticals. These motions can be effectively studied using variable temperature measurements, with the changes in the rate of motion allowing the energy barriers for rotation to be determined.

Motions occurring on a timescale slower than the size of the anisotropic interaction will give rise to a distribution of resonances that reflect the orientational distribution of the molecules within the sample. When the timescale of motions is comparable or larger than the size of the interaction, the lineshape reflects the dynamic averaging of the anisotropic interaction, the degree and extent of which is dependent of the range of orientations and frequency at which the different orientations are sampled. Chemical shift anisotropy and dipolar interactions typically have interaction sizes of several kHz resulting in the CSA and dipolar interactions exhibiting sensitivity to motion on the 10^3 -10^4 s^1 timescale. Since the quadrupolar interactions typically span 10's kHz to MHz in size, they are sensitive to comparatively faster motions ($10^6 – 10^9$ s^{-1}).

In the studies described in this chapter we have used ^{14}N NMR to study the motion exhibited by the quaternary ammonium group in the ACh salts. As discussed above, the quaternary ammonium group in these salts is highly symmetric ensuring that the spectrum can be excited using a conventional direct acquisition pulse sequence. However, despite the relatively small size of the quadrupolar interaction, detection of the powder pattern is still plagued by poor sensitivity as a result of the relatively low Larmor frequency and, thus, probe ringing. The spectra have, therefore, been measured under MAS, where the intensities are focused into a family of sidebands whose relative intensities reflect the properties of the underlying quadrupolar interaction.

Through the analysis of these sideband families using a modified implementation of the Herzfeld-Berger analysis [75-76] we have been able to characterise the motions that the ^{14}N experience and

study how they vary as a function of temperature. At lower temperatures where motions are effectively frozen, a broad distribution of ^{14}N resonances will be observed that reflect the static quadrupolar interaction (as seen in the quadrupole simulations shown in Section 3.3.1). At higher temperatures the energy in the system will be sufficient to support intermediate motions, which reflect themselves in the spectrum as central intensity in the ^{14}N spectrum and apparent asymmetric quadrupolar interactions. At higher temperatures, the motions enter the fast limit and the observed spectra will once more take on the form of a Pake pattern, albeit one whose quadrupolar interaction is scaled according to the orientation of the quadrupolar interaction with respect to the angle of motional averaging.

3.1.1.2 T_1 Relaxation

As discussed in Section 1.3.1, the T_1 is sensitive to fluctuating fields occurring on the nanosecond timescale and therefore, complements well data obtained from lineshape analysis. In contrast to liquid state NMR where relaxation is typically dominated by the molecular tumbling in solution, in the solid-state the relaxation is dominated by molecular processes occurring within the solid-system (e.g. rotation of a quaternary ammonium group, flipping of aromatic sidechains in proteins).

Since T_1 relaxation is a process driven by fluctuations in the local magnetic field, the strength of the spin interactions and the rate of motions causing these fluctuations is of great import. The spin-lattice relaxation process can, therefore, be influenced by contributions from multiple relaxation mechanisms such as CSA, dipole-dipole, quadrupole relaxation etc.[77] As for other quadrupolar nuclei, ^{14}N has relatively short T_1 relaxation times as the typically sizeable (MHz) quadrupolar interaction gives rise to large fluctuations in the local magnetic field, ensuring that it acts as an efficient source of relaxation; this is in contrast to spins that only experience fluctuations from the CSA and dipolar interactions (spin < 1). Therefore, the amplitude of the fluctuating fields generated at the quaternary ammonium site as a result of these spin interactions will differ (quadrupolar>dipolar>CSA); this will impact the T_1 relaxation times observed.

In the case of ACh salts, the small size of the quadrupolar interaction is consistent with the static *CASTEP* simulations (Section 2.3.2.5), exhibiting coupling strengths in the order of kHz (ACh iodide – ~40 kHz, ACh bromide – ~250 kHz) rather than MHz. Measurement of the ^{14}N T_1 can provide us with valuable insights as to the energy barriers associated with dynamics in systems.

3.2 Materials and Methods

3.2.1 Materials

The materials used in this chapter are characterised in detail in Chapter 2. Details of experimental methods used to obtain NMR data are described Section 1.4.2.

3.2.2 Fitting of T_1 relaxation

T_1 saturation recovery experiments were conducted (Section 3.3.3: Relaxation Experiments) and the data was fitted to obtain T_1 values. The sidebands were integrated and summed to provide the intensities. The intensities were then plotted as a function of relaxation time and fitted to Equation 3.1, where A_1 and A_2 reflect the amplitude of the signal and T_1 is the relaxation time constant:

Equation 3.1

$$M_z(t) = A_1 - A_2\left(1 - e^{\frac{-t}{T_1}}\right)$$

The T_1 values were obtained by fitting the above function to the sum of the intensities in the sideband family, and ignores any variation arising from T_1 anisotropy. The script used for this is in Appendix E.6.

3.2.3 Herzfeld-Berger Analysis of Quadrupolar Nuclei

In order to quantitatively analyse the ^{14}N MAS lineshapes presented in Section 3.3.2, we analysed the spinning-sideband intensities in the spectra using a modified version of the Herzfeld-Berger approach [75-76]; this allowed us to obtain the quadrupolar parameters, such as the quadrupolar coupling constant (C_Q) and asymmetry parameter (η), corresponding to ^{14}N site of the quaternary ammonium compounds. The powder averaging was performed according to Cheng [78] with 1154 powder orientations per spectrum. The full code for the analysis is shown in Appendix E.7. The equation to calculate the intensity of sidebands for a given anisotropic interaction can be expressed as:

Equation 3.2

$$I(N\omega_r) = \frac{1}{4\pi}\int_0^{2\pi} \delta\alpha \int_0^{\pi} \delta\beta \, sin\beta |F(\alpha,\beta,N\omega_r)|^2$$

where I is the intensity of N, the sideband which relies on the spinning frequency, ω_r. α and β are the Euler angles which describe the orientation of the molecule, and $F(\alpha,\beta,N\omega_r) = \exp(i\Phi^{aniso})$ describes the decaying anisotropic interaction, in this case the quadrupolar interaction.

The intensities of the sidebands can be calculated using Equation 3.3:

Equation 3.3

$$F = \frac{1}{2\pi}\int_0^{2\pi} \exp\left[i(N\theta + \Delta_-\tau_-(\alpha,\beta,\theta) + \Delta_+\tau_+(\beta,\theta))\right]d\theta$$

Where τ_- and τ_+ are defined by Equation 3.4 and Equation 3.5. The line intensities depend on the values of Δ_- and Δ_+ which are defined by Equation 3.6 and Equation 3.7.

Equation 3.4

$$\tau_-(\alpha,\beta,\theta) = \left(\frac{1}{24}\right)\cos(2\alpha)\,[3+\cos(2\beta)]\sin(2\theta) - \left(\frac{1}{6}\right)\sin(2\alpha)\,cos\beta\,\cos(2\theta) - \left(\frac{\sqrt{2}}{6}\right)\cos(2\alpha)\,sin\theta - \left(\frac{\sqrt{2}}{3}\right)\sin(2\alpha)sin\beta cos\theta$$

Equation 3.5

$$\tau_+(\beta,\theta) = \left(\frac{1}{24}\right)[\cos(2\beta)-1]\sin(2\theta) + \left(\frac{\sqrt{2}}{6}\right)\sin(2\beta)\,sin\theta$$

Equation 3.6

$$\Delta_- = \left(\frac{(\Phi^{aniso}\times\eta)}{\omega_r}\right)$$

Equation 3.7

$$\Delta_+ = \left(\frac{(\Phi^{aniso}\times 3)}{\omega_r}\right)$$

3.3 Results

3.3.1 ^{14}N MAS Simulation

For the purposes of comparison with subsequent experimental data, the ^{14}N MAS-NMR spectra were simulated in *SPINACH* [19] for each of the salts (Figure 3.3) using the outputs of the static numerical *CASTEP* calculations conducted in Section 2.3.2.5. The simulated lineshapes presented below provide a visual reference for static ACh salts; as expected, varying lineshapes are observed for each salt reflecting the difference in the quadrupole interaction. The differences in these spectra reflect the differences in the EFG arising from the structure, as the *ab initio* calculations take no account of dynamics that the quaternary ammonium group may be experiencing. The script used to simulate this data is shown in Appendix E.5.

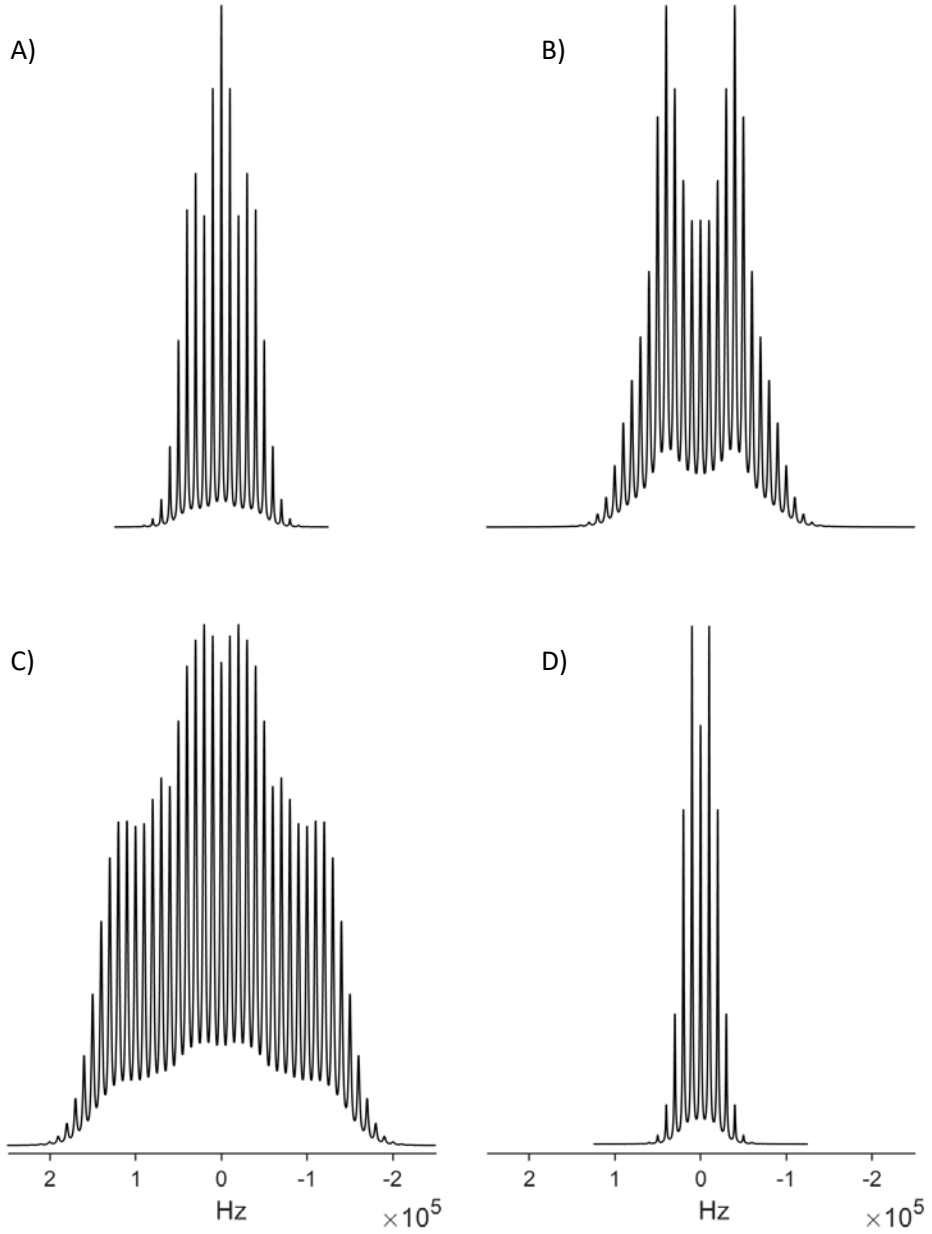

Figure 3.3: A figure showing simulated ^{14}N MAS spectra using SPINACH, reflecting the distribution of sidebands with an artificial line broadening added for (A) ACh perchlorate (B) ACh chloride (C) ACh bromide (D) ACh iodide. All structures were optimised in CASTEP using crystal structures obtained at 100 K. Artificial line broadening of 5 Hz applied.

3.3.2 ^{14}N Magic-Angle Spinning Lineshapes

3.3.2.1 Variable Temperature ^{14}N Studies of Acetylcholine Perchlorate

The MAS ^{14}N spectra of ACh perchlorate acquired over a range of temperatures, 313 K to 218 K, using a direct acquisition pulse sequence, are shown in Figure 3.4. In each of the spectra (Figure 3.4A to F) the isotropic peak can be seen at -0.5 kHz with the sidebands spaced at 10 kHz (the spinning speed).

Comparison of the spectra with that simulated from the *CASTEP* parameters (where dynamics is ignored Figure 3.3) shows similar distributions of sideband intensities, suggesting that in this case there is limited motional averaging. At the spinning speeds used for this size of interaction the distribution of sideband intensities is expected to reflect the intensity in the static powder spectrum, and indeed, the significant intensity in the low order side bands is consistent with a non-axially symmetric tensor as predicted from our *CASTEP* simulation. Notably, the absence of the clear horns associated with the classical Pake pattern expected from the axially symmetric quadrupolar interaction is what would be expected in the case of fast motional averaging.

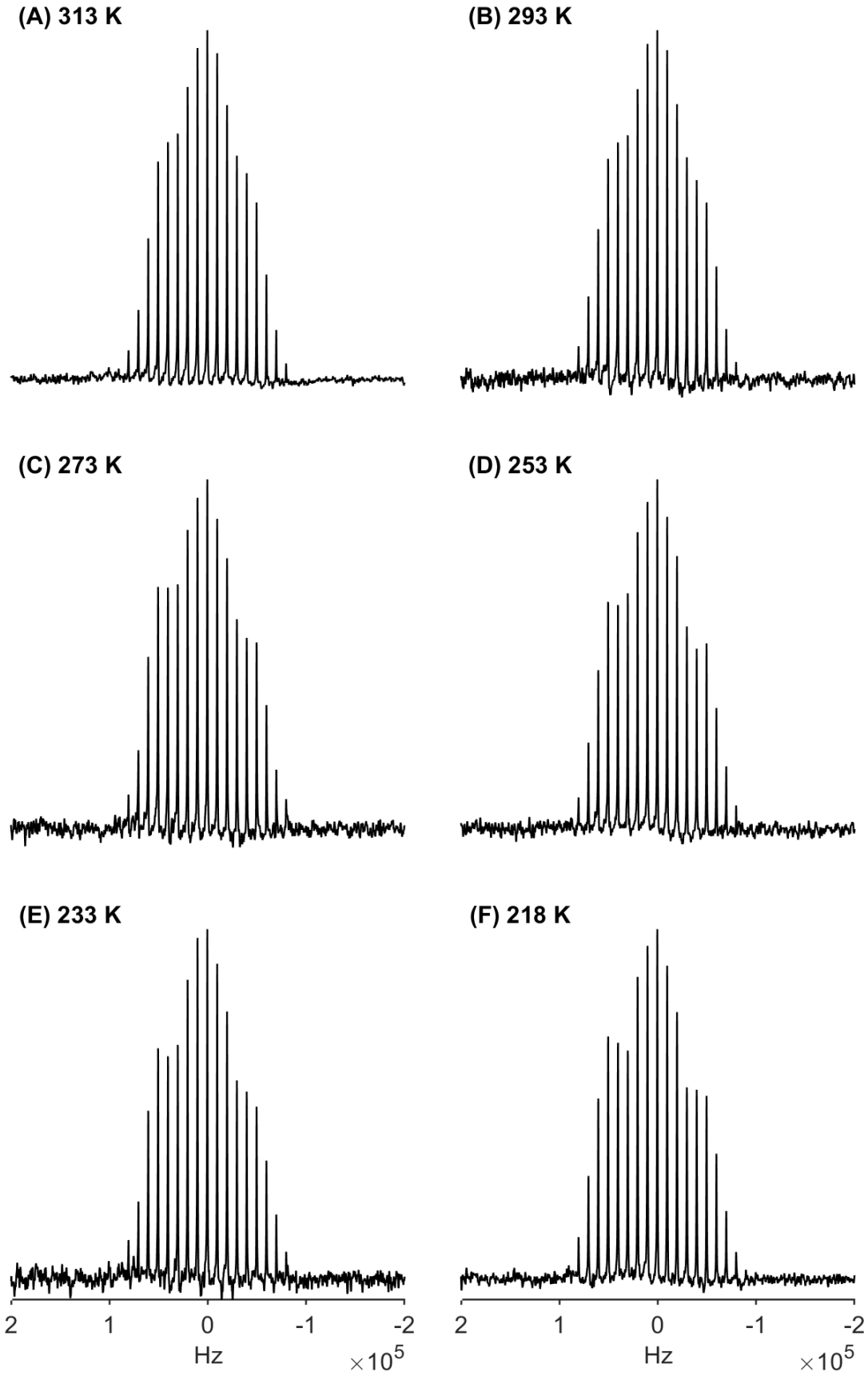

Figure 3.4: VT ^{14}N spectra of ACh perchlorate, MAS 10 kHz. Acquired at temperatures indicated using a direct acquisition pulse sequence.

3.3.2.2 Variable Temperature ^{14}N Studies of Acetylcholine Chloride

The MAS ^{14}N spectra of ACh chloride acquired over a range of temperatures, 313 K to 218 K, using a direct acquisition pulse sequence, are shown in Figure 3.5.

At higher temperatures (Figure 3.5A and B), an intense isotropic peak can be seen at -0.5 kHz on top of a family of sidebands. However, the spectra at lower temperatures (Figure 3.5C, D, E and F) show that the higher order sidebands begin to dominate and the isotropic peak is no longer the most intense peak. At lower temperatures (<273 K), the spectra are more consistent with what would be expected from an axially symmetric powder pattern with the main intensity at ±¾ of the C_Q. The experimental spectra shown in Figure 3.5 show good agreement with the simulated ^{14}N MAS lineshape shown in Section 3.3.1, Figure 3.3B , specifically as the temperature is lowered below 253 K.

At high temperatures, the lineshape is suggestive of rotational motions at the ^{14}N site about the CH_2-N bond (C_3' axis) which are sufficiently rapid to motionally average the quadrupole interaction. Qualitatively speaking, the absence of scaling of the quadrupolar coupling informs us that although the motions are significantly reduced, the quadrupolar coupling is largely unchanged.

The presence of the dominant isotropic peak with low intensity higher order sidebands is indicative of a non-axially symmetric tensor, suggestive of intermediate or intermediate-to-slow motions on the quadrupolar timescale. As the sample is cooled the lineshape begins to show a sideband pattern more typical of an axially symmetric tensor where the higher order sidebands are more intense than the isotropic peak; this indicates that the motions are in the intermediate-to-slow motional regime or entering a slow motional regime.

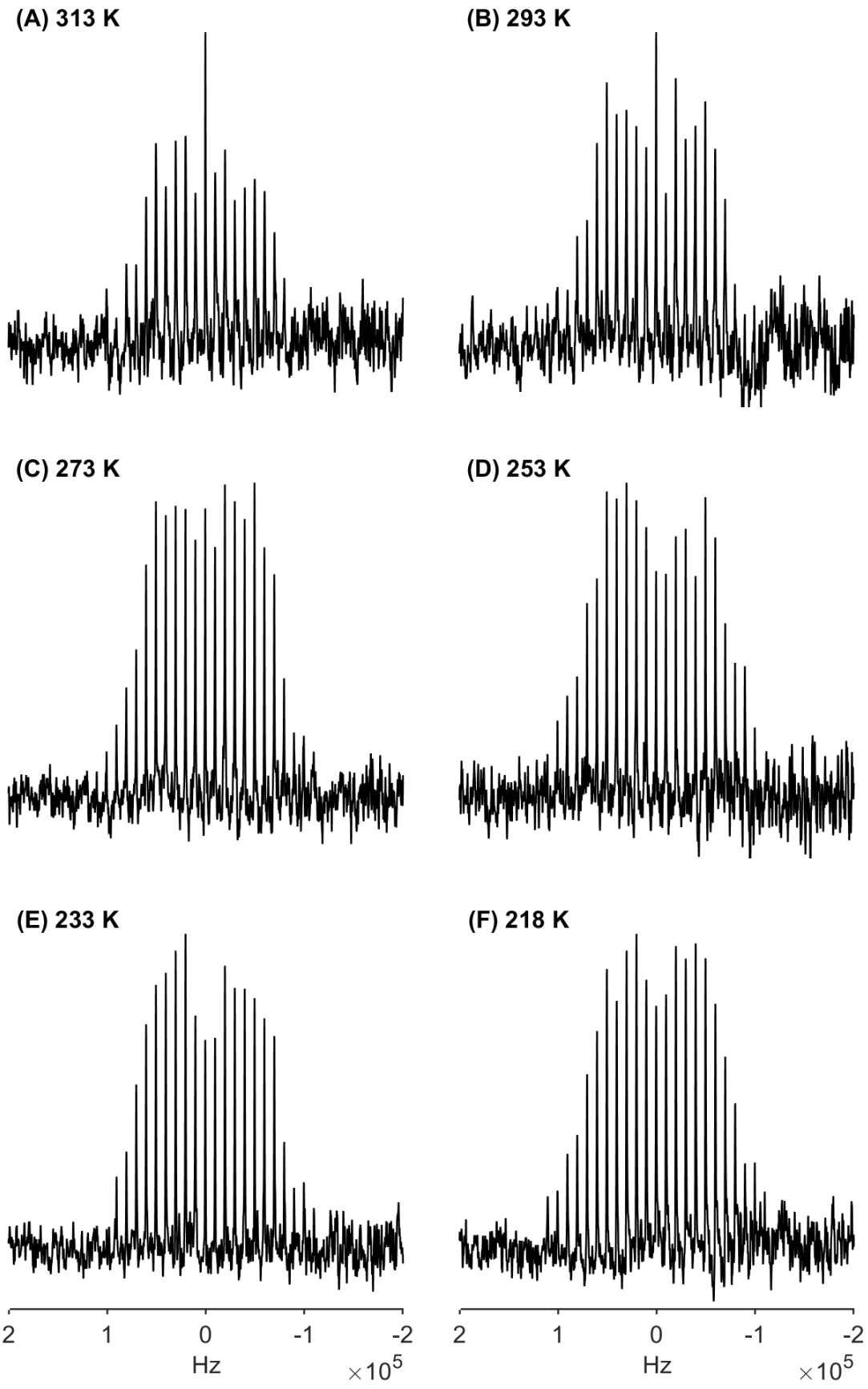

Figure 3.5: VT ^{14}N spectra of ACh chloride, MAS 10 kHz. Acquired at temperatures indicated using a direct acquisition pulse sequence.

3.3.2.3 **Variable Temperature ^{14}N Studies of Acetylcholine Bromide**

MAS ^{14}N spectra of ACh bromide (Figure 3.6) was measured across a range of temperatures, 313 K to 218 K. In each of the spectra (Figure 3.6A to F) the isotropic peak can be seen at -0.5 kHz and remains the most intense line through the temperature range studied, with the sidebands spaced at 10 kHz. The spectra show an increase in spectral linewidth as the sample is cooled as evidenced by the reduction in signal to noise at lower temperatures.

A narrow resonance is seen at the isotropic chemical shift, superimposed on a family of sidebands, spanning +/- 100 kHz from the central resonance. At 293 K there is some evidence of an underlying Pake like pattern, with sidebands of maximal intensity at ±30 kHz. However, below this temperature, the intensity decays with increasing sideband order indicative of a non-axially symmetry powder pattern, characteristic of intermediate exchange.

There is some variation between the simulated ^{14}N lineshape in Figure 3.3 (and the static quadrupolar coupling constant, ~220 kHz, from Section 2.3.2.5) and the experimental lineshape (C_Q of ~100 kHz). This indicates that either the quaternary ammonium group in ACh bromide undergoes some rotation which significantly reduces the quadrupolar interaction, or the entire spectrum was not excited. However, this was initially checked using piece-wise acquisition[79-80] to measure any signal up and down-field from the resonances reported here. The absence of any signal up or downfield from those shown indicates that the sideband family is an accurate reflection of the ^{14}N quadrupolar spectrum.

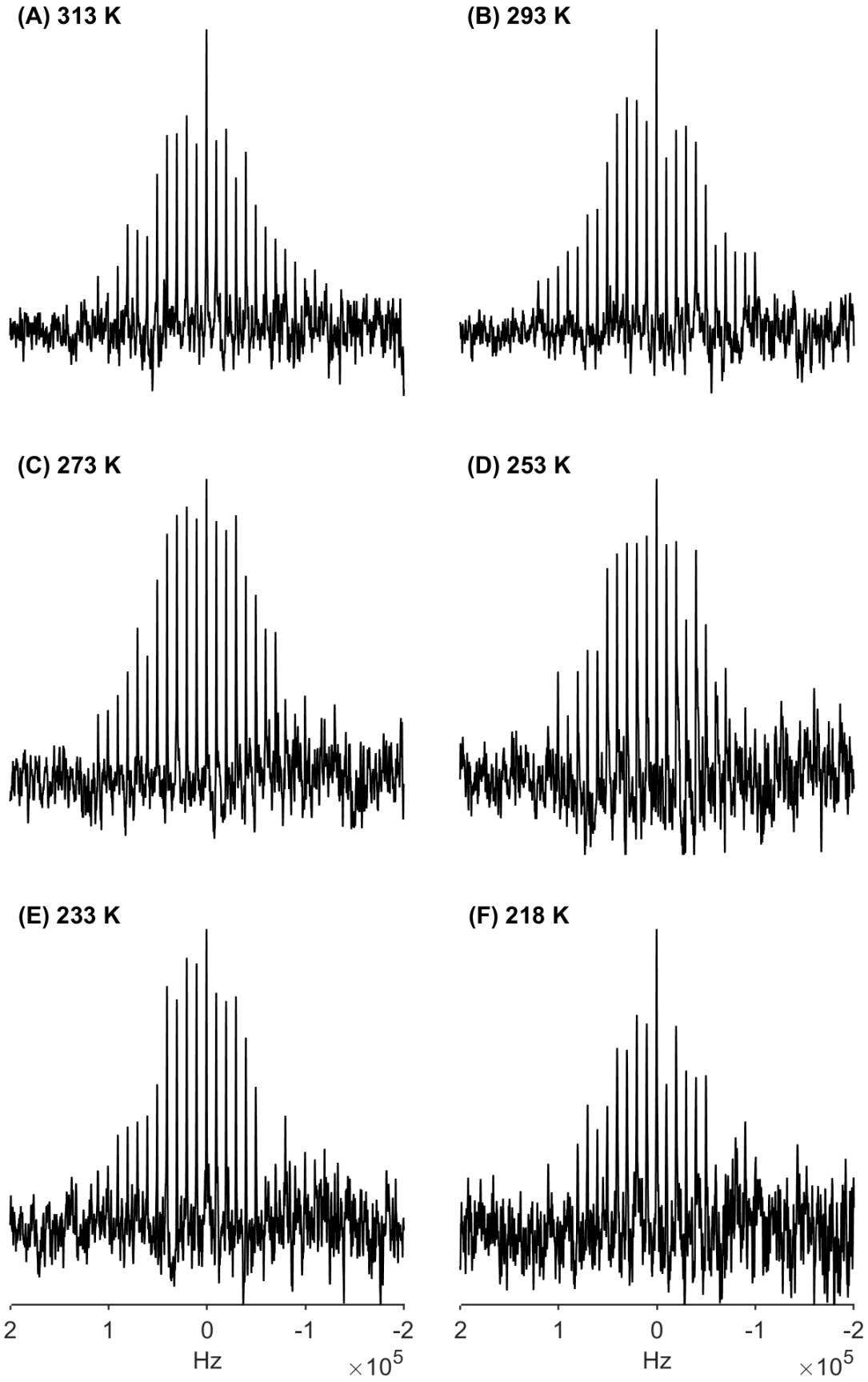

Figure 3.6: VT ^{14}N spectra of ACh bromide, MAS 10 kHz. Acquired at temperatures indicated using a direct acquisition pulse sequence.

3.3.2.4 Variable Temperature ^{14}N Studies of Acetylcholine Iodide

The MAS ^{14}N spectra of ACh iodide acquired over a range of temperatures are shown in Figure 3.7. The isotropic peak, as for the other salts, is observed at -0.5 kHz with the sidebands spaced at 10 kHz.

Interestingly, the ACh iodide lineshape immediately resembles an axially symmetric sideband pattern and possesses fewer sidebands Figure 3.7A; this suggests a smaller quadrupolar interaction reflecting either a intrinsically small quadrupolar interaction or increased dynamic averaging of the quadrupolar interaction. Comparison to the ^{14}N simulated lineshape in Figure 3.3D shows good agreement, indicating that the smaller C_Q observed in the experimental lineshape is a result of the geometry at the quaternary ammonium site rather than scaling caused by rotation about the axis of motional averaging.

As the sample is cooled, the linewidth decreases resulting in increased spectral intensity at low temperatures (Figure 3.7A to F); this suggests that as the temperature is lowered, the motional regime is moving away from one of unfavourable T_2 relaxation/interference with MAS.

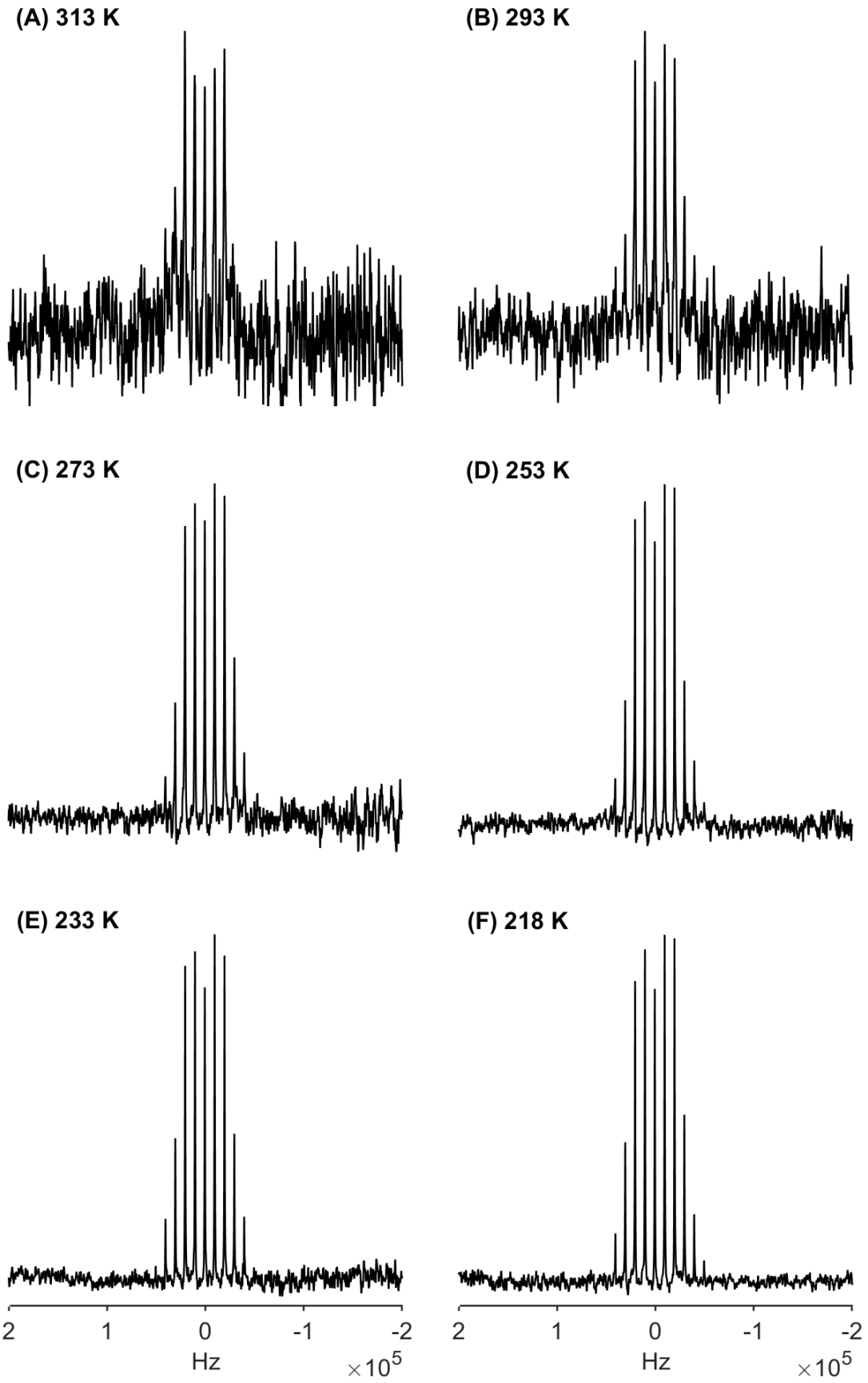

Figure 3.7: VT ^{14}N spectra of ACh iodide, MAS 10 kHz. Acquired at temperatures indicated using a direct acquisition pulse sequence.

3.3.2.5 Lineshape and EFG Tensor Analysis

The complex sideband patterns in the ^{14}N MAS spectra for ACh perchlorate, chloride, bromide and iodide shown above suggest that the presence of different halide counterions influences the observable dynamics occurring at the nitrogen site. There is, however, little variation in the lineshapes as the temperature is lowered, indicating that either 1) the motional processes of the quaternary ammonium group show little change on a timescale which would influence the averaging of the quadrupolar couplings or 2) the axis of motional averaging is collinear with the axis of rotation of the $H_2C\text{-}N(CH_3)_3$ bond (C_3' axis).

In the case of ACh perchlorate and iodide, the spectra simulated using the static quadrupolar couplings obtained from the *CASTEP* calculations (Section 3.3.1, Figure 3.3) show good agreement with the experimental spectra indicating very little scaling of the quadrupolar interaction. This suggests that any motional averaging at the site is occurring on a timescale too slow to average the quadrupolar interaction (inconsistent with the ^{2}H NMR data[1]), or that the axis of motional averaging is aligned with a component of the tensor.

For both ACh chloride and bromide, however, there is some variation in the lineshape as the sample is cooled. The data is consistent with previous deuterium NMR studies (Figure 3.2B), which probed the methyl group dynamics, and showed that there was a significant reduction in the rotation of the quaternary ammonium group at ~253 K. As the deuterium NMR data suggests, the rotation of the ammonium group about the C_3' axis ($CH_2\text{-}N(CH_3)_3$ bond) appears to slow, suggesting that the changes observed in the ^{14}N spectra arise from a reduction in the motional averaging about the CH_2-N bond. A comparison to the simulated spectra shows some agreement to the experimental spectra at low temperatures (218 K). This indicates that there is some scaling of the quadrupolar interaction, especially in the case of ACh bromide where the simulated lineshape shows sidebands spanning ~200 kHz, as opposed to the experimental lineshape which shows the manifold of spinning sidebands to span ~150 kHz.

To fully understand how motion about the C_3' axis influence the ^{14}N lineshapes, it is important to first understand how the ^{14}N quadrupolar interaction is aligned with the axis of motional averaging, as this will determine which elements of the quadrupolar tensor become motionally averaged. In a hypothetical case, where one axis of the tensor is aligned with the C_3' axis, the aligned component will remain invariant under rotational averaging whilst, under fast rotation, the remaining two components will be motionally averaged.

Inspection of the *CASTEP* simulations (Section 2.3.2.5) for all four ACh salts reveals that the tensors are not axially symmetric; this is analogous with the sideband manifold observed in the experimental and simulated ^{14}N spectrum.

In the case of ACh perchlorate and bromide, the V_{XX} component of each tensor shows a degree of collinearity with the C_3' axis, while ACh chloride and iodide appear to be aligned with the V_{ZZ}. As mentioned above, these tensors are not axially symmetric and one of the two motionally averaged components for each salt are significantly smaller than the remaining averaged component.

It is difficult to rationalise these observations, as rotation about the C_3' axis would result in an averaging of at least two components of the quadrupole interaction, something not exhibited in the lineshapes for ACh perchlorate and iodide; these observations, therefore, require further analysis.

A more quantitative analysis is provide in Section 3.3.3 (Herzfeld-Berger Analysis).

3.3.3 Herzfeld-Berger Analysis

A more quantitative analysis of the lineshapes obtained was performed to accurately characterise the quadrupolar coupling constant (C_Q) and the asymmetry value, η. To achieve this, we adopted a modified version of the Herzfeld-Berger (HB) analysis [75] that permits the characterisation of the quadrupolar interaction in MAS spectra [81]; this is shown in Section 3.2.3. This analysis provides a quantitative picture as to the changes in C_Q and η as a function of temperature, and therefore any changes in dynamics.

The fitted C_Q values are shown in Figure 3.8A; we can see that as the temperature is lowered from 313 K to 218 K, the quadrupolar coupling constants show an overall increase of ~10 kHz for both the perchlorate and chloride salts. This indicates that there are changes in the dynamics at the quaternary ammonium group of both these ACh salts on a timescale that influences the lineshape. ACh iodide shows a C_Q of ~47 kHz, the smallest coupling constant among the family of salts, with very little variation over the temperature range measured; this suggests that there is little change in the dynamics of the quaternary ammonium group on a timescale that would influence the averaging of the quadrupolar interaction. In the case of ACh bromide, the poor spectral intensity leads to a greater uncertainty in the results rendering the interpretation somewhat ambiguous.

Comparison of these HB fits to the static quadrupolar parameters (shown in Section 2.3.2.5) obtained via *CASTEP* calculations, shows some agreement between the two. The calculated static C_Q for ACh perchlorate is ~85 kHz and the characterised quadrupolar coupling constant is ~80 kHz at the lowest temperature measured. In the case of ACh chloride, the *CASTEP* output is ~145 kHz and the HB fit of the experimental lineshape at the lowest temperature is ~100 kHz; this indicates the presence of significant motional averaging about the C_3' axis resulting in a scaled C_Q. This is possibly a result of more hindered motions as the sample is cooled. ACh iodide has a static C_Q value of ~50 kHz and the experimental lineshape produces a C_Q of ~47 kHz, invariant as a function of temperature; this is indicative of a little no change in the dynamics of the quaternary ammonium group. The largest difference appears in the case of ACh bromide, where the static quadrupole coupling is ~227 kHz, whereas the majority of the HB fits provide values around ~80 kHz. Though the signal to noise precludes a more accurate reading, this is suggestive of motions on the timescale of the quadrupolar interaction which effectively scaling the C_Q.

The calculated values for the asymmetry parameter plotted as a function of temperature is shown in Figure 3.8B. The non-zero values of η, for all 4 ACh salts suggest that the ^{14}N spectra in Section 3.3.2 do not possess an axially symmetric sideband pattern. This correlates with the discussion of the EFG tensor presented above (Section 3.3.2.5), where the components of the tensor being motionally averaged are not equal.

The asymmetry parameters obtained experimentally for ACh perchlorate show little variation as the temperature is dropped with η values ~0.85 (resembling the static η value shown in Section 2.3.2.5) showing little deviation; this is indicative of intermediate motions on the quadrupolar timescale which do not change as the sample is cooled. In the case of ACh chloride, we observe a gradual decrease in the asymmetry parameter as the temperature is lowered, indicating that the ^{14}N sideband pattern begins to resemble that of an axially symmetric tensor, indicating a change in motions on the quadrupolar timescale. For ACh iodide, the asymmetry value at 313 K is much lower compared to the rest of the temperatures; this is likely due to the fact that the lineshape at 313 K resembles the most axially symmetric sideband pattern of all the spectra. At 293 K and below, however, the η value stays relatively constant, ~0.5, indicating little change in the dynamics at the quaternary ammonium site on a timescale which would influence the lineshape. For ACh bromide, similar to the C_Q fits, the poor spectral quality produces significant uncertainty which hinders an accurate interpretation of the results.

Once again, a comparison to the asymmetry parameters obtained via *CASTEP* calculations tells us that the quadrupolar interaction is indeed non-axial. ACh perchlorate and bromide share similar η values of ~0.75 and ~0.7, respectively. The HB fits at high temperatures for both these salts produced values of ~0.8 (though, again, the signal to noise precludes accurate interpretation for the bromide salt). Interestingly, the simulated η value for ACh chloride (0.24) is not analogous with that produced from the HB fit (~0.8). This η value obtained from fitting the lineshape decreases as the sample is cooled, however, suggesting that the lineshape reflects the suppression of motions occurring at the quaternary ammonium site which give rise to the lineshape observed.

The HB analysis of the salts provided some estimates of the predicted quadrupolar couplings over the temperature range studied; this allows us to monitor the motions as a function of motions which influence the quadrupolar interaction and thus the ^{14}N lineshape. The asymmetry parameter provided information on the symmetry of the tensor and therefore the dynamics that influence the lineshape. The comparison of the experimentally obtained quadrupolar parameters to the static quadrupolar parameters informs us of any potential dynamics occurring at the quaternary ammonium site.

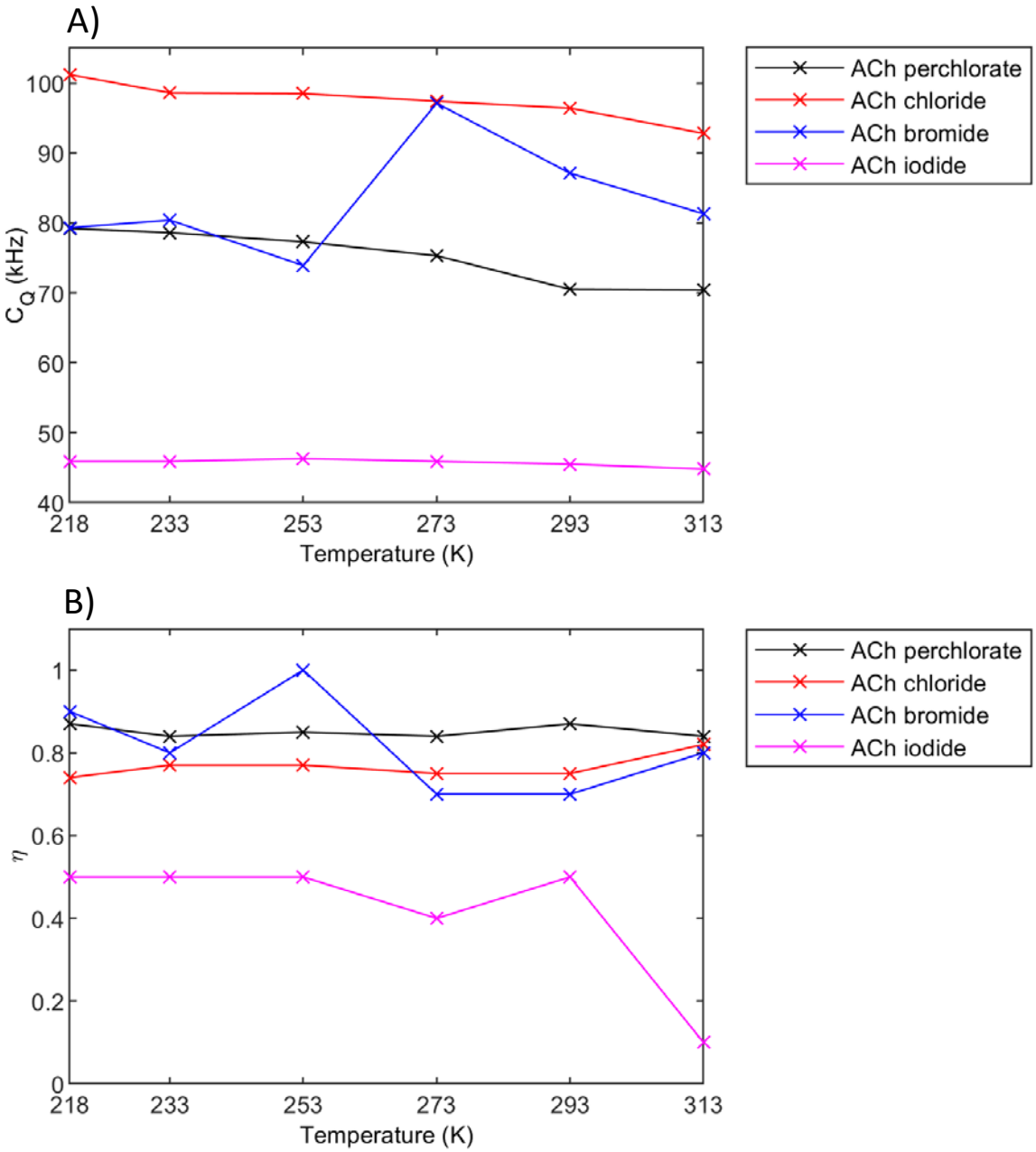

Figure 3.8: Plots showing A) Quadrupolar Coupling Constants and B) Asymmetry parameters obtained for ACh perchlorate, chloride, bromide and iodide using Herzfeld-Berger analysis,

3.3.4 Relaxation Analysis

To complement the lineshape study, we performed a T_1 relaxation analysis to characterize any changes in nanosecond motions at the quaternary ammonium site. All raw saturation recovery plots are shown in Appendix B.

3.3.4.1 T_1 Relaxation Analysis of Acetylcholine Perchlorate

The T_1 values obtained from fitting the saturation recovery curves plotted as a function of temperature is shown in Figure 3.9. We can see that as the temperature is decreased, the T_1 increases indicative of a reduction in the density of motions occurring on the nanosecond (ns) timescale. The T_1 increased by ~4 orders of magnitude as the sample is cooled below 253 K. It is worthy of note as we shall see later, that the T_1 for the perchlorate salt is significantly shorter than the other salts studied suggesting that significant dynamics are occurring on the nanosecond timescale.

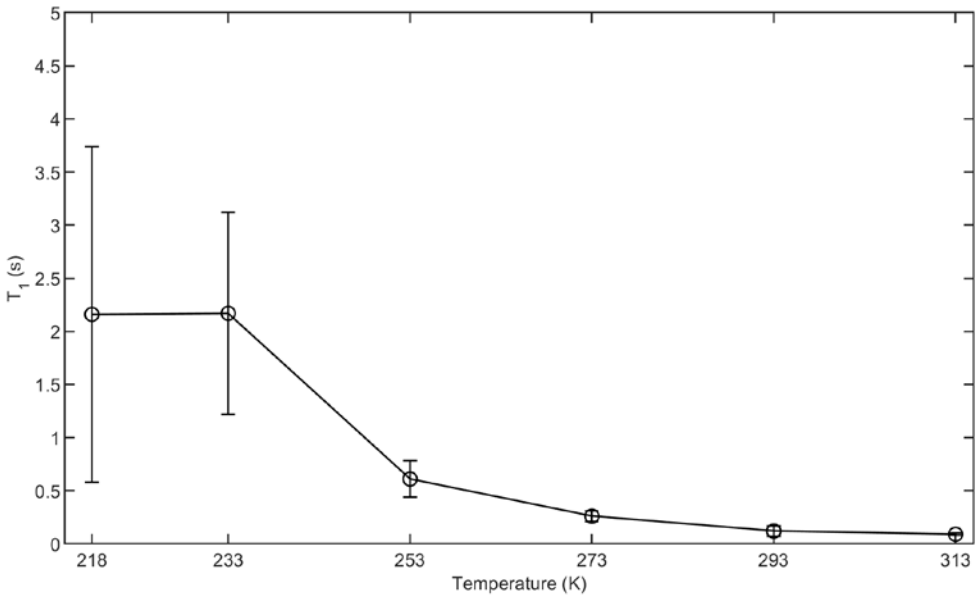

Figure 3.9: A plot displaying T_1 (sec) as a function of temperature (K) for ACh perchlorate, with 95% confidence bounds.

3.3.4.2 T_1 Relaxation Analysis of Acetylcholine Chloride

The T_1 values obtained from fitting the saturation recovery curves measured over range of temperatures, 313 K to 218 K, for ACh chloride is shown in Figure 3.10. As the temperature is lowered, we observe an increase in the T_1 relaxation times consistent with a lower density of motions on the ns timescale, though the change in a factor of 3.5 is smaller than that of the perchlorate salt which increased by a factor of 20 . We observe an increase from ~10 seconds at 313 K to ~35 seconds at 218 K. Interestingly, the relaxation times are significantly longer than those observed for the perchlorate salt, suggesting that the processes that drive the relaxation are supressed.

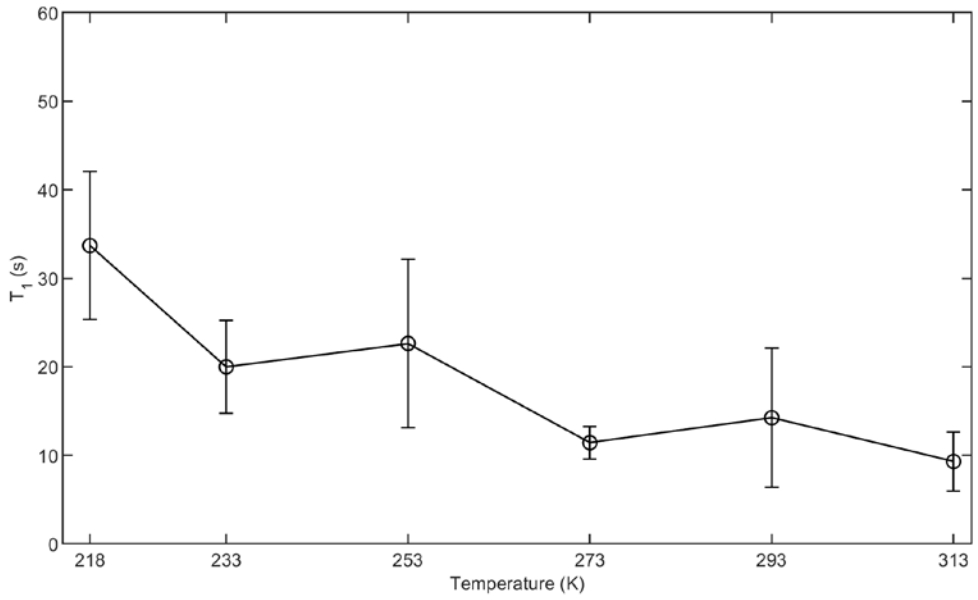

Figure 3.10: A plot displaying T_1 (sec) as a function of temperature (K) for ACh chloride, with 95% confidence bounds.

3.3.4.3 T_1 Relaxation Analysis of Acetylcholine Bromide

T_1 values for ACh bromide measured over range of temperatures (313 K to 218 K) is shown in Figure 3.11. As with the perchlorate and chloride salt, we observe an increase in T_1 as the sample is cooled; this is analogous with a lower density of motions on the nanosecond timescale. The relaxation times observed are, once again, considerably larger for the bromide salt than the perchlorate salt; this indicates a suppression of the motions that drive the relaxation process. A noteworthy observation is the steep increase in T_1 values between 233 K and 218 K; interestingly, it is around these temperatures (230 K to 190 K) that the central feature disappears in ^{2}H lineshape (Figure 3.2) and an increase in the intensity of the powder lineshape is observed.

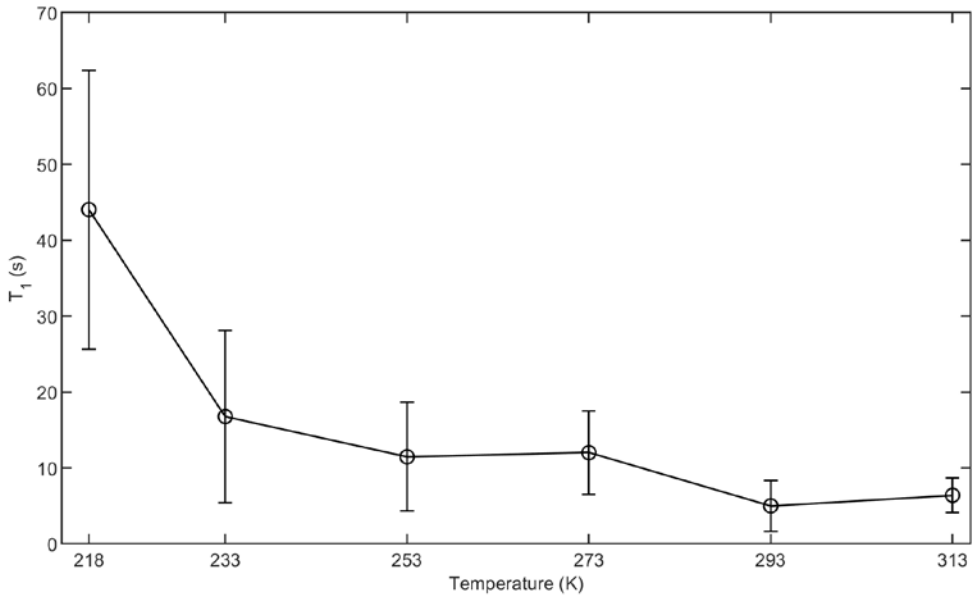

Figure 3.11: A plot displaying T_1 (sec) as a function of temperature (K) for ACh bromide, with 95% confidence bounds.

3.3.4.4 T_1 Relaxation Analysis of Acetylcholine Iodide

T_1 values obtained by fitting the saturation curves for ACh iodide, measured over range of temperatures, 313 K to 218 K, is shown in Figure 3.12. Again, we observe an increase in T_1 values as the sample is cooled analogous to the other salts, indicating a lower density of motions on the nanosecond timescale as the temperature is lowered. The large T_1 values once again indicate a reduction in the motions that drive the relaxation process. Interestingly, below 253 K (Figure 3.12), the T_1 values show a steeper increase suggesting that these motions driving the relaxation process are reduced further at 233 K and 218 K.

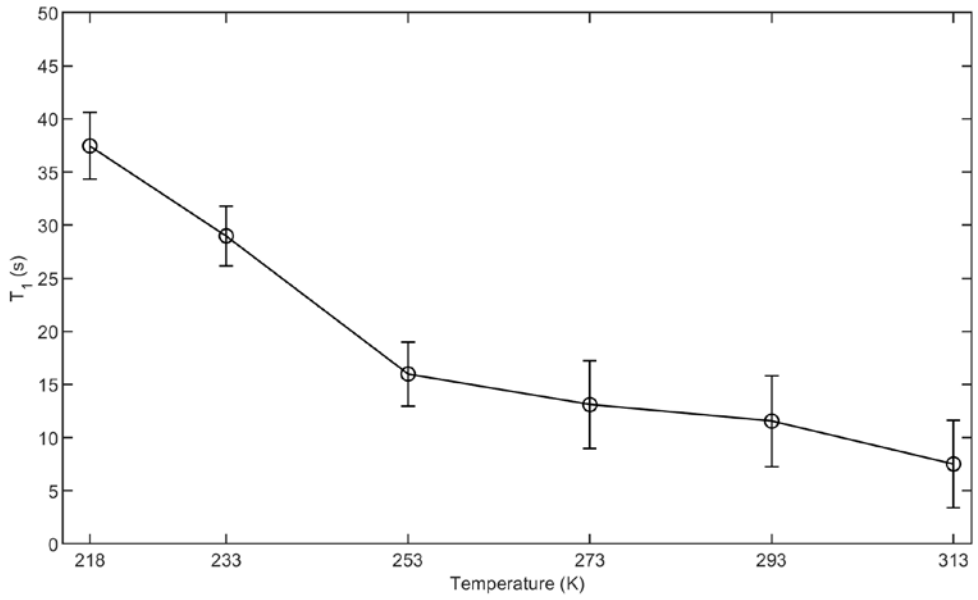

Figure 3.12: A plot displaying T_1 (sec) as a function of Temperature (K) for ACh iodide, with 95% confidence bounds.

3.3.4.5 Relaxation Analysis Summary

The T_1 relaxation analysis of the ACh salts produced results atypical for quadrupolar nuclei which in general undergo rapid relaxation as a result of the large fluctuations in the local magnetic field and EFG caused by the usually sizeable quadrupolar interaction. In the liquid state T_1 relaxation is dominated by the rapid isotropic tumbling, which for small molecules such as these is on the timescale of nanoseconds. In contrast, in the solid-state, relaxation is dominated by the anisotropic motions within the molecular solid.

The *CASTEP* simulations reveal that in the static case, the size of the quadrupolar interaction is intrinsically small, suggesting that the quadrupolar interaction will generate proportionally smaller fluctuations in the field.

Interestingly, in the case of ACh perchlorate, the T_1 values are significantly shorter than ACh chloride, bromide and iodide increasing from ~0.1 seconds to ~2 seconds, whereas the halide salts showed much larger increases in T_1 ranging from ~10 seconds to ~40 seconds (Figure 3.13). This suggests that motions that influence the relaxation are largely suppressed in the case of the halide salts (ACh chloride, bromide and iodide). A more detailed discussion of the relaxation processes occurring will be undertaken later in Section 3.4.

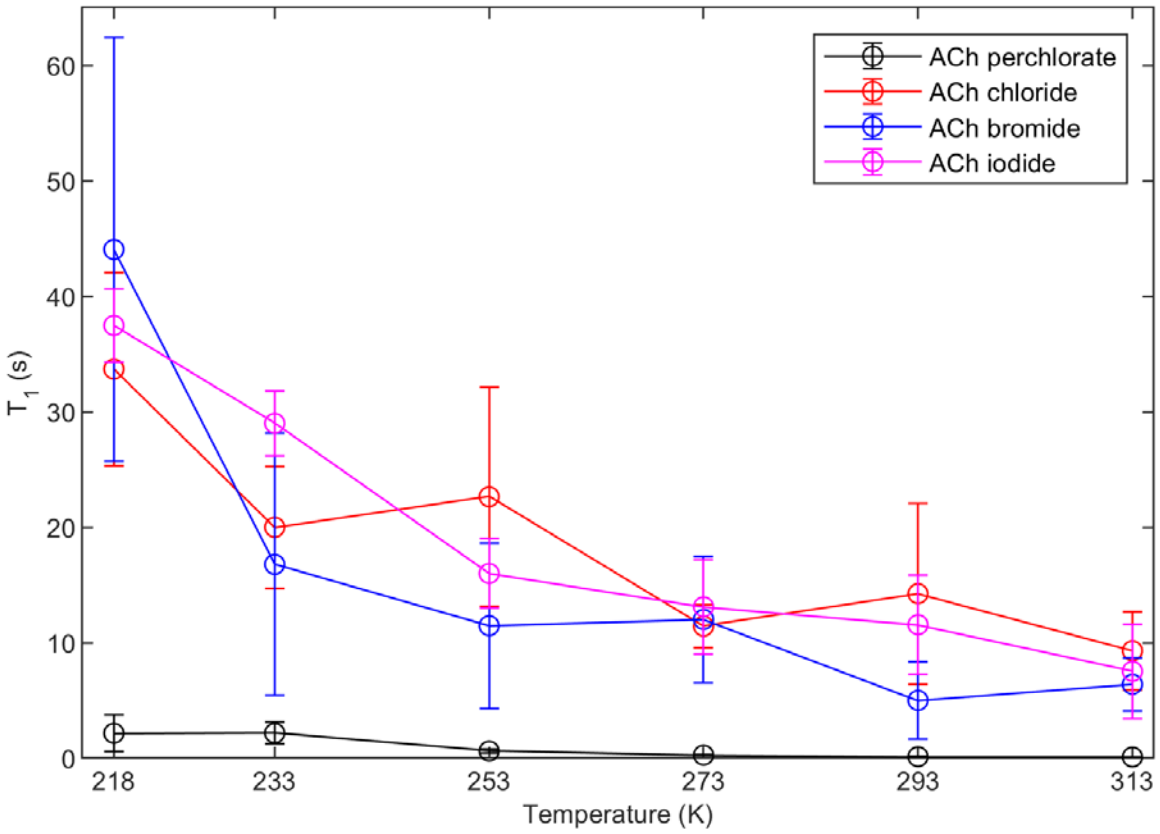

Figure 3.13: A plot showing all T_1 values obtained for each ACh salt as a function of temperature to visually aid comparison: ACh perchlorate (black), ACh chloride (red), ACh bromide (blue) and ACh iodide (magenta)

3.4 Discussion

In this chapter, we showed that exploitation of the natural abundance ^{14}N isotope can lead to a wealth of information on the dynamics and interactions occurring at the quaternary ammonium site. The investigation was carried out on a family of ACh salts, which due to their well characterized nature and relatively low quadrupolar interaction, make them model systems to probe the internal dynamics at this important pharmacophore.

The ^{14}N NMR spectra shown in Section 3.3.2 obtained for ACh perchlorate, chloride, bromide and iodide exhibit distinct complex sideband patterns as the temperature of the sample is lowered. The spectra resemble the simulations shown in Figure 3.3 (specifically ACh perchlorate and iodide), which were performed using the *CASTEP* output obtained in the absence of motion. This indicates that the type of counterion present in the salt plays a crucial part in the dynamics occurring at the nitrogen site as well as determining the behaviour of the quadrupolar interaction. A large variation was seen specifically between the iodide salt and the three other salts, with both the calculated an measured quadrupolar interaction significantly smaller for ACh iodide than ACh perchlorate, chloride and bromide. Comparison of the ^{14}N MAS spectra and the simulated spectra suggest that either the quaternary ammonium group is static (contrary to deuterium data from previous work [1]) or the axis of motional averaging is collinear with the quadrupole interaction. In the case of the iodide and perchlorate it appears as though the spectra reflect the static spectra, despite the acknowledged rapid motion of the quaternary ammonium group in the perchlorate salt, and these observations require further analysis.

The lineshapes pertaining to ACh chloride and bromide show some indication of motional averaging of the quadrupolar interaction, since the simulated C_Q (performed in static conditions) appears larger than observed in the experimental lineshape, and this is mirrored in the Herzfeld-Berger (HB) analysis. This correlates with the HB fits discussed in Section 3.3.3, though in the case of ACh bromide, the signal to noise precludes accurate interpretation of the quadrupolar parameters. The asymmetry parameter for ACh chloride obtained through fitting the ^{14}N lineshape using HB analysis is higher than the η value obtained via static calculations. This increase in asymmetry parameter is indicative of a motionally averaged lineshape arising from motions entering the intermediate timescale which would result in more intensity in the centre of the spectra, as seen in previous static ^{2}H spectra (Figure 3.2).

The T_1 relaxation data presented a challenge to interpret, since the values were atypical of those seen in traditional quadrupolar nuclei. However, if we analyse the phenomenon as a result of contributions from multiple spin interactions coupled with the information obtained from the *CASTEP* simulations and lineshape analysis we can attempt to rationalise it.

With the exception of ACh perchlorate (~0.1 seconds – ~2 seconds), the ACh salts show large increases in T_1 as the temperature is decreased from 313 K to 218 K; ACh chloride showed an increase from ~10 seconds to ~35 seconds, ACh bromide increased from ~7 seconds to ~40 seconds and finally ACh iodide increased from ~7 seconds to ~37 seconds.

The increase in T_1 observed above suggests a reduction of motions on the nanosecond timescale. The relaxation process is driven by fluctuations in the local magnetic field arising from the anisotropic interactions such as CSA, dipolar and quadrupolar. In comparison to the quadruple and dipole relaxation mechanisms, the contribution from the CSA is negligible. If the relaxation was driven by contributions from only the quadrupole interaction, the gradual increase in C_Q (observed in the HB analysis specifically for ACh perchlorate and chloride) would result in shorter T_1 values; since this is not the case, the relaxation is most likely driven by contributions from both the quadrupolar and dipolar interactions which are both in the order of kHz.

In the case of the contribution from the quadrupolar interaction, as discussed in Section 3.3.2.5, the quadrupolar tensors shows some degree of collinearity with the axis of motional averaging (C_3'); however, the components being averaged (differing for each of the ACh salts) are different sizes, a fact we gleaned from the ^{14}N lineshape, HB analysis and the static *CASTEP* calculations. We also know from previous ^2H work[1] that the rotation of the N-methyl groups are restricted as the samples are cooled, which means the rotational correlation times change which could lead to a fluctuating field that significantly influences the relaxation. This relaxation effect is due to the ammonium group experiencing fluctuations in the transverse plane which is a result of the interactions at the site (quadrupolar, dipolar, CSA etc.). These fluctuations are directly influenced by heating and cooling the sample, as we saw in Section 1.3.1 and Section 1.3.1.1. Therefore, as the correlation time changes, the T_1 values should reflect the changes occurring in the fluctuations. Due to its size, the quadrupolar interaction usually dominates the T_1 relaxation of quadrupolar nuclei.

In the case of ACh perchlorate, the lineshape analysis suggests there is very little variation in the quadrupolar interaction over the temperature range studied. This indicates that there are no significant changes occurring to the motions on the nanosecond timescale. This is consistent with the ^2H spectra[1] which only show small changes in lineshape at lower temperatures indicating that of the rotational motions of the methyl and/or quaternary ammonium group are beginning to slow

For both ACh chloride and bromide, it can be surmised from previous work and the work discussed above that the rotation of the methyl groups and the quaternary ammonium group (motions about the C_3 and C_3' axes, respectively) become more hindered as the sample is cooled. Since the experimental C_Q and asymmetry parameters do not show a large change and the simulated static values in comparison are vastly different for both parameters, the considerable jump in T_1 values is unexpected. However, the relaxation process may be influenced again by contributions from the

dipolar couplings (as well as the quadrupole relaxation mechanism) pertaining to the proximate methyl groups, which are shown to enter an intermediate motional regime as the temperature is decreased. As these motions become more hindered, it may lead to a more unfavourable spin-lattice relaxation.

In the case of ACh iodide, there is little evidence of the presence of motions on the timescale that would scale the quadrupolar interaction; this was gleaned from the invariant η value as the sample was cooled observed in the HB analysis, matching the C_Q and η in the *CASTEP* calculation. This means that the large rise in T_1 at the ^{14}N site must arise, in part, from contributions from the dipole-dipole interaction between the proximate methyl protons which are hindered as the temperature is dropped. Since previous work informs us that the quaternary ammonium group does indeed undergo rapid motion, there could be some fluctuations in the local magnetic field due to motional averaging of the two unequal components of the EFG tensor pertaining to each salt.

In this chapter we have shown that each of the ACh spectra measured show reasonable agreement with the static spectra predicted on the basis of the EFG calculated in *CASTEP*; in the case of ACh chloride and bromide, however, the comparatively smaller C_Q values obtained via HB analysis show indications of motional averaging about the C_3' axis, something that is readily reconciled with the ^2H NMR data. The large increase of T_1 observed for ACh iodide is difficult to rationalise, since there does not appear to be any observable change in the quadrupolar parameters or motions which may give rise to this process. We postulate that the T_1 relaxation phenomenon is driven by contributions from both the quadrupole interaction and rotational motion of the N-methyl group; the latter may be a result of chemical exchange, a dynamic process which can be probed experimentally by heating and cooling the sample. In order to make a more a conclusive hypothesis, these observations require further analysis.

Chapter 4 Investigations into Dynamics in Acetylcholine Salts by ^{13}C MAS-NMR.

4.1 Introduction

Solid-state Nuclear Magnetic Resonance (SS-NMR) is a vital non-destructive analysis tool used to study molecular structure and dynamics in microcrystalline and amorphous solids. It is integral to the pharmaceutical industry to characterise polymorphs to understand the pharmacokinetics and pharmacodynamics that take place in the solid state.

The solid-state form of an API (active pharmaceutical ingredient) is integral to the final formulised product and can exist in multiple polymorphs, where more than one structure of a molecule can exist. This can influence the solubility, bioavailability, physical stability and dynamics in the sample.[82] Polymorphism can be a result of several things including drug formulation, storage, API physical state etc.[44] Some typical methods of ascertaining the solid-state form of an API (crystalline, amorphous solid or solvate) are Differential Scanning Calorimetry (DSC), Infrared Spectroscopy (IR), Raman Spectroscopy and X-ray powder diffraction (XRD) analysis. The issue arises when one requires information on the entire product and not just the API; SS-NMR, however, can provide unique information on the ensemble system and allows for the study of the API directly in its formulated state. The elucidation of chemical structure as well as a keen insight on the conformation and dynamics present can be gained as resonance frequencies of the nuclei will differ according to their spatial relations. [82-85] By interpreting the spectra accurately, however, one can obtain more than just chemical shifts; studying the lineshape can provide important insight into underlying dynamics such as motional processes.

One of the most common forms of solid-state NMR used to study pharmaceuticals is Magic Angle Spinning-NMR (MAS-NMR). This method provides well resolved spectra which reflect the different packing and structures that the API may adopt. In some cases, however, the lineshapes obtained are more complex, and this reflects motional process that are occurring inside the molecular solid. MAS-NMR is sensitive to all motional timescales (for instance, T_1: ns, T_2: µs, exchange processes: µs - ms) though spectra tend to be broadened by incomplete averaging of anisotropic interactions. Lineshapes are also influenced by dynamic processes in molecules which cause a modulation in the NMR parameters as a function of time. The nucleus experiences differing time-dependent quantities such as local environments, relative orientations, atomic distances and so on. This in turn provides varying chemical shifts, providing information on the type, timescale and magnitude of the motions. Obtaining data on these types of motions and motional models is vital in order to

understand the many functionally important mechanisms that occur in biomolecules on the microsecond-to-millisecond timescale.[83, 86]

In this chapter we report on a series of studies on crystalline ACh salts. Of particular interest is the quaternary ammonium group as this is a widely used pharmacophore in the pharmaceutical sector, as it facilitates the formation of cation-pi interactions between drug and receptor. Extensive research into the motional properties of quaternary ammonium groups have revealed that these functional groups exhibit complex motional processes (about the C_3 and C_3', Section 3.1) [1, 73, 87-88] that reflect the packing of local environment, and NMR studies of deuterated molecules have shown that these motional processes can impact on the spectra obtained [1, 73]. In this chapter, we will investigate how these motional processes influence the ^{13}C CP-MAS spectra of the ACh salts. Our studies have revealed that the complex motion exhibited by the quaternary ammonium group can lead to significant changes in the ^{13}C CP-MAS lineshape.

Using the static NMR parameters obtained via *ab initio* quantum mechanical calculations in Section 2.3.2, we have performed numerical simulations that accurately reproduce these motional averaged lineshapes. This allows us to characterize the rates of motion occurring and provides insights into the activation energy for these motions.

This solid understanding of the link between the drugs structure and the ^{13}C CP-MAS lineshape is important if ^{13}C CP-MAS is to be routinely used for the characterisation of drugs in the pharmaceutical sector. In the following sections I have described the theory that underlies the methods employed that will help in the interpretation of the ^{13}C lineshapes and the dynamics present in the system.

4.2 Materials and Methods

The materials used in this chapter are characterised in detail in Chapter 2. Details of experimental methods used to obtain NMR data are described Section 1.4.5.

4.2.1 Numerical Simulations of Exchange CP-MAS NMR Lineshapes

To understand the dynamics that are taking place at the N-methyl group ($C^{5,\ 6\ \&\ 7}$), numerical simulations of ^{13}C lineshapes were carried out.

The chemical exchange model we have implemented is discussed in detail in Section 1.3.4: Chemical Exchange. The chemical exchange simulations were performed using *SPINACH* v.2.1.4400 [19], an open-source spin dynamics simulation library. These simulations require the NMR parameters for a single ACh molecule (chosen from unit cells for each salt using *CHIMERA* [89]) which were obtained from the static *CASTEP* [34] numerical simulations (Section 2.3.2) using a conversion script (coded by Dr Ilya Kuprov).

The simulations were performed using Fokker Planck formalism to remove the time dependency of the nuclear spin and MAS Hamiltonians. The size of space was increased incrementally and converged at a value of 5. The FID was subsequently processed by applying a line broadening of 70 Hz to mirror that of the experiments. Three N-methyl ^{13}C sites were chosen for each salt to perform the multi-site chemical exchange calculations with 12,800 powder points and zero-filled to 16,384 points before FT. The magnetic field strength applied was 14.1 T with a MAS rate of 10 kHz. For the nuclei ^{13}C, the chemical shift tensors, Euler angles (converted from the chemical shift tensors), internuclear coordinates were obtained from the *CASTEP* calculations. The exchange rate was arrayed to simulate the lineshape that most matched the experimental lineshape. An example of a script used for the calculation of chemical exchange is shown in Appendix E.1.

4.3 Variable Temperature Studies of the CP-MAS Lineshapes of ACh Salts

Room temperature measurements of the ACh salts were conducted to investigate the effect of the counterions on the lineshape.

The spectra of ACh perchlorate (Figure 4.2A) reveals the presence of five well resolved resonances, Lorentzian in nature. On the basis of previously published assignments [90] these can be assigned as shown in Table 4.1. For each of the other ACh salts studied the C-methyl and CO are again well resolved; however, in contrast to the perchlorate salt, ACh chloride, bromide and iodide (Figure 4.2B, C and D respectively) exhibit more complex lineshapes in the region of 50 ppm - 70 ppm arising from a superimposition of the methyls of the quaternary ammonium group and the CH_2's of the ethanolamine backbone.

Table 4.1: Table of ^{13}C chemical shifts corresponding to spectra shown in Figure 17

Site	ACh ClO_4^- (ppm)	ACh Cl (ppm)	ACh Br (ppm)	ACh I (ppm)
CH_3 (C^1)	23	24	22	22
COO (C^2)	175	175	174	175
OCH_2 (C^3)	62	60	62	~58
NCH_2 (C^4)	67	63	67	~68
$(CH_3)_3$ ($C^{5,6,7}$)	57	55	56	~58

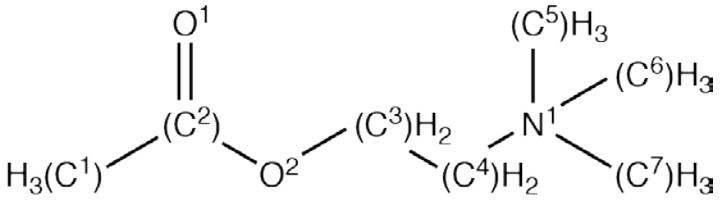

Figure 4.1: Chemical structure of acetylcholine with carbon sites labelled.

The ACh chloride spectrum (Figure 4.2B) shows broad overlapping peaks from 55 ppm to 65 ppm resulting in reduced spectral intensity and the N-methyl peak at 55 ppm is much less intense than the N-methyl peak of the ACh perchlorate. Figure 4.2C (ACh bromide) shows a broad intense N-methyl resonance at 56 ppm behind which there appears to be the presence of an additional peak which may pertain to the OCH_2 peak which is typically at ~62 ppm. ACh iodide (Figure 4.2D) shows a broad, complex lineshape between 55 ppm and 70 ppm. The N-methyl peak dominates the region between ~50 ppm and ~70 ppm. Due to the broad nature of the lineshape, the CH_2 groups cannot be accurately assigned.

The differences in carbon-13 lineshape observed for the ACh salt at room temperature led us to hypothesize that the differences observed in Figure 4.2 reflect differences in the dynamics of the quaternary ammonium group. This arises from differences in conformation and crystal packing in the different ACh salts, as had been previously observed in deuterium NMR and relaxation studies of ACh salts [1] and other quaternary ammonium groups. As with the ^{14}N lineshapes (Chapter 3), by studying the ^{13}C lineshapes of the ACh salts as a function of temperature, one can determine the motional characteristics of the quaternary ammonium groups in each system.

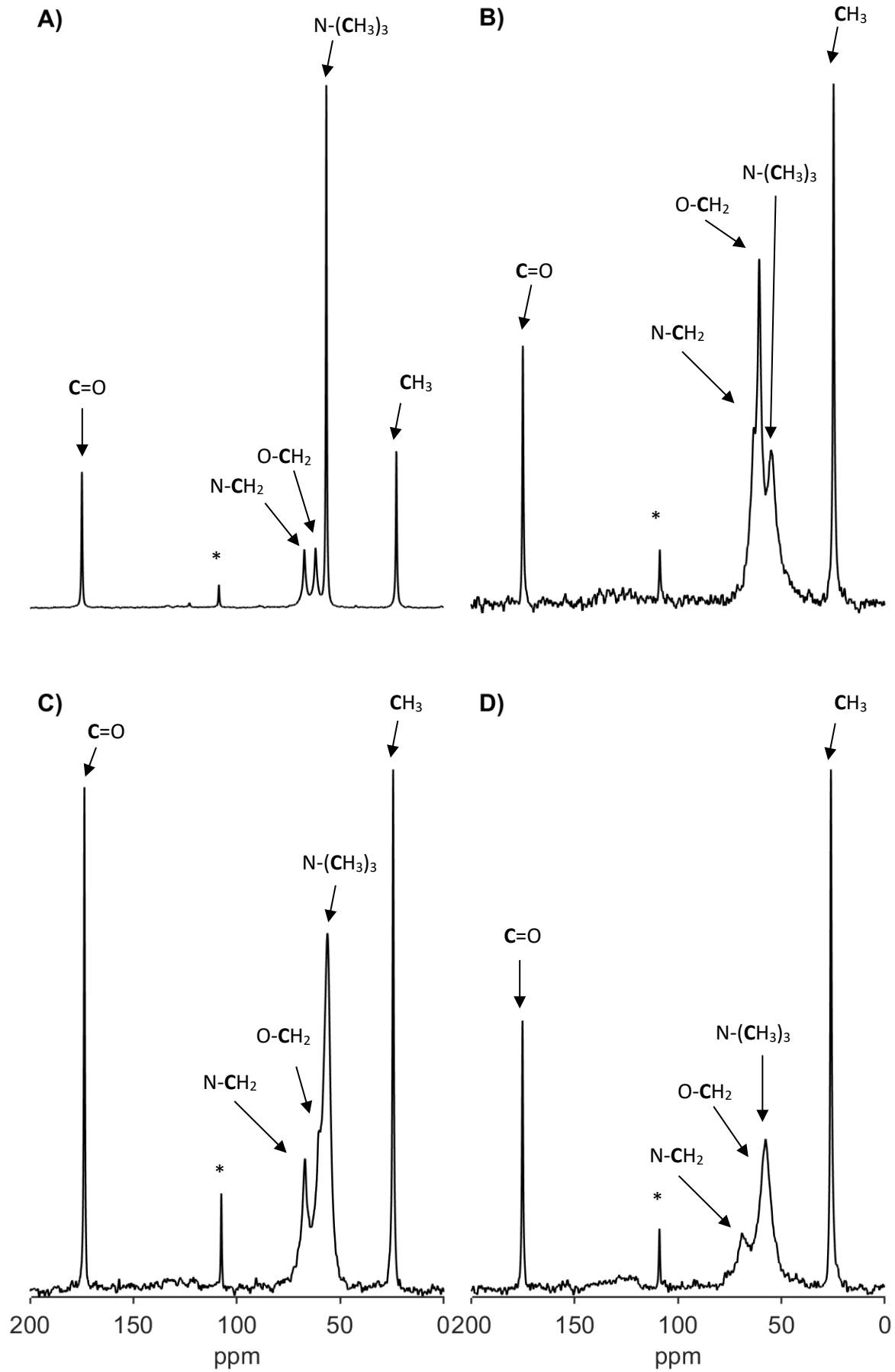

Figure 4.2. Carbon-13 CP-MAS spectra of ACh perchlorate (A), chloride (B), bromide (C), iodide (D) with peaks assigned to corresponding sites. Data acquired at 293 K with 10 kHz MAS. Sidebands appear at same positions in all CP spectra and are highlighted in each figure with (*).

4.3.1 Variable Temperature CP-MAS Studies of ACh Perchlorate

CP-MAS ^{13}C spectra (Figure 4.3) of ACh perchlorate were measured across a range of temperatures to assess the influence of temperature on the spectra. Five peaks are clearly resolved at each temperature that correspond to the five magnetically equivalent carbon atoms in the ACh and are assigned based on previous work [90]. If, as we hypothesize, the complex lineshapes arise from motional processes that are occurring on the micro- to milli-second timescale, this would suggest that in the case of the ACh perchlorate either such motions are absent (and the three N-methyls are magnetically equivalent), or they are, even at the lowest temperature, occurring in the fast limit such that a single average peak is observed.

A more careful analysis of the N-methyl at lower temperature reveals modest changes in the lineshape; the linewidth remains at ~80 Hz from 313 K to 253 K, and as the temperature drops to 233 K and 218 K (Figure 4.3A and F) we observe a change in linewidth to 87 Hz and 92 Hz, respectively. These changes in linewidth at the lower temperatures suggest that a reduction in the motion is occurring resulting in an increase in the density of motions in the milli/microsecond timescale. This is in agreement with previous deuterium NMR data [1, 90] where changes to the ^{2}H lineshape below 230 K indicated a change in the motion of the quaternary ammonium group.

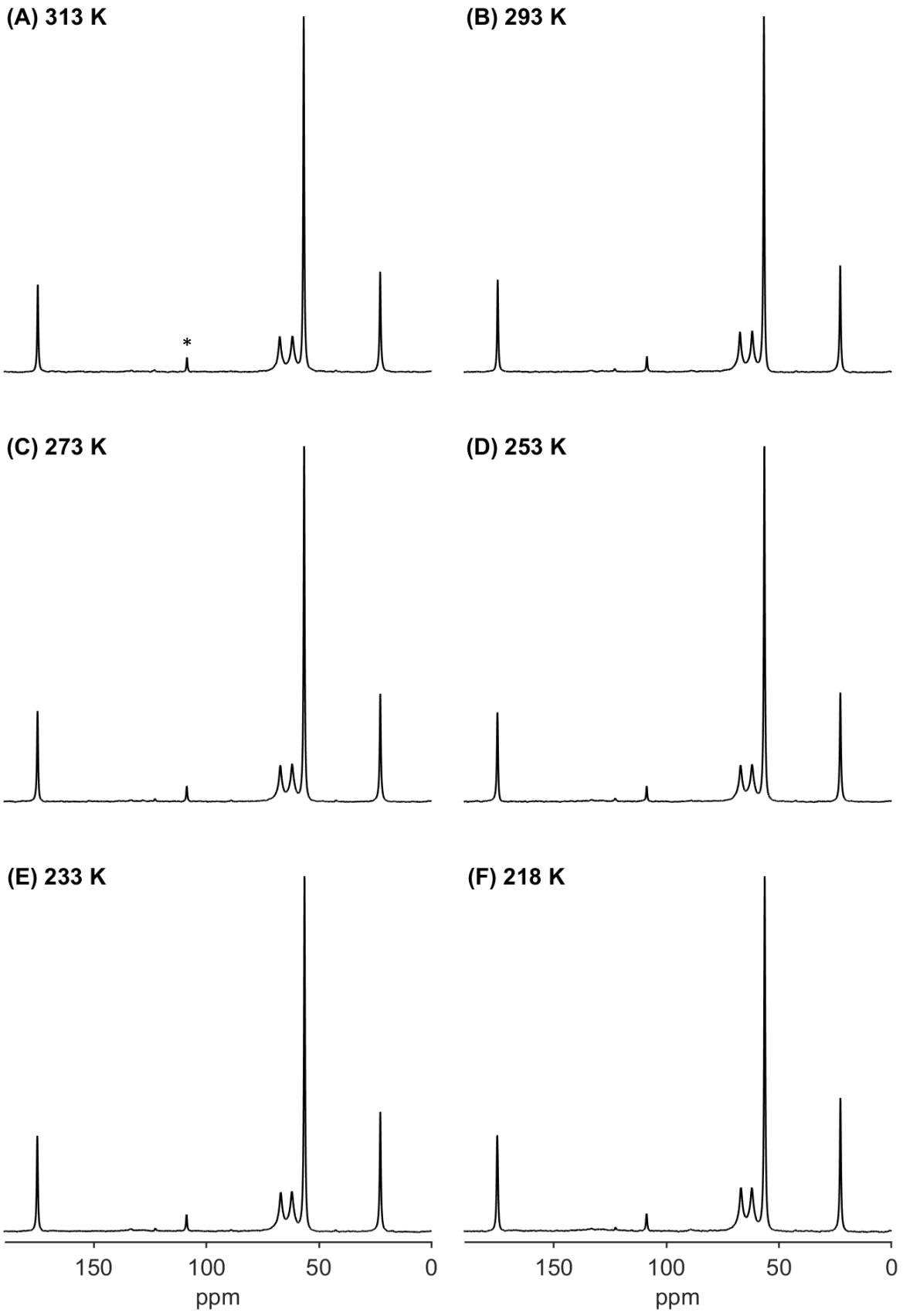

Figure 4.3: VT ^{13}C CP-MAS spectra of ACh perchlorate. Data acquired at temperatures indicated and sideband denoted with (*)..

4.3.2 Variable Temperature CP-MAS Studies of ACh Chloride

CP-MAS ^{13}C measurements (Figure 4.4) of ACh chloride were performed over a range of temperatures. The COO and CH_3 peaks at 175 ppm and 24 ppm respectively remain invariant to the temperature change, retaining its relative intensities and lineshape. The spectral envelope belonging to the N-methyl carbons and the two CH_2 carbons exhibit strong temperature dependence; superimposing the spectra revealed the peaks attributed to the CH_2 carbons to show little change, whereas, the broad N-methyl resonances changes drastically, particularly between the two lowest temperatures.

Due to the complexity in the lineshape between 50 ppm and 65 ppm, assigning of the N-methyl and $(CH_2)_2$ resonances accurately is challenging. The significant variation in lineshape over the temperature range studied is indicative of changes in the amplitude of frequency of motions on the μs and ms timescale.

Figure 4.4A, B and C (313 K, 293 K and 273 K) show the N-methyl peak at 55 ppm exhibiting invariance in the intensity until the temperature is decreased and we observe the intensity rise (Figure 4.4D and E) before decreasing marginally in Figure 4.4F. Upon closer examination of Figure 4.4F, 213 K, the presence of an additional resonance is observed at the N-methyl peak (51 ppm and 55 ppm).

The change in N-methyl lineshape between temperatures 233 K and 218 K (Figure 4.4E and F) is indicative of motions that are entering the slow motional regime; the broad single peak in Figure 4.4E signifies motions in the intermediate motional regime and the presence of the additional carbon resonance at 51 ppm in spectrum implies motions entering the slow motional regime, with individual sites becoming resolved.

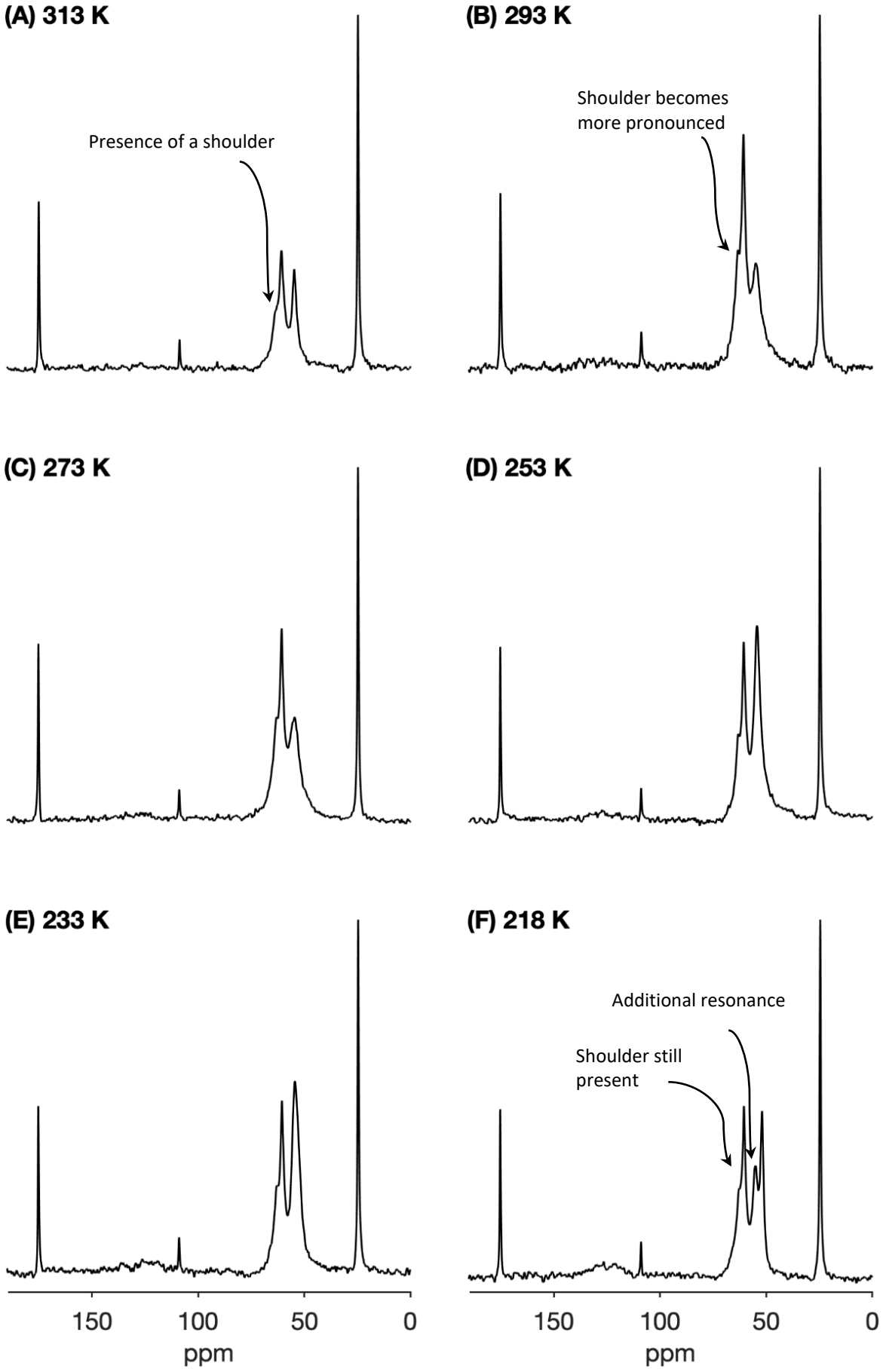

Figure 4.4: VT ^{13}C CP-MAS spectra of ACh chloride, MAS 10 kHz. Data acquired at temperatures indicated and sidebands denoted with (*). The presence of any additional N-methyl resonances are indicated on the spectrum.

4.3.3 Variable Temperature CP-MAS Studies of ACh Bromide

CP-MAS ^{13}C spectra of ACh bromide measured across a range of temperatures are shown in Figure 4.5. At each temperature the two resonances corresponding to the CH_3 and the COO are well resolved at 22 ppm and 174 ppm respectively. Between 50 ppm and 65 ppm the signals from the CH_2's and the N-methyl carbons form a complex lineshape. At lower temperatures three sites are clearly resolved, two from the CH_2's (NCH_2 and OCH_2), as well as the resonance appearing at 56 ppm pertaining to the N-methyl carbons.

Figure 4.5 shows little variation in lineshape above 273 K; below 273 K, however, the broad N-methyl peak observed at 56 ppm begins to change and we observe the appearance of a peak from behind the N-methyl which would be consistent with the CH_2 resonance at ~61 ppm. As the temperature decreases to 273 K (Figure 4.5C), however, we see the shoulder evolve into a more defined peak at 61 ppm, on which we observe a hump (indicated in Figure 4.5C), a chemical shift we previously attributed to the OCH_2 site for ACh perchlorate. Figure 4.5D (253 K) reveals the presence of a second N-methyl resonance at 54.5 ppm in conjunction with the N-methyl peak at 55.5 ppm; the peak at 61 ppm retains the "hump" at 62 ppm. As the sample is cooled further, a reduction in spectral intensity is observed, specifically at the OCH_2, NCH_2 and N-methyl sites.

As the sample is cooled below 253 K, the reduced spectral intensity impedes accurate interpretation of the data; however, the existence of multiple resonances at lower temperatures is evidence of the N-methyl carbons beginning to occupy different magnetic environments.

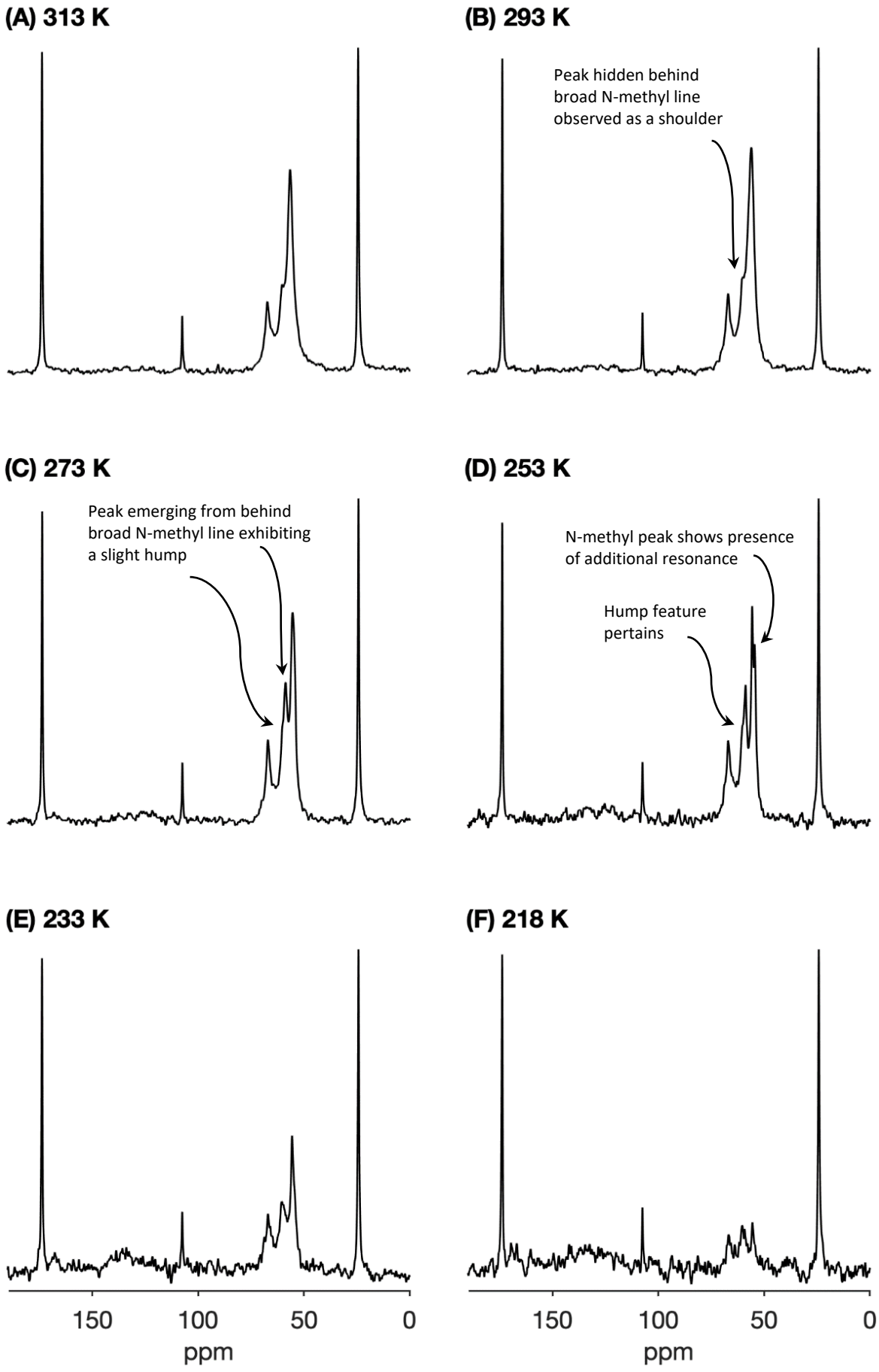

Figure 4.5: VT ^{13}C CP-MAS spectra of ACh bromide, MAS 10 kHz. Data acquired at temperatures indicated and sidebands denoted with (*). The presence of any additional N-methyl resonances are indicated on the spectrum.

4.3.4 Variable Temperature CP-MAS Studies of ACh Iodide

The CP-MAS ^{13}C spectra of ACh iodide measured across a range of temperatures are shown in Figure 4.6. The ACh iodide lineshape shows sharp CH_3 and COO lines at 22 ppm and 175 ppm; the relative intensities of these two peaks do not vary over the range of temperatures measure. The spectra show the signal attributed to the N-methyl carbons at 58 ppm is sufficiently broad to obscure the CH_2 signals at ~68 ppm.

The NCH_2 and OCH_2 peaks (~68 ppm) are difficult to assign as there is significant overlap from the broad N-methyl peak. Further examination of the N-methyl peak in Figure 4.6C, however, reveals the presence of two resonances at 58.4 ppm and 57.3 ppm. As the temperature is lowered to 253 K (Figure 4.6D) the N-methyl peak gains intensity and the resonances at 58.6 ppm and 56.9 ppm are more pronounced, and we observe the presence of a “shoulder” appearing at 55.5 ppm. The N-methyl lineshape between Figure 4.6D and E does not show much variation and this was confirmed by superimposing the spectra. As the sample is cooled to 218 K (Figure 4.6F), however, three overlapped N-methyl resonances are observed at 58.3 ppm, 57.2 ppm and 54.1 ppm.

The appearance of multiple resonances at the N-methyl sites as the temperature is lowered indicates that the sites are occupying different environments.

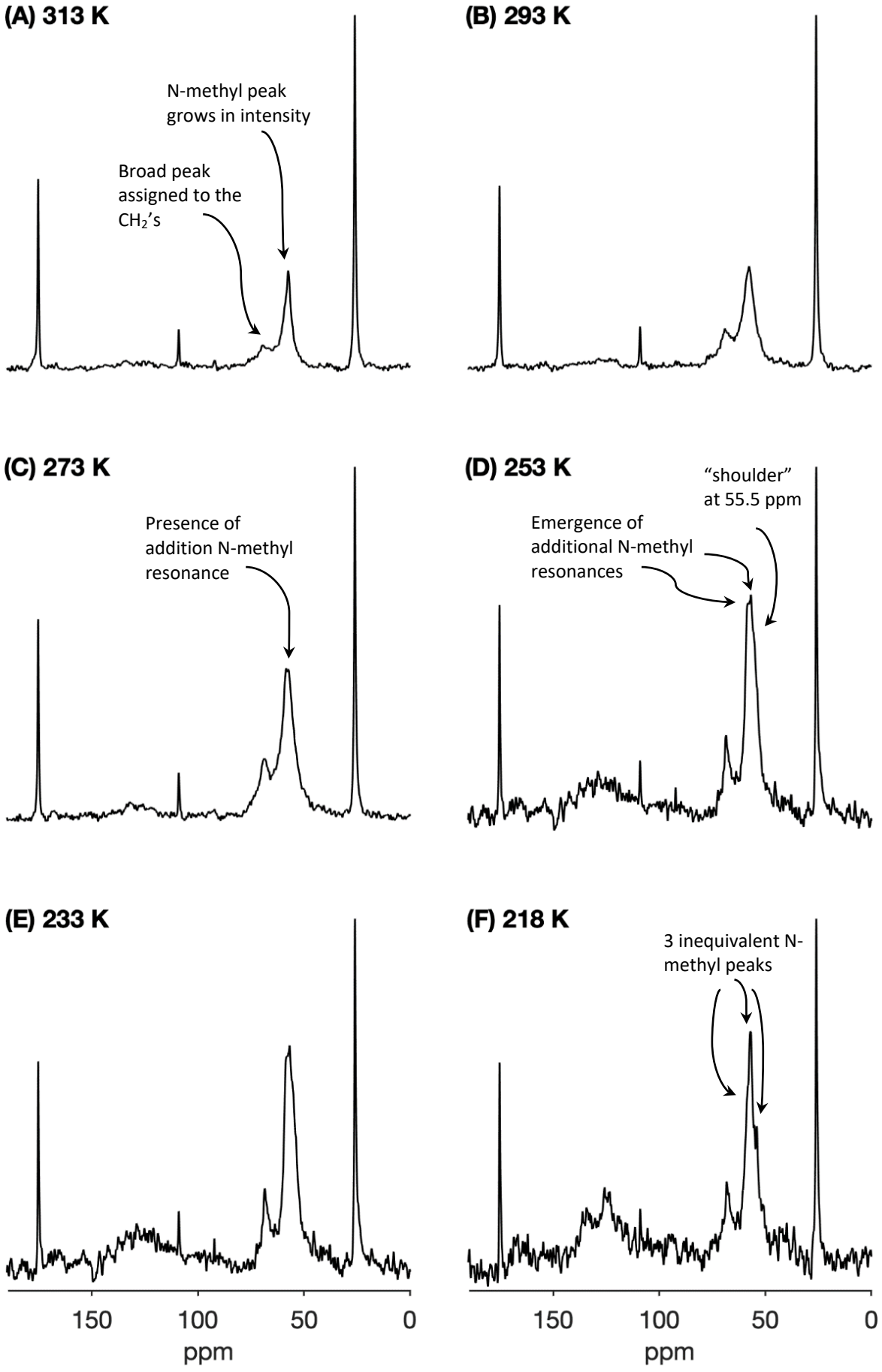

Figure 4.6: VT ^{13}C CP-MAS spectra of ACh iodide, MAS 10 kHz. Data acquired at temperatures indicated and sidebands denoted with (*). The presence of any additional N-methyl resonances are indicated on the spectrum.

4.3.5 Lineshape Analysis Summary

These observations indicate that the complex lineshapes that arise in the N-methyl region of the spectrum (~50 ppm - 60 ppm) arise from the dynamics experienced by the quaternary ammonium group that are occurring on the micro- to millisecond timescale. Previous studies (Figure 3.2) have indicated that the quaternary ammonium group undergoes rotational dynamics, with the methyl groups hopping between the three sites. This would suggest that the broadening observed is a result of chemical exchange between the three sites that is occurring on the timescale of the chemical shift/MAS. The effects of such processes on the lineshape are readily accessible with numerical simulations, however they demand a detailed knowledge of the nuclear spin interactions (e.g. chemical shielding anisotropy etc) and their relative orientations.

These parameters were obtained by performing a series of *CASTEP* calculations, as described in Section 2.3.2. These parameters were then used to model the motional processes by performing numerical calculations which simulate the chemical exchange process. In the following sections, lineshapes will be compared with exchange simulations assuming exchange between the three N-methyl sites, assuming the geometries and tensor properties derived from XRD and *CASTEP* simulations (Chapter 2).

4.4 Chemical Exchange Lineshape Simulations

The chemical exchange CP-MAS lineshape simulations were performed using the NMR parameters obtained via the *CASTEP* calculations. In the following section, the simulated CP-MAS lineshapes for the N-methyl carbons experiencing 3 site chemical exchange are shown.

4.4.1 Lineshape Comparison of Acetylcholine Perchlorate

The perchlorate salt showed little variation in linewidth across the temperature range studied (Figure 4.7). The *CASTEP* simulations, indicated that the three methyl groups occupied three chemically distinct environments giving rise the chemical shifts at 52.4 ppm, 54.3 ppm and 59.1 ppm; this suggests that the experimental lineshape is a result of fast motional averaging. Exchange lineshapes were calculated (with 70 Hz linebroadening added to mirror that added to the experimental data) and visually compared with the experimental data.

Figure 4.7A, B, C and D show the presence of a single resonance assigned to the N-methyl carbons which is consistent with an exchange rate of 400,000 s^{-1}. Interestingly, as we lower temperature to 233 K and 218 K (Figure 4.7E and F), the lineshapes are consistent with exchange rates of 370,000 s^{-1} and 350,000 s^{-1}, respectively.

This indicates that a change in motional timescale occurs at the N-methyl group as one reaches low temperatures, though it is modest change in dynamics. From previous work [1], the nitrogen-14 (Chapter 3) and carbon-13 data shown above paired with the XRD data (Section 2.3.1: XRD Results) we see that despite the counterion being in close proximity to the quaternary ammonium group, the relative free rotation of this group does not appear impinged.

It can be hypothesised that the motions present at the N-methyl site have a low activation barrier, further explaining the large exchange rates. At temperatures exceeding 233 K the lineshape comparison indicates dynamics in the fast motional; the comparison at 233 K and 228 K show fast motions entering a fast-to-intermediate motional regime, where a single resonance is observed though broadened by the slowing of the rapid chemical exchange of the N-methyl sites.

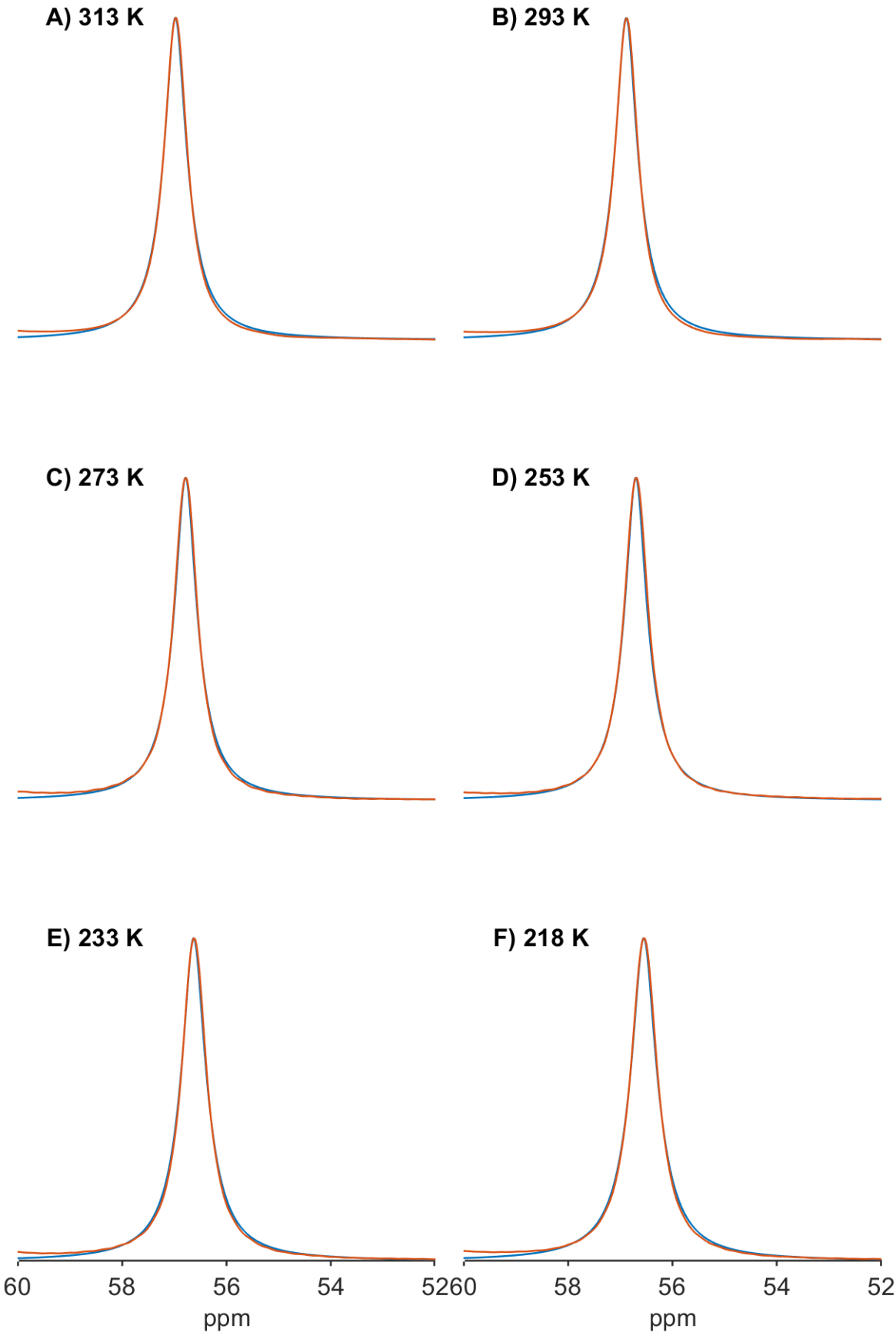

Figure 4.7: Figure showing magnified ^{13}C VT spectra showing magnified N-methyl lineshape (blue) superimposed with simulated chemical exchange lineshape (orange) for ACh perchlorate

4.4.2 Lineshape Comparison of Acetylcholine Chloride

The ACh chloride lineshapes (Figure 4.8), as previously discussed, were difficult to interpret as the N-methyl peak exhibited a complex lineshape, frequently of low intensity. The *CASTEP* simulations revealed the presence of 3 magnetically inequivalent N-methyl carbon sites, suggesting that the complex experimental lineshape observed is a result of the motional averaging. At exchange rates exceeding 250 s^{-1}, a single resonance is observed in 5 of the 6 spectra shown below.

At 313 K (Figure 4.8A), the experimental data was best fit by modelling the exchange between the three methyl sites with a rate of 7000 s^{-1}. As the temperature was lowered to 293 K and 273 K, the lineshapes were consistent with exchange rate between the sites of 1400 s^{-1} and 1200 s^{-1}. Lowering the temperature further to 253 K and 233 K showed that the N-methyl peaks are better resolved from the CH_2 envelope, and the resonances are more consistent with exchange rates of 1900 s^{-1} and 1800 s^{-1}, respectively. At the lowest temperature used in this study (218 K, Figure 4.8F), the N-methyl is split into two resonances, which is consistent with modelling the motion between the three methyl groups with an exchange rate of 250 s^{-1}, although we note that the simulations do not mirror the relative intensities of the experimental lineshapes.

The rate of exchange of the methyl groups present in ACh chloride appears to be comparable to the FID; this causes the complexity seen in the lineshape between 293 K and 233 K.

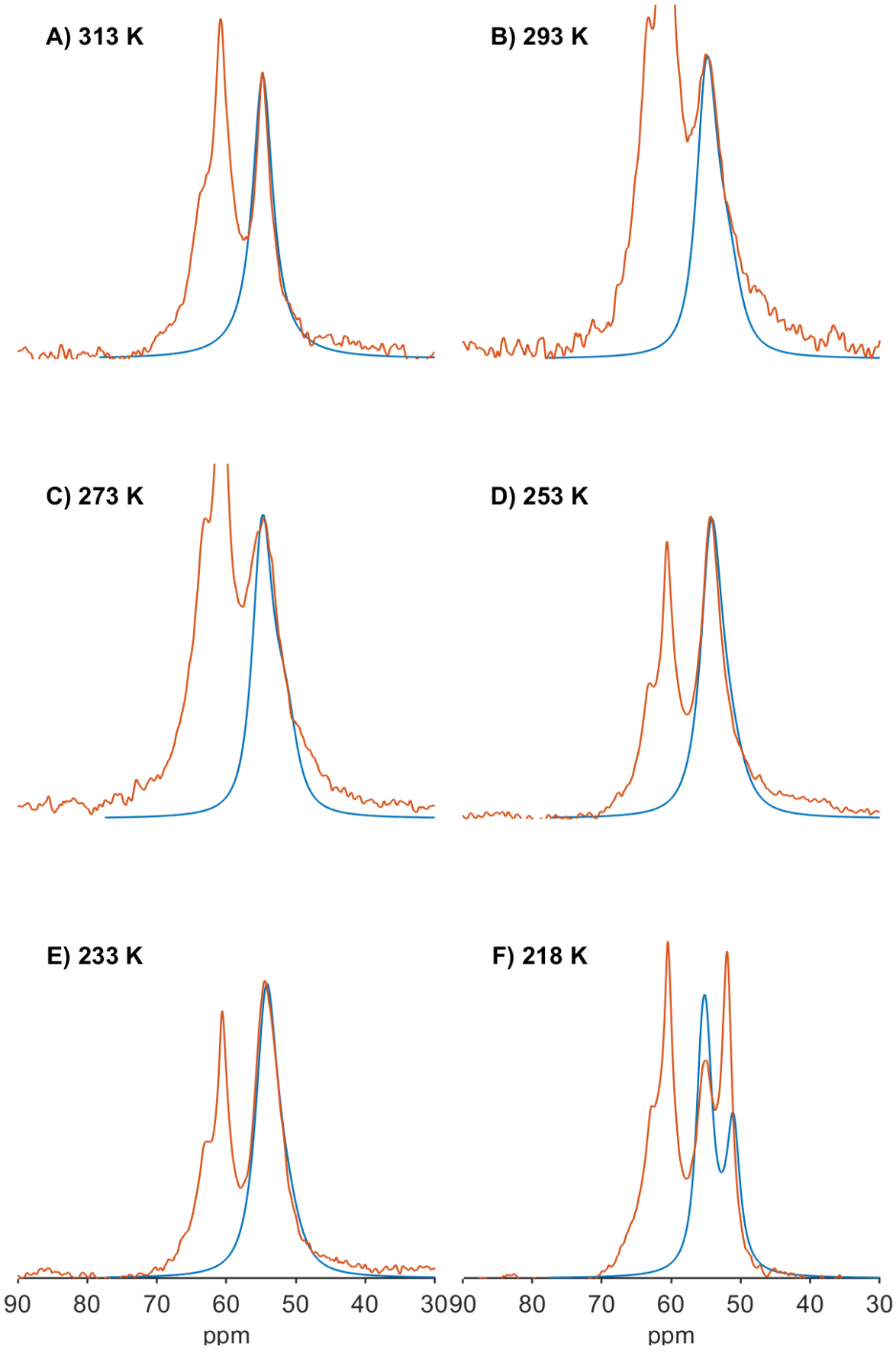

Figure 4.8: Comparison between ^{13}C VT spectra showing magnified N-methyl lineshape (blue) superimposed with simulated chemical exchange lineshape (orange) for ACh chloride

4.4.3 Lineshape Comparison of Acetylcholine Bromide

ACh bromide displayed a varying N-methyl lineshape Figure 4.9 across the temperature range studied. The static *CASTEP* simulations, analogous to the previous salts, also revealed the presence of 3 magnetically inequivalent N-methyl carbon sites giving rise to chemical shifts of 53.8 ppm, 54.3 ppm and 57.7 ppm, suggesting chemical exchange is the likely reason for the presence of the single peak single peak observed at 313 K and 293K (Figure 4.9A and B). The single N-methyl resonance observed, however, possesses a "shoulder" which as the sample is cooled becomes more pronounced.

Modelling the exchange between the methyl sites with an exchange rate of 600 s^{-1} results in a lineshape in agreement with the experimentally determined lineshape (Figure 4.9A), with the small shoulder observed at 57 ppm being reproduced in the experimental data. Reduction of the temperature to 293 K resulted in little change in the experimental lineshape, and again modelling the lineshape with an exchange rate of 600 s^{-1} yielded good agreement with experimental data.

Lowering the temperature to 273 K (Figure 4.9C), the N-methyl resonance becomes split into two distinct resonances, which are consistent with exchange between the sites occurring at a rate of 100 s^{-1}. Further changes are visible in the spectra as the temperature drops to 253 K consistent with an exchange of 20 s^{-1} (Figure 4.9D), with limited evidence of a third resonance appearing. Although this is not apparent in the simulation plotted with a linewidth of 70 Hz (the linebroadening applied to the experimental data), data processed with 20 Hz linebroadening (not shown) also exhibits the splitting of the peak as observed in the experimental data, at 53.8 ppm, 54.3 ppm and 57.7 ppm. As the temperature is lowered to 233 K and 218 K (Figure 4.9E and F), the experimental lineshapes become broader and are consistent with exchange rates of 10 s^{-1} and 5 s^{-1}, respectively; we note however, a discrepancy in the intensity of the N-methyl resonance in Figure 4.9E, at 57.7 ppm.

The exchange rate values for ACh bromide are much lower than both the perchlorate and chloride salts (600 s^{-1} at 313 K as opposed to 400,000 s^{-1} and 7000 s^{-1}, respectively). This indicates that the activation barrier is much higher, resulting in more hindered motions.

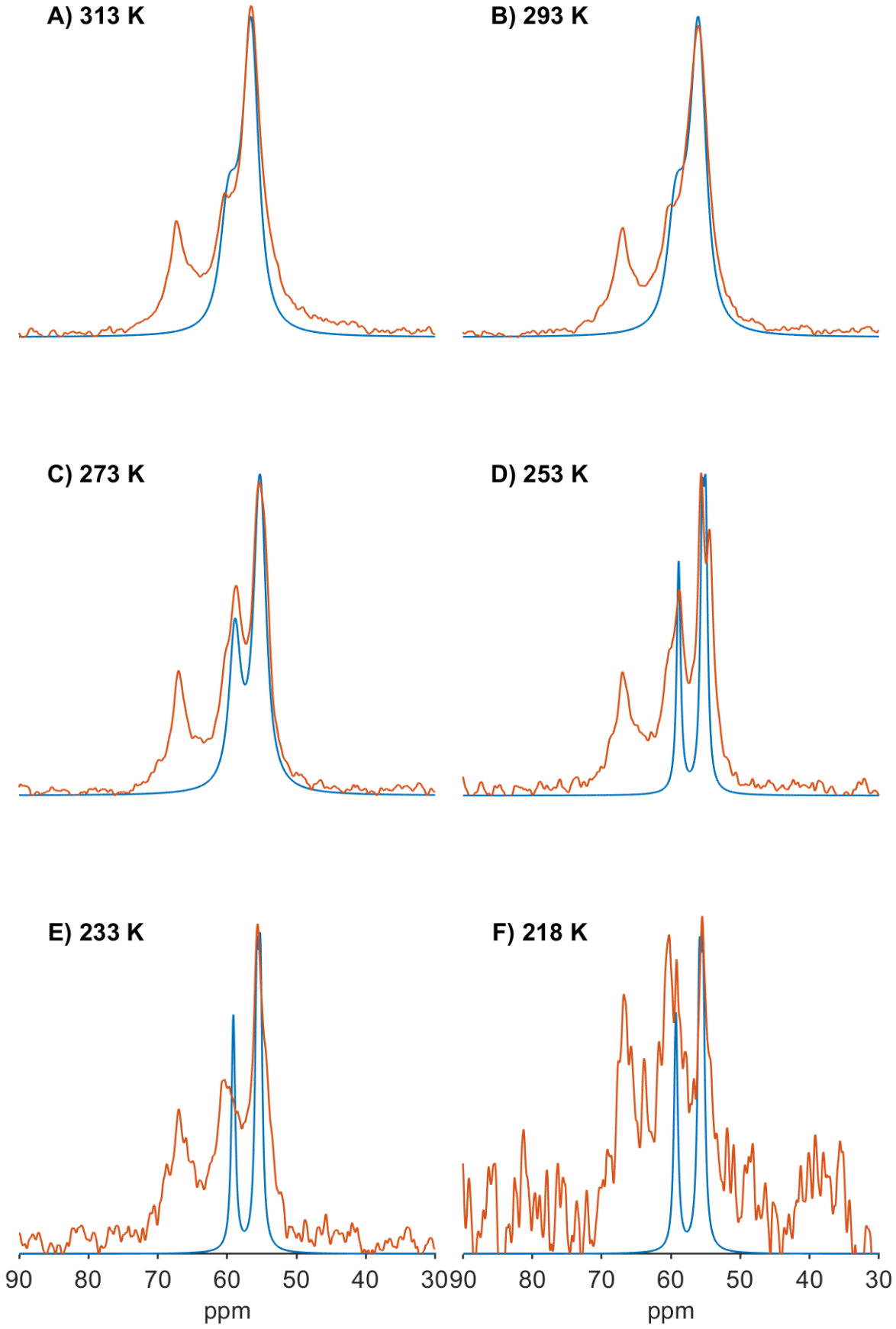

Figure 4.9: Comparison between ^{13}C VT spectra showing magnified N-methyl lineshape (blue) superimposed with simulated chemical exchange lineshape (orange) for ACh bromide

4.4.4 Lineshape Comparison of Acetylcholine Iodide

The ACh iodide spectra shown in Figure 4.10 are poorly resolved with only two peaks between 50 ppm and 70 ppm, the region typically attributed to the N-methyl, OCH_2 and NCH_2 sites. The *CASTEP* simulation revealed that the N-methyl carbons are magnetically inequivalent, suggesting that the broad resonance observed is a reflection of the chemical exchange process between the three sites. This gives rise to the broad resonance seen in Figure 4.10A which is consistent with simulated exchange between the three sites occurring on a timescale of 1800 s^{-1}.

As the temperature is lowered the experimental lineshape becomes broader. At 298 K, 273 K, 253 K and 233 K the lineshapes can be reproduced by modelling exchange between the three sites with rates of 800 s^{-1}, 700 s^{-1}, 600 s^{-1} and 500 s^{-1}, where two resonances are apparent. Further reduction in temperature to 218 K results in the appearance of 3 distinct resonances, which is consistent with exchange between the methyl groups occurring on a timescale of 200 s^{-1}.

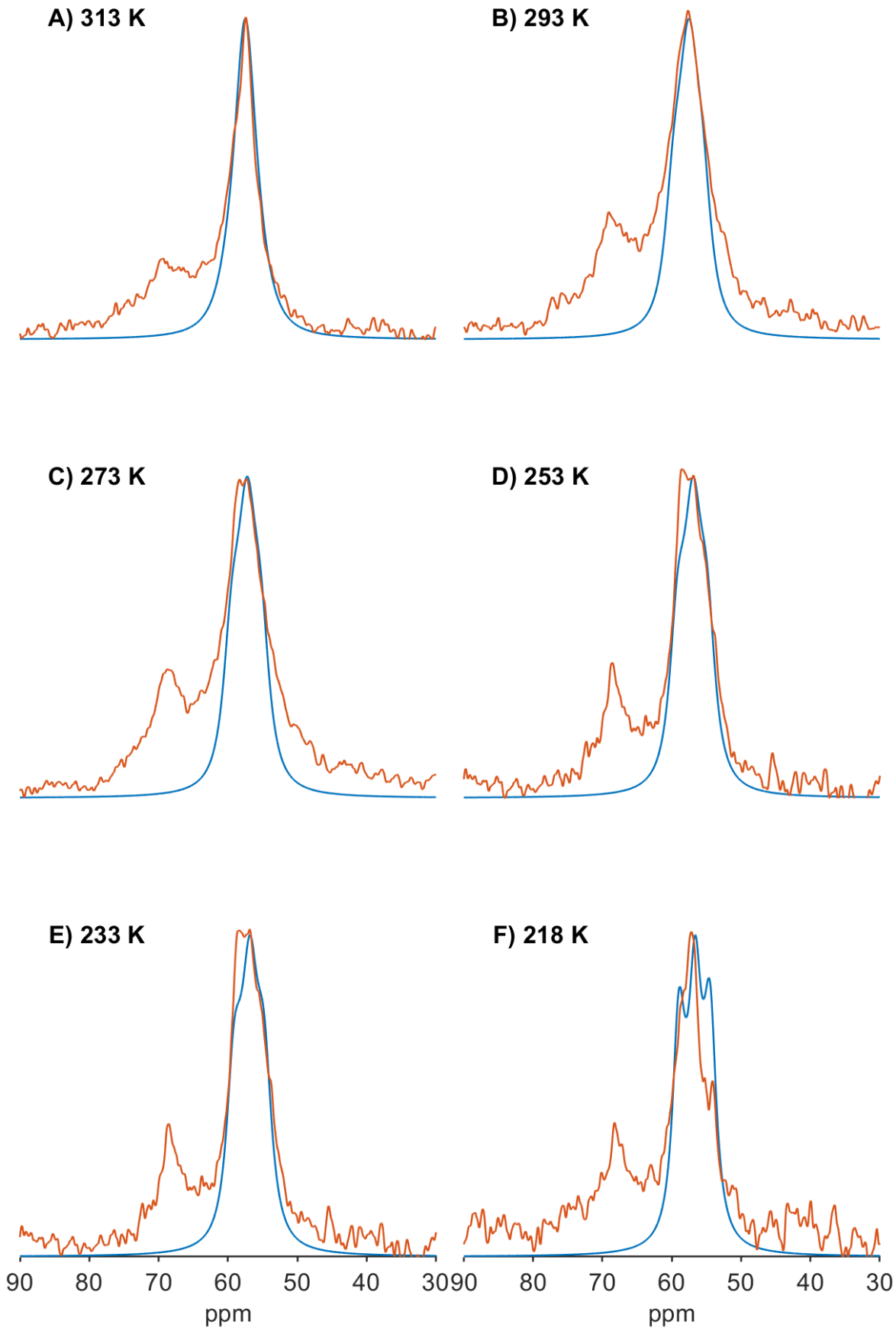

Figure 4.10: Comparison between ^{13}C VT spectra showing magnified N-methyl lineshape (blue) superimposed with simulated chemical exchange lineshape (orange) for ACh iodide

4.4.5 Chemical Exchange Lineshape Summary

The exchange rates which were consistent with the N-methyl resonances produced in the ^{13}C spectra are shown in Figure 4.11 as a function of temperature. Note that since the number of data points is lacking, an accurate Arrhenius plot cannot be presented. Acquisition of more data points and carrying out computational fitting of the lineshapes may allow for a more rigorous interpretation of the data and extraction of activation energies. Since this is a visual inspection, there may be a degree of error. This deviation is unique to each salt; for instance, since the N-methyl groups in the ACh perchlorate salt exhibit motions in the fast limit, the lineshape changes when the exchange rate is changed by ±25,000 s^{-1}. For ACh chloride and bromide the deviation is clear at ±25 s^{-1} (±2 s^{-1} for ACh chloride to simulate the lowest temperature, 218 K) and for ACh iodide ±5 s^{-1}.

We can see immediately, that ACh perchlorate showed the largest exchange rates by several orders of magnitude; at 313 K, the rate of exchange consistent with the N-methyl lineshape was ~400,000 s^{-1} compared to 7000 s^{-1}, 600 s^{-1} and 1800 s^{-1} for ACh chloride, bromide and iodide, respectively. This is consistent with the motional model we have discussed above where the N-methyl rotation in ACh perchlorate has a much lower energy barrier than the other systems. The decrease in exchange rate at 233 K and 218 K (370,000 s^{-1} and 350,000 s^{-1}) signifies a modest change in motional timescale and the absence of any magnetically inequivalent N-methyl sites suggests dynamics in the fast motional regime entering an intermediate (or fast-to-intermediate) regime. In contrast to this, the relatively low exchange rates for ACh chloride, bromide and iodide suggest a higher energy barrier for the rotation of the quaternary ammonium group. The evolution of the broad N-methyl peak for both the chloride and iodide salt into 2 and 3 magnetically inequivalent methyl sites, respectively, is suggestive of motions which were initially in the intermediate motional regime being supressed and entering a slow or slow-to-intermediate motional regime. ACh bromide exhibited the slowest exchange rate of the salts, with the experimental lineshape at high temperatures (313 K and 293 K) being consistent with an exchange rate 600 s-1; we observe the presence of an additional N-methyl resonance, unseen at high temperatures for any other salts, which becomes better resolved as the temperature is lowered. This resonance is evidence of magnetically inequivalent N-methyl carbons at high temperatures indicating that the energy barrier for the N-methyl group rotation is much higher than for the other salts. Interestingly, ACh iodide is the only salt that revealed the presence of 3 potential N-methyl resonances over the range of temperatures measured.

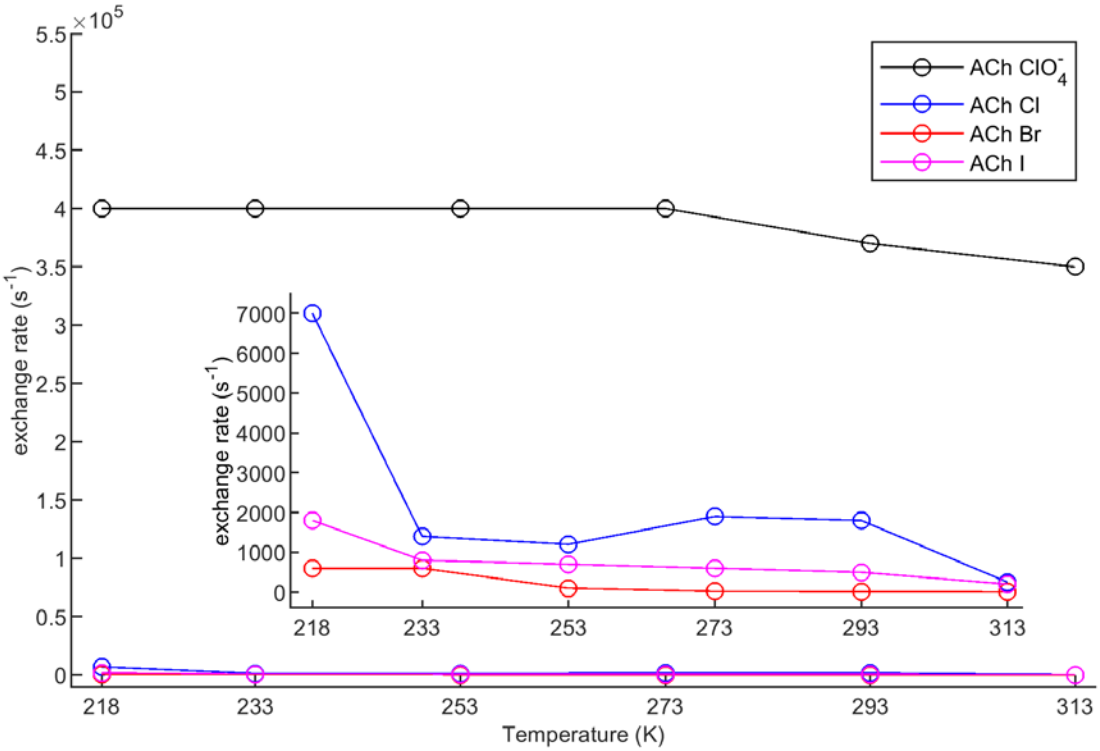

Figure 4.11: Plot displaying the exchange rates for ACh salts. Subplot shows magnified plots corresponding to ACh chloride, bromide and iodide which exhibit much lower exchange rate values than ACh perchlorate

4.5 Relaxation Analysis

4.5.1 Introduction

Modelling of the lineshapes revealed that for each of the ACh salts studied, the N-methyl groups of the quaternary ammonium group exhibited complex lineshapes due to chemical exchange on the milli- to micro-second timescale. Motions on this timescale are also known to influence relaxation in the rotating frame ($T_{1\rho}$ relaxation, see Section 1.3.3), which can significantly influence the sensitivity of CP measurements as described in Sections 1.3.3 and 1.4.5. To investigate how these motional processes effected the CP dynamics, the temperature dependence of the cross-polarization intensity was monitored as a function of contact time. The carbon sites observed are shown in Figure 4.1.

4.5.2 Acetylcholine Perchlorate Cross-Polarization Build-up

The build-up of ^{13}C magnetization as a function of contact time for ACh perchlorate measured across a range of temperatures are shown in Figure 4.12. The sites of interest $C^{5,6,7}$, the N-methyls, exhibits a consistently slow build-up (long T_{HC}) over the range of temperatures studied only plateauing when the contact time reach 6000 μs. The lack of decay in the build-up at high temperatures suggests an absence of $T_{1\rho}$ relaxation indicating a lack of change in motions occurring on the ms timescale. As the sample is cooled, however, the decay in intensity suggests an increase in the density of motions on the ms timescale.

The CH_2 groups, $C^{3,4}$, exhibit rapid build-ups indicating the presence of strong dipolar interactions and a low density of motions on the ms timescale. The carbonyl site, C^2, shows a very long T_{HC} due to a lack of close proximity protons to efficiently transfer polarization. The C^1 site exhibits a build-up characteristic of methyl group such that the motion of the methyl protons average the dipolar interaction resulting in relatively long T_{HC} build-ups which become shorter as the sample is cooled and the rotational motion becomes less rapid.

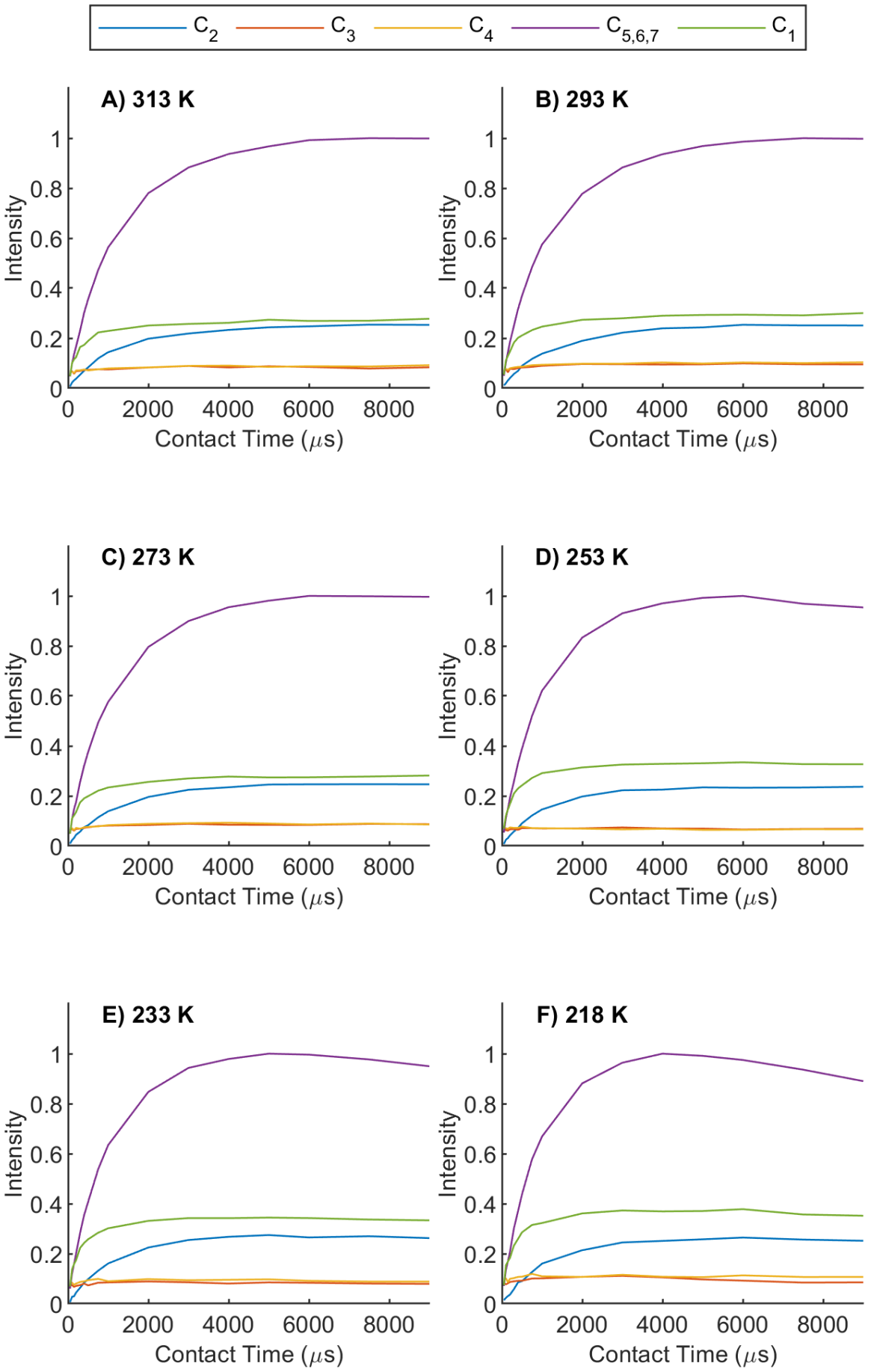

Figure 4.12: VT build-up plots of ACh perchlorate, MAS 10 kHz. Acquired at temperatures indicated using a CP MAS pulse sequence. Each colour corresponds to the intensity of each ^{13}C peak.

4.5.3 Acetylcholine Chloride Cross-Polarization Build-up

The build-up of carbon-13 magnetization of ACh chloride as a function of contact time is shown in Figure 4.13, measured over a range of temperatures, 313 K to 218 K. The consistently rapid T_{HC} build-up and $T_{1\rho}$ decay as we lower the temperature indicates a low density of motions on the microsecond and millisecond timescale. Unsurprisingly, the carbonyl and methyl sites show the slowest build-up of magnetization due to the limited number of protons near the COO carbon and motional averaging occurring at the methyl group, resulting in inefficient polarization transfer. The short $T_{1\rho}$ seen in Figure 4.13A and Figure 4.13B is indicative of motions occurring on the millisecond timescale. The change in the build-up and decay of the magnetization observed in the CH_2 carbons, $C^{3,4}$, as the sample is cooled indicates that the motion of the quaternary ammonium group influences the relaxation of all the protons within the system, a result of spin diffusion at the MAS frequency.

Interestingly, the $T_{1\rho}$ values for ACh chloride appear to change inconsistently with temperature, a trait observed in the lineshape studies. The decay of the signal in Figure 4.13A and Figure 4.13B (previously attributed to the millisecond motions) becomes less rapid at temperatures 273 K and 253 K (Figure 4.13C and Figure 4.13D) leading to longer $T_{1\rho}$ values suggesting a change in motions on the millisecond timescale. As the temperature is lowered to 233 K and 218 K (Figure 4.13E and Figure 4.13F), we observe once again a rapid decay in the signal resulting in short $T_{1\rho}$ similar to that seen at the highest temperature (Figure 4.13A).

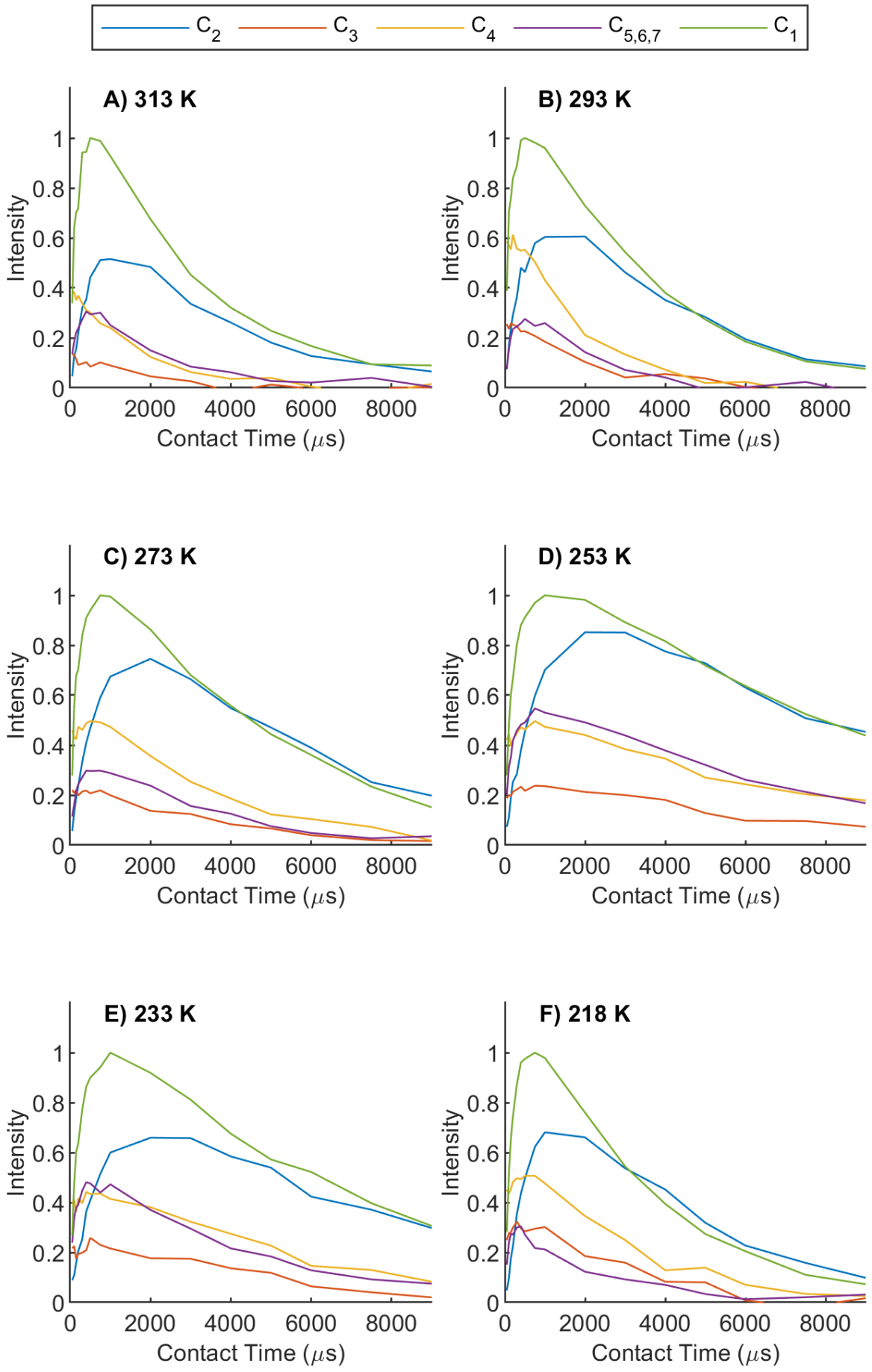

Figure 4.13: VT build-up plots of ACh chloride, MAS 10 kHz. Acquired at temperatures indicated using a CP MAS pulse sequence. Each colour corresponds to the intensity of each ^{13}C peak.

4.5.4 Acetylcholine Bromide Cross-Polarization Build-up

The build-up of ^{13}C magnetization as a function of contact time for ACh bromide measured across a range of temperatures is shown in Figure 4.14. The build-up profiles mirror the profiles seen for the other systems with the methyls and carbonyl sites exhibiting slower build-up in magnetization due to weak proton to carbon couplings as a result of proximity and motional averaging. Interestingly, as the temperature is lowered, the rate of signal decay increases suggesting short $T_{1\rho}$ at the lower temperatures and a higher density of motions in the micro- to millisecond timescale.

Since the CH_2 sites also exhibit an increase in the rate of decay as the temperature is lowered, we postulate that the motion of the quaternary ammonium group acts as an efficient source of relaxation for all the protons in the sample, likely due to spin-diffusion at the spinning speed, 10 kHz.

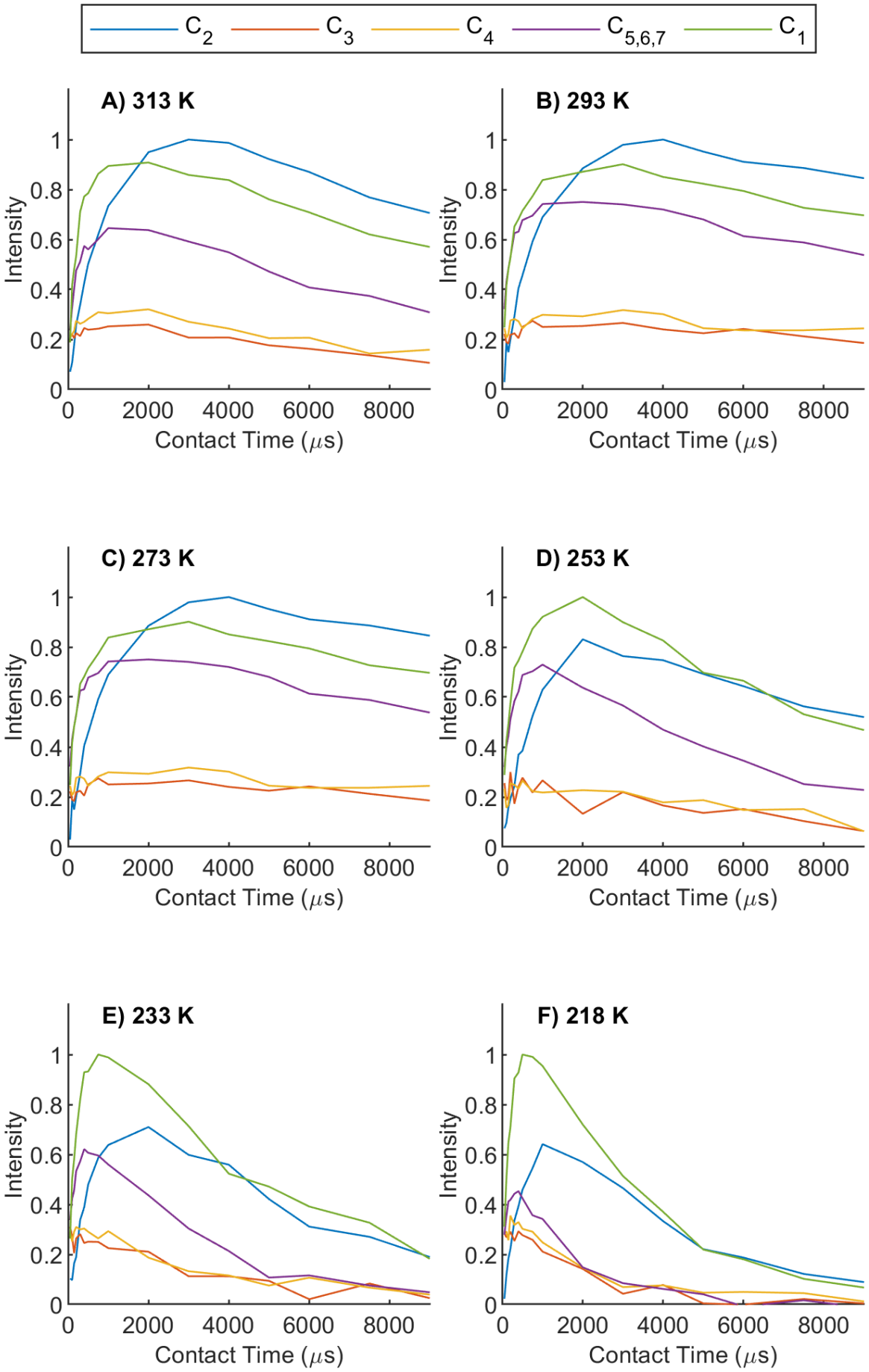

Figure 4.14: VT build-up plots of ACh bromide, MAS 10 kHz. Acquired at temperatures indicated using a CP MAS pulse sequence. Each colour corresponds to the intensity of each ^{13}C peak.

4.5.5 Acetylcholine Iodide Cross-Polarization Build-up

The build-up of ^{13}C magnetization is shown in Figure 4.15, measured across a range of temperatures (313 K to 218 K) as a function of contact time. Just as with the other salts, the carbonyl and methyl sites exhibit slower build-up magnetization as a result of motional averaging and proximity leading to weak dipolar couplings. Interestingly, the build-up of magnetization for all sites as we lower the temperature contrasts what we observed for ACh perchlorate, chloride and bromide for which the rate of signal decay increased indicating short $T_{1\rho}$; the build-up profile for ACh iodide, however, suggests longer $T_{1\rho}$ values and shorter T_{HC} as the sample is cooled suggesting that motions that are in both the micro- and millisecond timescale are undergoing changes. At higher temperatures, the short $T_{1\rho}$ values are indicative of a high density of motions on the millisecond timescale.

In contrast to the bromide salt, the intensity in the signal of the N-methyl carbon sites observed for ACh iodide increases as we lowered the temperature. Again, as with the other systems for the CH_2 sites, the change in the rate of signal decay as the sample is cooled suggests that the motion of the quaternary ammonium group influences the relaxation of the protons in the system.

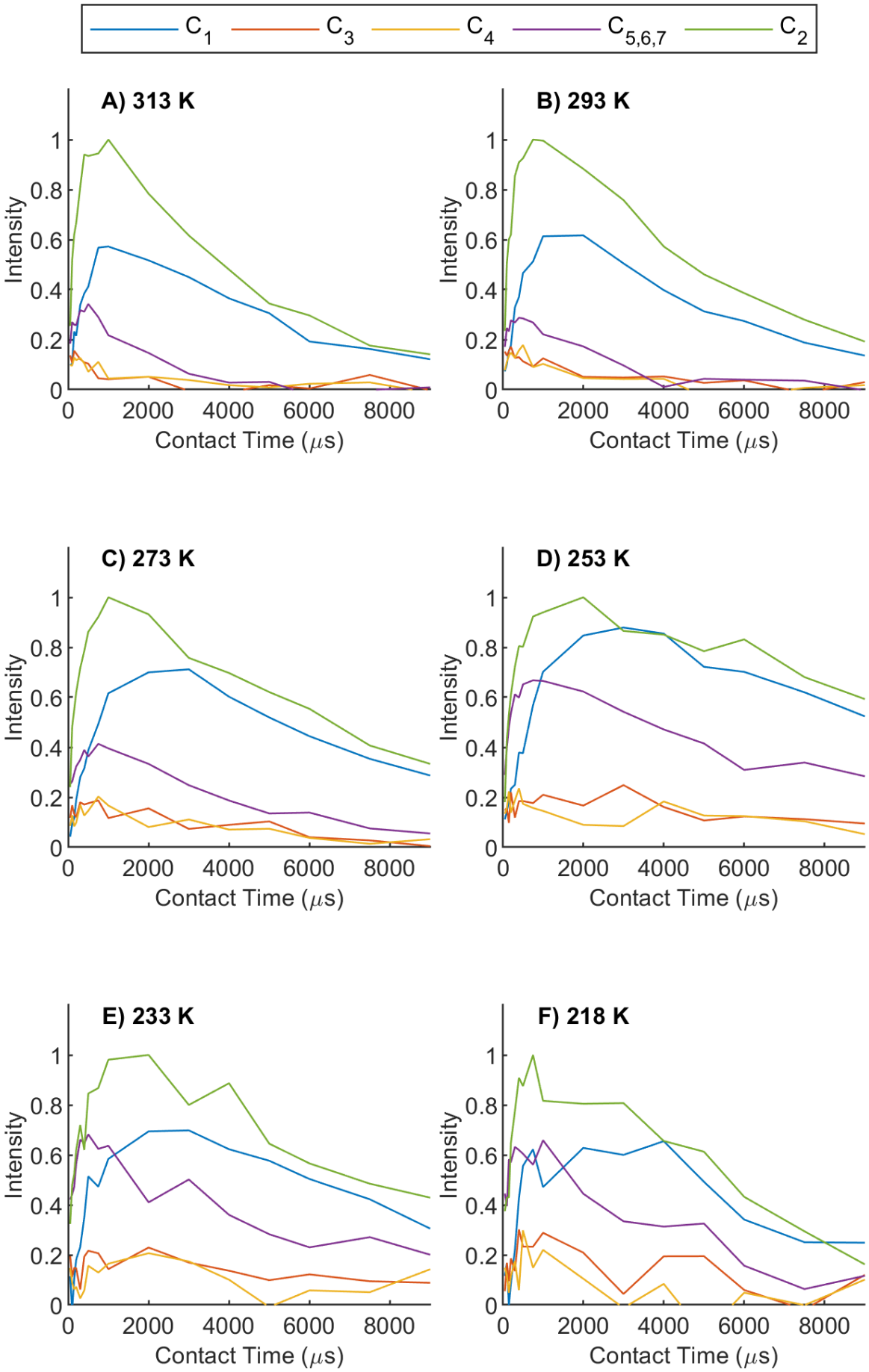

Figure 4.15: VT build-up plots of ACh iodide, MAS 10 kHz. Acquired at temperatures indicated using a CP MAS pulse sequence. Each colour corresponds to the intensity of each ^{13}C peak.

4.5.6 Relaxation Analysis Summary

The CP build-up data shown in Section 4.5 offers a wealth of information on the dynamics occurring in the family of ACh salts, specifically information on the N-methyl carbon sites observed in the NMR spectrum. The build-up and decay of the intensity, measured using the parameters T_{HC} and $T_{1\rho}$, provided a timescale for the motions present at the carbon site.

As predicted, the N-methyl carbons of ACh perchlorate showed very little change in motions on the ms timescale until low temperatures (233 K and 218 K) were reached indicating an increase in the density of motions on the ms timescale. The slow T_{HC} build-up indicates the presence of a high density of motions on the microsecond timescale. In contrast to the perchlorate salt, at high temperatures the ACh chloride shows variation in decay of magnetization, indicative of a change in the motions occurring on the millisecond timescale. The change in the decay of the magnetization observed in the CH_2 carbons, as the temperature is lowered indicates that the motion of the quaternary ammonium group influences the relaxation of the protons in the sample.

The build-up profiles for ACh bromide show a relatively long T_{HC} and $T_{1\rho}$ for the N-methyl carbons, compared to the chloride salt indicating a high density of motions in the micro- and millisecond timescale. As the sample is cooled the T_{HC} becomes shorter due to the slowing of the motions resulting in more efficient polarization transfer from the neighbouring protons to the observed carbon. The $T_{1\rho}$ also becomes shorter indicating changes in the motions in millisecond timescale.

Interestingly, the build-up plots for ACh iodide show an increase in both the $T_{1\rho}$ and T_{HC} as the temperature is lowered; the trend shown here is the opposite to that which is observed for the ACh bromide where the $T_{1\rho}$ and T_{HC} decreased as the sample was cooled. This indicates that there is a low density of motions on the millisecond timescale at higher temperatures (short $T_{1\rho}$) and as we lower the temperature the motions on the ms timescale undergo changes. The intensity of the N-methyl peaks also increase as the temperature was decreased, in contrast with ACh bromide where the intensity decreased.

From the observed build-up plots, it is clear that the motions at the N-methyl sites are heavily influenced by temperature and the type of counterion present. A solid understanding of the timescales of these motions are integral if we are to utilise NMR to observe motions in quaternary ammonium groups in larger systems.

4.6 Discussion

SS-NMR is a useful technique for investigating the molecular structure and dynamics in important biomolecules; this is an integral element of the pharmaceutical industry as many properties of the final product depend on the molecular structure, dynamics and type of polymorph present. An important pharmacophore, the quaternary ammonium group in a family of ACh salts were investigated using CP-MAS in order to gain insight into the conformation and dynamics present.

Interestingly, conducting CP-MAS measurements on the 4 salts, ACh perchlorate, chloride, bromide and iodide, at 293 K (Figure 4.2) produced ^{13}C spectra with distinct lineshapes. Although the spectra showed similarity in the sites pertaining to the carbon backbone, the presence of the different counterions produced complex lineshapes for the quaternary ammonium groups. In order to aid the analysis of many crystalline pharmaceuticals in which the quaternary ammonium group is ubiquitous, we must understand the origins of the observed complex lineshapes.

We postulated that the differences in the ^{13}C CP-MAS spectra may be due to different dynamics present in each of the salts (Section 4.3); in order to investigate this hypothesis we undertook a range of variable temperature NMR measurements (313 K to 218 K) which revealed that in all cases but the perchlorate (Figure 4.3), significant changes in the lineshape were observed, suggesting the presence of different dynamics at the quaternary ammonium sites. At the lower temperatures, ACh chloride, bromide and iodide (Figure 4.4, Figure 4.5 and Figure 4.6) all showed the presence of 2 or more resonances at the N-methyl sites indicating the presence of magnetically inequivalent quaternary ammonium carbons.

The dynamics characterised in our lineshape analysis (Section 4.3) is also mirrored in the analysis of the CP dynamics (Section 4.5: Relaxation Analysis), where the salts that exhibited a high density of motions on the millisecond timescale (ACh chloride, bromide and iodide) also exhibited relatively short magnetization build-up.

To interpret the spectra and characterise the dynamics that are occurring, we undertook numerical calculations to obtain the necessary NMR parameters. This is shown in detail in Chapter 2: Materials, Sample Characterisation and Calculation of NMR Parameters.

Once the spin interactions were calculated, the properties were used to simulate the CP-MAS lineshape, under the assumption that the quaternary ammonium methyls are undergoing 3 site chemical exchange (Section 4.4). The exchange simulations revealed that the N-methyl single resonance observed for ACh perchlorate (Figure 4.7) is a result of motions several orders of magnitude greater (400,000 s^{-1}) than ACh chloride, bromide and iodide (Figure 4.8, Figure 4.9 and Figure 4.10). However, by visually fitting the exchange simulations to the ^{13}C spectra showed that

at lower temperatures, the lineshape broadens and the exchange rate was decreased to achieve a good comparison indicating that motions are beginning to slow at lower temperatures. Chemical exchange simulations of ACh chloride (Figure 4.11, for ease of comparison) produced the second largest exchange rate (7000 s^{-1}), after ACh perchlorate, for the best comparison to the experimental lineshape at the highest temperature (313 K). ACh bromide and iodide both have comparatively lower exchange rates at high temperature (600 s^{-1} and 1800 s^{-1}). Interestingly, the bromide and iodide salts exhibited contrasting build-up profiles; the $T_{1\rho}$ values became shorter as the temperature was decreased, whereas the iodide salt showed an increase in the $T_{1\rho}$.

In this chapter, we have shown that the dynamics of the N-methyl carbons influence the lineshape in CP-MAS spectra and the relaxation of the protons in the sample. We have observed that in the case of ACh perchlorate, all the sites show an absence of $T_{1\rho}$ decay suggestive of intermediate or fast motions; however, for the halide salts (ACh chloride, bromide and iodide), we see a change in the $T_{1\rho}$ as the temperature is lowered indicating more hindered motions. These complex motional properties of the quaternary ammonium groups reflect the packing of the local environment, which is a vital facet of the pharmaceutical sector, since they facilitate the formation of cation-pi interactions between the drug and receptor.

Chapter 5 Quadrupolar Nuclei as a Tool for Studying Lipid Phase Behaviour

5.1 Introduction

Integral membrane proteins are of key interest in structural biology. Located on the cell surface they play an important role in the transport of both materials and information into and out of the cell.[91-92] Due to their accessibility and roles in these important processes, integral membrane proteins are key sites for pharmacological intervention with over 60% of currently markets drugs targeting integral membrane proteins. Despite their importance in the treatment of disease, at the molecular level they remain some of the most challenging systems to study in biology; although representing 25% of the proteins expressed in the human genome, they represent only 1% of all protein structures that are deposited within the protein database. Many of the challenges of studying integral membrane proteins stems from them fact that they are embedded in the lipid bilayer, a fluid lipid matrix composed of phospholipids, sterols (in the case of human's cholesterol [93]), sphingolipids [94] and glycolipids [95-96]. The lipids present within the bilayer are chemically and structurally diverse, exhibiting a range of headgroups and acyl chains that can influence the physical properties of the lipid bilayer and a range of phase behaviours. The presence of so many different classes of lipids has been shown to have structural and functional implications on integral membrane proteins [97-100], with lipids modulating the function of integral membrane proteins and vice-versa. Since the 1970's it has been clear that the function of integral membrane proteins has been regulated by the presence of particular classes of lipids and the lengths of the acyl chains that they contain [101], leading to the concept of an annulus of lipids that exchange slowly between the proteins hydrophobic surface and the bulk lipids in the bilayer. More recently, non-annular lipids have also been identified that essentially act as co-factors binding to specific binding sites on integral membrane proteins [102-104]. Furthermore, it is becoming apparent that the proteins may play an important role in recruiting particular classes of lipids, with implications for raft formation, processes that have been linked, amongst other things, to the regulation of signalling pathways [105-106], membrane remodelling associated with viral replication [107] and protein trafficking [108]. These studies emphasize the need for effective tools to understand how lipids and proteins interact with each other, and how the presence of membrane proteins can modulate the dynamics and structure of the lipid bilayers.

The site at which these lipids and proteins are synthesised is called the endoplasmic reticulum (ER); after synthesis they are transported though the Golgi apparatus and packaged into lipid vesicles to their appropriate location within the cell. [109] As the proteins pass from the ER to the Golgi apparatus

they may undergo post-translational modifications such as glycosylation.[110] Fukutin-1 (Fk-1) is one of a family of glycosyltransferases that is found in the cis-Golgi compartment of the Golgi apparatus, facing the ER. These glycosyltransferases are thought to be involved in the O-linked glycosylation of proteins as they pass through the Golgi compartments.[111] In this thesis we investigate how Fukutin-I interacts with the lipids within the ER/Golgi as part of a wider study to understand how L/P (lipid/protein) interactions may regulate protein trafficking. The absence of Fk-1 has been shown to lead to Fukuyama muscular dystrophy, where the hypoglycosylation of components of the extracellular matrix leads to a lack of structural integrity and a weakening of the tissue.[109] The question posed is how these glycosyltransferases are retained in the ER/Golgi.[76, 112] Two hypotheses have been proposed: the first is a retrieval process that, allows the transferases to pass to latter Golgi compartments where peptide motifs are recognised that lead to their translocation back to the cis-Golgi compartment. The second is one of retention, where the short transmembrane domain (TMD) found in these glycosyltransferases interacts favourably with the thinner bilayers found in the cis-Golgi compartment preventing the entry of these proteins into the vesicles that are transferred to latter compartments.[69, 113]

Since its inception solid-state NMR (ssNMR) has played an important role in the study of membrane structure and dynamics, with wideline deuterium NMR and phosphorous NMR widely used to study the dynamics and phase behaviour of lipid systems [114] [115-116]. In order to investigate the effect of Fk-1 on the order of lipid bilayers, we performed a series of ssNMR measurements on phospholipid headgroups and investigated the order of the acyl chains within the lipid as a function of Fk-1 concentrations. Solid-state NMR is a useful tool for studying the dynamics of transmembrane proteins [117] in lipid bilayers since, unlike in solution state NMR, there is no principal restriction on protein to lipid size of the lipoprotein complex that can be studied. Solution state NMR is limited since it relies on the intrinsic tumbling of the molecules to average the anisotropic interactions which can cause major line broadening and in the case of large proteins this tumbling is greatly reduced.[118] Conversely, samples studied using ssNMR are not limited by size as they can be mechanically rotated via MAS. This averages the anisotropy, allowing one to study the behaviour of various lipid/protein mixtures.[119] Static measurements can also provide a wealth of information on the underlying anisotropic interactions and the order within the phospholipid bilayers [120]. The behaviour of the lipid bilayer in the presence of proteins is important as specific lipid interactions can modulate the activity of proteins and peptide-lipid interactions can affect the lipid bilayer and protein structure.[118, 121-123] As mentioned above, eukaryotic cells typically have a high concentration of other lipids, such as cholesterol [93] and sphingomyelin [124]; however, in the ER/Golgi apparatus this is limited as these lipids are transported to the plasma membrane. 1-palmitoyl-2-oleoyl-glycero-3-phosphocholine (POPC) is used as a model eukaryotic lipid as it is abundant in mammalian cells [125]

and contains a choline headgroup, the dynamics of which we explored in Chapter 2 and can be investigated by observing the quaternary ammonium site via ^{14}N measurements.

The spin interaction that dominates the ^{14}N NMR spectra of POPC is the quadrupolar interaction (between the electric field gradient and the quadrupole moment of the nitrogen nucleus). This interaction is anisotropic in nature, and the observed resonance positions will depend on both the dynamics present within the sample and the orientation of the anisotropic interaction with respect to the magnetic field. The ^{14}N in the POPC headgroup has proven to be a particularly useful reporter of headgroup geometry, as the rotation of the lipid about its long axis in the liquid crystalline bilayer, results in a scaling of the quadrupolar interaction which reflect the orientation of the headgroup with respect to the bilayer normal. As reported by Lindstrom[76], this makes it a powerful technique to study how surface charge and protein packing can influence headgroup geometry. We have complemented these investigation of the lipid headgroup with ^{2}H NMR measurements of deuterated POPC allowing us to observe the dynamics in the lipid chain. By modifying the concentrations of Fk-1 in the POPC lipid mixtures, we can observe the influence Fk-1 has on the dynamics in the choline headgroup and the acyl chain; this will reflect the packing of the lipids and enable us to investigate the favourability of the interaction between Fk-1 and the lipids as a function of concentration of POPC.

5.1.1 Materials

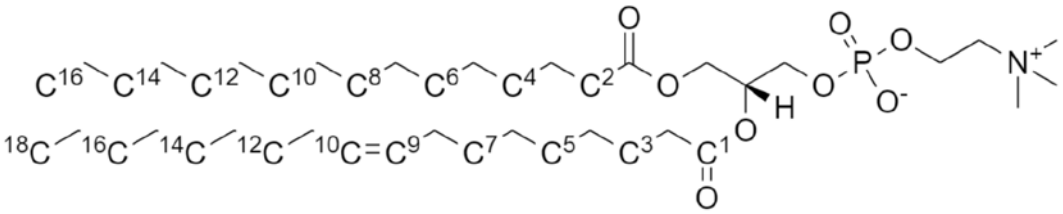

Figure 5.1: Chemical structure of POPC, with acyl chain carbons labelled in superscript

D-31 chain deuterated 1-palmitoyl-2-oleoyl-glycero-3-phosphocholine (POPC) (Figure 5.1) were obtained from *Avanti Lipids*. Multilamellar vesicles were prepared by co-solubilization of 7 mg lipids in methanol (3:1 v/v). The samples were dried under high vacuum before the lipid film was resuspended in 21 µl of deionized water. The samples were then subjected to 8 freeze-thaw cycles.

Fukutin-1 (Fk-1) (MQRINKNVVL ALLTLTSSAF LLFQLYYYKH YLSARN) was introduced to the multilamellar vesicles in concentrations of 1% mol of Fk-1 (100:1, POPC:Fk-1), 0.5% mol of Fk-1 (200:1, POPC:Fk-1) and 0.25% mol of Fk-1 (400:1, POPC:Fk-1).

5.1.2 NMR Pulse Sequences

The NMR methods implemented and processing of the data in this chapter are discussed in detail in Chapter 1.4.2: Direct Acquisition and Section 1.4.4: Quadrupolar Echo.

5.2 Results

5.2.1 ^{14}N NMR Study of POPC and Lipid/Protein Mixtures

To understand how Fk-1 influences the lipid headgroup we conducted a series of MAS NMR measurements on the quadrupolar nucleus, ^{14}N. For ease of reference, for the remainder of this chapter POPC and the POPC:Fk-1 Lipid/Protein (L/P) mixtures 100:1, 200:1 and 400:1 will henceforth be termed POPC, 100:1 L/P, 200:1 L/P, 400:1 L/P, respectively. The representative ^{14}N MAS spectra acquired at temperatures 278 K, 268 K and 258 K for POPC (A), 100:1 L/P (B), 200:1 L/P (C) and 400:1 L/P (D) are shown in Figure 5.2; these spectra show measurements taken above, at and below the nominal phase transition temperature for a pure POPC bilayer. Although the number of sidebands and signal to noise does not permit the accurate determination of the size of the quadrupolar interaction, the ratio of the relative intensity of the 1st order sidebands to the isotropic lines is plotted for the complete range of temperatures studied (Figure 5.3 with corresponding spectra presented in Appendix D.1) for each of the different L/P ratios.

The representative spectra in Figure 5.2 show a trend in the sideband intensity between varying concentrations of L/P mixtures at the same temperature, indicating the change in mobility of the phospholipid headgroup. Both the 100:1 and 200:1 L/P mixtures exhibit increased sideband intensity, with 200:1 (Figure 5.2C), rather surprisingly being larger than that of 100:1 (Figure 5.2B); this suggests an increase in the quadrupolar coupling as the concentration of protein introduced to the system is halved. Interestingly, in contrast to the 100:1 and 200:1 L/P (Figure 5.2B and Figure 5.2C) mixtures, the lineshape for the 400:1 mixture (Figure 5.2D) displayed much lower intensity in the sidebands than the spectra at higher concentrations of protein.

The quadrupolar splitting observed is similar to that observed by Lindstrom *et al.* [76], with a single resonance at the isotropic shift with sidebands spaced at intervals of the spinning speed. Note the presence of additional sidebands in Lindstrom's work reflects the lower spinning speeds employed. The ^{14}N NMR measurements of the POPC headgroup, although similar in chemical structure to the ACh salts studied previously (Chapter 3), exhibited a far smaller quadrupolar coupling compared to the quadrupolar coupling exhibited at the nitrogen site of the family of ACh salts. The broad spectra with complex sideband patterns were not observed for the headgroups, indicating that there are significantly greater motions that average the quadrupolar interaction. As reported previously, by Lindstrom, this scaling reflects the motion of the lipid about its long axis, on a timescale sufficiently rapid to average the quadrupolar interaction (Figure 5.2 and Figure 5.3).

Figure 5.3 shows a plot of sidebands in all four mixtures from the lowest to the highest temperatures studied, their intensities increasing as the temperature was lowered. This indicates an increase in the quadrupolar coupling as a result of a reduction in the mobility of the lipid

headgroup. In contrast to the pure POPC (Figure 5.3, trace in black), the 100:1 and 200:1 mixtures (respectively, red and blue traces) across all temperatures exhibit higher sidebands, indicating a slight increase in the observed quadrupolar coupling. The increased quadrupolar coupling can result from a decrease in the overall headgroup mobility [76], and/or a change in the relative orientation in the lipid headgroup with the head group aligning closer to the bilayer surface.

This restriction in dynamics may in part reflect repulsion between the positively charged quaternary ammonium group and the positively charged residues in the extramembranous domains of the protein. These observations differ from those reported by Lindstrom et al.[76] who studied a positively charged peptide binding in equilibrium at the bilayer surface, which resulted in compensation of the bilayer surface charge and the resulting reorientation of the headgroup dipole. In contrast, in the case of Fk-I, the peptide is embedded in the bilayer, and the positive charges are held close to the bilayer surface, resulting in electrostatic repulsion between the positively charged sidechains of the arginine and lysine residues present and the quaternary ammonium group. We believe the repulsion between the quaternary ammonium groups of the lipids and peptides at these low L/P ratios, serves to reduce dynamics by limiting the conformational space that the lipid headgroup can sample (Figure 5.4).

From the analysis of the sideband intensity (Figure 5.3), it is apparent that the maximal sideband intensity occurs at the L/P ration of 200:1. Although one could explain the increase in sideband intensity through motional restriction, this is hard to rationalise as naively one would expect these effects to be maximal at the lowest L/P ratios. It is conceivable that the change in quadrupolar interaction/sideband intensity is rationalised through a change in the tilt of the lipid headgroup in response to the change in surface charge. Again, though this is difficult to rationalise, as the reduction in peptide concentration would result in a reduction of positive charge near the surface of the bilayer. This would result in a more neutral bilayer surface that is typically associated with a tilt in the headgroup approaching the magic angle and a reduction in the sideband intensity/quadrupolar interaction. This would suggest that the 50% increase in sideband intensity may reflect other interactions that would move the headgroup away from the magic angle and/or reduce headgroup mobility. However, from our data we cannot unambiguously assign these, and this remains the subject of further investigation.

Contrary to the data corresponding to the 100:1 and 200:1 L/P mixtures discussed above (Figure 5.3, red and blue traces), the lineshape for the 400:1 mixture (Figure 5.3, magenta trace) displayed much less intensity in the sidebands than the spectra at higher concentrations of protein or even the pure POPC. We see that above the phase transition (>271 K) the intensity of the sideband for 400:1 L/P is lower, indicative of a greater degree of motional averaging in the presence of Fk-1. This suggests that at 400:1 L/P, the peptide increases the volume at the top of the lipid headgroup

resulting in greater mobility in the lipids. There is little evidence that the POPC is interacting with the protein which would lead to an increase in quadrupolar interaction (though if this was only a small fraction of the lipids, we may not be able to discern it from the more mobile bulk lipids).

Plots of the sideband intensity as a function of temperature (Figure 5.3) reveal that the largest step change in the POPC spectrum occurs between 283 K and 278K, slightly higher than the reported phase transition reported for POPC (270 K). Surprisingly similar changes are seen in the 100:1 L/P sample. In contrast, the 200:1 and 400:1 L/P samples exhibited a more gradual increase in the sideband intensity, and therefore reduction in headgroup dynamics. If the increases in quadrupolar interaction do indeed reflect changes in mobility and changes from the liquid crystalline to gel phase, this suggests that at these concentrations the presence of the Fukutin-I in the bilayer makes the phase transition less cooperative in the headgroup region. We note though that in each case as the temperature is lowered there is a significant reduction in the headgroup mobility. Interestingly, these changes occur at a higher temperature than the spectral changes observed in our ^{2}H data (Section 5.2.2), which indicate a T_m of 270 K, suggesting that the reduction in mobility observed upon lowering the temperature influences the headgroups prior to the lipid chains.

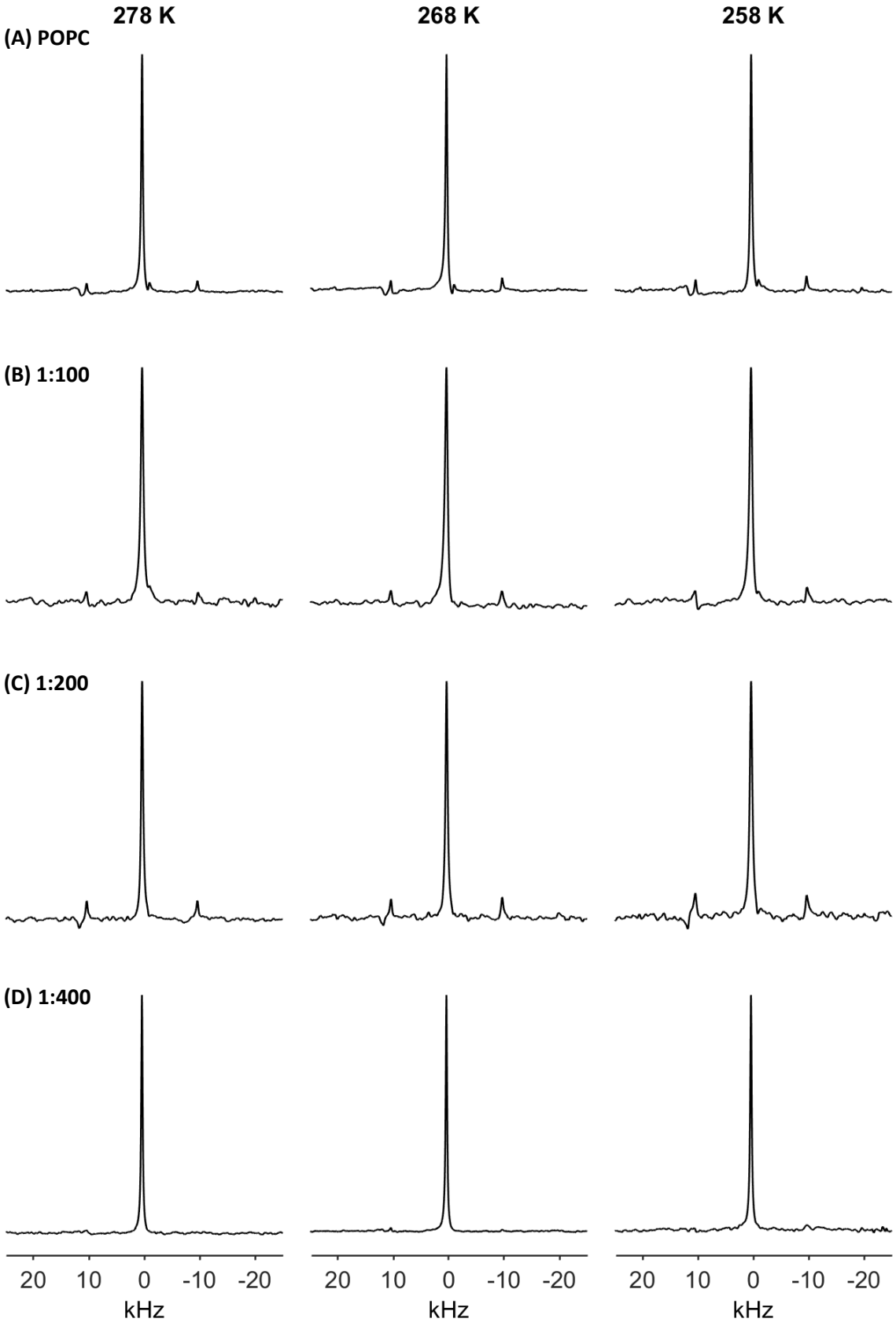

Figure 5.2: Figure showing ^{14}N MAS spectra of POPC (A) and lipid-peptide mixtures 1:100 (B), 1:200 (C) and 1:400 (D) at 278 K, 268 K and 258 K. Spectra obtained at 10 kHz MAS using a Direct Acquisition pulse program.

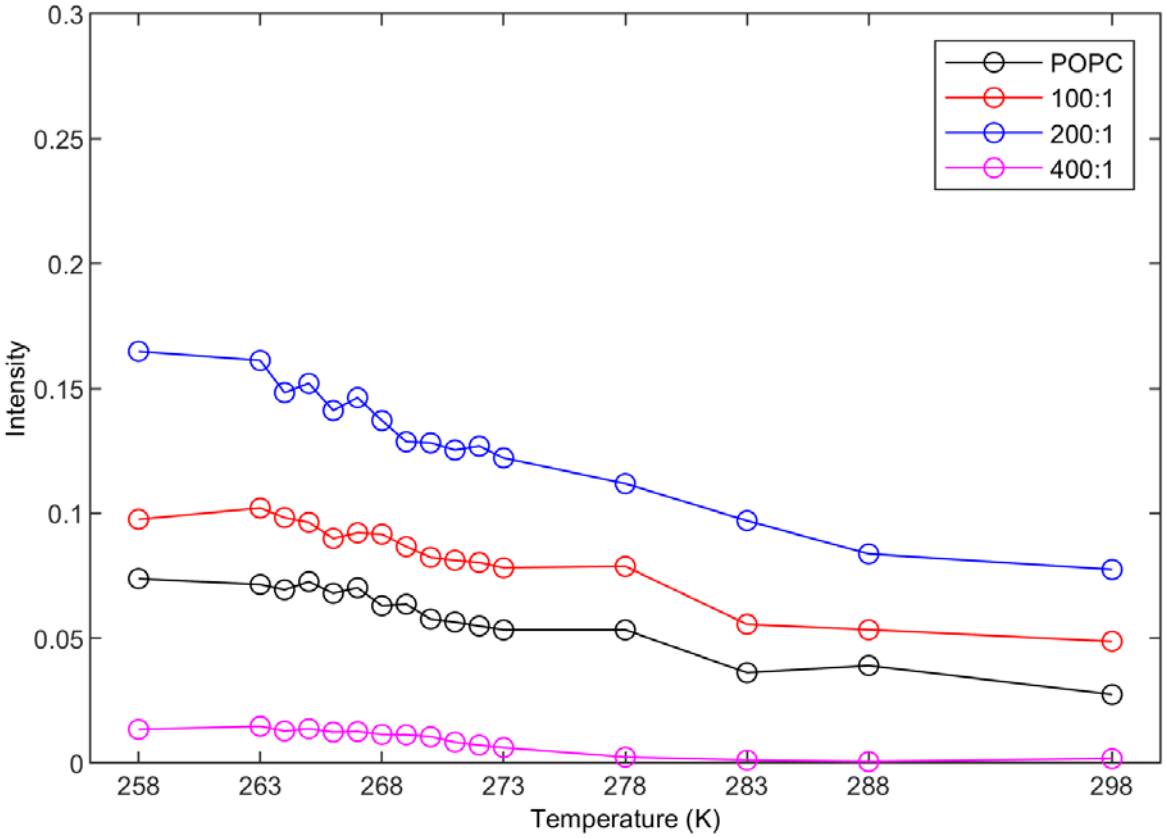

Figure 5.3: A plot showing the sideband intensities (sum of both sidebands) for POPC (black) and the L/P mixtures 100:1 (red), 200:1 (blue) and 400:1 (magenta).

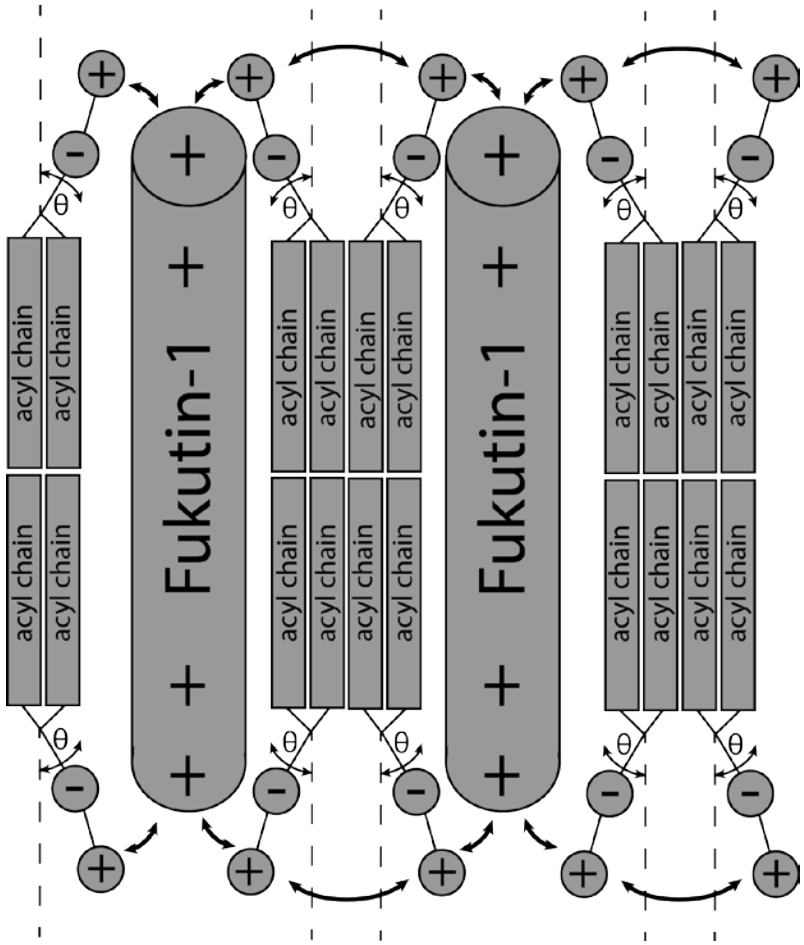

Figure 5.4: Schematic model of an instance when the positive charge of the protein repels the positively charged choline headgroup. This results in reduced dynamics about θ, the axis of motional averaging, due to a limited conformational space.

5.2.2 ^{2}H NMR Study of POPC, POPC:Fk-1 (100:1, 200:1 and 400:1)

The ^{14}N spectra recorded above provide valuable insights into the dynamics in the headgroup region. To assess how these changes are mirrored in the lipid chains, complementary ^{2}H solid-state NMR spectra were recorded of POPC at the same lipid to protein ratios.

5.2.3 Influence of Fk-1 on the Order within POPC Bilayers

To assess the influence of the Fk-1 on chain dynamics, static ^{2}H spectra were recorded for POPC, 100:1, 200: 1 and 400:1 L/P mixtures (1%, 0.5% and 0.25% mol Fk-1) across a range of temperatures, 298 to 258 K with special focus on the phase transition temperature and below. These are shown in Appendix D.2: Figure 6.9, Figure 6.10, Figure 6.11 and Figure 6.12. Representative ^{2}H static spectra acquired at temperatures 278 K, 268 K and 258 K for POPC (A), 100:1 (B), 200:1 (C) and 400:1 (D) L/P mixtures are shown in Figure 5.5, with other data in Appendix D.2.

At a higher temperature, 278 K, POPC, 100:1, 200:1 and 400:1 L/P mixtures (respectively Figure 5.5A Figure 5.5B, Figure 5.5C and Figure 5.5D) show that the spectra are composed of a family of Pake patterns arising from the individual CD_2 groups in the acyl chains, with the individual splitting resolved due to the increasing order in the chains as one moves from the methyl groups to the CD_2's next to the glycerol backbone. These spectra are typical of lipid in a liquid crystalline lipid bilayer.[123, 126-127] Comparison of the representative spectra at 278 K (Figure 5.5A, B, C and D at 278 K) reveals that the presence of Fk-1 within the POPC bilayer does not influence the dynamics within the bilayer, with the resolved quadrupolar splitting from the POPC showing no significant changes. We do, however, observe some small variation in the intensity of the resonances pertaining to the terminal CD_3 group.

As the temperature is lowered (268 K, Figure 5.5) there is a noticeable loss in the resolution of the individual Pake patterns arising from the CD_2 groups as a result of the increase in linewidth as the motions in the bilayer are slowly supressed as the gel phase is achieved (>271 K). As the temperature falls from 268 K to 258 K, a significant change in the ^{2}H lineshape with intensity spread across ~100 kHz and broadening of the spectra is observed (Figure 5.5). This arises as the chains become progressively more ordered. At the lowest temperature, 258 K, the intensity in the spectrum pertaining to the highest protein concentration 100:1 L/P (Figure 5.5B) shows a significant lack of intensity in the wings compared to that of the pure POPC spectrum (Figure 5.5A). As the concentration of Fk-1 is decreased, however, some of this intensity re-emerges (200:1 L/P, Figure 5.5C) and finally in Figure 5.5D, for 400:1 L/P, we observe wings that are comparable to that seen in the pure POPC spectrum (Figure 5.5A). This indicates that at low concentration, the amount of peptide present in the mixture is insufficient to disrupt the behaviour in the bulk lipid resulting in an ordering in the acyl chains.

The presence of peptides in the bilayer can also influence selectively the mobility of the lipids at differing points through the bilayer; for instance, it can increase lateral pressure to reduce lipid chain mobility, whilst increasing the spacing between lipid headgroup thereby enhancing mobility.

The deuterium spectra measured over a range of temperatures with specific focus on the phase transition temperatures (Appendix D.2), allow for us to probe the dynamics of the acyl chain by observing the individual splittings. The packing at the phospholipid headgroup can influence the packing at the chain and, therefore, the extent of chain dynamics taking place.

As the concentration of Fk-1 in the POPC bilayer is increased, the first major variation observed in each case is a change around the phase transition temperature, ~271 K (Appendix D.2), where although the profiles observed are similar to those for the pure lipid, the temperature and the range over which they transition from the liquid crystalline to the gel phase differs. This will be discussed in more detail in Section 5.2.4: Influence of Fk-1 on the Phase Behaviour of POPC Bilayers.

As the temperature is further reduced, differences are seen in the gel phase spectra (269 K, 268 K and 267 K); these are more pronounced in the L/P mixtures with a greater concentration of Fk-1 (100:1 and 200:1, respectively Appendix D.2 Figure 6.10 and Figure 6.11) and appear titratable, with little difference observed between pure POPC and 400:1 L/P mixture (Appendix D.2: Figure 6.12). These variations may reflect the influence Fk-1 has on the packing of the lipid chains in the gel phase. Typically, the packing of the chains in the gel phase is highly organised, and the presence of the Fk-1 may well result in significant deformations that would allow for the dynamics that give rise to the change in lineshape.

At higher temperatures (> 272 K), all samples exhibit a similar trend in the order in the acyl chain, with little variation between the lineshapes. Once we reach 272 K, we observe an increase in the order from positions C^{18} to C^{13}; this is further evidenced as we lower the temperature below the T_m, 271 K, where we observe a loss of signal in the individual resonances attributed to the sites along the acyl chain. This is indicative in a change of lineshape resulting from the reduction of mobility as the bilayer starts to pass through the phase transition. Interestingly, the lineshape for the L/P mixture with lowest concentration of POPC:Fk-1 (400:1) (Appendix D.2: Figure 6.12), showed the presence of residual resonances of the acyl chain at 267 K and 266 K, indicating a slower transition into the gel phase relative to the other L/P mixtures. Below the phase transition temperature, the 400:1 L/P mixture showed the closest resemblance to the pure POPC spectra (Figure 5.5 and Figure 6.12) indicating that the presence of Fk-1 disrupts the order in the lipid chains as they enter the gel phase.

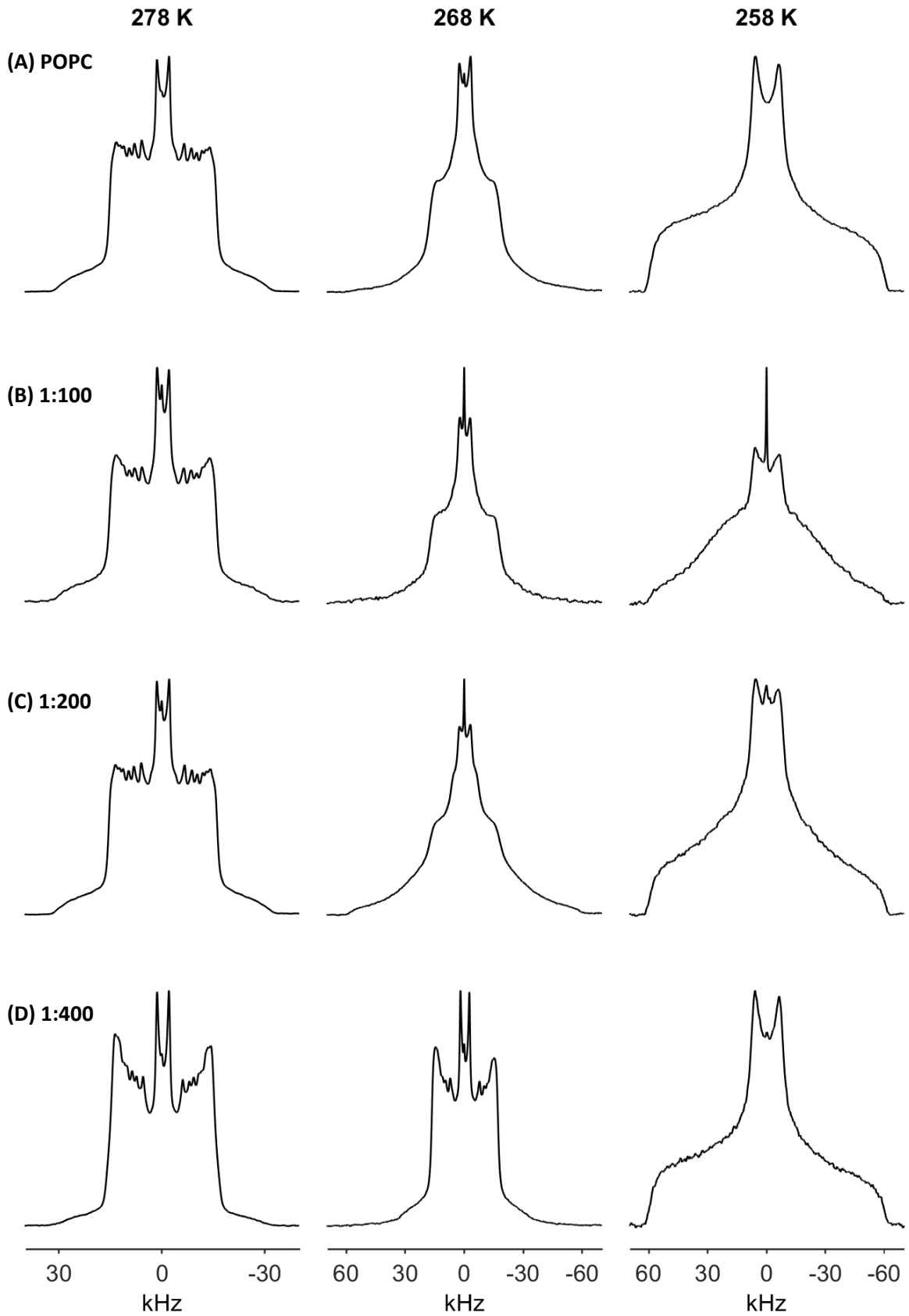

Figure 5.5: Figure showing ^{2}H static spectra of POPC (A) and lipid-peptide mixtures 1:100 (B), 1:200 (C) and 1:400 (D) at 278 K, 268 K and 258 K.

5.2.4 Influence of Fk-1 on the Phase Behaviour of POPC Bilayers

The analysis of the lineshapes in Sections 5.2.2 and 5.2.3 show that above the phase transition temperature (<271 K), the POPC bilayers exist in the fluid liquid crystalline bilayer phase [123, 127]. At lower temperatures the POPC enters a gel like phase, which results in a broadening of the spectrum, where the only significant motion present is in the terminal CD_3 group.

To quantitatively analyse how Fk-1 influences the phase transition temperature, we have conducted a second moment analysis. Figure 5.6 shows a plot displaying the deuterium second moments which we use to interpret the motions as a function of temperature; increases in the second moment corresponds to an increase in the width of the deuterium envelope which correlates with a reduction in the mobility of the acyl chains.[128] We can see that at higher temperatures, all samples exhibit a similar trend in second moments, with the exception of the 100:1 L/P mixture sample (Figure 5.6, red trace), which is consistently higher, indicative of a greater degree of order in the bilayer. As the temperature drops below 271 K all samples start to show an increase in the second moment, typical of the lipids passing through their phase transition. The POPC, 100:1 and 200:1 (Figure 5.6, respectively the red trace and blue trace) samples exhibit a similar phase transition temperature, of 267 K, with the 400:1 sample (Figure 5.6, magenta trace) having a lower phase transition at 265 K. Below the phase transition the second moments continue to increase slowly, but interestingly this increase appears to be slower with increasing concentrations of Fk-1 suggesting that the presence of the peptide, disrupts the order present in the POPC acyl chains as they enter the gel phase.

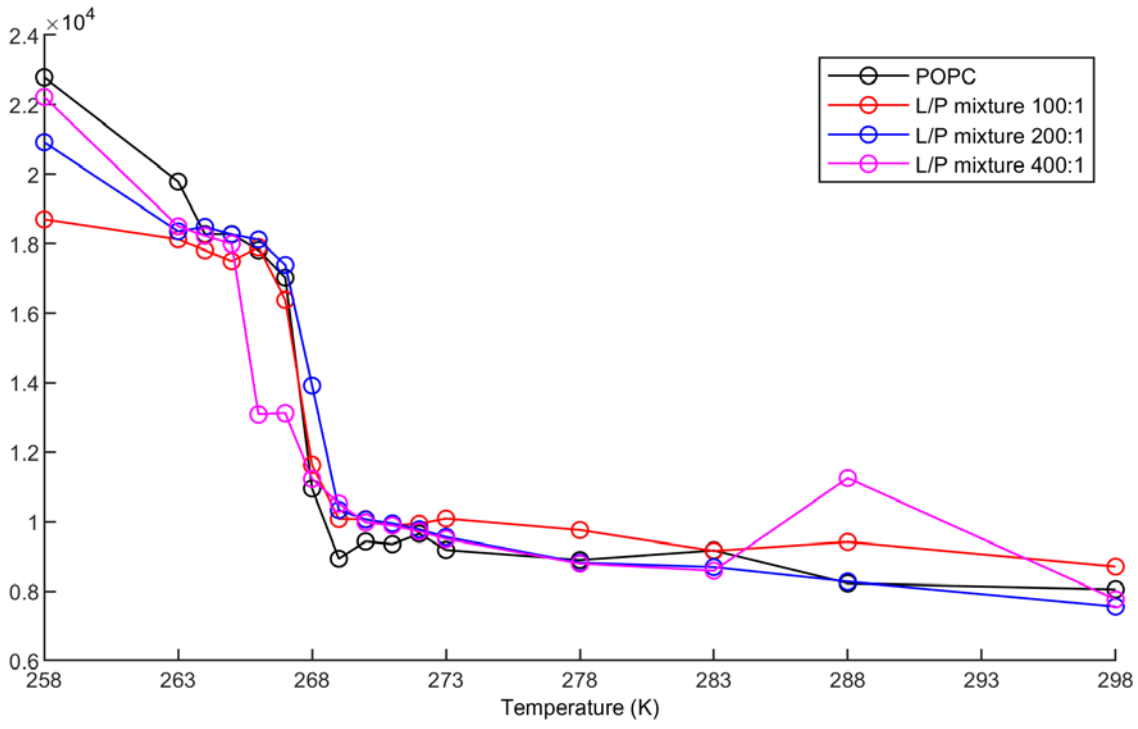

Figure 5.6: A plot of deuterium second moments as a function of temperature for POPC (black), L/P (POPC: Fk-1) mixture 100:1 (red), L/P mixture 200:1 (blue) and L/P mixture 400:1 (magenta)

5.3 Discussion

The interaction of the transmembrane protein Fukutin-1 (Fk-1) with the surrounding lipid bilayer is thought to play a key role in determining its localisation in the ER/Golgi. In this work we have investigated how it interacts with a simplified model lipid bilayer composed of POPC, one of the most abundant phospholipids in the cell membrane. Studying the quadrupolar lineshapes corresponding to the choline headgroup and the acyl chain in the phospholipid as a function of temperature and concentration of Fk-1 has provided valuable insight into the dynamics and packing in the lipid bilayer.

The ^{14}N MAS spectra measured for the phospholipid and L/P mixtures displayed lineshapes significantly different to those seen in the ^{14}N MAS measurements of the ACh salts (Chapter 3) despite sharing similar structures. The presence of a single resonance with sidebands spaced at the spinning frequency indicates the presence of significant motions which scale the observed quadrupolar coupling at the quaternary ammonium site. The scaling of the quadrupolar interactions suggests that the presence of the peptide can influence the orientation and packing of the quaternary ammonium group present in the choline headgroup.

The ^{14}N data showed that at higher concentrations of the peptide, 100:1 and 200:1 (Figure 5.3, red and blue traces and Figure 5.2B and Figure 5.2C), the sidebands in the spectra reflected a quadrupolar interaction larger than that seen in the pure POPC sample (Figure 5.2A and Figure 5.3, black trace). This is indicative of an increase in the quadrupolar coupling which reflects a decrease in the mobility of the choline headgroup and/or a tilt of the headgroup away from the magic angle. The spectra for the L/P mixture with the lowest concentration of peptide, 400:1 (Figure 5.2D and Figure 5.3, magenta trace) showed much less intensity in the sidebands indicating an increase in the motions influencing the lineshape and so a reduction in the quadrupolar coupling. We postulate that this is due to instability in the packing of the lipids providing a greater volume in which the choline headgroup can move leading to a greater motional averaging of the quadrupolar interaction.

To complement the ^{14}N data, static ^{2}H NMR measurements were conducted (Section 5.2.2) offering a wealth of information on the dynamics of the acyl chains and the packing of the phospholipids. At high temperatures we observed a series of resonances attributed to the CD_2 groups in the acyl chains for all for samples indicating that the presence of the peptide at high temperatures does not influence the dynamics in the lipid bilayer. As the temperature is lowered, we observe a loss in the resolution of these individual Pake patterns indicating a suppression of motions in the bilayer. As the lipids reach the T_m, we see distinct differences in the lineshapes between the POPC and each of the L/P mixtures (100:1, 200:1 and 400:1) (Figure 5.5 and Appendix D.2) indicating varying dynamics

in the bilayer as they transition from the liquid crystalline phase to the gel phase. The second moment analysis (Section 5.2.4) was conducted for a more quantitative analysis which indicated that the POPC, 100:1 and 200:1 (Figure 5.6, black, red and blue trace) samples share similar phase transition temperatures, while the 400:1 L/P mixture (Figure 5.6, magenta trace) has a lower phase transition. The moment analysis and the ^{14}N data, which showed greater mobility in the choline headgroup, indicate that at low concentrations of Fk-1 (400:1), the protein-lipid interaction is sufficient to disrupt the order in the lipid bilayer, allowing for a reduction in the quadrupolar coupling and an increase in the dynamics giving rise to the ^{2}H lineshape which resembles the POPC lineshape.

In this chapter we have shown that measuring both MAS and static NMR spectra of quadrupolar nuclei in relatively large biomolecules provides valuable insight on the dynamics and packing in the system. We can see that the influence of Fk-1 on the phospholipid bilayer can be investigated by observing the spectra as a function of concentration of the protein and temperature.

Chapter 6 Conclusion

Throughout this project we have explored the potential of solid-state NMR (ssNMR) as a tool for the investigation into the dynamics of important biomolecules, specifically utilising naturally occurring isotopes to probe the underlying anisotropic interactions and thus the motions which give rise to the lineshapes.

A family of acetylcholine (ACh) salts were chosen as model systems to investigate the potential of using ^{14}N NMR spectroscopy as a tool to probe the internal dynamics of the quaternary ammonium group. Previous ^{2}H work[1] has indicated that there are two axes of motional averaging present: (1) The rotation of the entire quaternary ammonium group about the $H_2C\text{-}N(CH_3)_3$ bond labelled the C_3' and (2) the rotational of the individual methyl groups (the C_3 axis)

We begin by exploring the physical properties of the ACh salts by generating 4 crystal structures using XRD for ACh perchlorate, chloride, bromide and iodide (Section 2.3.1). The XRD analysis also provided valuable information on the conformation of the backbone structure of the ACh salts. The torsion angles obtained (Section 2.3.1.2) presented two different conformations of the backbone structure, with ACh perchlorate and chloride taking one and the ACh bromide and iodide taking the other. We learnt that though the salts share similar chemical structures, the physical structures were vastly different; this suggests that the type of counterion present in the salt significantly alters the geometry. ACh iodide, interestingly, also has the largest unit cell with 2 molecules in the asymmetric unit cell.

Using this newly obtained crystal data, a series of *ab initio* quantum mechanical *CASTEP* calculations were performed to acquire the spin interactions present in the ACh salts. These calculations provided the necessary NMR parameters (CSA, quadrupolar couplings, asymmetry parameters etc.) required to carry out ^{13}C and ^{14}N lineshape simulations to aid in the interpretation of subsequent experimental data. Since these are the static values, one can make quantitative and qualitative comparisons to the experimental data to determine whether any motions are present. The numerical calculations of the spin interactions revealed the presence of 3 magnetically inequivalent N-methyl sites and that the quadrupolar interactions at the nitrogen site of each ACh salt are relatively small (as expected).

By exploiting the abundant ^{14}N nuclei, we observed the dynamics at the nitrogen site for ACh perchlorate, chloride, bromide and iodide as a function of temperature (Section 3.3.2); we saw significant variation in the lineshapes, suggesting that the presence of different counterions influences the dynamics of the quaternary ammonium group. Sideband patterns typical of non-axially symmetric tensors were observed at higher temperatures for all salts. The Herzfeld Berger

analysis showed good agreement to the quadrupolar parameters obtained for ACh perchlorate and iodide, but showed significantly reduced quadrupolar coupling constants for ACh chloride and bromide, indicating the presence of motions. This suggests a suppression of the motions on the timescale that would average the quadrupolar interaction, resulting in a slight scaling of the C_Q.

The T_1 relaxation measurements on the ^{14}N spin (Section 3.3.2.5) revealed uncharacteristically long T_1 values for the quadrupolar nuclei, ranging from ~7 seconds to ~35 seconds for ACh chloride, bromide and iodide as the temperature was lowered and even the perchlorate salt increasing by a factor of ~20 (~0.1 seconds to ~2 seconds). The long T_1 values observed, compared to the 100 ms typically reported for ^{14}N sites that exhibit MHz size coupling suggesting a more complicated relaxation behaviour is present in quaternary ammonium salts that exhibit smaller quadrupolar couplings. Furthermore, the large changes seen over the temperature range studied suggests significant change in the nanosecond motions are occurring in the sample. Since the quadrupolar tensors show a degree of collinearity with the axis of motional averaging, and the C_Q does not significantly change as the temperature is lowered, we postulate that the quadrupolar relaxation mechanism is not the only anisotropic interaction driving the relaxation process. As the CSA is small compared to the quadrupolar and dipolar interactions, the relaxation is most likely driven by contributions from both the quadrupolar and dipolar interactions (from the N-methyl protons) which are both in the order of kHz. Since the averaged components of the EFG tensor are unequal in size for all salts, the rotational motion may cause the fluctuating field which contributes to the spin-lattice relaxation. We have seen in previous ^{2}H static NMR measurements[1] which probe the methyl protons that as the sample is cooled, the rotation of the N-methyl groups also become more hindered. The temperatures at which the T_1 begin to increase (for instance, significant increase for ACh bromide at 233 K to 218 K) also coincide with the temperatures at which the intermediate motions (of the methyl and/or quaternary ammonium group) giving rising to the deuterium lineshape are supressed (Figure 3.2).

From these experiments, we learned that the presence of different counterions in the sample influences the motions of the quaternary ammonium group and the rotation of methyl groups; we hypothesized that quadrupolar and dipolar interactions can act as an efficient source of relaxation in these crystalline solids. We also postulated that the N-methyl groups undergo rapid chemical exchange.

In order to further investigate the complex motions exhibited by the quaternary ammonium group in the ACh salts and the chemical exchange model postulated, we undertook a series of magic angle spinning Cross-polarization (CP-MAS) measurements to observe the N-methyl groups (Section 4.2.1). Interestingly, the CP-MAS measurements on the 4 salts produced unique and complex ^{13}C lineshapes, specifically between 50 ppm and 60 ppm which we attributed to the N-methyl sites.

This is contrary to the static *CASTEP* calculations undertook as the individual methyl resonances obtained from the simulations were not observed. We saw significant changes in the lineshape as the temperature was lowered for all salts except ACh perchlorate, a trait mirrored in the ACh perchlorate ^{14}N lineshape (Figure 3.4), where the central broad intensity did not appear to vary as the sample was cooled. The sites pertaining to the ^{13}C backbone of the ACh molecule showed similarities in all 4 salts, indicating that the different counterions present in the sample influenced the dynamics of the N-methyl carbons. We also saw that the lineshapes at lower temperatures for ACh chloride, bromide and iodide (Figure 4.4, Figure 4.5 and Figure 4.6) revealed the presence of 2 or more resonances at the N-methyl site, indicating the presence of magnetically inequivalent methyl groups which at higher temperatures is observed as an exchange broadened average of the different conformations due to rotation.

To further explore these dynamics that influence the lineshape, we performed a series of CP-MAS lineshape simulations using *SPINACH* under the assumption that the 3 methyl carbons are undergoing chemical exchange. This was performed using the NMR parameters obtained via *CASTEP* obtained in Section 2.3.2. The chemical exchange simulations (Section 4.4) were visually compared to the experimental lineshapes and showed good fits when the rate of exchange was lowered as the temperature was decreased, showing a suppression of motions. The ACh perchlorate lineshape which appeared to show little variation was best matched with exchange rates several orders of magnitude greater than the other three salts. We did, however, observe an increase in linewidth at the two lowest temperatures where the exchange rate had to be lowered to achieve the best match. In contrast to the large exchange rate which best matched the lineshape for ACh perchlorate (~400,000 s^{-1}), the chloride, bromide and iodide salts showed rates <7000 s^{-1}. As the exchange rates were lowered, we observed the appearance of additional resonances which we attributed to the different N-methyl carbons, suggestive of motions which were initially in the intermediate motional regime being supressed and entering a slow or slow-to-intermediate motional regime.

From the exchange simulations, we know that the chemical exchange rates are in the milli- to microsecond timescale. Since motions on this timescale are known to influence relaxation in the rotating frame ($T_{1\rho}$), we measured the build-up of ^{13}C magnetization as a function of contact time for the 4 salts, to explore the influence of temperature and counterion on the individual sites (Section 4.5). Aside from the N-methyl site, the build-up and decay of magnetization for the sites corresponding to the backbone carbons of the perchlorate salt showed little variation over the temperature range explored (313 K to 218 K). At lower temperatures, however, the decay in magnetization suggests change in motions on the millisecond timescale. In contrast to the perchlorate salt (Figure 4.12), we saw that ACh chloride, bromide and iodide (Figure 4.13, Figure 4.14 and Figure 4.15) show changes in the build-up and decay of magnetization throughout the

temperature range studied, which suggests changes in the motions occurring in the micro- and millisecond timescale. The CH_2 sites for these three salts also show changes in the rate of decay in magnetization as the temperature is lowered, indicating that the motion of the N-methyls influences the relaxation of the protons in the system. An interesting trend to note is the decay in magnetization of the iodide salt (Figure 4.15), where the $T_{1\rho}$ values increased as the temperature was lowered indicating a high density of motions on the millisecond timescale, contrasting that seen for the bromide salt (Figure 4.14). This contrasting behaviour was also observed in the ^{14}N lineshape where the linewidth for ACh bromide (Figure 3.6) increased as the sample was cooled, resulting in reduced spectral intensity, whereas ACh iodide (Figure 3.7) showed improved spectral resolution as the sample was cooled.

Investigation into the dynamics of the N-methyl carbons allowed us to obtain information that aided the interpretation of the atypical ^{14}N T_1 data and the relaxation model described in Section 3.3.4. In the case of the iodide and perchlorate salts the ^{14}N quadrupolar couplings observed were largely invariant as the temperature was lowered and mirrored the static values obtained from the *CASTEP* simulations. Despite this, the ^{14}N T_1 values increased for both the iodide and perchlorate, suggesting that the shorter relaxation times observed at higher temperatures are a reflection of motion within the quaternary ammonium group. This is reflected in the carbon-13 lineshape and $T_{1\rho}$ analysis which both indicate a slowing of motions as the temperature is lowered to 218 K. Although these properties are sensitive to motions on the micro-/millisecond timescale this suggests that an overall reduction in quaternary ammonium group dynamics is sufficient to increase the ^{14}N T_1. The bromide and chloride salts also exhibit a large increase in the ^{14}N T_1 upon cooling, suggesting motions in the quaternary ammonium group influence the rates of T_1 relaxation. In this instance, however, we see an increase in the size of the quadrupolar interaction in addition to the reduction in quaternary ammonium group mobility observed from changes in $T_{1\rho}$ and ^{13}C lineshapes. as the temperature is lowered. In these cases, this suggests that fluctuation in field arising from both fluctuations of the quadrupolar interaction and dipolar interaction may contribute to the ^{14}N T_1 relaxation. This contrasts to ^{14}N sites exhibiting large (MHz) quadrupolar interactions where the quadrupolar interaction is the dominant source of relaxation.

To extend these studies from small molecules to larger biomolecular systems, we have utilized ^{14}N MAS-NMR spectroscopy, in conjunction with ^{2}H NMR to study the quaternary ammonium group present in the head group of phosphatidylcholine. Mirroring the lineshape analysis that we performed for the acetylcholine salts we used changes in the ^{14}N spectra to investigate how POPC interacts with the transmembrane domain of the glycosyltransferase Fk-1 (Chapter 5). POPC was selected as a model sample as it is abundant in eukaryotic cells and has a choline headgroup, which contains a quaternary ammonium group, the dynamics of which we studied using ^{14}N in Chapter 2. We saw that the motions of the quaternary ammonium group gave rise to complex sideband

patterns resembling non-axially symmetric tensors as a result of motions in the intermediate motional regime. In contrast to the lineshapes observed for the acetylcholine salts, the quaternary ammonium group in the choline headgroup of the phospholipid, though similar in structure to the salts, exhibited a much lower quadrupolar coupling constant, revealing a sharp central feature with sidebands spaced at ±1 times the MAS frequency, 10 kHz (Section 5.2.1). This suggests that the dynamics in the choline headgroup in the lipid bilayer is significantly different to the dynamics observed in the ACh salts indicating a difference in the motions that influence the quadrupolar interaction which give rise to the lineshape observed.

Measurement of the ^{14}N spectra of the phospholipid without the presence of Fk-1 (Figure 5.3, trace in black) showed a gradual increase in the intensity of the sidebands as the temperature is lowered, suggesting an increase in the quadrupolar coupling constant as a result of suppression of the motions averaging the quadrupolar interaction. Between 270 K and 266 K (Figure 5.3), where the phase transition from the liquid-crystalline phase to the gel phase occurs, little variation is observed in the intensity in the sidebands, indicating little change in the mobility of the phospholipid headgroup. As we introduce the protein to the phospholipid system, we see considerable changes to the sidebands in the spectra which reflects the quadrupolar couplings and, thus, the mobility of the choline headgroup. At high concentrations of Fk-1, 100:1 and 200:1 (1% and 0.5% mol of Fk-1) (Figure 5.3, traces in red and blue respectively), the spectra show a significant increase in the intensity in the sidebands in comparison to the pure POPC lineshape, suggesting an increase in the C_Q and thus a suppression of the headgroup mobility. The 400:1 lipid/protein (L/P) mixture (Figure 5.3, trace in magenta), in contrast, showed a considerable decrease in the C_Q in comparison to the pure POPC. The data acquired for the 400:1 L/P mixture does not fit the expected trend where one would expect an increase in the C_Q as the concentration of protein introduced to the system is lowered. Given the unexpected results, this L/P mixture should be repeated and if proven correct, form the basis of a more extended range of L/P mixtures around this concentration to investigate the effect of introducing low concentrations of protein to the lipid mixtures. If the acquired data does indeed prove to be correct, one plausible explanation is that where low concentrations of protein is present in the sample, the packing in the lipid bilayer is disrupted increasing the volume in which the choline headgroup is situated. Another explanation is that the axis of rotation is closer to the magic angle. This is, however, less plausible since the positively charged sidechains of the arginine and lysine residues present give rise to electrostatic repulsion between the protein and the positive charge of the quaternary ammonium group of the peptide. This results in the choline headgroup being pushed away from magic angle (demonstrated in Figure 5.4), resulting in an observable increase in the C_Q. If, however, the choline headgroup started off at an angle much greater than the magic angle, the repulsion between the headgroup and the protein would result in an axis of rotation closer to the magic angle, leading to a reduction of the C_Q. Since the

headgroups in lipids tend to possess a tilt angle around ~54°, this is unlikely. The low C_Q observed for the 400:1 L/P mixture in comparison with the pure POPC suggests that the bulk lipids have greater motional freedom when a low concentration of protein is introduced to the system; this allows for an increase in mobility resulting in the decreased quadrupolar couplings observed. In the case of higher concentrations of the peptide in the sample, the peptide is embedded in the bilayer, and the positive charges are held close to the bilayer surface. This leads to electrostatic repulsion between the aforementioned positively charged sidechains residues present and the positively charged quaternary ammonium group. As a result, there is limited conformation space in which the choline headgroup can freely move leading to limited dynamics and an increase in C_Q.

The ^{2}H static NMR spectra (Section 5.2.2 and Appendix D.2) obtained with a solid echo allowed us to observe the order in the acyl chains, which is related to the packing proficiency of the phospholipids. A second moment analysis (Section 5.2.4) allowed us to quantitatively examine the phase behaviour of the phospholipid bilayers as a function of temperature and concentration of Fk-1. We see from Figure 5.6 that above the T_m (phase transition temperature), with the exception of the 100:1 L/P mixture (Figure 5.6, trace in red), the samples share similar second moments; the higher moments exhibited by the 100:1 L/P mixture suggests a greater degree of order in the acyl chains. As we go pass through the T_m, the L/P mixture with the lowest concentration of Fk-1 (400:1, Figure 5.6 trace in magenta) shows a slower increase in moment; <263 K, however, the second moment for 400:1 is closer to that of the pure POPC sample suggesting that in the gel phase they share similar dynamics. In contrast to this, as the concentration of protein is increased, we see an increased disruption in the order of the lipids. This is reflected in the lineshape analysis (Section 5.2.3, Appendix D.2 Figure 6.9, Figure 6.10, Figure 6.11 and Figure 6.12) where below the T_m, the individual splittings attributed to the CD_2 sites along the acyl chain for the 100:1 and 200:1 L/P mixtures experience a loss in signal at higher temperatures than the 400:1 L/P mixture; this suggests a slower transition into the gel phase at low concentration of Fk-1. As evidenced by the moment analysis, at 258 K the 400:1 L/P mixture shares a close resemblance to the ^{2}H POPC spectra (Figure 5.5A and D, and Figure 5.6 black and magenta traces); this suggests that at high concentrations of protein, the presence of Fk-1 disrupts the order in the acyl chains as they enter the gel phase.

To summarise, we have shown in this project that ssNMR has proven an extremely useful tool in the investigation of the dynamics and motions, especially in the exploitation of the natural abundance ^{14}N nucleus. We have postulated a motional model and a relaxation mechanism for the quadrupolar nuclei in the quaternary ammonium groups in the ACh salts, by conducting MAS ^{14}N measurements, with the use of CP-MAS and simulations to complement the findings. Furthermore, we have shown the potential of observing the ^{14}N spin in conjunction with the ^{2}H, from which we

gleaned useful insight into the dynamics of the choline headgroup and the order in the bilayer respectively, of the phospholipid POPC.

Appendix A XRD Data

A.1 ACh Perchlorate

Crystal Data and Experimental

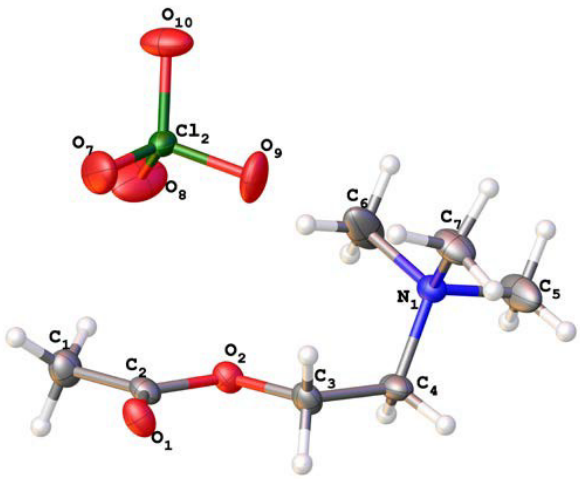

Experimental. Single colourless block-shaped crystals of Acetylcholine Perchlorate were recrystallized from methanol by slow evaporation. A suitable crystal 0.10×0.10×0.02 mm3 was selected and mounted on a MITIGEN holder on an ROS diffractometer. The crystal was kept at a steady T = 100(2) K during data collection. The structure was solved with the ShelXS structure solution program using the Direct Methods solution method and by using Olex2 as the graphical interface. The model was refined with version 2018/3 of ShelXL using Least Squares minimisation.

Crystal Data. $C_7H_{16}ClNO_6$, M_r = 245.66, orthorhombic, *Pbca* (No. 61), a = 11.9879(6) Å, b = 9.6418(4) Å, c = 19.3129(14) Å, $\alpha = \beta = \gamma = 90°$, V = 2232.3(2) Å^3, T = 100(2) K, Z = 8, Z' = 1, μ(MoK$_\alpha$) = 0.352, 13735 reflections measured, 2558 unique (R_{int} = 0.0404) which were used in all calculations. The final wR_2 was 0.1431 (all data) and R_1 was 0.0566 (I > 2(I)).

Compound	**Acetylcholine Perchlorate**
Formula	$C_7H_{16}ClNO_6$
$D_{calc.}$ / g cm^{-3}	1.462
μ/mm^{-1}	0.352
Formula Weight	245.66
Colour	colourless
Shape	block
Size/mm^3	0.10×0.10×0.02
T/K	100(2)
Crystal System	orthorhombic
Space Group	*Pbca*
a/Å	11.9879(6)
b/Å	9.6418(4)
c/Å	19.3129(14)
α/°	90
β/°	90
γ/°	90
V/Å^3	2232.3(2)
Z	8
Z'	1
Wavelength/Å	0.71073
Radiation type	MoK$_\alpha$
Θ_{min}/°	2.109
Θ_{max}/°	27.485
Measured Refl.	13735
Independent Refl.	2558
Reflections with I > 2(I)	2143
R_{int}	0.0404
Parameters	161
Restraints	76
Largest Peak	0.617
Deepest Hole	-0.367
GooF	1.093
wR_2 (all data)	0.1431
wR_2	0.1367
R_1 (all data)	0.0698
R_1	0.0566

Structure Quality Indicators

Reflections:	d min (Mo) 0.77	I/σ 29.0	Rint 4.04%	complete 100% (IUCr) 100%
Refinement:	Shift 0.000	Max Peak 0.6	Min Peak -0.4	GooF 1.093

A colourless block-shaped crystal with dimensions 0.10×0.10×0.02 mm^3 was mounted on a MITIGEN holder. Data were collected using an ROS diffractometer operating at T = 100(2)K.

Data were measured using profile data from ω-scans using MoK_α radiation. The total number of runs and images was based on the strategy calculation from the program CrysAlisPro. The maximum resolution that was achieved was Θ = 27.485° (0.77 Å).

The diffraction pattern was indexed the total number of runs and images was based on the strategy calculation from the program CrysAlisPro and the unit cell was refined using CrysAlisPro on 3203 reflections, 23% of the observed reflections.

Data reduction, scaling and absorption corrections were performed using CrysAlisPro. The final completeness is 99.90 % out to 27.485° in Θ. A multi-scan absorption correction was performed using CrysAlisPro using spherical harmonics as implemented in SCALE3 ABSPACK. The absorption coefficient μ of this material is 0.352 mm^{-1} at this wavelength (λ = 0.711Å) and the minimum and maximum transmissions are 0.710 and 1.000.

The structure was solved and the space group *Pbca* (# 61) determined by the ShelXS structure solution program using Direct Methods and refined by Least Squares using version 2018/3 of ShelXL. All non-hydrogen atoms were refined anisotropically. Hydrogen atom positions were calculated geometrically and refined using the riding model.

There is a single molecule in the asymmetric unit, which is represented by the reported sum formula. In other words: Z is 8 and Z' is 1.

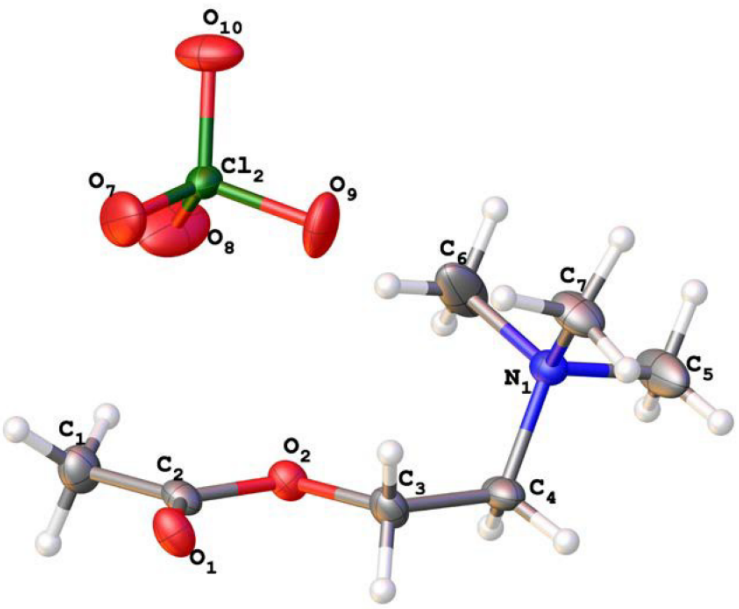

Figure 1: Acetylcholine perchlorate

Data Plots: Diffraction Data

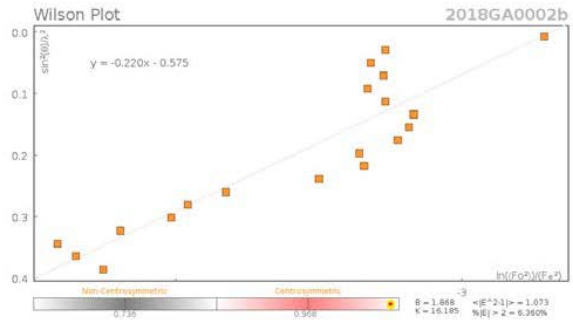

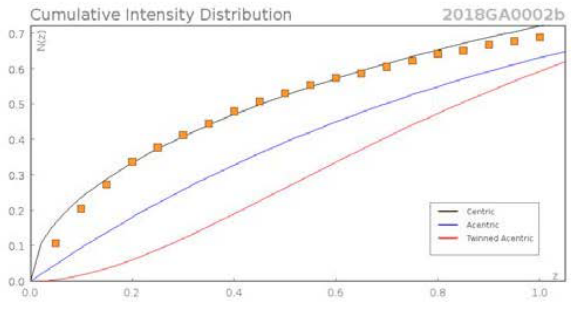

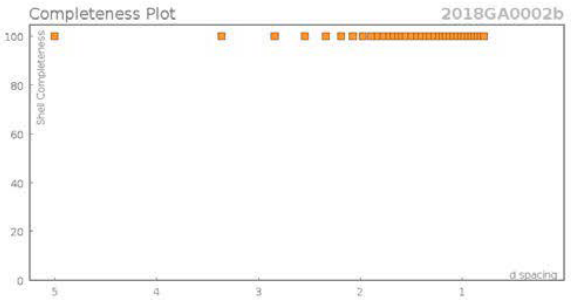

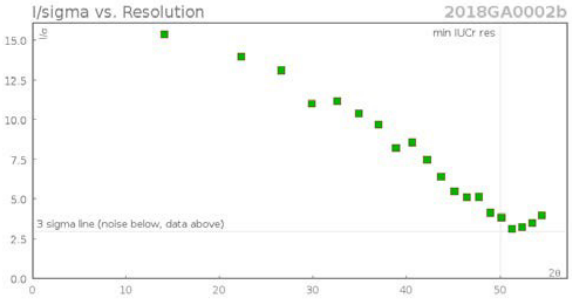

Data Plots: Refinement and Data

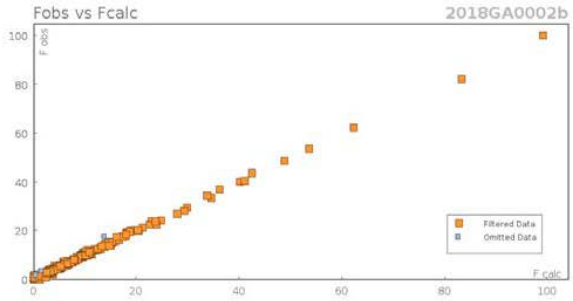

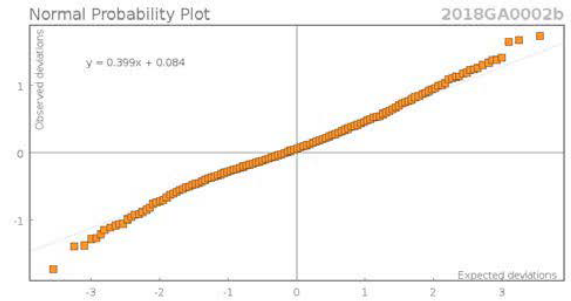

Reflection Statistics

Total reflections (after filtering)	14982	Unique reflections	2558
Completeness	0.999	Mean I/σ	19.04
hkl_{max} collected	(15, 11, 25)	hkl_{min} collected	(-15, -12, -24)
hkl_{max} used	(15, 12, 24)	hkl_{min} used	(0, 0, 0)
Lim d_{max} collected	100.0	Lim d_{min} collected	0.36
d_{max} used	10.19	d_{min} used	0.77
Friedel pairs	2697	Friedel pairs merged	1
Inconsistent equivalents	0	R_{int}	0.0404
R_{sigma}	0.0345	Intensity transformed	0
Omitted reflections	0	Omitted by user (OMIT hkl)	14
Multiplicity	(8172, 3057, 216, 12)	Maximum multiplicity	13
Removed systematic absences	1233	Filtered off (Shel/OMIT)	0

Table 1: Fractional Atomic Coordinates ($\times 10^4$) and Equivalent Isotropic Displacement Parameters ($Å^2 \times 10^3$) for Acetylcholine Perchlorate. U_{eq} is defined as 1/3 of the trace of the orthogonalised U_{ij}.

Atom	x	y	z	U_{eq}
O2	6483.0(14)	3663.9(18)	6340.9(9)	20.9(4)
O1	7466.2(16)	5332(2)	5816.9(9)	25.7(4)
N1	4146.9(17)	2302(2)	5948.6(11)	18.4(4)
C2	7203.2(19)	4744(3)	6337.7(14)	20.9(5)
C3	6067(2)	3310(3)	5666.0(13)	23.6(5)
C4	5327(2)	2047(3)	5711.7(15)	24.7(6)
C1	7618(2)	5069(3)	7047.1(14)	28.2(6)
C7	3547(2)	3231(3)	5456.6(17)	31.7(7)
C6	4108(3)	2920(4)	6651.3(16)	44.7(9)
C5	3555(3)	945(3)	5942(2)	42.2(9)
Cl2	4718.3(17)	7290.6(18)	6393.8(11)	20.3(4)
O7	5428(2)	8332(3)	6109(2)	45.6(9)
O8	5276(3)	6449(4)	6883.9(16)	54.3(10)
O9	4344(2)	6415(3)	5839.4(12)	39.1(9)
O10	3747(3)	7918(3)	6709(2)	40.8(8)
Cl1	4567(13)	7314(17)	6473(8)	14(3)
O3	4064(17)	7240(30)	5837(10)	31(6)
O4	5450(20)	8220(30)	6491(17)	48(8)
O5	4940(20)	6050(20)	6698(16)	46(8)
O6	3730(30)	7750(40)	6913(17)	65(10)

Table 2: Anisotropic Displacement Parameters ($\times 10^4$) Acetylcholine Perchlorate. The anisotropic displacement factor exponent takes the form: $-2\pi^2[h^2a^{*2} \times U_{11} + ... + 2hka^* \times b^* \times U_{12}]$

Atom	U_{11}	U_{22}	U_{33}	U_{23}	U_{13}	U_{12}
O2	19.2(8)	23.5(9)	20.1(9)	3.3(7)	-0.3(7)	-1.0(7)
O1	20.9(9)	31.3(10)	24.8(9)	8.2(8)	-2.4(8)	-6.3(8)
N1	17.2(10)	16.5(10)	21.6(10)	2.0(8)	1.2(8)	0.8(8)
C2	13.6(11)	21.7(12)	27.4(13)	2.6(10)	-0.5(10)	1.9(10)
C3	18.1(12)	28.7(13)	24.0(13)	0.0(11)	2.4(10)	-4.8(11)
C4	17.0(12)	20.6(12)	36.6(15)	-1.3(11)	3.3(10)	3.1(10)
C1	27.1(14)	35.0(15)	22.6(13)	-0.2(11)	-2.2(11)	-3.3(12)
C7	20.8(13)	29.0(14)	45.2(17)	13.3(13)	-2.1(12)	4.8(12)
C6	28.1(15)	85(3)	21.3(14)	-10.2(16)	6.7(12)	-11.9(17)
C5	25.6(15)	18.4(14)	83(3)	5.4(15)	7.6(16)	-2.6(12)
Cl2	18.2(6)	20.2(5)	22.6(6)	-5.0(4)	-2.4(5)	3.9(4)
O7	36.7(15)	32.5(14)	68(3)	-10.7(14)	12.6(14)	-17.1(11)
O8	61(2)	64(2)	37.1(16)	-1.4(15)	-20.6(15)	36.2(18)
O9	54.0(17)	38.6(19)	24.8(12)	-10.3(10)	-7.3(11)	-16.6(14)
O10	35.8(15)	31.9(14)	55(2)	6.2(14)	18.2(14)	13.4(11)

Table 3: Bond Lengths in Å for Acetylcholine Perchlorate.

Atom	Atom	Length/Å
O2	C2	1.353(3)
O2	C3	1.437(3)
O1	C2	1.197(3)
N1	C4	1.507(3)
N1	C7	1.491(3)
N1	C6	1.483(4)

Atom	Atom	Length/Å
N1	C5	1.488(3)
C2	C1	1.491(4)
C3	C4	1.510(4)
Cl2	O7	1.426(3)
Cl2	O8	1.414(3)
Cl2	O9	1.435(3)

Atom	Atom	Length/Å
Cl2	O10	1.446(3)
Cl1	O3	1.370(18)
Cl1	O4	1.37(2)

Atom	Atom	Length/Å
Cl1	O5	1.372(19)
Cl1	O6	1.38(2)

Table 4: Bond Angles in ° for Acetylcholine Perchlorate.

Atom	Atom	Atom	Angle/°
C2	O2	C3	113.61(19)
C7	N1	C4	111.0(2)
C6	N1	C4	111.9(2)
C6	N1	C7	109.0(2)
C6	N1	C5	110.2(3)
C5	N1	C4	107.6(2)
C5	N1	C7	107.0(2)
O2	C2	C1	111.8(2)
O1	C2	O2	122.4(2)
O1	C2	C1	125.8(2)
O2	C3	C4	110.0(2)
N1	C4	C3	116.0(2)
O7	Cl2	O9	108.3(2)
O7	Cl2	O10	110.34(19)
O8	Cl2	O7	112.3(2)
O8	Cl2	O9	108.0(2)
O8	Cl2	O10	109.8(2)
O9	Cl2	O10	108.0(2)
O3	Cl1	O4	113.3(15)
O3	Cl1	O5	112.4(15)
O3	Cl1	O6	104.2(16)
O4	Cl1	O6	110.6(17)
O5	Cl1	O4	107.7(15)
O5	Cl1	O6	108.4(17)

Table 5: Torsion Angles in ° for Acetylcholine Perchlorate.

Atom	Atom	Atom	Atom	Angle/°
O2	C3	C4	N1	80.6(3)
C2	O2	C3	C4	176.6(2)
C3	O2	C2	O1	-0.5(3)
C3	O2	C2	C1	-179.6(2)
C7	N1	C4	C3	61.9(3)
C6	N1	C4	C3	-60.1(3)
C5	N1	C4	C3	178.7(3)

Table 6: Hydrogen Fractional Atomic Coordinates ($\times 10^4$) and Equivalent Isotropic Displacement Parameters ($Å^2 \times 10^3$) for Acetylcholine Perchlorate. U_{eq} is defined as 1/3 of the trace of the orthogonalised U_{ij}.

Atom	x	y	z	U_{eq}
H3A	6699.59	3118.84	5350.6	28
H3B	5637.6	4098.87	5474.72	28
H4A	5299.98	1604.1	5249.41	30
H4B	5676.82	1376.66	6033.69	30
H1A	7096.45	4698.79	7391.12	42
H1B	7678.3	6076.35	7102.65	42
H1C	8353.63	4644.79	7113.72	42
H7A	3844.81	4174.76	5495.27	47
H7B	2749.5	3237.33	5568.58	47
H7C	3651.73	2893.2	4982.51	47
H6A	4478.91	2298.82	6980.29	67
H6B	3328.52	3050.44	6790.72	67
H6C	4489.11	3818.74	6647.41	67
H5A	3559.54	565.15	5471.64	63
H5B	2782.32	1078.05	6094.79	63
H5C	3932.1	299.12	6256.19	63

Table 7: Atomic Occupancies for all atoms that are not fully occupied in Acetylcholine Perchlorate.

Atom	Occupancy	Atom	Occupancy	Atom	Occupancy	Atom	Occupancy
Cl2	0.899(8)	O9	0.899(8)	O3	0.101(8)	O6	0.101(8)
O7	0.899(8)	O10	0.899(8)	O4	0.101(8)		
O8	0.899(8)	Cl1	0.101(8)	O5	0.101(8)		

A.2 ACh Chloride

Crystal Data and Experimental

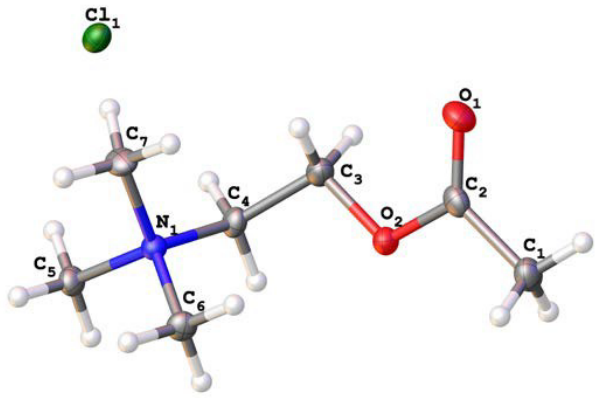

Experimental. Single orange lath-shaped crystals of Acetylcholine Chloride were recrystallized from a mixture of acetonitrile and toluene by solvent layering. A suitable crystal 0.40×0.10×0.05 mm^3 was selected and mounted on a MITIGEN holder on a DOT diffractometer. The crystal was kept at a steady T = 100.00(10) K during data collection. The structure was solved with the ShelXT structure solution program using the Intrinsic Phasing solution method and by using Olex2 as the graphical interface. The model was refined with version 2018/3 of ShelXL using Least Squares minimisation.

Crystal Data. $C_7H_{16}ClNO_2$, M_r = 181.66, orthorhombic, $P2_12_12_1$ (No. 19), a = 6.30780(10) Å, b = 9.9019(2) Å, c = 15.3171(2) Å, $\alpha = \beta = \gamma = 90°$, V = 956.69(3) $Å^3$, T = 100.00(10) K, Z = 4, Z' = 1, μ(CuK$_\alpha$) = 3.203, 6923 reflections measured, 1716 unique (R_{int} = 0.0217) which were used in all calculations. The final wR_2 was 0.0622 (all data) and R_1 was 0.0219 (I > 2(I)).

Compound	**Acetylcholine Chloride**
Formula	$C_7H_{16}ClNO_2$
$D_{calc.}$ / g cm^{-3}	1.261
μ/mm^{-1}	3.203
Formula Weight	181.66
Colour	orange
Shape	lath
Size/mm^3	0.40×0.10×0.05
T/K	100.00(10)
Crystal System	orthorhombic
Flack Parameter	0.484(17)
Hooft Parameter	0.482(4)
Space Group	$P2_12_12_1$
a/Å	6.30780(10)
b/Å	9.9019(2)
c/Å	15.3171(2)
α/°	90
β/°	90
γ/°	90
V/$Å^3$	956.69(3)
Z	4
Z'	1
Wavelength/Å	1.54176
Radiation type	CuK$_\alpha$
Θ_{min}/°	5.319
Θ_{max}/°	70.229
Measured Refl.	6923
Independent Refl.	1716
Reflections with I > 2(I)	1701
R_{int}	0.0217
Parameters	105
Restraints	0
Largest Peak	0.184
Deepest Hole	-0.159
GooF	1.094
wR_2 (all data)	0.0622
wR_2	0.0621
R_1 (all data)	0.0220
R_1	0.0219

Structure Quality Indicators

Reflections:	d min (Cu) 0.82	I/σ 64.6	Rint 2.17%	complete 99% (IUCr) 96%
Refinement:	Shift 0.001	Max Peak 0.2	Min Peak -0.2	GooF 1.094

An orange lath-shaped crystal with dimensions 0.40×0.10×0.05 mm^3 was mounted on a MITIGEN holder. Data were collected using a DOT diffractometer operating at T = 100.00(10)K.

Data were measured using ω scans using CuK$_\alpha$ radiation. The total number of runs and images was based on the strategy calculation from the program CrysAlisPro . The maximum resolution that was achieved was Θ = 70.229° (0.82 Å).

The diffraction pattern was indexed The total number of runs and images was based on the strategy calculation from the program CrysAlisPro and the unit cell was refined using CrysAlisPro on 5809 reflections, 84% of the observed reflections.

Data reduction, scaling and absorption corrections were performed using CrysAlisPro . The final completeness is 99.50 % out to 70.229° in Θ. A multi-scan absorption correction was performed using CrysAlisPro 1.171.39.46b (Rigaku Oxford Diffraction) using spherical harmonics as implemented in SCALE3 ABSPACK. The absorption coefficient μ of this material is 3.203 mm^{-1} at this wavelength (λ = 1.542Å) and the minimum and maximum transmissions are 0.695 and 1.000.

The structure was solved and the space group $P2_12_12_1$ (# 19) determined by the ShelXT structure solution program using Intrinsic Phasing and refined by Least Squares using version 2018/3 of ShelXL . All non-hydrogen atoms were refined anisotropically. Hydrogen atom positions were calculated geometrically and refined using the riding model. Hydrogen atom positions were calculated geometrically and refined using the riding model.

_refine_special_details: Refined as a 2-component inversion twin.

_exptl_absorpt_process_details: CrysAlisPro 1.171.39.46b (Rigaku Oxford Diffraction) using spherical harmonicsas implemented in SCALE3 ABSPACK.

There is a single molecule in the asymmetric unit, which is represented by the reported sum formula. In other words: Z is 4 and Z' is 1.

The Flack parameter was refined to 0.484(17). Determination of absolute structure using Bayesian statistics on Bijvoet differences using the Olex2 results in 0.482(4). Note: The Flack parameter is used to determine chirality of the crystal studied, the value should be near 0, a value of 1 means that the stereochemistry is wrong, and the model should be inverted. A value of 0.5 means that the crystal consists of a racemic mixture of the two enantiomers.

Data Plots: Refinement and Data

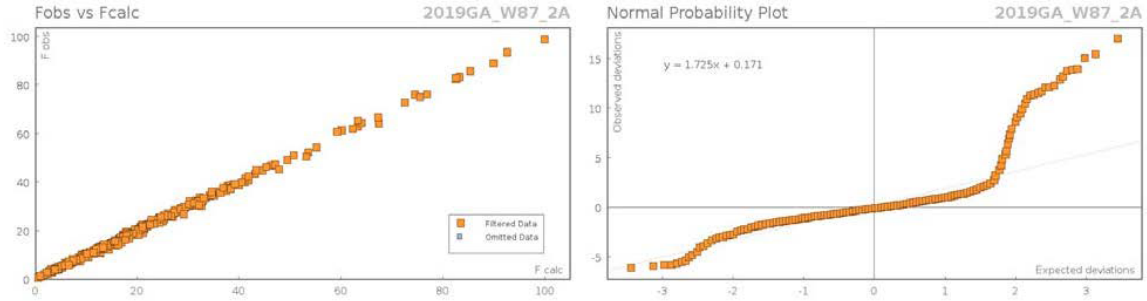

Reflection Statistics

Total reflections (after filtering)	6965	Unique reflections	1716
Completeness	0.941	Mean I/σ	49.51
hkl_{max} collected	(7, 12, 18)	hkl_{min} collected	(-6, -11, -17)
hkl_{max} used	(7, 12, 18)	hkl_{min} used	(-7, 0, 0)
Lim d_{max} collected	100.0	Lim d_{min} collected	0.77
d_{max} used	9.9	d_{min} used	0.82
Friedel pairs	1122	Friedel pairs merged	0
Inconsistent equivalents	9	R_{int}	0.0217
R_{sigma}	0.0155	Intensity transformed	0
Omitted reflections	0	Omitted by user (OMIT hkl)	0
Multiplicity	(2138, 938, 745, 95, 43, 19, 1)	Maximum multiplicity	16
Removed systematic absences	42	Filtered off (Shel/OMIT)	0

Images of the Crystal on the Diffractometer

Table 1: Fractional Atomic Coordinates ($\times 10^4$) and Equivalent Isotropic Displacement Parameters ($Å^2 \times 10^3$) for Acetylcholine Chloride. U_{eq} is defined as 1/3 of the trace of the orthogonalised U_{ij}.

Atom	x	y	z	U_{eq}
Cl1	7633.2(7)	6535.4(4)	8349.0(3)	18.13(14)
O2	4078(2)	5390.1(12)	5071.4(8)	17.9(3)
O1	5069(2)	7273.5(14)	4361.6(10)	28.0(3)
N1	7293(3)	3936.5(14)	6437.2(9)	14.2(3)
C2	4092(3)	6224.5(18)	4371.8(13)	18.8(4)
C7	9315(3)	4716(2)	6354.9(13)	20.8(4)
C6	7087(3)	2994.2(18)	5674.0(11)	18.5(4)
C4	5386(3)	4856.1(19)	6521.0(12)	16.9(4)
C3	5131(3)	5931.3(19)	5832.2(12)	20.6(4)
C1	2779(4)	5684.2(19)	3639.6(12)	22.7(4)
C5	7392(3)	3120.7(18)	7267.2(11)	17.8(4)

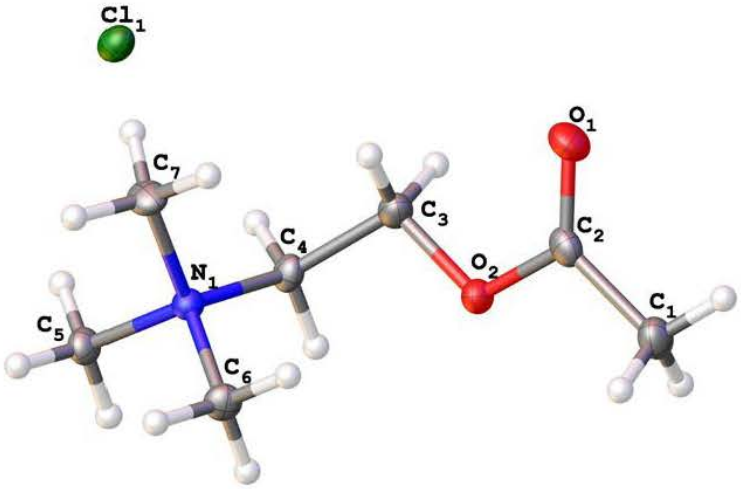

Figure 1:

Data Plots: Diffraction Data

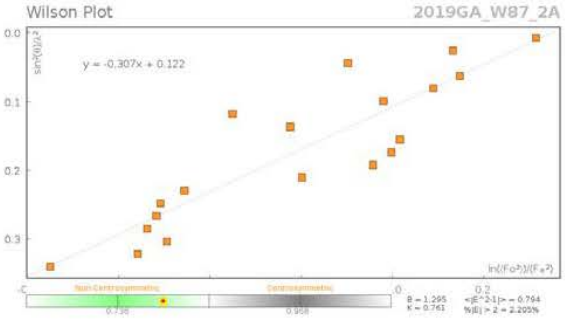

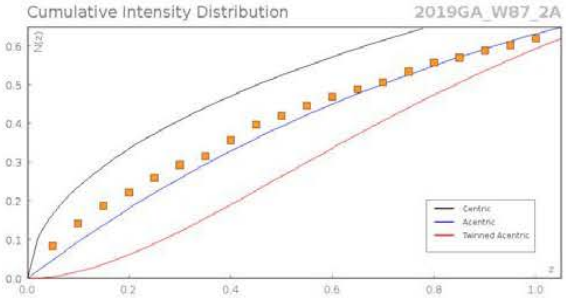

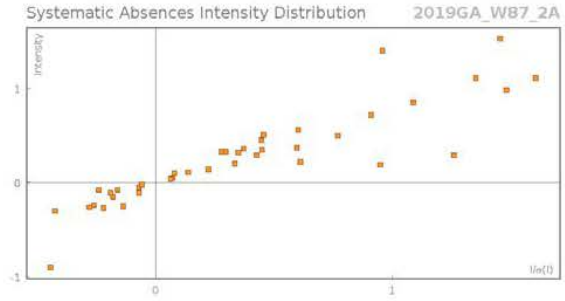

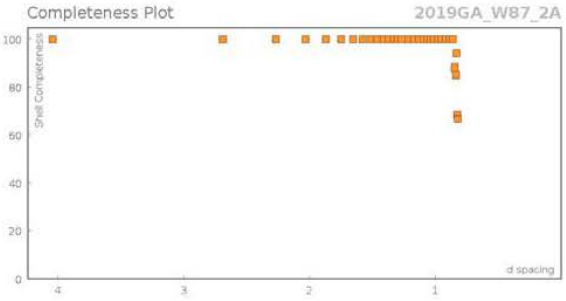

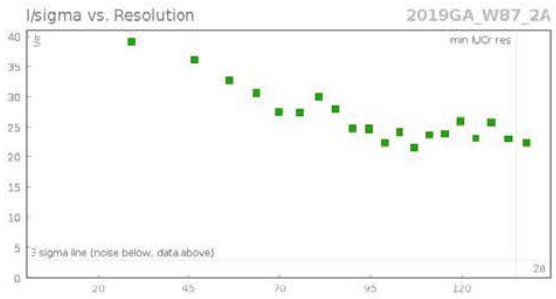

Table 2: Anisotropic Displacement Parameters ($\times 10^4$) Acetylcholine Chloride. The anisotropic displacement factor exponent takes the form: $-2\pi^2[h^2a^{*2} \times U_{11} + ... + 2hka^* \times b^* \times U_{12}]$

Atom	U_{11}	U_{22}	U_{33}	U_{23}	U_{13}	U_{12}
Cl1	15.4(2)	19.9(2)	19.1(2)	-3.06(14)	-1.01(17)	0.81(17)
O2	19.5(7)	16.6(6)	17.5(6)	1.9(5)	-3.9(6)	-0.5(6)
O1	32.0(8)	18.7(7)	33.3(8)	7.7(6)	-5.1(7)	-3.4(6)
N1	13.1(8)	14.7(7)	14.8(7)	0.8(5)	0.4(6)	-1.0(6)
C2	17.5(9)	17.1(9)	21.8(9)	2.5(7)	0.6(8)	4.8(8)
C7	13.3(9)	20.1(9)	29.0(10)	2.5(8)	2.1(8)	-4.2(8)
C6	20.3(10)	19.0(9)	16.1(8)	-3.2(7)	0.8(8)	1.1(7)
C4	13.1(9)	19.7(9)	17.8(9)	-1.4(7)	-1.4(8)	3.3(7)
C3	22.3(10)	16.9(9)	22.7(9)	-2.3(7)	-6.1(8)	1.6(8)
C1	26.3(12)	21.9(9)	20.0(9)	1.7(7)	-4.0(9)	2.9(9)
C5	19.2(9)	19.3(8)	15.0(8)	3.6(6)	-1.3(8)	-0.3(8)

Table 3: Bond Lengths in Å for Acetylcholine Chloride.

Atom	Atom	Length/Å	Atom	Atom	Length/Å
O2	C2	1.353(2)	N1	C4	1.514(2)
O2	C3	1.444(2)	N1	C5	1.508(2)
O1	C2	1.208(2)	C2	C1	1.493(3)
N1	C7	1.496(2)	C4	C3	1.508(2)
N1	C6	1.501(2)			

Table 4: Bond Angles in ° for Acetylcholine Chloride.

Atom	Atom	Atom	Angle/°	Atom	Atom	Atom	Angle/°
C2	O2	C3	114.17(14)	C5	N1	C4	106.47(14)
C7	N1	C6	109.19(15)	O2	C2	C1	111.87(16)
C7	N1	C4	111.97(13)	O1	C2	O2	122.59(18)
C7	N1	C5	108.19(15)	O1	C2	C1	125.54(18)
C6	N1	C4	111.78(14)	C3	C4	N1	116.76(16)
C6	N1	C5	109.10(13)	O2	C3	C4	110.59(15)

Table 5: Hydrogen Fractional Atomic Coordinates ($\times 10^4$) and Equivalent Isotropic Displacement Parameters (Å$^2 \times 10^3$) for Acetylcholine Chloride. U_{eq} is defined as 1/3 of the trace of the orthogonalised U_{ij}.

Atom	x	y	z	U_{eq}
H7A	10497.12	4110.54	6406.18	31
H7B	9386.14	5382.11	6809.26	31
H7C	9358.67	5155.02	5796.43	31
H6A	7036.97	3508	5142.88	28
H6B	5807.58	2476.38	5731.47	28
H6C	8283.51	2395.78	5659.62	28
H4A	4121.54	4298.82	6518.2	20
H4B	5455.57	5297.41	7085.71	20
H3A	4307.53	6675.03	6066.59	25
H3B	6513.69	6276.05	5667.63	25
H1A	3461.9	4905.36	3394.12	34
H1B	2626.24	6365.19	3198.01	34
H1C	1405.74	5434.7	3856.08	34
H5A	8597.24	2529.82	7247.92	27
H5B	6120.98	2594.44	7324.44	27
H5C	7519.42	3718.44	7757.89	27

A.3 ACh Bromide

Crystal Data and Experimental

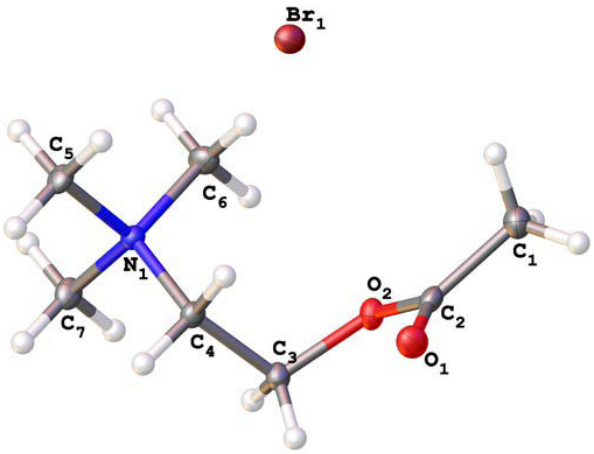

Experimental. Single colourless plate-shaped crystals of Acetylcholine Bromide were recrystallized from ethanol by slow cooling. A suitable crystal 0.15×0.08×0.05 mm3 was selected and mounted on a MITIGEN holder on a DOT diffractometer. The crystal was kept at a steady T = 100.00(10) K during data collection. The structure was solved with the ShelXT structure solution program using the Intrinsic Phasing solution method and by using **Olex2** as the graphical interface. The model was refined with version 2018/3 of ShelXL using Least Squares minimisation.

Crystal Data. $C_7H_{16}BrNO_2$, M_r = 226.12, monoclinic, $P2_1/n$ (No. 14), a = 7.07220(10) Å, b = 13.44950(10) Å, c = 10.95230(10) Å, β = 108.6910(10)°, α = γ = 90°, V = 986.814(19) Å^3, T = 100.00(10) K, Z = 4, Z' = 1, μ(CuK$_\alpha$) = 5.359, 21769 reflections measured, 1858 unique (R_{int} = 0.0468) which were used in all calculations. The final wR_2 was 0.0747 (all data) and R_1 was 0.0273 (I > 2(I)).

Compound	Acetylcholine Bromide
Formula	$C_7H_{16}BrNO_2$
$D_{calc.}$ / g cm^{-3}	1.522
μ/mm^{-1}	5.359
Formula Weight	226.12
Colour	colourless
Shape	plate
Size/mm^3	0.15×0.08×0.05
T/K	100.00(10)
Crystal System	monoclinic
Space Group	$P2_1/n$
a/Å	7.07220(10)
b/Å	13.44950(10)
c/Å	10.95230(10)
α°	90
β°	108.6910(10)
γ°	90
V/Å^3	986.814(19)
Z	4
Z'	1
Wavelength/Å	1.54178
Radiation type	CuK$_\alpha$
Θ_{min}°	5.385
Θ_{max}°	70.289
Measured Refl.	21769
Independent Refl.	1858
Reflections with I > 2(I)	1857
R_{int}	0.0468
Parameters	104
Restraints	0
Largest Peak	0.443
Deepest Hole	-1.096
GooF	1.164
wR_2 (all data)	0.0747
wR_2	0.0747
R_1 (all data)	0.0273
R_1	0.0273

Structure Quality Indicators

Reflections:	d min (Cu) 0.82	I/σ 64.8	Rint 4.68%	complete 100% (IUCr) 100%
Refinement:	Shift -0.001	Max Peak 0.4	Min Peak -1.1	GooF 1.164

A colourless plate-shaped crystal with dimensions 0.15×0.08×0.05 mm^3 was mounted on a MITIGEN holder. Data were collected using a DOT diffractometer operating at T = 100.00(10)K.

Data were measured using ω scans using CuK_α radiation. The total number of runs and images was based on the strategy calculation from the program **CrysAlisPro** The maximum resolution that was achieved was Θ = 70.289° (0.82 Å).

The diffraction pattern was indexed The total number of runs and images was based on the strategy calculation from the program **CrysAlisPro** and the unit cell was refined using **CrysAlisPro** on 19858 reflections, 91% of the observedreflections.

Data reduction, scaling and absorption corrections were performed using **CrysAlisPro** . The final completeness is 99.60 % out to 70.289° in Θ. A multi-scan absorption correction was performed using CrysAlisPro 1.171.39.46b using spherical harmonics as implemented in SCALE3 ABSPACK.. The absorption coefficient μ of this material is
5.359 mm^{-1} at this wavelength (λ = 1.542Å) and the minimum and maximum transmissions are 0.491 and 1.000.

The structure was solved and the space group $P2_1/n$ (# 14) determined by the **ShelXT** structure solution program using Intrinsic Phasing and refined by Least Squares using version 2018/3 of **ShelXL**. All non-hydrogen atoms were refined anisotropically. Hydrogen atom positions were calculated geometrically and refined using the riding model. Hydrogen atom positions were calculated geometrically and refined using the riding model.

_exptl_absorpt_process_details: CrysAlisPro 1.171.39.46b using spherical harmonics as implemented in SCALE3 ABSPACK.

The value of Z' is 1.

Data Plots: Diffraction Data

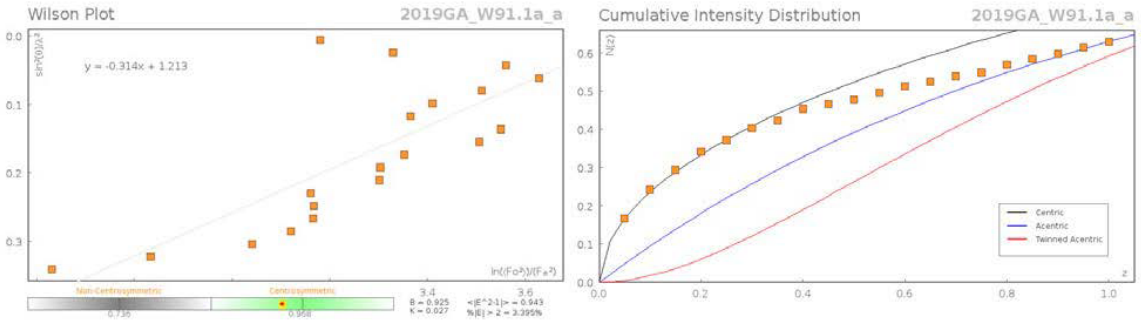

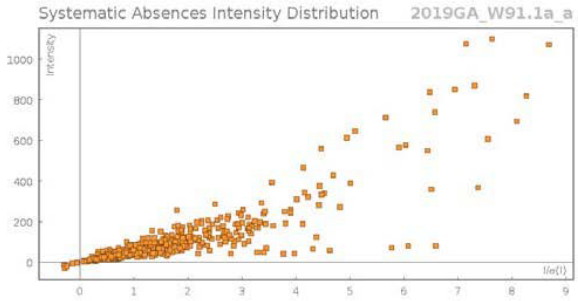

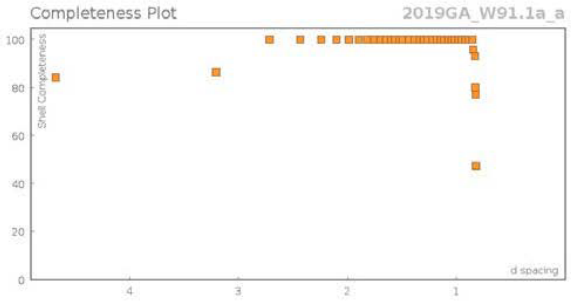

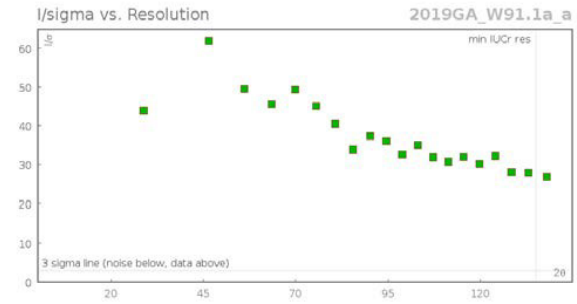

Data Plots: Refinement and Data

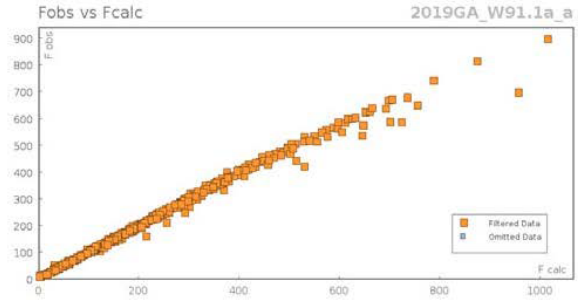

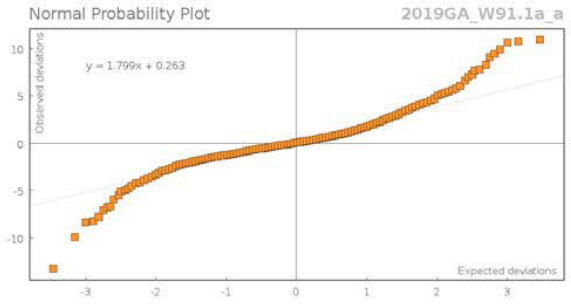

Reflection Statistics

Total reflections (after filtering)	22480	Unique reflections	1858
Completeness	0.985	Mean I/σ	64.49
hkl_{max} collected	(8, 16, 13)	hkl_{min} collected	(-8, -16, -13)
hkl_{max} used	(8, 16, 13)	hkl_{min} used	(-8, 0, 0)
Lim d_{max} collected	100.0	Lim d_{min} collected	0.77
d_{max} used	13.45	d_{min} used	0.82
Friedel pairs	2590	Friedel pairs merged	1
Inconsistent equivalents	110	R_{int}	0.0468
R_{sigma}	0.0154	Intensity transformed	0
Omitted reflections	0	Omitted by user (OMIT hkl)	0
Multiplicity	(1206, 1299, 1015, 814, 666, 448, 313, 184, 106, 81, 50, 23, 8)	Maximum multiplicity	38
Removed systematic absences	711	Filtered off (Shel/OMIT)	0

Images of the Crystal on the Diffractometer

Table 1: Fractional Atomic Coordinates ($\times 10^4$) and Equivalent Isotropic Displacement Parameters ($Å^2 \times 10^3$) for Acetylcholine Bromide. U_{eq} is defined as 1/3 of the trace of the orthogonalised U_{ij}.

Atom	x	y	z	U_{eq}
Br1	6410.5(3)	6160.3(2)	2851.4(2)	15.75(12)
O2	4399(2)	8680.6(10)	4925.4(14)	14.8(3)
O1	3920(2)	9000.1(11)	2829.0(15)	18.6(3)
N1	2436(2)	6539.8(11)	4954.5(15)	11.1(3)
C2	5034(3)	8924.9(13)	3917(2)	14.5(4)
C5	2074(3)	5602.5(14)	4165.4(19)	14.8(4)
C6	4587(3)	6570.1(15)	5772.1(19)	16.2(4)
C7	1138(3)	6525.7(15)	5804.1(19)	15.6(4)
C1	7257(3)	9031.7(16)	4334(2)	19.1(4)
C3	2300(3)	8428.4(14)	4587.0(19)	14.3(4)
C4	1886(3)	7395.9(14)	4010.2(17)	12.3(4)

Table 2: Anisotropic Displacement Parameters ($\times 10^4$) Acetylcholine Bromide. The anisotropic displacement factor exponent takes the form: $-2\pi^2[h^2a^{*2} \times U_{11} + \ldots + 2hka^* \times b^* \times U_{12}]$

Atom	U_{11}	U_{22}	U_{33}	U_{23}	U_{13}	U_{12}
Br1	16.20(17)	16.83(16)	15.10(16)	3.38(6)	6.24(11)	1.56(6)
O2	15.6(7)	13.7(6)	15.3(7)	0.6(5)	5.3(6)	-3.5(5)
O1	18.4(7)	19.5(7)	18.3(8)	5.8(6)	6.5(6)	0.5(6)
N1	12.0(8)	9.5(8)	11.7(7)	0.0(6)	3.9(6)	0.1(6)
C2	17.8(10)	8.4(9)	19.2(11)	0.8(7)	8.5(9)	-0.5(7)
C5	18.1(9)	10.2(9)	17.1(9)	-2.8(7)	6.9(8)	-1.5(7)
C6	13.4(10)	16.7(10)	15.7(9)	0.7(7)	0.7(8)	1.2(7)
C7	19.7(10)	14.5(9)	16.2(9)	0.0(7)	11.0(8)	-1.8(7)
C1	16.6(10)	17.0(9)	24.1(11)	0.9(8)	7.2(8)	-2.4(8)
C3	13.4(9)	12.8(10)	18.4(10)	0.0(7)	7.4(8)	-1.8(7)
C4	13.3(9)	11.3(9)	12.1(8)	2.1(7)	3.9(7)	-0.2(7)

Table 3: Bond Lengths in Å for Acetylcholine Bromide.

Atom	Atom	Length/Å
O2	C2	1.360(3)
O2	C3	1.451(2)
O1	C2	1.203(3)
N1	C5	1.503(2)
N1	C6	1.499(2)
N1	C7	1.502(2)
N1	C4	1.513(2)
C2	C1	1.497(3)
C3	C4	1.515(2)

Table 4: Bond Angles in ° for Acetylcholine Bromide.

Atom	Atom	Atom	Angle/°
C2	O2	C3	115.25(15)
C5	N1	C4	106.63(14)
C6	N1	C5	108.63(14)
C6	N1	C7	109.58(15)
C6	N1	C4	112.14(14)
C7	N1	C5	108.70(14)
C7	N1	C4	111.04(14)
O2	C2	C1	111.28(18)
O1	C2	O2	122.9(2)
O1	C2	C1	125.8(2)
O2	C3	C4	111.46(15)
N1	C4	C3	116.09(15)

Table 5: Hydrogen Fractional Atomic Coordinates ($\times 10^4$) and Equivalent Isotropic Displacement Parameters ($Å^2 \times 10^3$) for Acetylcholine Bromide. U_{eq} is defined as 1/3 of the trace of the orthogonalised U_{ij}.

Atom	x	y	z	U_{eq}
H5A	2927.13	5593.04	3637.64	22
H5B	704.63	5579.41	3625.45	22
H5C	2359.77	5036.4	4729	22
H6A	4894.42	5993.23	6316.43	24
H6B	4831.63	7158.39	6296	24
H6C	5414.47	6578.13	5227.51	24
H7A	-238.75	6499.23	5279.14	23
H7B	1370.61	7116.89	6322.43	23
H7C	1454.28	5952.09	6354.02	23
H1A	7747.56	9189.96	5236.27	29
H1B	7607.98	9555.04	3850.73	29
H1C	7842.59	8418.77	4184.22	29
H3A	1516.74	8909.72	3971.43	17
H3B	1893.14	8461.37	5351.92	17
H4A	473.71	7348.41	3531.97	15
H4B	2608.27	7317.92	3398	15

A.4 ACh Iodide

Crystal Data and Experimental

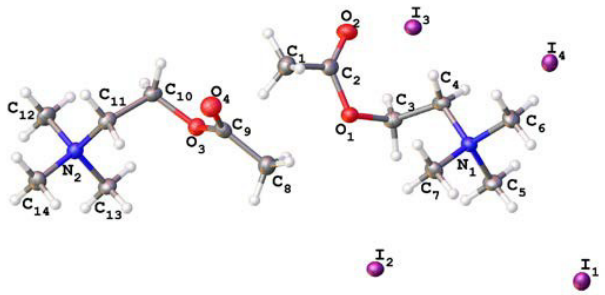

Experimental. Single colourless cut plate-shaped crystals of Acetylcholine Iodide were recrystallized from methanol and ethanol as an antisolvent by vapour diffusion. A suitable crystal 0.24×0.15×0.02 mm3 was selected and mounted on a MITIGEN holder on a DOT diffractometer. The crystal was kept at a steady T = 100(2) K during data collection. The structure was solved with the olex2.solve structure solution program using the Charge Flipping solution method and by using Olex2 as the graphical interface. The model was refined version 2018/3 of ShelXL using Least Squares minimisation.

Crystal Data. $C_7H_{16}INO_2$, M_r = 273.11, orthorhombic, *Pnma* (No. 52), a = 31.3060(3) Å, b = 11.49901(13) Å, c = 11.49253(15) Å, $\alpha = \beta = \gamma = 90°$, V = 4137.17(8) Å^3, T = 100(2) K, Z = 16, Z' = 2, μ(CuK$_\alpha$) = 24.024, 71754 reflections measured, 3794 unique (R_{int} = 0.0502) which were used in all calculations. The final wR_2 was 0.0660 (all data) and R_1 was 0.0230 (I > 2(I)).

Compound	**Acetylcholine Iodide**
Formula	$C_7H_{16}INO_2$
$D_{calc.}$ / g cm^{-3}	1.754
μ/mm^{-1}	24.024
Formula Weight	273.11
Colour	colourless
Shape	cut plate
Size/mm^3	0.24×0.15×0.02
T/K	100(2)
Crystal System	orthorhombic
Space Group	*Pnma*
a/Å	31.3060(3)
b/Å	11.49901(13)
c/Å	11.49253(15)
α/°	90
β/°	90
γ/°	90
V/Å^3	4137.17(8)
Z	16
Z'	2
Wavelength/Å	1.54178
Radiation type	CuK$_\alpha$
Θ_{min}/°	4.098
Θ_{max}/°	68.265
Measured Refl.	71754
Independent Refl.	3794
Reflections with I > 2(I)	3570
R_{int}	0.0502
Parameters	209
Restraints	0
Largest Peak	0.462
Deepest Hole	-0.985
GooF	1.112
wR_2 (all data)	0.0660
wR_2	0.0650
R_1 (all data)	0.0242
R_1	0.0230

Structure Quality Indicators

Reflections:	d min (Cu) 0.83	I/σ 54.5	Rint 5.02%	complete 100% (IUCr) 100%
Refinement:	Shift -0.004	Max Peak 0.5	Min Peak -1.0	GooF 1.112

A colourless cut plate-shaped crystal with dimensions 0.24×0.15×0.02 mm^3 was mounted on a MITIGEN holder. Data were collected using a DOT diffractometer operating at T = 100(2)K.

Data were measured using profile data from ω-scans using CuK_α radiation. The total number of runs and images was based on the strategy calculation from the program CrysAlisPro. The maximum resolution that was achieved was Θ = 68.265° (0.83 Å).

The diffraction pattern was indexed the total number of runs and images was based on the strategy calculation from the program CrysAlisPro and the unit cell was refined using CrysAlisPro on 33728 reflections, 47% of the observed reflections.

Data reduction, scaling and absorption corrections were performed using CrysAlisPro . The final completeness is 99.80 % out to 68.265° in Θ. A Gaussian absorption correction was performed using CrysAlisPro 1.171.39.46b. Numerical absorption correction based on Gaussian integration over a multifaceted crystal model empirical absorption correction using spherical harmonics as implemented in SCALE3 ABSPACK. The absorption coefficient μ of this material is 24.024 mm^{-1} at this wavelength (λ = 1.542Å) and the minimum and maximum transmissions are
0.047 and 0.720.

The structure was solved and the space group *Pnna* determined by the olex2.solve structure solution program using Charge Flipping and refined by Least Squares using version 2018/3 of ShelXL. All non-hydrogen atoms were refined anisotropically. Hydrogen atom positions were calculated geometrically and refined using the riding model.

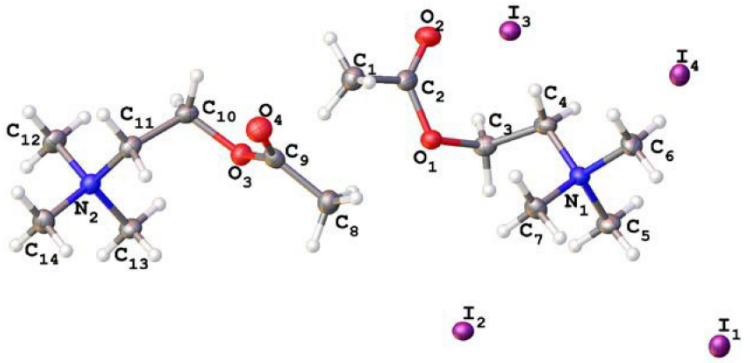

Figure 1: Acetylcholine iodide

_exptl_absorpt_process_details: CrysAlisPro 1.171.39.46b. Numerical absorption correction based on gaussian integration over a multifaceted crystal modelEmpirical absorption correctionusing spherical harmonicsas implemented in SCALE3 ABSPACK.

Data Plots: Diffraction Data

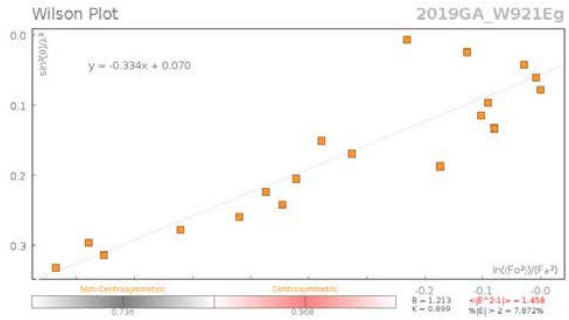

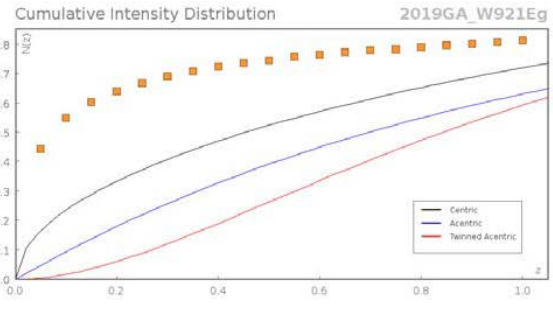

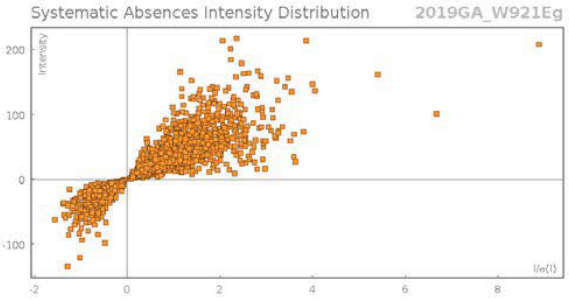

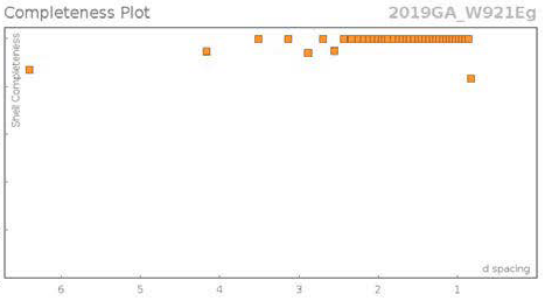

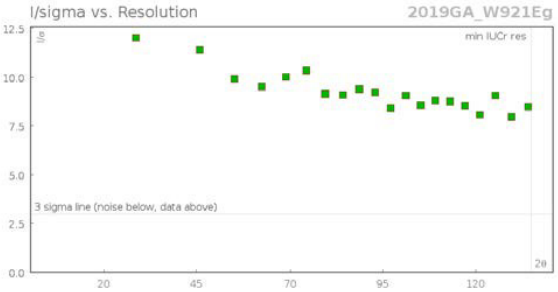

Data Plots: Refinement and Data

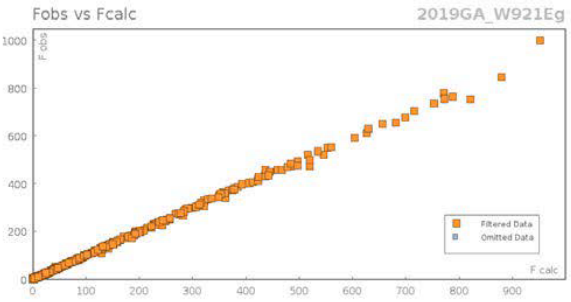

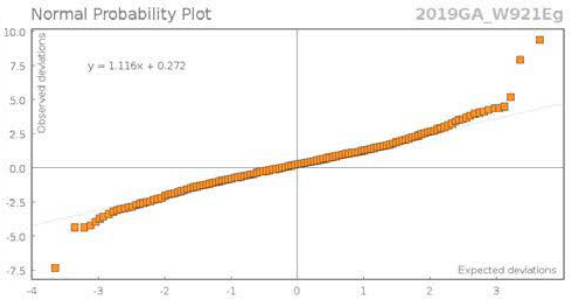

Reflection Statistics

Total reflections (after filtering)	76885	Unique reflections	3794
Completeness	0.998	Mean I/σ	39.19
hkl_{max} collected	(37, 13, 13)	hkl_{min} collected	(-37, -13, -13)
hkl_{max} used	(37, 13, 13)	hkl_{min} used	(0, 0, 0)
Lim d_{max} collected	100.0	Lim d_{min} collected	0.77
d_{max} used	11.5	d_{min} used	0.83
Friedel pairs	10158	Friedel pairs merged	1
Inconsistent equivalents	0	R_{int}	0.0502
Rsigma	0.0184	Intensity transformed	0
Omitted reflections	0	Omitted by user (OMIT hkl)	0
Multiplicity	(5475, 6908, 4480,	Maximum multiplicity	47
Removed systematic absences	5131	Filtered off (Shel/OMIT)	0

Images of the Crystal on the Diffractometer

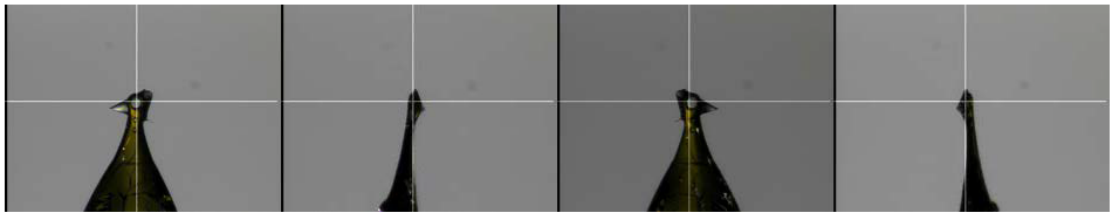

Table 1: Fractional Atomic Coordinates ($\times 10^4$) and Equivalent Isotropic Displacement Parameters ($Å^2 \times 10^3$) for Acetylcholine Iodide. U_{eq} is defined as 1/3 of the trace of the orthogonalised U_{ij}.

Atom	x	y	z	U_{eq}
I_3	5993.5(2)	7500	2500	19.95(8)
I_2	5920.1(2)	12500	-2500	18.92(8)
I_1	7667.1(2)	12500	-2500	23.72(8)
I_4	7306.2(2)	12500	2500	21.20(8)
C_6	6909.9(7)	9291.7(19)	745(2)	25.7(5)
N_2	3404.9(6)	14788.8(15)	113.3(14)	19.6(4)
N_1	6590.7(6)	10104.2(14)	207.2(15)	19.8(4)
O_3	4403.6(4)	14191.3(12)	753.8(12)	21.9(3)
O_1	5589.7(4)	10753.9(12)	805.0(12)	22.0(3)
C_5	6827.9(7)	10957.9(19)	-537.8(19)	25.3(5)
O_2	5539.5(5)	10985.0(14)	2745.5(12)	28.3(3)
C_{14}	3083.5(7)	14253.8(19)	-700.5(19)	25.5(5)
O_4	4459.4(5)	12255.3(12)	993.8(14)	28.1(3)
C_1	5010.4(6)	9843(2)	1738(2)	27.4(5)
C_8	4985.7(6)	13269(2)	-156(2)	27.4(5)
C_9	4597.4(7)	13145.2(17)	588.9(17)	21.7(4)
C_{11}	3635.4(7)	13806.8(16)	725.1(17)	21.2(4)
C_3	5976.6(7)	11437.3(17)	834.4(18)	22.5(4)
C_{10}	4019.2(7)	14160.6(17)	1445.2(17)	22.1(4)
C_4	6357.8(7)	10712.5(17)	1190.4(17)	22.0(4)
C_2	5398.0(6)	10584.0(17)	1857.9(17)	21.8(4)
C_{12}	3168.6(7)	15541.8(19)	962.9(19)	25.1(5)
C_{13}	3711.9(7)	15509.7(18)	-576.5(18)	23.1(4)
C_7	6284.7(7)	9420.7(18)	-524.1(18)	23.4(4)

Table 2: Anisotropic Displacement Parameters ($\times 10^4$) Acetylcholine Iodide. The anisotropic displacement factor exponent takes the form: $-2\pi^2[h^2a^{*2} \times U_{11} + \ldots + 2hka^* \times b^* \times U_{12}]$

Atom	U_{11}	U_{22}	U_{33}	U_{23}	U_{13}	U_{12}
I_3	23.17(12)	17.82(13)	18.86(13)	0.04(6)	0	0
I_2	22.75(13)	16.71(13)	17.31(13)	0.27(6)	0	0
I_1	22.66(13)	24.77(14)	23.72(14)	-6.08(7)	0	0
I_4	20.30(13)	20.46(13)	22.83(13)	-5.04(7)	0	0
C_6	24.5(11)	25.7(11)	26.9(11)	7.6(9)	-1.6(9)	2.5(9)
N_2	20.8(9)	17.0(7)	20.9(9)	-1.3(7)	1.4(7)	-1.0(6)
N_1	21.2(9)	20.2(8)	18.0(8)	1.8(6)	-1.4(7)	-0.7(7)
O_3	22.7(7)	18.8(7)	24.3(7)	0.0(6)	0.8(6)	0.1(5)
O_1	22.8(7)	24.3(7)	18.8(7)	0.2(6)	0.4(5)	-0.8(6)
C_5	28.9(11)	25.1(11)	22.0(10)	7.6(9)	1.0(8)	-4.1(9)
O_2	33.6(9)	31.6(8)	19.6(7)	-1.3(6)	-0.6(7)	-1.2(7)

Atom	U_{11}	U_{22}	U_{33}	U_{23}	U_{13}	U_{12}
C_{14}	24.5(11)	24.8(11)	27.3(11)	-7.2(9)	-1.8(9)	-2.1(9)
O_4	33.3(9)	18.9(7)	32.2(8)	0.5(6)	1.3(7)	-0.9(6)
C_1	26.1(12)	26.8(12)	29.4(12)	1.2(10)	1.8(8)	-0.6(8)
C_8	24.7(12)	28.8(12)	28.8(12)	-1.8(10)	0.6(8)	1.4(8)
C_9	25.0(10)	20.7(9)	19.5(9)	-2.9(8)	-4.9(8)	1.2(8)
C_{11}	24.5(10)	14.8(9)	24.2(10)	0.2(8)	5.2(8)	-0.6(8)
C_3	28.0(10)	18.0(9)	21.6(10)	0.0(8)	1.7(8)	-3.1(8)
C_{10}	27.7(10)	20.6(9)	18.1(9)	0.6(8)	3.0(8)	2.0(8)
C_4	26.5(11)	23.0(10)	16.5(9)	0.2(8)	-1.0(8)	-5.6(8)
C_2	23.7(10)	18.8(9)	22.9(10)	2.8(8)	1.1(8)	4.8(8)
C_{12}	27.9(11)	21.5(10)	26.0(11)	-7.1(9)	4.7(9)	2.2(8)
C_{13}	25.3(11)	21.8(10)	22.2(10)	5.0(8)	2.3(8)	-2.9(8)
C_7	25.8(11)	22.3(10)	22.0(10)	-5.0(8)	-4.6(8)	-1.4(8)

Table 3: Bond Lengths in Å for Acetylcholine Iodide.

Atom	Atom	Length/Å	Atom	Atom	Length/Å
C_6	N_1	1.501(3)	O_3	C_{10}	1.442(2)
N_2	C_{14}	1.505(3)	O_1	C_3	1.444(2)
N_2	C_{11}	1.513(3)	O_1	C_2	1.365(2)
N_2	C_{12}	1.500(3)	O_2	C_2	1.204(3)
N_2	C_{13}	1.497(3)	O_4	C_9	1.204(3)
N_1	C_5	1.499(3)	C_1	C_2	1.489(3)
N_1	C_4	1.516(3)	C_8	C_9	1.494(3)
N_1	C_7	1.497(3)	C_{11}	C_{10}	1.515(3)
O_3	C_9	1.361(2)	C_3	C_4	1.512(3)

Table 4: Bond Angles in ° for Acetylcholine Iodide.

Atom	Atom	Atom	Angle/°	Atom	Atom	Atom	Angle/°
C_{14}	N_2	C_{11}	107.60(15)	C_9	O_3	C_{10}	115.29(15)
C_{12}	N_2	C_{14}	108.11(17)	C_2	O_1	C_3	115.21(15)
C_{12}	N_2	C_{11}	111.31(15)	O_3	C_9	C_8	111.02(18)
C_{13}	N_2	C_{14}	109.06(16)	O_4	C_9	O_3	122.51(19)
C_{13}	N_2	C_{11}	110.69(16)	O_4	C_9	C_8	126.5(2)
C_{13}	N_2	C_{12}	109.98(16)	N_2	C_{11}	C_{10}	115.58(16)
C_6	N_1	C_4	107.48(15)	O_1	C_3	C_4	111.61(15)
C_5	N_1	C_6	108.24(17)	O_3	C_{10}	C_{11}	111.55(16)
C_5	N_1	C_4	111.21(15)	C_3	C_4	N_1	115.61(16)
C_7	N_1	C_6	109.29(16)	O_1	C_2	C_1	110.99(18)
C_7	N_1	C_5	109.88(16)	O_2	C_2	O_1	122.33(19)
C_7	N_1	C_4	110.66(16)	O_2	C_2	C_1	126.7(2)

Table 5: Hydrogen Fractional Atomic Coordinates ($\times 10^4$) and Equivalent Isotropic Displacement Parameters ($Å^2 \times 10^3$) for Acetylcholine Iodide. U_{eq} is defined as 1/3 of the trace of the orthogonalised U_{ij}.

Atom	x	y	z	U_{eq}
H_5	7076.31	8913.08	130.29	39
H_6	6759.6	8699.91	1202.32	39
H_4	7102.14	9731.67	1254.24	39
H_3	7023.57	11412.45	-51.86	38
H_2	6623.83	11481.46	-917.05	38
H_1	6991.26	10537.9	-1131.49	38
H_{26}	3232.24	13778.62	-1280.98	38
H_{24}	2923.04	14870.98	-1093.86	38

Atom	x	y	z	U_{eq}
H_{25}	2886.02	13763.51	-256.59	38
H_{15}	4835.88	10127.4	1089.95	41
H_{14}	4843.8	9875.58	2459.29	41
H_{16}	5096.39	9037.48	1586.11	41
H_{18}	4899.25	13437.99	-958.28	41
H_{17}	5149.72	12543.08	-138.68	41
H_{19}	5162.92	13906.42	138.75	41
H_{23}	3730.3	13238.75	131.62	25
H_{22}	3429.31	13405.07	1240.33	25
H_{13}	5940.67	12086.9	1391.27	27
H_{12}	6028.77	11774.63	54.7	27
H_{21}	3968.11	14938.89	1786.13	27
H_{20}	4056.87	13601.94	2092.64	27
H_{10}	6260.46	10116.63	1752.77	26
H_{11}	6563.38	11222.7	1600.09	26
H_{32}	3006.67	16135.3	538.76	38
H_{31}	3373.13	15920.5	1485.52	38
H_{30}	2971.68	15061.46	1419.4	38
H_{27}	3872.12	15007.46	-1109.46	35
H_{29}	3910.78	15900.86	-46.97	35
H_{28}	3553.78	16093.07	-1024.88	35
H_{9}	6443.91	8970.58	-1103.88	35
H_{7}	6088.49	9953.9	-920.34	35
H_{8}	6121.26	8890.22	-26.82	35

Appendix B Nitrogen-14 T_1 saturation recovery curves

B.1 ACh Perchlorate

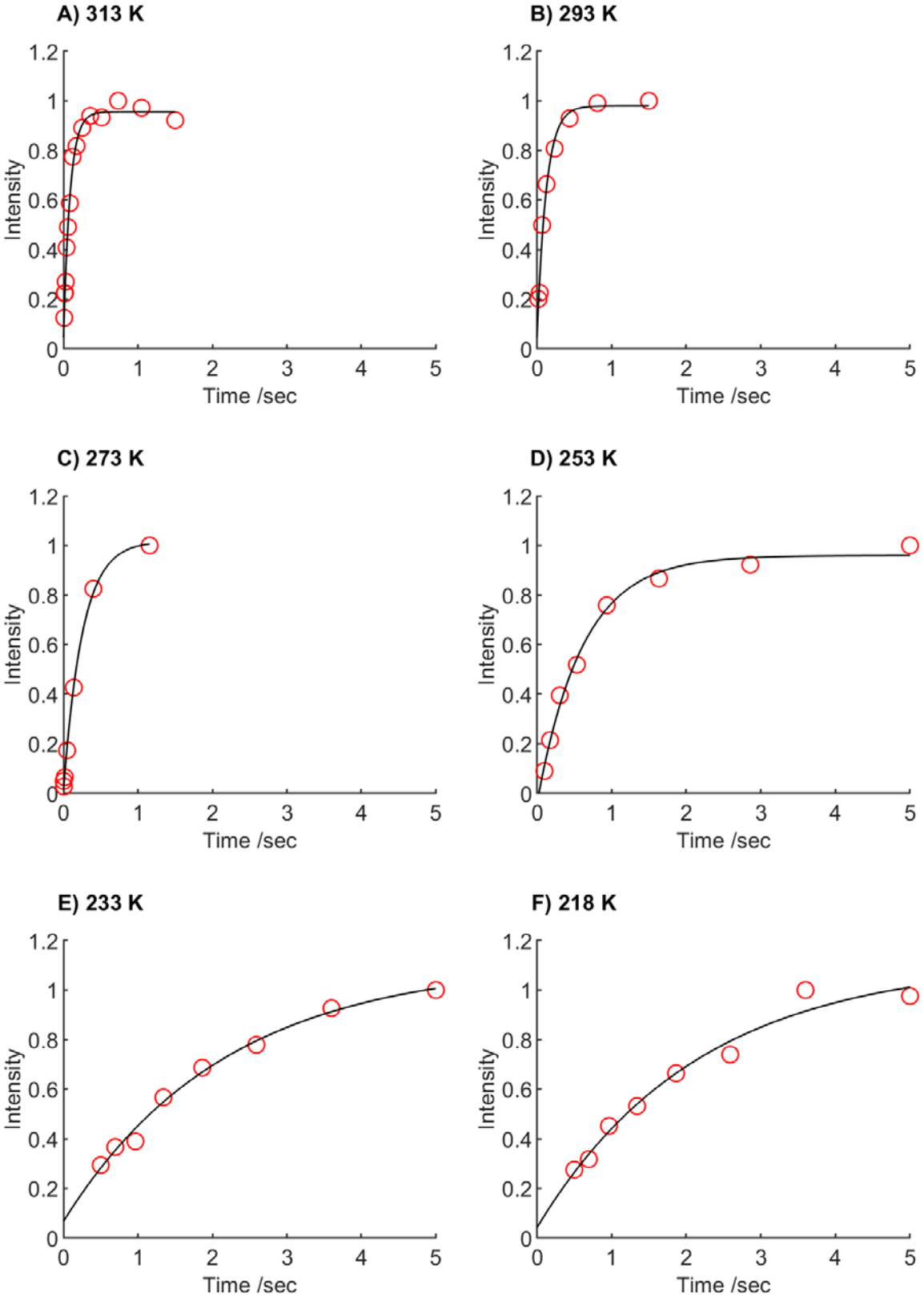

Figure 6.1: Fitted T_1 data measured on ACh perchlorate, MAS 10 kHz. Acquired at temperatures indicated using a saturation recovery pulse sequence.

B.2 ACh Chloride

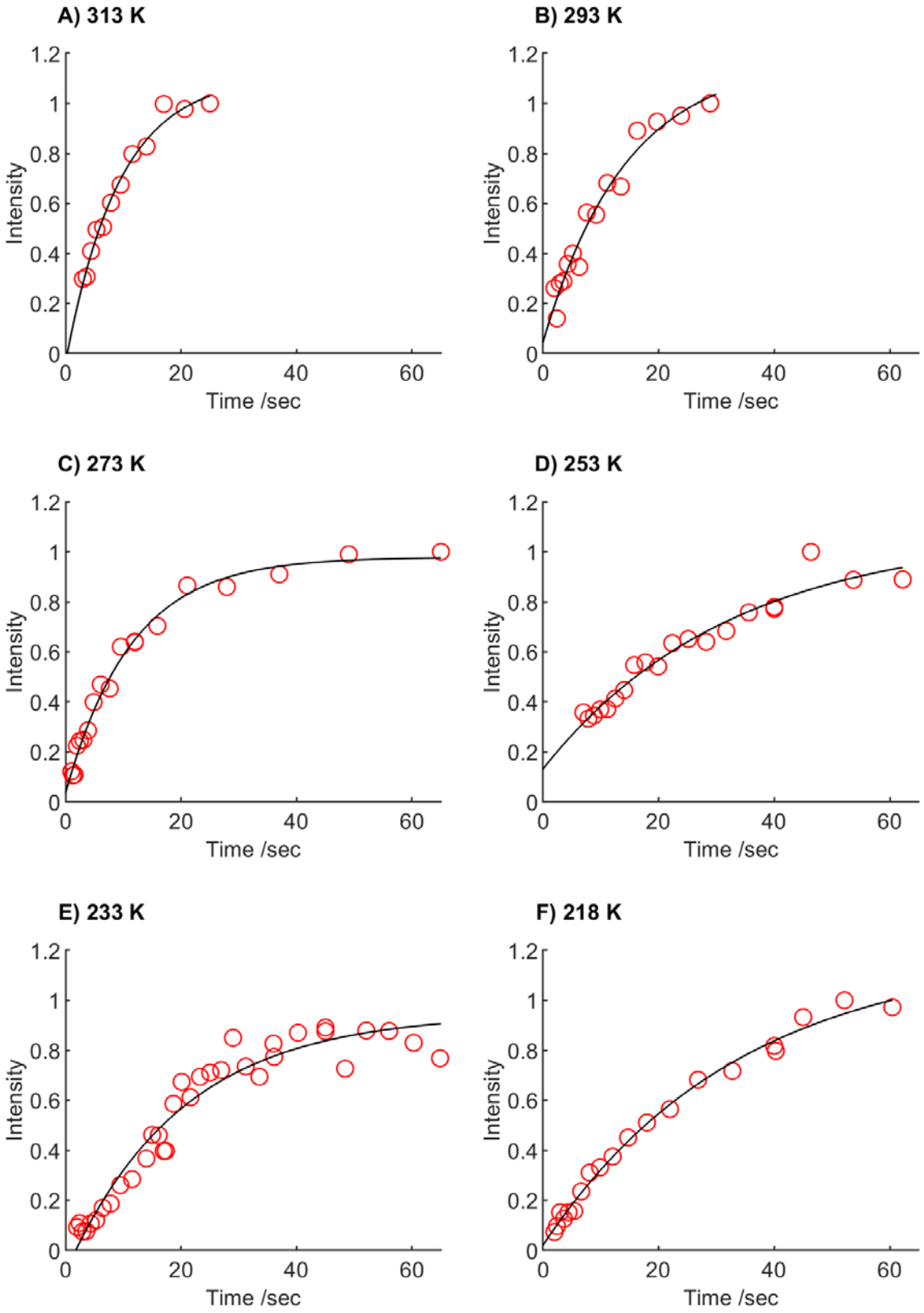

Figure 6.2: Fitted T_1 data measured on ACh chloride , MAS 10 kHz. Acquired at temperatures indicated using a saturation recovery pulse sequence.

B.3 ACh Bromide

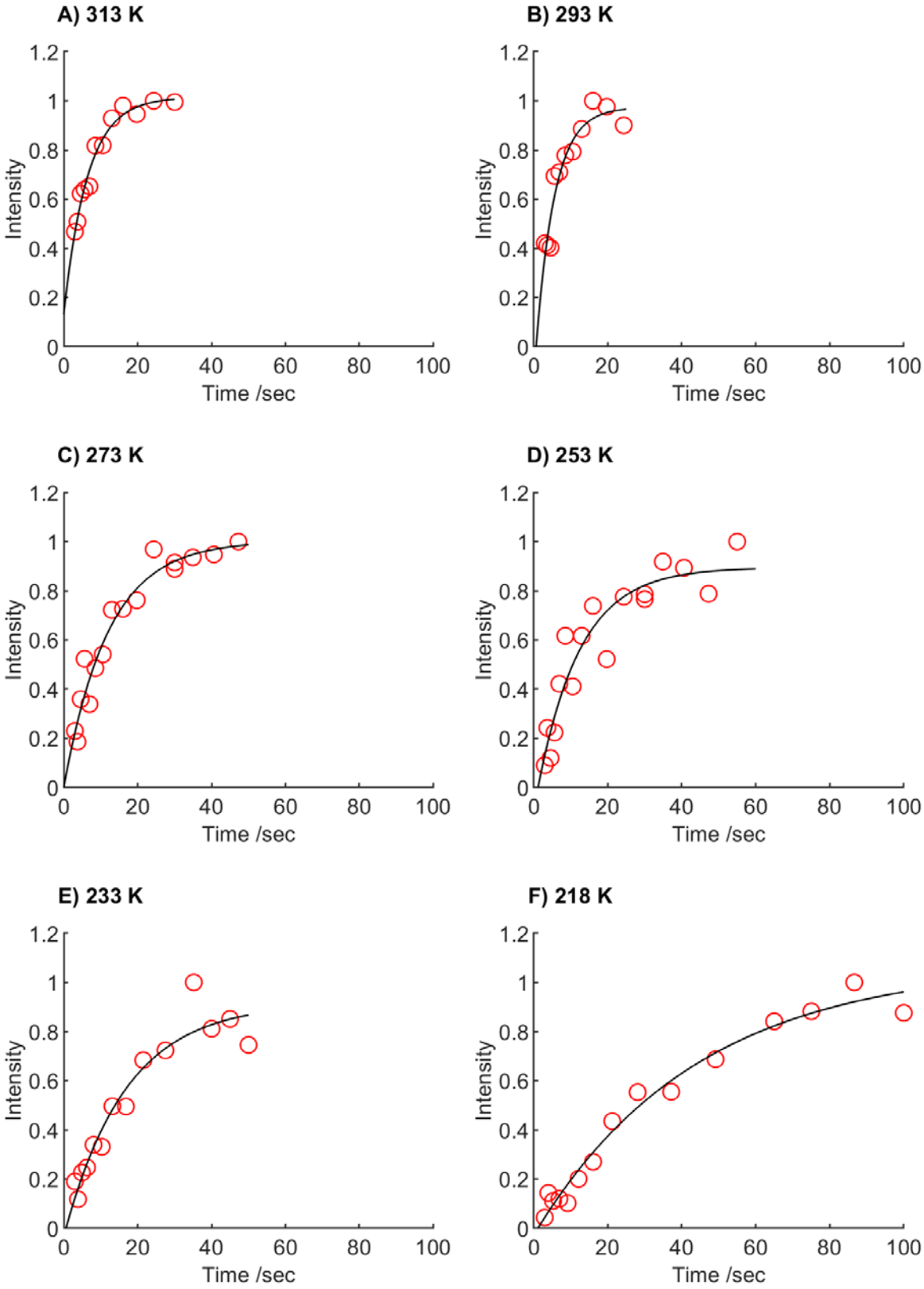

Figure 6.3: Fitted T_1 data measured on ACh bromide , MAS 10 kHz. Acquired at temperatures indicated using a saturation recovery pulse sequence.

B.4 ACh Iodide

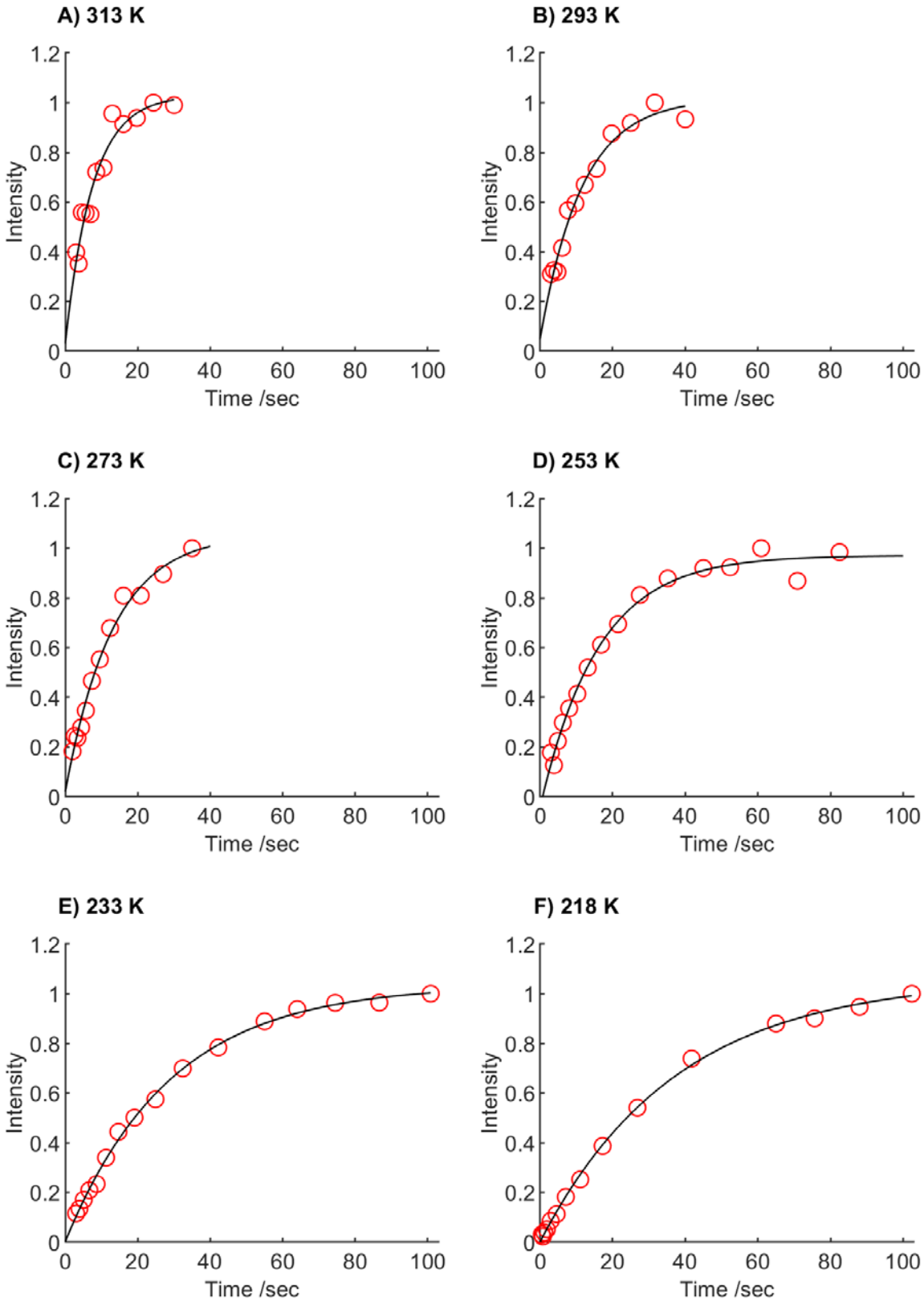

Figure 6.4:Fitted T_1 data measured on ACh iodide , MAS 10 kHz. Acquired at temperatures indicated using a saturation recovery pulse sequence.

Appendix C Simulations

C.1 *CASTEP* NMR Calculation Outputs

C.1.1 ACh Perchlorate

Site	δ iso (ppm)	δ aniso (ppm)	δ reduced aniso (ppm)	δ asymm	δ 1 (ppm)	δ 2 (ppm)	δ 3 (ppm)	alpha	beta	gamma
C=O (C^2)	179.8384	-144.2602	-96.1735	0.3190	243.2648	212.5854	83.6649	101.7188	62.9576	43.5260
C=O (C^2)	179.8384	-144.2602	-96.1735	0.3190	243.2648	212.5854	83.6649	-78.2812	62.9576	-136.4740
C=O (C^2)	179.8384	-144.2602	-96.1735	0.3190	243.2648	212.5854	83.6649	101.7188	62.9576	43.5260
C=O (C^2)	179.8384	-144.2602	-96.1735	0.3190	243.2648	212.5854	83.6649	78.2812	62.9576	136.4740
C=O (C^2)	179.8384	-144.2602	-96.1735	0.3190	243.2648	212.5854	83.6649	-101.7188	62.9576	-43.5260
C=O (C^2)	179.8384	-144.2602	-96.1735	0.3190	243.2648	212.5854	83.6649	-78.2812	62.9576	-136.4740
C=O (C^2)	179.8384	-144.2602	-96.1735	0.3190	243.2648	212.5854	83.6649	78.2812	62.9576	136.4740
C=O (C^2)	179.8384	-144.2602	-96.1735	0.3190	243.2648	212.5854	83.6649	-101.7188	62.9576	-43.5260
O-CH_2 (C^3)	65.0781	58.7006	39.1337	0.1103	43.3536	47.6689	104.2118	4.7877	153.6495	-146.7614
O-CH_2 (C^3)	65.0781	58.7006	39.1337	0.1103	43.3536	47.6689	104.2118	-175.2123	153.6495	33.2386
O-CH_2 (C^3)	65.0781	58.7006	39.1337	0.1103	43.3536	47.6689	104.2118	4.7877	153.6495	-146.7614
O-CH_2 (C^3)	65.0781	58.7006	39.1337	0.1103	43.3536	47.6689	104.2118	-4.7877	153.6495	-33.2386
O-CH_2 (C^3)	65.0781	58.7006	39.1337	0.1103	43.3536	47.6689	104.2118	175.2123	153.6495	146.7614
O-CH_2 (C^3)	65.0781	58.7006	39.1337	0.1103	43.3536	47.6689	104.2118	-175.2123	153.6495	33.2386
O-CH_2 (C^3)	65.0781	58.7006	39.1337	0.1103	43.3536	47.6689	104.2118	-4.7877	153.6495	-33.2386
O-CH_2 (C^3)	65.0781	58.7006	39.1337	0.1103	43.3536	47.6689	104.2118	175.2123	153.6495	146.7614
N-CH_2 (C^4)	69.4441	66.7848	44.5232	0.2639	41.3067	53.0584	113.9673	5.6944	110.5227	-8.0558
N-CH_2 (C^4)	69.4441	66.7848	44.5232	0.2639	41.3067	53.0584	113.9673	-174.3056	110.5227	171.9442
N-CH_2 (C^4)	69.4441	66.7848	44.5232	0.2639	41.3067	53.0584	113.9673	5.6944	110.5227	-8.0558
N-CH_2 (C^4)	69.4441	66.7848	44.5232	0.2639	41.3067	53.0584	113.9673	-5.6944	110.5227	-171.9442
N-CH_2 (C^4)	69.4441	66.7848	44.5232	0.2639	41.3067	53.0584	113.9673	174.3056	110.5227	8.0558
N-CH_2 (C^4)	69.4441	66.7848	44.5232	0.2639	41.3067	53.0584	113.9673	-174.3056	110.5227	171.9442

Site	δ iso (ppm)	δ aniso (ppm)	δ reduced aniso (ppm)	δ asymm	δ 1 (ppm)	δ 2 (ppm)	δ 3 (ppm)	alpha	beta	gamma
N-CH_2 (C^4)	69.4441	66.7848	44.5232	0.2639	41.3067	53.0584	113.9673	-5.6944	110.5227	-171.9442
N-CH_2 (C^4)	69.4441	66.7848	44.5232	0.2639	41.3067	53.0584	113.9673	174.3056	110.5227	8.0558
C-methyl (C^1)	19.1193	43.6481	29.0988	0.2048	1.5901	7.5498	48.2181	114.5569	19.0232	29.6713
C-methyl (C^1)	19.1193	43.6481	29.0988	0.2048	1.5901	7.5498	48.2181	-65.4431	19.0232	-150.3287
C-methyl (C^1)	19.1193	43.6481	29.0988	0.2048	1.5901	7.5498	48.2181	114.5569	19.0232	29.6713
C-methyl (C^1)	19.1193	43.6481	29.0988	0.2048	1.5901	7.5498	48.2181	65.4431	19.0232	150.3287
C-methyl (C^1)	19.1193	43.6481	29.0988	0.2048	1.5901	7.5498	48.2181	-114.5569	19.0232	-29.6713
C-methyl (C^1)	19.1193	43.6481	29.0988	0.2048	1.5901	7.5498	48.2181	-65.4431	19.0232	-150.3287
C-methyl (C^1)	19.1193	43.6481	29.0988	0.2048	1.5901	7.5498	48.2181	65.4431	19.0232	150.3287
C-methyl (C^1)	19.1193	43.6481	29.0988	0.2048	1.5901	7.5498	48.2181	-114.5569	19.0232	-29.6713
N-methyl	52.4345	78.2364	52.1576	0.2293	20.3759	32.3355	104.5921	-103.3711	51.0553	-48.4323
N-methyl	52.4345	78.2364	52.1576	0.2293	20.3759	32.3355	104.5921	-103.3711	51.0553	-48.4323
N-methyl	52.4345	78.2364	52.1576	0.2293	20.3759	32.3355	104.5921	103.3711	51.0553	48.4323
N-methyl	52.4345	78.2364	52.1576	0.2293	20.3759	32.3355	104.5921	103.3711	51.0553	48.4323
N-methyl	54.3742	74.3854	49.5903	0.1019	27.0526	32.1055	103.9645	118.7287	16.8905	87.1414
N-methyl	54.3742	74.3854	49.5903	0.1019	27.0526	32.1055	103.9645	118.7287	16.8905	87.1414
N-methyl	54.3742	74.3854	49.5903	0.1019	27.0526	32.1055	103.9645	-118.7287	16.8905	-87.1414
N-methyl	54.3742	74.3854	49.5903	0.1019	27.0526	32.1055	103.9645	-118.7287	16.8905	-87.1414
N-methyl	59.1386	86.2289	57.4859	0.1029	27.4374	33.3538	116.6245	-3.2027	92.4118	-114.9742
N-methyl	59.1386	86.2289	57.4859	0.1029	27.4374	33.3538	116.6245	-3.2027	92.4118	-114.9742
N-methyl	59.1386	86.2289	57.4859	0.1029	27.4374	33.3538	116.6245	-176.7973	92.4118	114.9742
N-methyl	59.1386	86.2289	57.4859	0.1029	27.4374	33.3538	116.6245	-176.7973	92.4118	114.9742
N-methyl	52.4345	78.2364	52.1576	0.2293	20.3759	32.3355	104.5921	76.6289	51.0553	131.5677
N-methyl	52.4345	78.2364	52.1576	0.2293	20.3759	32.3355	104.5921	-76.6289	51.0553	-131.5677
N-methyl	54.3742	74.3854	49.5903	0.1019	27.0526	32.1055	103.9645	-61.2713	16.8905	-92.8586
N-methyl	54.3742	74.3854	49.5903	0.1019	27.0526	32.1055	103.9645	61.2713	16.8905	92.8586
N-methyl	59.1386	86.2289	57.4859	0.1029	27.4374	33.3538	116.6245	176.7973	92.4118	65.0258

Site	δ iso (ppm)	δ aniso (ppm)	δ reduced aniso (ppm)	δ asymm	δ 1 (ppm)	δ 2 (ppm)	δ 3 (ppm)	alpha	beta	gamma
N-methyl	59.1386	86.2289	57.4859	0.1029	27.4374	33.3538	116.6245	3.2027	92.4118	-65.0258
N-methyl	52.4345	78.2364	52.1576	0.2293	20.3759	32.3355	104.5921	76.6289	51.0553	131.5677
N-methyl	52.4345	78.2364	52.1576	0.2293	20.3759	32.3355	104.5921	-76.6289	51.0553	-131.5677
N-methyl	54.3742	74.3854	49.5903	0.1019	27.0526	32.1055	103.9645	-61.2713	16.8905	-92.8586
N-methyl	54.3742	74.3854	49.5903	0.1019	27.0526	32.1055	103.9645	61.2713	16.8905	92.8586
N-methyl	59.1386	86.2289	57.4859	0.1029	27.4374	33.3538	116.6245	176.7973	92.4118	65.0258
N-methyl	59.1386	86.2289	57.4859	0.1029	27.4374	33.3538	116.6245	3.2027	92.4118	-65.0258

C.1.2 ACh Chloride

Site	δ iso (ppm)	δ aniso (ppm)	δ reduced aniso (ppm)	δ asymm	δ 1 (ppm)	δ 2 (ppm)	δ 3 (ppm)	alpha	beta	gamma
C=O (C^2)	180.7738	-145.7300	-97.1533	0.3296	245.3596	213.3413	83.6205	152.9279	158.5691	131.0838
C=O (C^2)	180.7738	-145.7300	-97.1533	0.3296	245.3596	213.3413	83.6205	-152.9279	158.5691	48.9162
C=O (C^2)	180.7738	-145.7300	-97.1533	0.3296	245.3596	213.3413	83.6205	-27.0721	158.5691	-48.9162
C=O (C^2)	180.7738	-145.7300	-97.1533	0.3296	245.3596	213.3413	83.6205	27.0721	158.5691	-131.0838
O-CH_2 (C^3)	64.0163	60.4363	40.2909	0.2392	39.0519	48.6899	104.3072	3.1918	151.2705	-137.5327
O-CH_2 (C^3)	64.0163	60.4363	40.2909	0.2392	39.0519	48.6899	104.3072	-3.1918	151.2705	-42.4673
O-CH_2 (C^3)	64.0163	60.4363	40.2909	0.2392	39.0519	48.6899	104.3072	-176.8082	151.2705	42.4673
O-CH_2 (C^3)	64.0163	60.4363	40.2909	0.2392	39.0519	48.6899	104.3072	176.8082	151.2705	137.5327
N-CH_2 (C^4)	65.2097	58.0499	38.6999	0.4155	37.8197	53.8998	103.9096	116.1173	96.2489	-37.2067
N-CH_2 (C^4)	65.2097	58.0499	38.6999	0.4155	37.8197	53.8998	103.9096	116.1173	83.7511	37.2067
N-CH_2 (C^4)	65.2097	58.0499	38.6999	0.4155	37.8197	53.8998	103.9096	-116.1173	83.7511	-37.2067
N-CH_2 (C^4)	65.2097	58.0499	38.6999	0.4155	37.8197	53.8998	103.9096	-116.1173	96.2489	37.2067
C-methyl (C^1)	20.5698	43.9365	29.2910	0.2870	1.7218	10.1269	49.8608	-143.7645	151.1568	-149.1393
C-methyl (C^1)	20.5698	43.9365	29.2910	0.2870	1.7218	10.1269	49.8608	143.7645	151.1568	-30.8607
C-methyl (C^1)	20.5698	43.9365	29.2910	0.2870	1.7218	10.1269	49.8608	36.2355	151.1568	30.8607
C-methyl (C^1)	20.5698	43.9365	29.2910	0.2870	1.7218	10.1269	49.8608	-36.2355	151.1568	149.1393
N-methyl	50.5475	66.5244	44.3496	0.2571	22.6718	34.0736	94.8972	110.1728	90.8426	-145.6812
N-methyl	50.5475	66.5244	44.3496	0.2571	22.6718	34.0736	94.8972	110.1728	89.1574	145.6812
N-methyl	50.5475	66.5244	44.3496	0.2571	22.6718	34.0736	94.8972	69.8272	89.1574	-145.6812
N-methyl	50.5475	66.5244	44.3496	0.2571	22.6718	34.0736	94.8972	69.8272	90.8426	145.6812
N-methyl	54.3971	73.7253	49.1502	0.0617	28.3065	31.3375	103.5473	45.3762	39.8320	78.7854
N-methyl	54.3971	73.7253	49.1502	0.0617	28.3065	31.3375	103.5473	134.6238	39.8320	101.2146
N-methyl	54.3971	73.7253	49.1502	0.0617	28.3065	31.3375	103.5473	-134.6238	39.8320	-101.2146
N-methyl	54.3971	73.7253	49.1502	0.0617	28.3065	31.3375	103.5473	-45.3762	39.8320	-78.7854
N-methyl	55.2757	76.2983	50.8655	0.1316	26.4961	33.1898	106.1413	-60.7307	32.9232	-84.3452
N-methyl	55.2757	76.2983	50.8655	0.1316	26.4961	33.1898	106.1413	-119.2693	32.9232	-95.6548

Site	δ iso (ppm)	δ aniso (ppm)	δ reduced aniso (ppm)	δ asymm	δ 1 (ppm)	δ 2 (ppm)	δ 3 (ppm)	alpha	beta	gamma
N-methyl	55.2757	76.2983	50.8655	0.1316	26.4961	33.1898	106.1413	119.2693	32.9232	95.6548
N-methyl	55.2757	76.2983	50.8655	0.1316	26.4961	33.1898	106.1413	60.7307	32.9232	84.3452

C.1.3 ACh Bromide

Site	δ iso (ppm)	δ aniso (ppm)	δ reduced aniso (ppm)	δ asymm	δ 1 (ppm)	δ 2 (ppm)	δ 3 (ppm)	alpha	beta	gamma
C=O (C^2)	178.8254	-148.6598	-99.1065	0.2902	242.7568	214.0005	79.7189	-99.9565	65.1494	-159.8169
C=O (C^2)	178.8254	-148.6598	-99.1065	0.2902	242.7568	214.0005	79.7189	-99.9565	65.1494	-159.8169
C=O (C^2)	178.8254	-148.6598	-99.1065	0.2902	242.7568	214.0005	79.7189	99.9565	65.1494	159.8169
C=O (C^2)	178.8254	-148.6598	-99.1065	0.2902	242.7568	214.0005	79.7189	99.9565	65.1494	159.8169
O-CH_2 (C^3)	62.1987	57.8433	38.5622	0.9627	24.3557	61.4795	100.7610	-158.3262	78.5432	19.9268
O-CH_2 (C^3)	62.1987	57.8433	38.5622	0.9627	24.3557	61.4795	100.7610	-158.3262	78.5432	19.9268
O-CH_2 (C^3)	62.1987	57.8433	38.5622	0.9627	24.3557	61.4795	100.7610	158.3262	78.5432	-19.9268
O-CH_2 (C^3)	62.1987	57.8433	38.5622	0.9627	24.3557	61.4795	100.7610	158.3262	78.5432	-19.9268
N-CH_2 (C^4)	68.8127	54.7902	36.5268	0.3130	44.8333	56.2653	105.3395	-89.4851	55.3378	-89.4828
N-CH_2 (C^4)	68.8127	54.7902	36.5268	0.3130	44.8333	56.2653	105.3395	-89.4851	55.3378	-89.4828
N-CH_2 (C^4)	68.8127	54.7902	36.5268	0.3130	44.8333	56.2653	105.3395	89.4851	55.3378	89.4828
N-CH_2 (C^4)	68.8127	54.7902	36.5268	0.3130	44.8333	56.2653	105.3395	89.4851	55.3378	89.4828
C-methyl (C^1)	20.5675	39.2405	26.1603	0.2683	3.9781	10.9965	46.7278	-60.6020	76.1506	13.9972
C-methyl (C^1)	20.5675	39.2405	26.1603	0.2683	3.9781	10.9965	46.7278	-60.6020	76.1506	13.9972
C-methyl (C^1)	20.5675	39.2405	26.1603	0.2683	3.9781	10.9965	46.7278	60.6020	76.1506	-13.9972
C-methyl (C^1)	20.5675	39.2405	26.1603	0.2683	3.9781	10.9965	46.7278	60.6020	76.1506	-13.9972
N-methyl	57.6850	78.1390	52.0927	0.1079	28.8274	34.4499	109.7776	74.6818	58.1532	89.9008
N-methyl	57.6850	78.1390	52.0927	0.1079	28.8274	34.4499	109.7776	74.6818	58.1532	89.9008
N-methyl	57.6850	78.1390	52.0927	0.1079	28.8274	34.4499	109.7776	-74.6818	58.1532	-89.9008
N-methyl	57.6850	78.1390	52.0927	0.1079	28.8274	34.4499	109.7776	-74.6818	58.1532	-89.9008
N-methyl	54.2945	72.6024	48.4016	0.1915	25.4582	34.7293	102.6961	-101.1850	57.8000	-178.5751
N-methyl	54.2945	72.6024	48.4016	0.1915	25.4582	34.7293	102.6961	-101.1850	57.8000	-178.5751
N-methyl	54.2945	72.6024	48.4016	0.1915	25.4582	34.7293	102.6961	101.1850	57.8000	178.5751
N-methyl	54.2945	72.6024	48.4016	0.1915	25.4582	34.7293	102.6961	101.1850	57.8000	178.5751
N-methyl	53.7728	67.7778	45.1852	0.0816	29.3362	33.0242	98.9580	-92.9479	58.2011	-0.9034
N-methyl	53.7728	67.7778	45.1852	0.0816	29.3362	33.0242	98.9580	-92.9479	58.2011	-0.9034

Site	δ iso (ppm)	δ aniso (ppm)	δ reduced aniso (ppm)	δ asymm	δ 1 (ppm)	δ 2 (ppm)	δ 3 (ppm)	alpha	beta	gamma
N-methyl	53.7728	67.7778	45.1852	0.0816	29.3362	33.0242	98.9580	92.9479	58.2011	0.9034
N-methyl	53.7728	67.7778	45.1852	0.0816	29.3362	33.0242	98.9580	92.9479	58.2011	0.9034

C.1.4 ACh Iodide

Site	δ iso (ppm)	δ aniso (ppm)	δ reduced aniso ppm	δ asymm	δ 1 ppm	δ 2 ppm	δ 3 ppm	alpha	beta	gamma
C=O (C^2)	179.9155	-149.0749	-99.3833	0.3155	245.2867	213.9277	80.5322	22.0796	70.0539	137.6275
C=O (C^2)	179.9155	-149.0749	-99.3833	0.3155	245.2867	213.9277	80.5322	22.0796	70.0539	137.6275
C=O (C^2)	179.9155	-149.0749	-99.3833	0.3155	245.2867	213.9277	80.5322	22.0796	70.0539	137.6275
C=O (C^2)	179.9155	-149.0749	-99.3833	0.3155	245.2867	213.9277	80.5322	22.0796	70.0539	137.6275
C=O (C^2)	179.9155	-149.0749	-99.3833	0.3155	245.2867	213.9277	80.5322	157.9204	70.0539	-137.6275
C=O (C^2)	179.9155	-149.0749	-99.3833	0.3155	245.2867	213.9277	80.5322	157.9204	70.0539	-137.6275
C=O (C^2)	179.9155	-149.0749	-99.3833	0.3155	245.2867	213.9277	80.5322	157.9204	70.0539	-137.6275
C=O (C^2)	179.9155	-149.0749	-99.3833	0.3155	245.2867	213.9277	80.5322	157.9204	70.0539	-137.6275
C=O (C^2)	179.9083	-149.0626	-99.3751	0.3159	245.2943	213.8973	80.5332	-94.5611	50.4651	-26.2371
C=O (C^2)	179.9083	-149.0626	-99.3751	0.3159	245.2943	213.8973	80.5332	-94.5611	50.4651	-26.2371
C=O (C^2)	179.9083	-149.0626	-99.3751	0.3159	245.2943	213.8973	80.5332	-94.5611	50.4651	-26.2371
C=O (C^2)	179.9083	-149.0626	-99.3751	0.3159	245.2943	213.8973	80.5332	-94.5611	50.4651	-26.2371
C=O (C^2)	179.9083	-149.0626	-99.3751	0.3159	245.2943	213.8973	80.5332	-85.4389	50.4651	-153.7629
C=O (C^2)	179.9083	-149.0626	-99.3751	0.3159	245.2943	213.8973	80.5332	-85.4389	50.4651	-153.7629
C=O (C^2)	179.9083	-149.0626	-99.3751	0.3159	245.2943	213.8973	80.5332	-85.4389	50.4651	-153.7629
C=O (C^2)	179.9083	-149.0626	-99.3751	0.3159	245.2943	213.8973	80.5332	-85.4389	50.4651	-153.7629
O-CH_2 (C^3)	61.3167	57.9044	38.6030	0.9487	23.7031	60.3274	99.9197	162.3008	92.7094	28.3024
O-CH_2 (C^3)	61.3167	57.9044	38.6030	0.9487	23.7031	60.3274	99.9197	162.3008	92.7094	28.3024
O-CH_2 (C^3)	61.3167	57.9044	38.6030	0.9487	23.7031	60.3274	99.9197	-162.3008	87.2906	28.3024
O-CH_2 (C^3)	61.3167	57.9044	38.6030	0.9487	23.7031	60.3274	99.9197	-162.3008	87.2906	28.3024
O-CH_2 (C^3)	61.3167	57.9044	38.6030	0.9487	23.7031	60.3274	99.9197	-162.3008	92.7094	-28.3024
O-CH_2 (C^3)	61.3167	57.9044	38.6030	0.9487	23.7031	60.3274	99.9197	-162.3008	92.7094	-28.3024
O-CH_2 (C^3)	61.3167	57.9044	38.6030	0.9487	23.7031	60.3274	99.9197	162.3008	87.2906	-28.3024
O-CH_2 (C^3)	61.3167	57.9044	38.6030	0.9487	23.7031	60.3274	99.9197	162.3008	87.2906	-28.3024
O-CH_2 (C^3)	61.3640	57.7849	38.5233	0.9551	23.7057	60.4990	99.8872	109.1583	61.2680	177.0349
O-CH_2 (C^3)	61.3640	57.7849	38.5233	0.9551	23.7057	60.4990	99.8872	109.1583	61.2680	177.0349

Site	δ iso (ppm)	δ aniso (ppm)	δ reduced aniso ppm	δ asymm	δ 1 ppm	δ 2 ppm	δ 3 ppm	alpha	beta	gamma
O-CH₂ (C^3)	61.3640	57.7849	38.5233	0.9551	23.7057	60.4990	99.8872	-109.1583	61.2680	-177.0349
O-CH₂ (C^3)	61.3640	57.7849	38.5233	0.9551	23.7057	60.4990	99.8872	-109.1583	61.2680	-177.0349
O-CH₂ (C^3)	61.3640	57.7849	38.5233	0.9551	23.7057	60.4990	99.8872	-70.8417	61.2680	-2.9651
O-CH₂ (C^3)	61.3640	57.7849	38.5233	0.9551	23.7057	60.4990	99.8872	-70.8417	61.2680	-2.9651
O-CH₂ (C^3)	61.3640	57.7849	38.5233	0.9551	23.7057	60.4990	99.8872	70.8417	61.2680	2.9651
O-CH₂ (C^3)	61.3640	57.7849	38.5233	0.9551	23.7057	60.4990	99.8872	70.8417	61.2680	2.9651
N-CH₂ (C^4)	71.2468	48.7153	32.4769	0.4665	47.4330	62.5836	103.7237	-33.9828	117.3268	127.2450
N-CH₂ (C^4)	71.2468	48.7153	32.4769	0.4665	47.4330	62.5836	103.7237	-146.0172	117.3268	-127.2450
N-CH₂ (C^4)	71.2468	48.7153	32.4769	0.4665	47.4330	62.5836	103.7237	-33.9828	117.3268	127.2450
N-CH₂ (C^4)	71.2468	48.7153	32.4769	0.4665	47.4330	62.5836	103.7237	146.0172	117.3268	-52.7550
N-CH₂ (C^4)	71.2468	48.7153	32.4769	0.4665	47.4330	62.5836	103.7237	33.9828	117.3268	52.7550
N-CH₂ (C^4)	71.2468	48.7153	32.4769	0.4665	47.4330	62.5836	103.7237	-146.0172	117.3268	-127.2450
N-CH₂ (C^4)	71.2468	48.7153	32.4769	0.4665	47.4330	62.5836	103.7237	146.0172	117.3268	-52.7550
N-CH₂ (C^4)	71.2468	48.7153	32.4769	0.4665	47.4330	62.5836	103.7237	33.9828	117.3268	52.7550
N-CH₂ (C^4)	71.3042	48.6471	32.4314	0.4660	47.5327	62.6443	103.7356	87.0546	44.9727	140.0693
N-CH₂ (C^4)	71.3042	48.6471	32.4314	0.4660	47.5327	62.6443	103.7356	-87.0546	44.9727	-140.0693
N-CH₂ (C^4)	71.3042	48.6471	32.4314	0.4660	47.5327	62.6443	103.7356	87.0546	44.9727	140.0693
N-CH₂ (C^4)	71.3042	48.6471	32.4314	0.4660	47.5327	62.6443	103.7356	-92.9454	44.9727	-39.9307
N-CH₂ (C^4)	71.3042	48.6471	32.4314	0.4660	47.5327	62.6443	103.7356	92.9454	44.9727	39.9307
N-CH₂ (C^4)	71.3042	48.6471	32.4314	0.4660	47.5327	62.6443	103.7356	-87.0546	44.9727	-140.0693
N-CH₂ (C^4)	71.3042	48.6471	32.4314	0.4660	47.5327	62.6443	103.7356	-92.9454	44.9727	-39.9307
N-CH₂ (C^4)	71.3042	48.6471	32.4314	0.4660	47.5327	62.6443	103.7356	92.9454	44.9727	39.9307
C-methyl (C^1)	21.8693	45.1115	30.0743	0.2152	3.5960	10.0683	51.9436	-18.9593	119.3722	-5.8530
C-methyl (C^1)	21.8693	45.1115	30.0743	0.2152	3.5960	10.0683	51.9436	161.0407	119.3722	174.1470
C-methyl (C^1)	21.8693	45.1115	30.0743	0.2152	3.5960	10.0683	51.9436	-18.9593	119.3722	-5.8530
C-methyl (C^1)	21.8693	45.1115	30.0743	0.2152	3.5960	10.0683	51.9436	161.0407	119.3722	174.1470
C-methyl (C^1)	21.8693	45.1115	30.0743	0.2152	3.5960	10.0683	51.9436	-161.0407	119.3722	5.8530

Site	δ iso (ppm)	δ aniso (ppm)	δ reduced aniso ppm	δ asymm	δ 1 ppm	δ 2 ppm	δ 3 ppm	alpha	beta	gamma
C-methyl (C^1)	21.8693	45.1115	30.0743	0.2152	3.5960	10.0683	51.9436	18.9593	119.3722	-174.1470
C-methyl (C^1)	21.8693	45.1115	30.0743	0.2152	3.5960	10.0683	51.9436	-161.0407	119.3722	5.8530
C-methyl (C^1)	21.8693	45.1115	30.0743	0.2152	3.5960	10.0683	51.9436	18.9593	119.3722	-174.1470
C-methyl (C^1)	21.9108	45.1390	30.0927	0.2170	3.5991	10.1298	52.0034	-73.8274	84.9323	-150.7838
C-methyl (C^1)	21.9108	45.1390	30.0927	0.2170	3.5991	10.1298	52.0034	106.1726	84.9323	29.2162
C-methyl (C^1)	21.9108	45.1390	30.0927	0.2170	3.5991	10.1298	52.0034	-73.8274	84.9323	-150.7838
C-methyl (C^1)	21.9108	45.1390	30.0927	0.2170	3.5991	10.1298	52.0034	106.1726	84.9323	29.2162
C-methyl (C^1)	21.9108	45.1390	30.0927	0.2170	3.5991	10.1298	52.0034	73.8274	84.9323	150.7838
C-methyl (C^1)	21.9108	45.1390	30.0927	0.2170	3.5991	10.1298	52.0034	-106.1726	84.9323	-29.2162
C-methyl (C^1)	21.9108	45.1390	30.0927	0.2170	3.5991	10.1298	52.0034	73.8274	84.9323	150.7838
C-methyl (C^1)	21.9108	45.1390	30.0927	0.2170	3.5991	10.1298	52.0034	-106.1726	84.9323	-29.2162
N-methyl	53.5113	-149.0626	-99.3751	0.3159	245.2943	213.8973	80.5332	-94.5611	50.4651	-26.2371
N-methyl	53.5113	-149.0626	-99.3751	0.3159	245.2943	213.8973	80.5332	85.4389	50.4651	153.7629
N-methyl	53.5113	-149.0626	-99.3751	0.3159	245.2943	213.8973	80.5332	94.5611	50.4651	26.2371
N-methyl	53.5113	-149.0626	-99.3751	0.3159	245.2943	213.8973	80.5332	-94.5611	50.4651	-26.2371
N-methyl	53.5113	73.8862	49.2574	0.1616	26.9931	34.9536	104.8595	138.5848	132.4543	-47.1886
N-methyl	53.5113	73.8862	49.2574	0.1616	26.9931	34.9536	104.8595	138.5848	132.4543	-47.1886
N-methyl	53.5113	73.8862	49.2574	0.1616	26.9931	34.9536	104.8595	-41.4152	132.4543	132.8114
N-methyl	53.5113	73.8862	49.2574	0.1616	26.9931	34.9536	104.8595	-41.4152	132.4543	132.8114
N-methyl	53.4280	78.3851	52.2567	0.1490	28.0024	35.7864	110.2795	-74.3040	65.0189	-43.2276
N-methyl	53.4280	78.3851	52.2567	0.1490	28.0024	35.7864	110.2795	105.6960	65.0189	136.7724
N-methyl	53.4280	45.1390	30.0927	0.2170	3.5991	10.1298	52.0034	-73.8274	84.9323	-150.7838
N-methyl	53.4280	45.1390	30.0927	0.2170	3.5991	10.1298	52.0034	106.1726	84.9323	29.2162
N-methyl	53.4280	73.8862	49.2574	0.1616	26.9931	34.9536	104.8595	-138.5848	132.4543	-132.8114
N-methyl	53.4280	73.8862	49.2574	0.1616	26.9931	34.9536	104.8595	41.4152	132.4543	47.1886
N-methyl	53.4280	74.0325	49.3550	0.1636	26.9117	34.9839	104.9803	-83.9897	57.7531	-126.7355
N-methyl	53.4280	74.0325	49.3550	0.1636	26.9117	34.9839	104.9803	96.0103	57.7531	53.2645

Site	δ iso (ppm)	δ aniso (ppm)	δ reduced aniso ppm	δ asymm	δ 1 ppm	δ 2 ppm	δ 3 ppm	alpha	beta	gamma
N-methyl	55.6021	78.9196	52.6131	0.1503	27.7665	35.6767	110.6413	6.4823	128.3218	-147.6542
N-methyl	55.6021	78.9196	52.6131	0.1503	27.7665	35.6767	110.6413	-173.5177	128.3218	32.3458
N-methyl	55.6021	45.1115	30.0743	0.2152	3.5960	10.0683	51.9436	-18.9593	119.3722	-5.8530
N-methyl	55.6021	45.1115	30.0743	0.2152	3.5960	10.0683	51.9436	161.0407	119.3722	174.1470
N-methyl	55.6021	67.8297	45.2198	0.0954	28.7433	33.0596	98.7312	38.5775	124.5942	40.1912
N-methyl	55.6021	67.8297	45.2198	0.0954	28.7433	33.0596	98.7312	38.5775	124.5942	40.1912
N-methyl	55.6021	74.0325	49.3550	0.1636	26.9117	34.9839	104.9803	-83.9897	57.7531	-126.7355
N-methyl	55.6021	74.0325	49.3550	0.1636	26.9117	34.9839	104.9803	96.0103	57.7531	53.2645
N-methyl	55.6253	74.0325	49.3550	0.1636	26.9117	34.9839	104.9803	-83.9897	57.7531	-126.7355
N-methyl	55.6253	74.0325	49.3550	0.1636	26.9117	34.9839	104.9803	-83.9897	57.7531	-126.7355
N-methyl	55.6253	74.0325	49.3550	0.1636	26.9117	34.9839	104.9803	96.0103	57.7531	53.2645
N-methyl	55.6253	74.0325	49.3550	0.1636	26.9117	34.9839	104.9803	96.0103	57.7531	53.2645
N-methyl	55.6253	74.0325	49.3550	0.1636	26.9117	34.9839	104.9803	-96.0103	57.7531	-53.2645
N-methyl	55.6253	74.0325	49.3550	0.1636	26.9117	34.9839	104.9803	-96.0103	57.7531	-53.2645
N-methyl	55.6253	74.0325	49.3550	0.1636	26.9117	34.9839	104.9803	83.9897	57.7531	126.7355
N-methyl	55.6253	74.0325	49.3550	0.1636	26.9117	34.9839	104.9803	83.9897	57.7531	126.7355
N-methyl	58.0227	78.3851	52.2567	0.1490	28.0024	35.7864	110.2795	74.3040	65.0189	43.2276
N-methyl	58.0227	78.3851	52.2567	0.1490	28.0024	35.7864	110.2795	74.3040	65.0189	43.2276
N-methyl	58.0227	78.3851	52.2567	0.1490	28.0024	35.7864	110.2795	-105.6960	65.0189	-136.7724
N-methyl	58.0227	78.3851	52.2567	0.1490	28.0024	35.7864	110.2795	-105.6960	65.0189	-136.7724
N-methyl	58.0227	78.3851	52.2567	0.1490	28.0024	35.7864	110.2795	-74.3040	65.0189	-43.2276
N-methyl	58.0227	78.3851	52.2567	0.1490	28.0024	35.7864	110.2795	-74.3040	65.0189	-43.2276
N-methyl	58.0227	78.3851	52.2567	0.1490	28.0024	35.7864	110.2795	105.6960	65.0189	136.7724
N-methyl	58.0227	78.3851	52.2567	0.1490	28.0024	35.7864	110.2795	105.6960	65.0189	136.7724
N-methyl	58.0282	78.9196	52.6131	0.1503	27.7665	35.6767	110.6413	6.4823	128.3218	-147.6542
N-methyl	58.0282	78.9196	52.6131	0.1503	27.7665	35.6767	110.6413	6.4823	128.3218	-147.6542
N-methyl	58.0282	78.9196	52.6131	0.1503	27.7665	35.6767	110.6413	-173.5177	128.3218	32.3458

Site	δ iso (ppm)	δ aniso (ppm)	δ reduced aniso ppm	δ asymm	δ 1 ppm	δ 2 ppm	δ 3 ppm	alpha	beta	gamma
N-methyl	58.0282	78.9196	52.6131	0.1503	27.7665	35.6767	110.6413	-173.5177	128.3218	32.3458
N-methyl	58.0282	78.9196	52.6131	0.1503	27.7665	35.6767	110.6413	173.5177	128.3218	147.6542
N-methyl	58.0282	78.9196	52.6131	0.1503	27.7665	35.6767	110.6413	173.5177	128.3218	147.6542
N-methyl	58.0282	78.9196	52.6131	0.1503	27.7665	35.6767	110.6413	-6.4823	128.3218	-32.3458
N-methyl	58.0282	78.9196	52.6131	0.1503	27.7665	35.6767	110.6413	-6.4823	128.3218	-32.3458

Appendix D Lipid Data

D.1 ^{14}N spectra

D.1.1 14N POPC Spectra

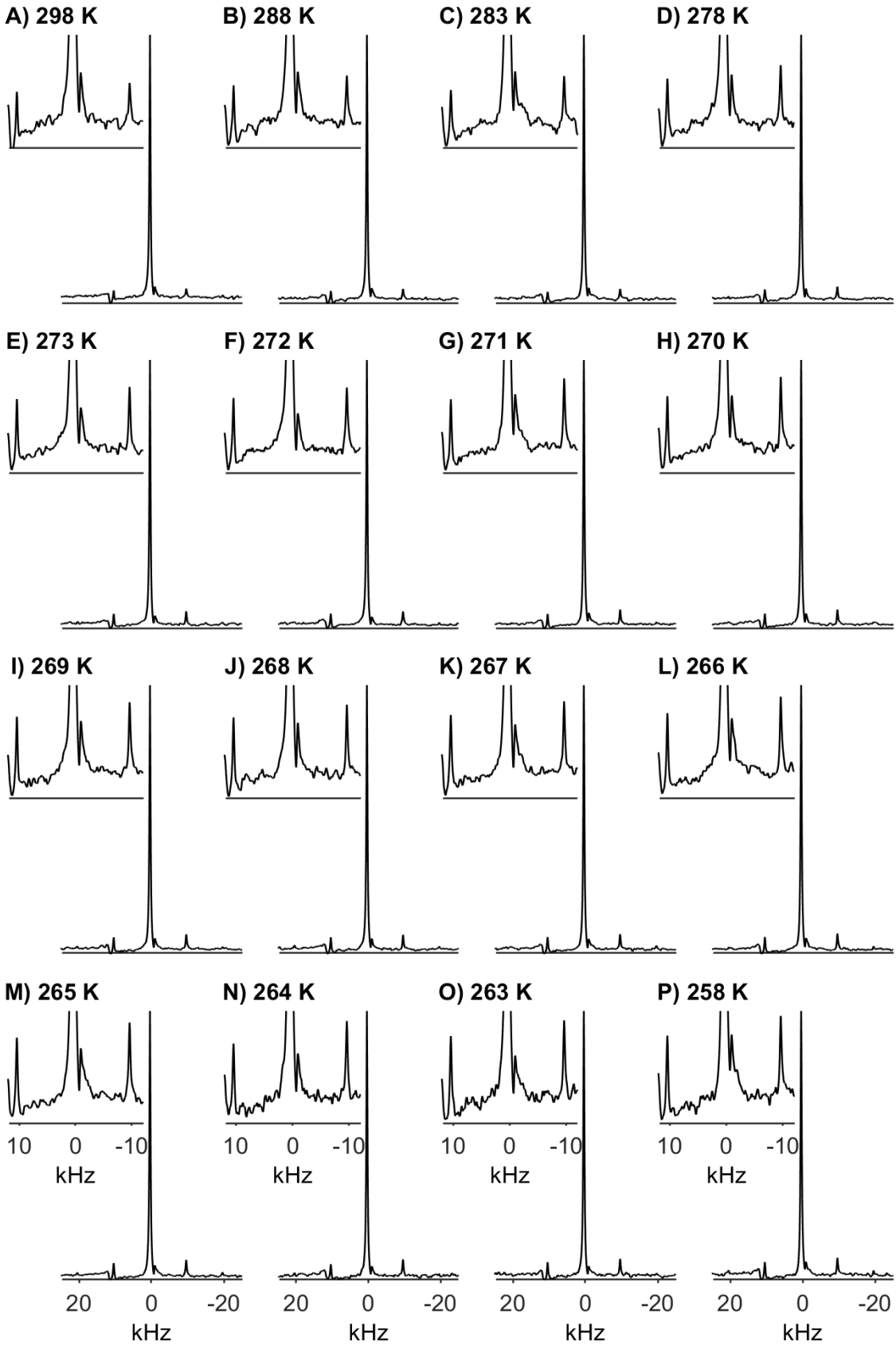

Figure 6.5: ^{14}N spectra of pure POPC at temperatures indicated, with corresponding subplots showing the sidebands magnified. Spectra acquired at 10 kHz spinning speed.

D.1.2 14N POPC:Fk-1 (100:1) superimposed over pure POPC

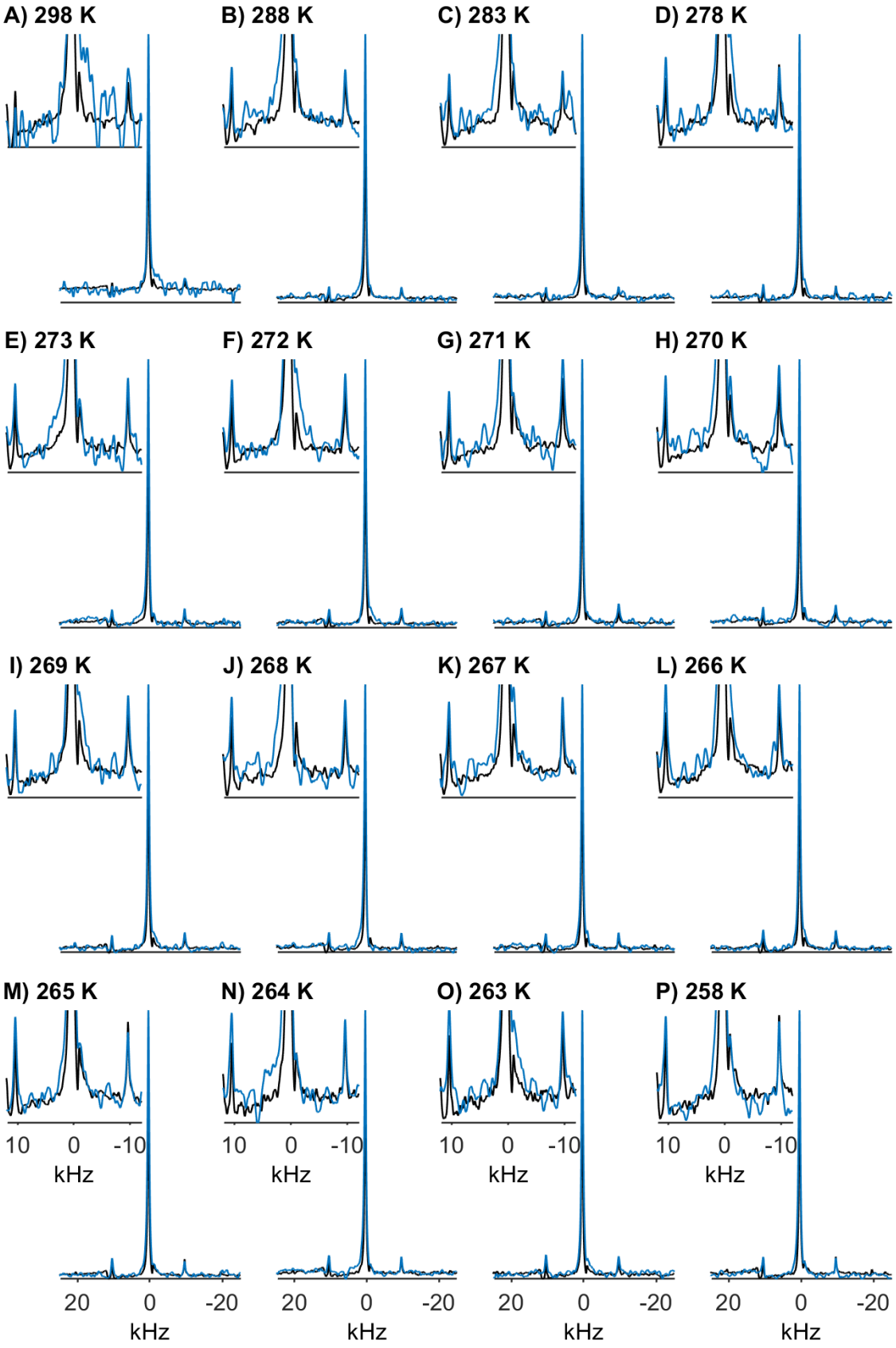

Figure 6.6: ^{14}N spectra of pure POPC (black) and POPC:Fk-1 mixture, 100:1 (blue) superimposed on at temperatures indicated, with corresponding subplots showing the sidebands magnified. Spectra acquired at 10 kHz spinning speed.

D.1.3 14N POPC:Fk-1 (200:1) superimposed over pure POPC

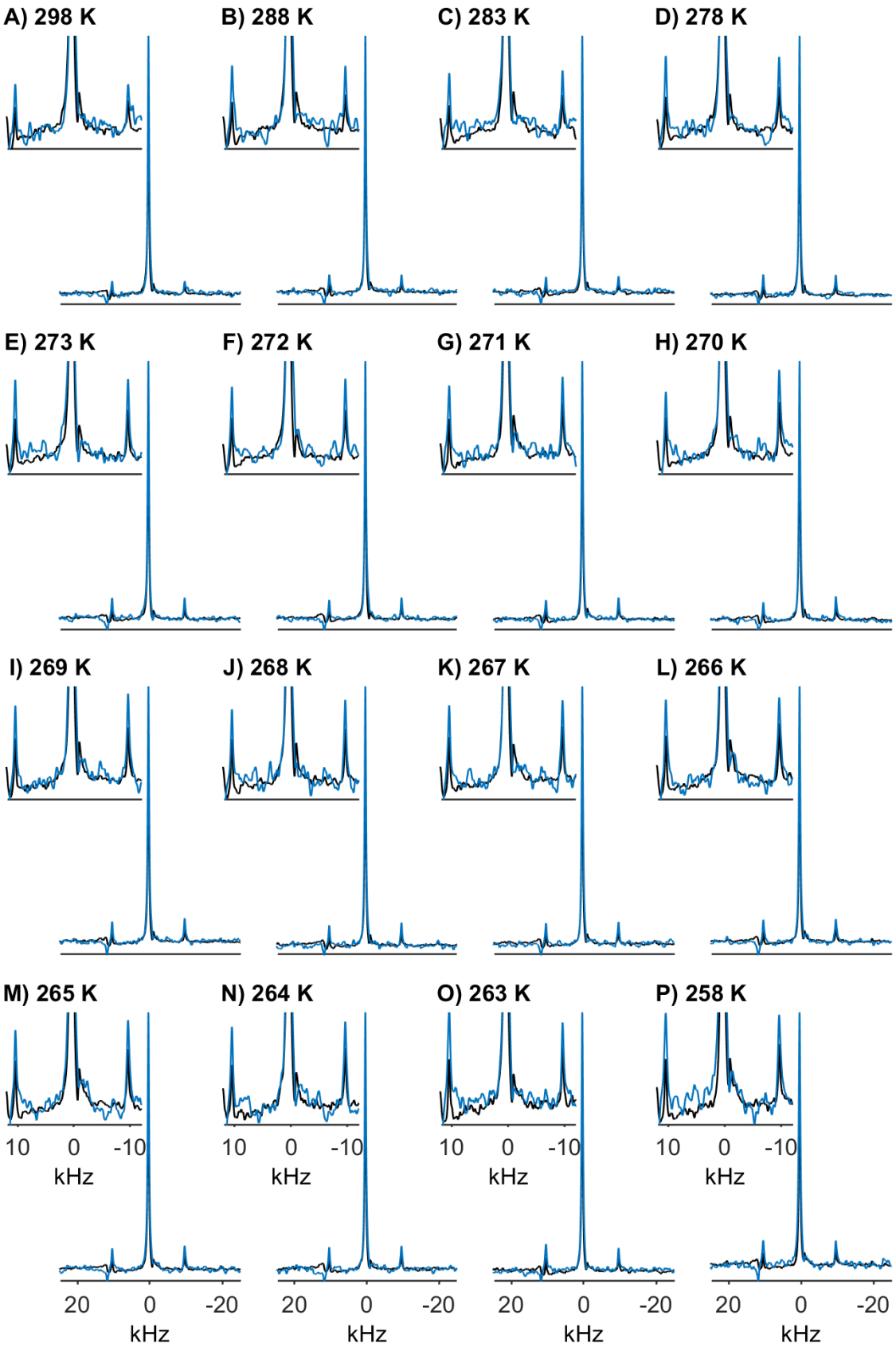

Figure 6.7: ^{14}N spectra of pure POPC (black) and POPC:Fk-1 mixture, 200:1 (blue) superimposed on at temperatures indicated, with corresponding subplots showing the sidebands magnified. Spectra acquired at 10 kHz spinning speed.

D.1.4 14N POPC:Fk-1 (400:1) superimposed over pure POPC

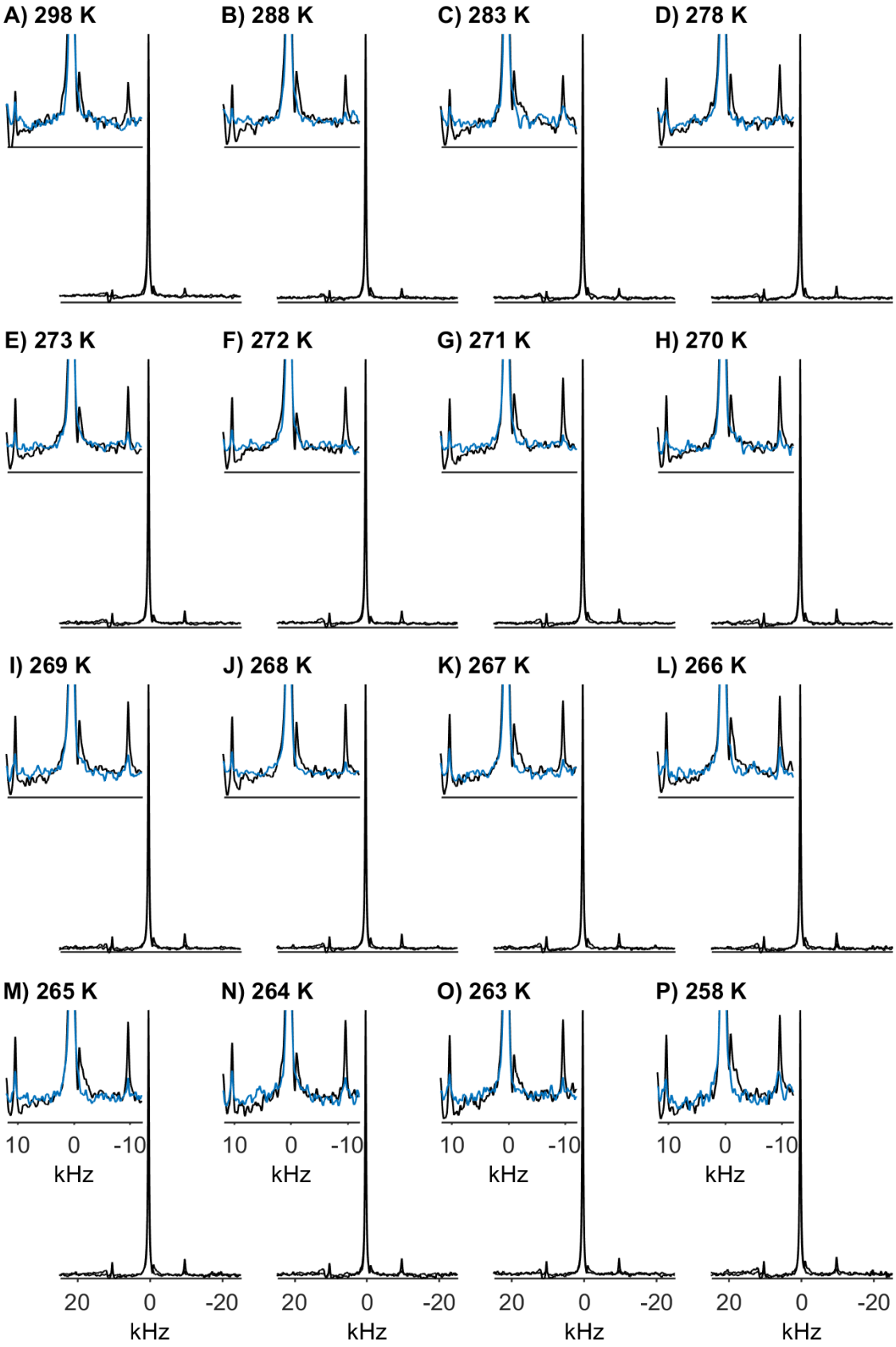

Figure 6.8: ^{14}N spectra of pure POPC (black) and POPC:Fk-1 mixture, 400:1 (blue) superimposed on at temperatures indicated, with corresponding subplots showing the sidebands magnified. Spectra acquired at 10 kHz spinning speed.

D.2 ^{2}H POPC Spectra

D.2.1 ^{2}H Spectra of pure POPC

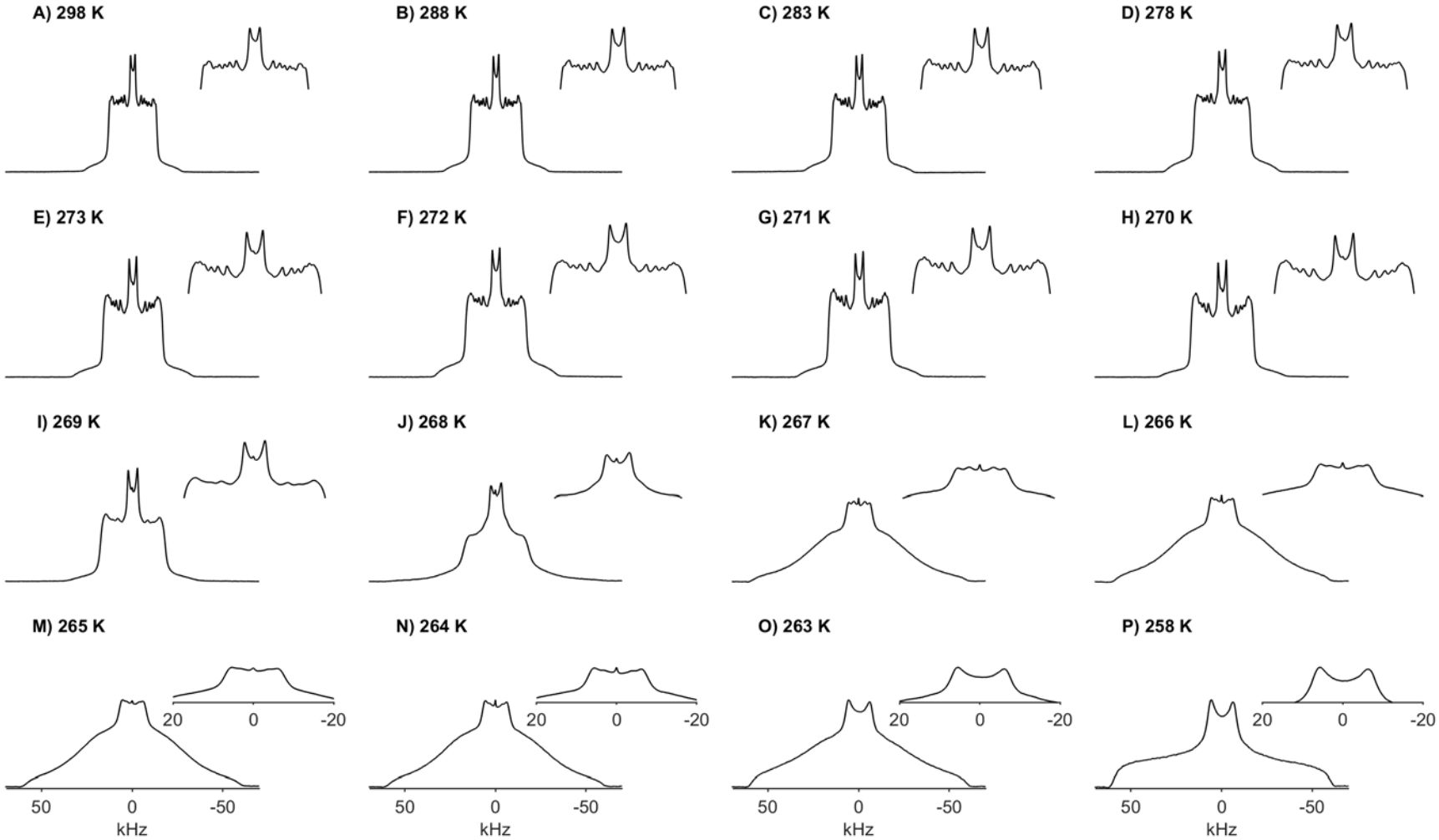

Figure 6.9: ^{2}H spectra of POPC, measured at temperatures indicated. Spectra acquired at 10 kHz spinning speed

D.2.2 ^{2}H Spectra of POPC:Fk-1 (100:1) superimposed over pure POPC

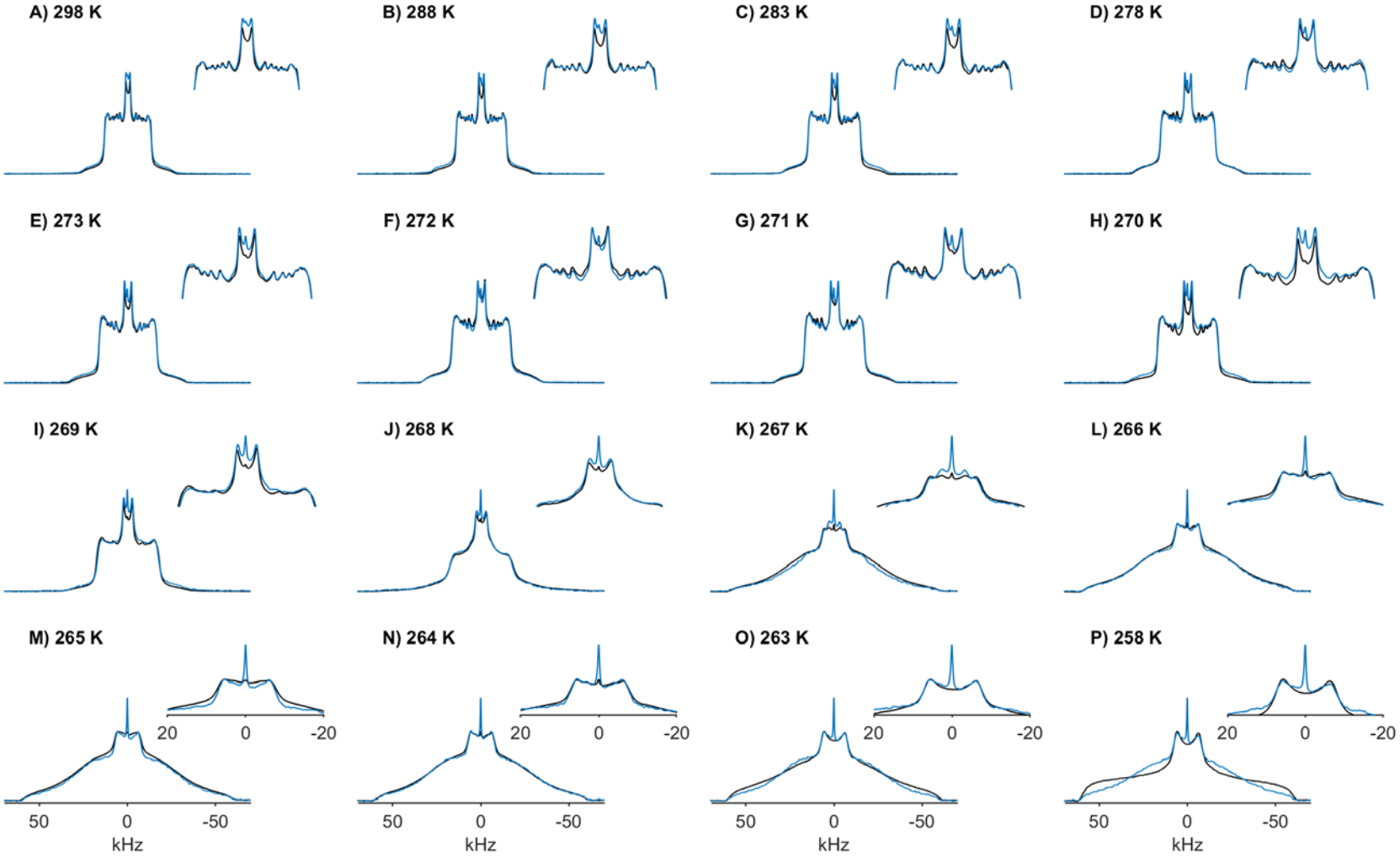

Figure 6.10: ^{2}H spectra of pure POPC (black) and POPC:Fk-1 mixture, 100:1 (blue) superimposed, measured at temperatures indicated. Spectra acquired at 10 kHz spinning speed

D.2.3 ^{2}H Spectra of POPC:Fk-1 (200:1) superimposed over pure POPC

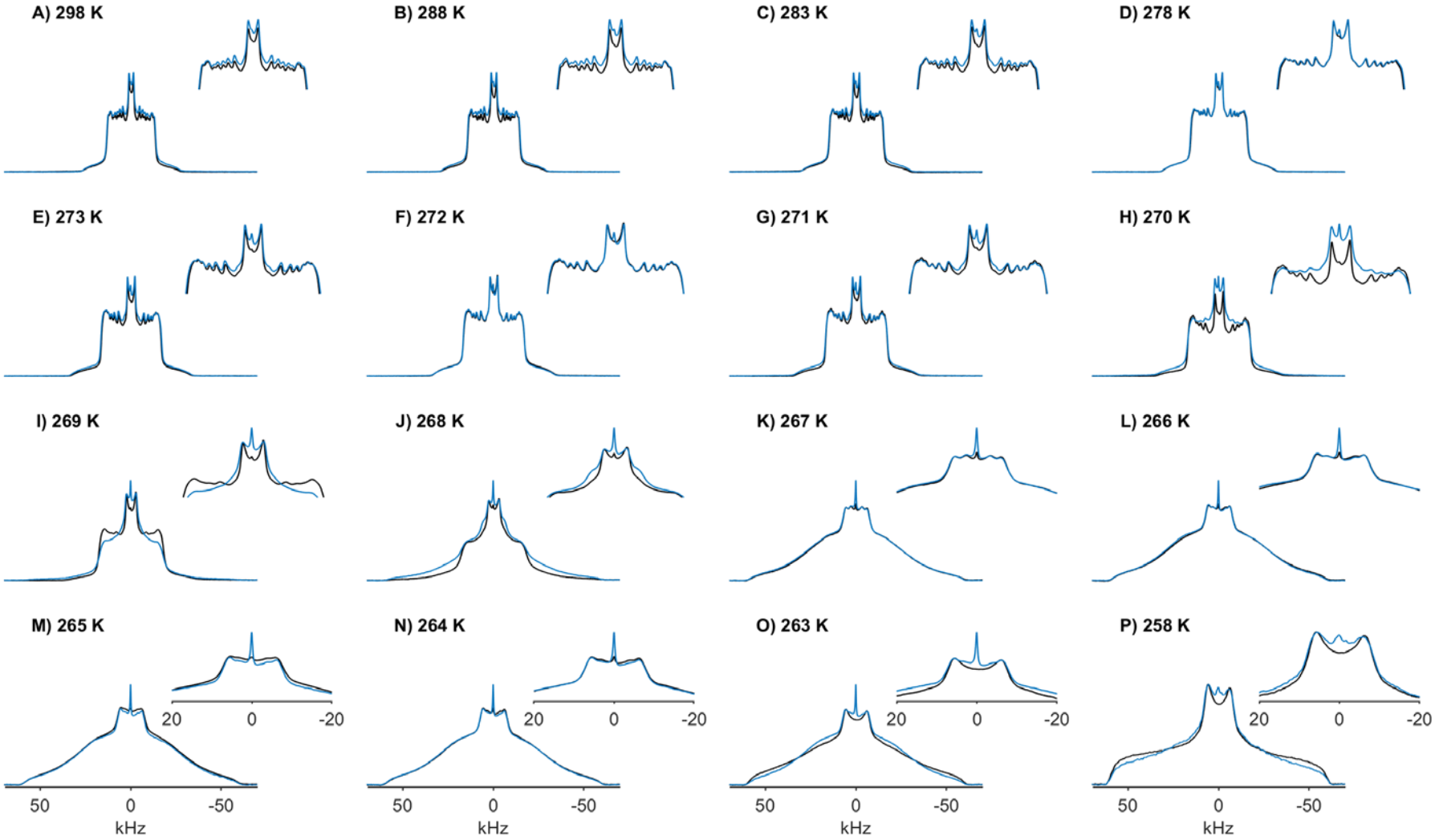

Figure 6.11: ^{2}H spectra of pure POPC (black) and POPC:Fk-1 mixture, 200:1 (blue) superimposed, measured at temperatures indicated. Spectra acquired at 10 kHz spinning speed.

D.2.4 ^{2}H Spectra of POPC:Fk-1 (400:1) superimposed over pure POPC

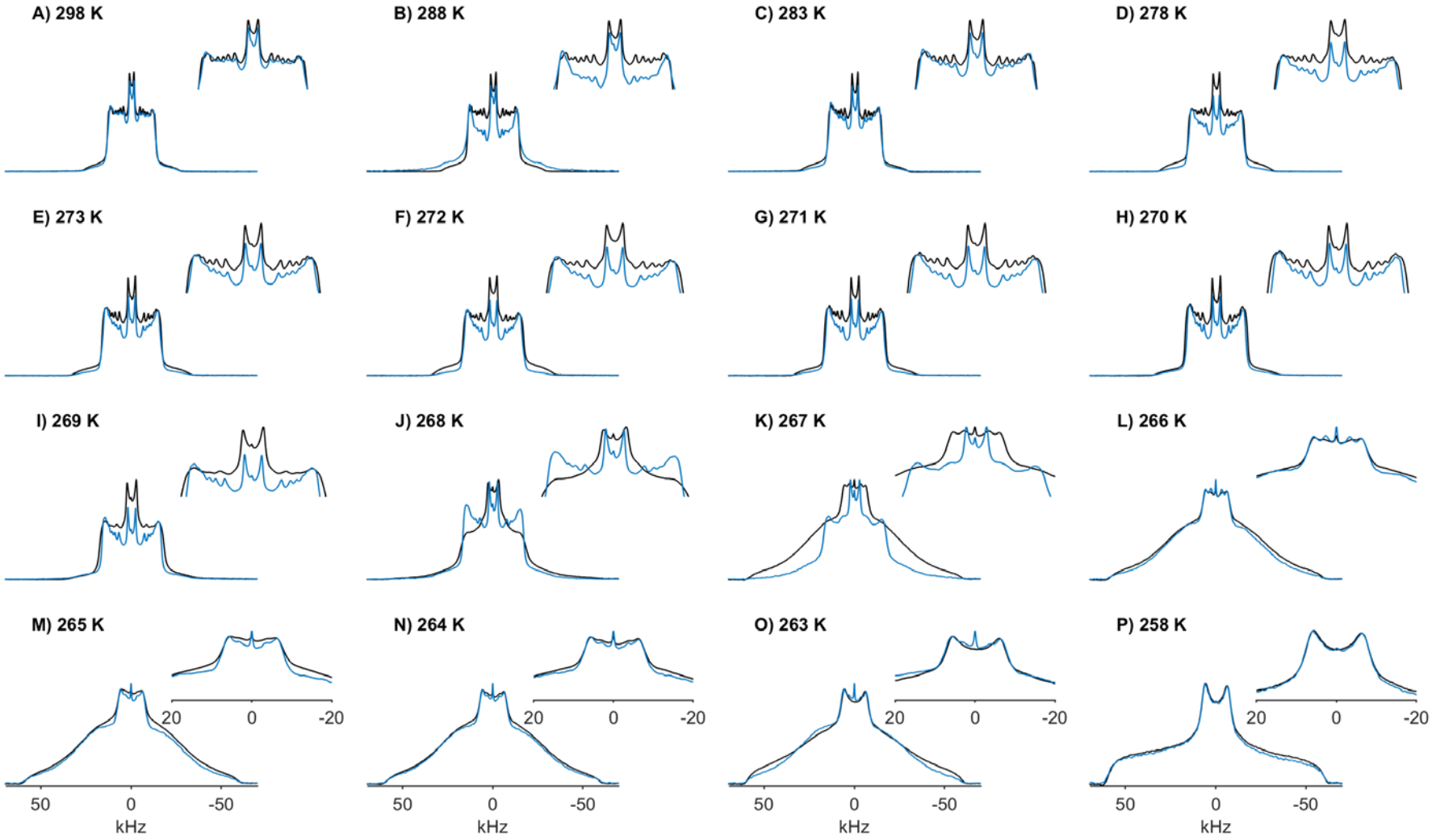

Figure 6.12: ^{2}H spectra of pure POPC (black) and POPC:Fk-1 mixture, 400:1 (blue) superimposed, measured at temperatures indicated. Spectra acquired at 10 kHz spinning speed.

Appendix E Scripts and Code

Comments in green. All parameters defined in detail at http://spindynamics.org/wiki

E.1 Chemical Exchange code – ACh chloride

```
% Chemical exchange in solid state under MAS.
% Calculation time: seconds

% Set chemical exchange rate
rates=[0:0.5:20]
rates=exp(1.0*rates);

% Cycle through exchange rates
for i=1:numel(rates)
    [spin_system(i),
params(i),fid(i,:),spectrum(i,:)]=mas_exchange_ex1000_Cl_real_methyl(rates(i));
end

% Plot
figure()
plot(real(spectrum)')

% Save results
save achcl_results_neweulers.mat spin_system params fid spectrum rates

function[spin_system,parameters,fid,spectrum]=mas_exchange_ex1500_ClO4(exrate)
% Clear up windows
 close all;

% Magnetic field
sys.magnet=14.1;

% Isotopes
sys.isotopes={'13C','13C','13C','13C','13C','13C','13C'};

% Chemical shift tensors - for ACh chloride
% CSA tensors and Euler Angles obtained from CASTEP simulations
inter.zeeman.eigs54=([169.6805 97.5448 94.5834])*-1+175; % C73 N(CH3)
inter.zeeman.euler54=[45.3761578500000 39.8320394600000 78.7854239800000];

inter.zeeman.eigs{2}=([170.5859 97.6358 90.9511])*-1+175; % C89 N(CH3)
inter.zeeman.euler{2}=[-60.7306806500000 32.9231874300000 -84.3451801300000]; %

inter.zeeman.eigs54=([168.6910 107.8559 96.8105])*-1+175; % C69 N(CH3)
inter.zeeman.euler54=[110.172791320000 90.8426355900000 -145.681181250000];
%
inter.zeeman.eigs54=([148.4483 98.0328 82.8898])*-1+175; % C77 N-CH2
inter.zeeman.euler54=[116.117263880000 96.2488924500000 -37.2066942200000];
%
inter.zeeman.eigs{5}=([151.1405 95.4536 86.3569])*-1+175; % C81 OCH2
inter.zeeman.euler{5}=[3.19184859000000 151.270465970000 -137.532676120000];
%
inter.zeeman.eigs54=([-99.8706 58.8040 23.7452])*-1+175; % C65 C=O
inter.zeeman.euler54=[152.927933660000 158.569061730000 131.083814030000];
%
inter.zeeman.eigs54=([183.2312 144.4603 135.5989])*-1+175; % C85 C-CH3
inter.zeeman.euler54=[-143.764513970000 151.156785300000 -149.139346760000];

% Coordinates
inter.coordinates={[4.65679547885184,3.25487804001466,9.16388657933209]; % C73
                   [4.85269686110033,3.36741619717784,11.5947086858989]; % C89
                   [6.09346829598174,4.95103775102687,10.2178151707387]; % C69
                   [3.61313900812535,5.12397618887989,10.4700808273065]; % C77
                   [3.43910838226487,6.17924927166370,9.40483825054286]; % C81
                   [2.76605022269565,6.46736413027410,7.15202169451109]; % C65
                   [2.13452340072535,5.80681070241468,5.96546510347895]}; % C85

% Chemical subsystems
inter.chem.parts={[1]
```

```
,...  % Site 1
                  [2],...  % Site 2
                  [3],...
                  [4],...
                  [5],...
                  [6],...
                  [7]};    % Site 3

% Chemical kinetics
% Reaction rate matrix for N-methyl carbons (3 site exchange)
inter.chem.rates=[-exrate  0.0  exrate 0.0 0.0 0.0 0.0; ...
                   exrate -exrate  0.0 0.0 0.0 0.0 0.0; ...
                   0.0  exrate -exrate 0.0 0.0 0.0 0.0; ...
                   0.0 0.0 0.0 0.0 0.0 0.0 0.0; ...
                   0.0 0.0 0.0 0.0 0.0 0.0 0.0; ...
                   0.0 0.0 0.0 0.0 0.0 0.0 0.0; ...
                   0.0 0.0 0.0 0.0 0.0 0.0 0.0]; ...

% Equilibrium concentrations
inter.chem.concs=equilibrate(inter.chem.rates,[1 1 1 1 1 1 1]',100)';

% Basis set
bas.formalism='sphten-liouv';
bas.approximation='none';

% SPINACH housekeeping
spin_system=create(sys,inter);
spin_system=basis(spin_system,bas);

% Experiment setup
parameters.rate=10000; % Spin rate Hz
parameters.axis=[1 1 1]; % MAS axis
parameters.max_rank=7;
parameters.grid='rep_2ang_12800pts_oct'; % number of pts
parameters.sweep=50000; % sweep width
parameters.offset=25000;
parameters.npoints=4096;
parameters.zerofill=16384; % zerofill
parameters.spins={'13C'}; % isotope
parameters.rho0=state(spin_system,'L+','13C','cheap');
parameters.coil=state(spin_system,'L+','13C','cheap');
parameters.verbose=0;

% Simulation
fid=singlerot(spin_system,@acquire,parameters,'nmr');

% Apodization
fid=apodization(fid,'exp-1d',10);

% Plotting
figure();
subplot(2,1,1); title('Free induction decay'); xlabel('time / seconds');
plot(linspace(0,parameters.npoints/parameters.sweep,parameters.npoints),real(fid)
);

% Fourier transform
spectrum=fftshift(fft(fid,parameters.zerofill));

% Plot Figure
subplot(2,1,2); title('Spectrum');
plot_1d(spin_system,real(spectrum),parameters);
xlim ([0 200]);

end
```

E.2 Unit Cell Files

E.2.1 ACh Perchlorate

```
%BLOCK LATTICE_CART
ang    # angstrom units
  11.987900000000000   0.000000000000000   0.000000000000000
   0.000000000000000   9.641800000000000   0.000000000000000
   0.000000000000000   0.000000000000000  19.312899999999999
%ENDBLOCK LATTICE_CART


%BLOCK POSITIONS_FRAC
Cl   0.471830000000000   0.729060000000000   0.639380000000000
Cl   0.028170000000000   0.270940000000000   0.139380000000000
Cl   0.528170000000000   0.270940000000000   0.360620000000000
Cl   0.028170000000000   0.229060000000000   0.639380000000000
Cl   0.471830000000000   0.770940000000000   0.139380000000000
Cl   0.971830000000000   0.729060000000000   0.860620000000000
Cl   0.971830000000000   0.770940000000000   0.360620000000000
Cl   0.528170000000000   0.229060000000000   0.860620000000000
Cl   0.456700000000000   0.731400000000000   0.647300000000000
Cl   0.043300000000000   0.268600000000000   0.147300000000000
Cl   0.543300000000000   0.268600000000000   0.352700000000000
Cl   0.043300000000000   0.231400000000000   0.647300000000000
Cl   0.456700000000000   0.768600000000000   0.147300000000000
Cl   0.956700000000000   0.731400000000000   0.852700000000000
Cl   0.956700000000000   0.768600000000000   0.352700000000000
Cl   0.543300000000000   0.231400000000000   0.852700000000000
O    0.648300000000000   0.366390000000000   0.634090000000000
O    0.851700000000000   0.633610000000000   0.134090000000000
O    0.351700000000000   0.633610000000000   0.365910000000000
O    0.851700000000000   0.866390000000000   0.634090000000000
O    0.648300000000000   0.133610000000000   0.134090000000000
O    0.148300000000000   0.366390000000000   0.866025403784439
O    0.148300000000000   0.133610000000000   0.365910000000000
O    0.351700000000000   0.866390000000000   0.866025403784439
O    0.746620000000000   0.533200000000000   0.581690000000000
O    0.753380000000000   0.466800000000000   0.081690000000000
O    0.253380000000000   0.466800000000000   0.418310000000000
O    0.753380000000000   0.033200000000000   0.581690000000000
O    0.746620000000000   0.966800000000000   0.081690000000000
O    0.246620000000000   0.533200000000000   0.918310000000000
O    0.246620000000000   0.966800000000000   0.418310000000000
O    0.253380000000000   0.033200000000000   0.918310000000000
O    0.542800000000000   0.833333333333333   0.610900000000000
O    0.957200000000000   0.166666666666667   0.110900000000000
O    0.457200000000000   0.166666666666667   0.389100000000000
O    0.957200000000000   0.333333333333333   0.610900000000000
O    0.542800000000000   0.666666666666667   0.110900000000000
O    0.042800000000000   0.833333333333333   0.889100000000000
O    0.042800000000000   0.666666666666667   0.389100000000000
O    0.457200000000000   0.333333333333333   0.889100000000000
O    0.527600000000000   0.644900000000000   0.688390000000000
O    0.972400000000000   0.355100000000000   0.188390000000000
O    0.472400000000000   0.355100000000000   0.311610000000000
O    0.972400000000000   0.144900000000000   0.688390000000000
```

```
O    0.527600000000000   0.855100000000000   0.188390000000000
O    0.027600000000000   0.644900000000000   0.811610000000000
O    0.027600000000000   0.855100000000000   0.311610000000000
O    0.472400000000000   0.144900000000000   0.811610000000000
O    0.434400000000000   0.641500000000000   0.583940000000000
O    0.065600000000000   0.358500000000000   0.083940000000000
O    0.565600000000000   0.358500000000000   0.416060000000000
O    0.065600000000000   0.141500000000000   0.583940000000000
O    0.434400000000000   0.858500000000000   0.083940000000000
O    0.934400000000000   0.641500000000000   0.916060000000000
O    0.934400000000000   0.858500000000000   0.416060000000000
O    0.565600000000000   0.141500000000000   0.916060000000000
O    0.374700000000000   0.791800000000000   0.670900000000000
O    0.125300000000000   0.208200000000000   0.170900000000000
O    0.625300000000000   0.208200000000000   0.329100000000000
O    0.125300000000000   0.291800000000000   0.670900000000000
O    0.374700000000000   0.708200000000000   0.170900000000000
O    0.874700000000000   0.791800000000000   0.829100000000000
O    0.874700000000000   0.708200000000000   0.329100000000000
O    0.625300000000000   0.291800000000000   0.829100000000000
O    0.406400000000000   0.724000000000000   0.583700000000000
O    0.093600000000000   0.276000000000000   0.083700000000000
O    0.593600000000000   0.276000000000000   0.416300000000000
O    0.093600000000000   0.224000000000000   0.583700000000000
O    0.406400000000000   0.776000000000000   0.083700000000000
O    0.906400000000000   0.724000000000000   0.916300000000000
O    0.906400000000000   0.776000000000000   0.416300000000000
O    0.593600000000000   0.224000000000000   0.916300000000000
O    0.545000000000000   0.822000000000000   0.649100000000000
O    0.955000000000000   0.178000000000000   0.149100000000000
O    0.455000000000000   0.178000000000000   0.350900000000000
O    0.955000000000000   0.322000000000000   0.649100000000000
O    0.545000000000000   0.678000000000000   0.149100000000000
O    0.045000000000000   0.822000000000000   0.850900000000000
O    0.045000000000000   0.678000000000000   0.350900000000000
O    0.455000000000000   0.322000000000000   0.850900000000000
O    0.494000000000000   0.605000000000000   0.669800000000000
O    0.006000000000000   0.395000000000000   0.169800000000000
O    0.506000000000000   0.395000000000000   0.330200000000000
O    0.006000000000000   0.105000000000000   0.669800000000000
O    0.494000000000000   0.895000000000000   0.169800000000000
O    0.994000000000000   0.605000000000000   0.830200000000000
O    0.994000000000000   0.895000000000000   0.330200000000000
O    0.506000000000000   0.105000000000000   0.830200000000000
O    0.373000000000000   0.775000000000000   0.691300000000000
O    0.127000000000000   0.225000000000000   0.191300000000000
O    0.627000000000000   0.225000000000000   0.308700000000000
O    0.127000000000000   0.275000000000000   0.691300000000000
O    0.373000000000000   0.725000000000000   0.191300000000000
O    0.873000000000000   0.775000000000000   0.808700000000000
O    0.873000000000000   0.725000000000000   0.308700000000000
O    0.627000000000000   0.275000000000000   0.808700000000000
N    0.414690000000000   0.230200000000000   0.594860000000000
N    0.085310000000000   0.769800000000000   0.094860000000000
N    0.585310000000000   0.769800000000000   0.405140000000000
N    0.085310000000000   0.730200000000000   0.594860000000000
N    0.414690000000000   0.269800000000000   0.094860000000000
N    0.914690000000000   0.230200000000000   0.905140000000000
N    0.914690000000000   0.269800000000000   0.405140000000000
```

N	0.585310000000000	0.730200000000000	0.905140000000000
C	0.720320000000000	0.474400000000000	0.633770000000000
C	0.779680000000000	0.525600000000000	0.133770000000000
C	0.279680000000000	0.525600000000000	0.366230000000000
C	0.779680000000000	0.974400000000000	0.633770000000000
C	0.720320000000000	0.025600000000000	0.133770000000000
C	0.220320000000000	0.474400000000000	0.866230000000000
C	0.220320000000000	0.025600000000000	0.366230000000000
C	0.279680000000000	0.974400000000000	0.866230000000000
C	0.606700000000000	0.331000000000000	0.566600000000000
C	0.893300000000000	0.669000000000000	0.066600000000000
C	0.393300000000000	0.669000000000000	0.433400000000000
C	0.893300000000000	0.831000000000000	0.566600000000000
C	0.606700000000000	0.169000000000000	0.066600000000000
C	0.106700000000000	0.331000000000000	0.933400000000000
C	0.106700000000000	0.169000000000000	0.433400000000000
C	0.393300000000000	0.831000000000000	0.933400000000000
C	0.532700000000000	0.204700000000000	0.571170000000000
C	0.967300000000000	0.795300000000000	0.071170000000000
C	0.467300000000000	0.795300000000000	0.428830000000000
C	0.967300000000000	0.704700000000000	0.571170000000000
C	0.532700000000000	0.295300000000000	0.071170000000000
C	0.032700000000000	0.204700000000000	0.928830000000000
C	0.032700000000000	0.295300000000000	0.428830000000000
C	0.467300000000000	0.704700000000000	0.928830000000000
C	0.761800000000000	0.506900000000000	0.704710000000000
C	0.738200000000000	0.493100000000000	0.204710000000000
C	0.238200000000000	0.493100000000000	0.295290000000000
C	0.738200000000000	0.006900000000000	0.704710000000000
C	0.761800000000000	0.993100000000000	0.204710000000000
C	0.261800000000000	0.506900000000000	0.795290000000000
C	0.261800000000000	0.993100000000000	0.295290000000000
C	0.238200000000000	0.006900000000000	0.795290000000000
C	0.354700000000000	0.323100000000000	0.545660000000000
C	0.145300000000000	0.676900000000000	0.045660000000000
C	0.645300000000000	0.676900000000000	0.454340000000000
C	0.145300000000000	0.823100000000000	0.545660000000000
C	0.354700000000000	0.176900000000000	0.045660000000000
C	0.854700000000000	0.323100000000000	0.954340000000000
C	0.854700000000000	0.176900000000000	0.454340000000000
C	0.645300000000000	0.823100000000000	0.954340000000000
C	0.410800000000000	0.292000000000000	0.665130000000000
C	0.089200000000000	0.708000000000000	0.165130000000000
C	0.589200000000000	0.708000000000000	0.334870000000000
C	0.089200000000000	0.792000000000000	0.665130000000000
C	0.410800000000000	0.208000000000000	0.165130000000000
C	0.910800000000000	0.292000000000000	0.834870000000000
C	0.910800000000000	0.208000000000000	0.334870000000000
C	0.589200000000000	0.792000000000000	0.834870000000000
C	0.355500000000000	0.094500000000000	0.594200000000000
C	0.144500000000000	0.905500000000000	0.094200000000000
C	0.644500000000000	0.905500000000000	0.405800000000000
C	0.144500000000000	0.594500000000000	0.594200000000000
C	0.355500000000000	0.405500000000000	0.094200000000000
C	0.855500000000000	0.094500000000000	0.905800000000000
C	0.855500000000000	0.405500000000000	0.405800000000000
C	0.644500000000000	0.594500000000000	0.905800000000000
H	0.669959000000000	0.311884000000000	0.535060000000000
H	0.830041000000000	0.688116000000000	0.035060000000000

```
H    0.330041000000000   0.688116000000000   0.464940000000000
H    0.830041000000000   0.811884000000000   0.535060000000000
H    0.669959000000000   0.188116000000000   0.035060000000000
H    0.169959000000000   0.311884000000000   0.964940000000000
H    0.169959000000000   0.188116000000000   0.464940000000000
H    0.330041000000000   0.811884000000000   0.964940000000000
H    0.563760000000000   0.409887000000000   0.547472000000000
H    0.936240000000000   0.590113000000000   0.047472000000000
H    0.436240000000000   0.590113000000000   0.452528000000000
H    0.936240000000000   0.909887000000000   0.547472000000000
H    0.563760000000000   0.090113000000000   0.047472000000000
H    0.063760000000000   0.409887000000000   0.952528000000000
H    0.063760000000000   0.090113000000000   0.452528000000000
H    0.436240000000000   0.909887000000000   0.952528000000000
H    0.529998000000000   0.160410000000000   0.524941000000000
H    0.970002000000000   0.839590000000000   0.024941000000000
H    0.470002000000000   0.839590000000000   0.475059000000000
H    0.970002000000000   0.660410000000000   0.524941000000000
H    0.529998000000000   0.339590000000000   0.024941000000000
H    0.029998000000000   0.160410000000000   0.975059000000000
H    0.029998000000000   0.339590000000000   0.475059000000000
H    0.470002000000000   0.660410000000000   0.975059000000000
H    0.567682000000000   0.137666000000000   0.603369000000000
H    0.932318000000000   0.862334000000000   0.103369000000000
H    0.432318000000000   0.862334000000000   0.396631000000000
H    0.932318000000000   0.637666000000000   0.603369000000000
H    0.567682000000000   0.362334000000000   0.103369000000000
H    0.067682000000000   0.137666000000000   0.896631000000000
H    0.067682000000000   0.362334000000000   0.396631000000000
H    0.432318000000000   0.637666000000000   0.896631000000000
H    0.709645000000000   0.469879000000000   0.739112000000000
H    0.790355000000000   0.530121000000000   0.239112000000000
H    0.290355000000000   0.530121000000000   0.260888000000000
H    0.790355000000000   0.969879000000000   0.739112000000000
H    0.709645000000000   0.030121000000000   0.239112000000000
H    0.209645000000000   0.469879000000000   0.760888000000000
H    0.209645000000000   0.030121000000000   0.260888000000000
H    0.290355000000000   0.969879000000000   0.760888000000000
H    0.767830000000000   0.607635000000000   0.710265000000000
H    0.732170000000000   0.392365000000000   0.210265000000000
H    0.232170000000000   0.392365000000000   0.289735000000000
H    0.732170000000000   0.107635000000000   0.710265000000000
H    0.767830000000000   0.892365000000000   0.210265000000000
H    0.267830000000000   0.607635000000000   0.789735000000000
H    0.267830000000000   0.892365000000000   0.289735000000000
H    0.232170000000000   0.107635000000000   0.789735000000000
H    0.835363000000000   0.464479000000000   0.711372000000000
H    0.664637000000000   0.535521000000000   0.211372000000000
H    0.164637000000000   0.535521000000000   0.288628000000000
H    0.664637000000000   0.964479000000000   0.711372000000000
H    0.835363000000000   0.035521000000000   0.211372000000000
H    0.335363000000000   0.464479000000000   0.788628000000000
H    0.335363000000000   0.035521000000000   0.288628000000000
H    0.164637000000000   0.964479000000000   0.788628000000000
H    0.384481000000000   0.417476000000000   0.549527000000000
H    0.115519000000000   0.582524000000000   0.049527000000000
H    0.615519000000000   0.582524000000000   0.450473000000000
H    0.115519000000000   0.917476000000000   0.549527000000000
H    0.384481000000000   0.082524000000000   0.049527000000000
```

```
H    0.884481000000000   0.417476000000000   0.950473000000000
H    0.884481000000000   0.082524000000000   0.450473000000000
H    0.615519000000000   0.917476000000000   0.950473000000000
H    0.274950000000000   0.323733000000000   0.556858000000000
H    0.225050000000000   0.676267000000000   0.056858000000000
H    0.725050000000000   0.676267000000000   0.443142000000000
H    0.225050000000000   0.823733000000000   0.556858000000000
H    0.274950000000000   0.176267000000000   0.056858000000000
H    0.774950000000000   0.323733000000000   0.943142000000000
H    0.774950000000000   0.176267000000000   0.443142000000000
H    0.725050000000000   0.823733000000000   0.943142000000000
H    0.365173000000000   0.289320000000000   0.498251000000000
H    0.134827000000000   0.710680000000000   0.998251000000000
H    0.634827000000000   0.710680000000000   0.501749000000000
H    0.134827000000000   0.789320000000000   0.498251000000000
H    0.365173000000000   0.210680000000000   0.998251000000000
H    0.865173000000000   0.289320000000000   0.001749000000000
H    0.865173000000000   0.210680000000000   0.501749000000000
H    0.634827000000000   0.789320000000000   0.001749000000000
H    0.447891000000000   0.229882000000000   0.698029000000000
H    0.052109000000000   0.770118000000000   0.198029000000000
H    0.552109000000000   0.770118000000000   0.301971000000000
H    0.052109000000000   0.729882000000000   0.698029000000000
H    0.447891000000000   0.270118000000000   0.198029000000000
H    0.947891000000000   0.229882000000000   0.801971000000000
H    0.947891000000000   0.270118000000000   0.301971000000000
H    0.552109000000000   0.729882000000000   0.801971000000000
H    0.332852000000000   0.305044000000000   0.679072000000000
H    0.167148000000000   0.694956000000000   0.179072000000000
H    0.667148000000000   0.694956000000000   0.320928000000000
H    0.167148000000000   0.805044000000000   0.679072000000000
H    0.332852000000000   0.194956000000000   0.179072000000000
H    0.832852000000000   0.305044000000000   0.820928000000000
H    0.832852000000000   0.194956000000000   0.320928000000000
H    0.667148000000000   0.805044000000000   0.820928000000000
H    0.448911000000000   0.381874000000000   0.664741000000000
H    0.051089000000000   0.618126000000000   0.164741000000000
H    0.551089000000000   0.618126000000000   0.335259000000000
H    0.051089000000000   0.881874000000000   0.664741000000000
H    0.448911000000000   0.118126000000000   0.164741000000000
H    0.948911000000000   0.381874000000000   0.835259000000000
H    0.948911000000000   0.118126000000000   0.335259000000000
H    0.551089000000000   0.881874000000000   0.835259000000000
H    0.355954000000000   0.056515000000000   0.547164000000000
H    0.144046000000000   0.943485000000000   0.047164000000000
H    0.644046000000000   0.943485000000000   0.452836000000000
H    0.144046000000000   0.556515000000000   0.547164000000000
H    0.355954000000000   0.443485000000000   0.047164000000000
H    0.855954000000000   0.056515000000000   0.952836000000000
H    0.855954000000000   0.443485000000000   0.452836000000000
H    0.644046000000000   0.556515000000000   0.952836000000000
H    0.278232000000000   0.107805000000000   0.609479000000000
H    0.221768000000000   0.892195000000000   0.109479000000000
H    0.721768000000000   0.892195000000000   0.390521000000000
H    0.221768000000000   0.607805000000000   0.609479000000000
H    0.278232000000000   0.392195000000000   0.109479000000000
H    0.778232000000000   0.107805000000000   0.890521000000000
H    0.778232000000000   0.392195000000000   0.390521000000000
H    0.721768000000000   0.607805000000000   0.890521000000000
```

```
H     0.393210000000000   0.029912000000000   0.625619000000000
H     0.106790000000000   0.970088000000000   0.125619000000000
H     0.606790000000000   0.970088000000000   0.374381000000000
H     0.106790000000000   0.529912000000000   0.625619000000000
H     0.393210000000000   0.470088000000000   0.125619000000000
H     0.893210000000000   0.029912000000000   0.874381000000000
H     0.893210000000000   0.470088000000000   0.374381000000000
H     0.606790000000000   0.529912000000000   0.874381000000000
%ENDBLOCK POSITIONS_FRAC


# Commented out pseudopotential block for easy editing
#%BLOCK SPECIES_POT
# H   H_00.usp
# C   C_00.usp
# N   N_00.usp
# O   O_00.usp
# Cl  Cl_00.usp
#%ENDBLOCK SPECIES_POT


%BLOCK SYMMETRY_OPS
# Symm. op. 1
   1.000000000000000   0.000000000000000   0.000000000000000
   0.000000000000000   1.000000000000000   0.000000000000000
   0.000000000000000   0.000000000000000   1.000000000000000
   0.000000000000000   0.000000000000000   0.000000000000000
# Symm. op. 2
  -1.000000000000000   0.000000000000000   0.000000000000000
   0.000000000000000  -1.000000000000000   0.000000000000000
   0.000000000000000   0.000000000000000  -1.000000000000000
   0.000000000000000   0.000000000000000   0.000000000000000
# Symm. op. 3
  -1.000000000000000   0.000000000000000   0.000000000000000
   0.000000000000000  -1.000000000000000   0.000000000000000
   0.000000000000000   0.000000000000000   1.000000000000000
   0.500000000000000   0.000000000000000   0.500000000000000
# Symm. op. 4
  -1.000000000000000   0.000000000000000   0.000000000000000
   0.000000000000000   1.000000000000000   0.000000000000000
   0.000000000000000   0.000000000000000   1.000000000000000
   0.500000000000000   0.500000000000000   0.000000000000000
# Symm. op. 5
   1.000000000000000   0.000000000000000   0.000000000000000
   0.000000000000000  -1.000000000000000   0.000000000000000
   0.000000000000000   0.000000000000000   1.000000000000000
   0.000000000000000   0.500000000000000   0.500000000000000
# Symm. op. 6
   1.000000000000000   0.000000000000000   0.000000000000000
   0.000000000000000   1.000000000000000   0.000000000000000
   0.000000000000000   0.000000000000000  -1.000000000000000
   0.500000000000000   0.000000000000000   0.500000000000000
# Symm. op. 7
   1.000000000000000   0.000000000000000   0.000000000000000
   0.000000000000000  -1.000000000000000   0.000000000000000
   0.000000000000000   0.000000000000000  -1.000000000000000
   0.500000000000000   0.500000000000000   0.000000000000000
```

```
# Symm. op. 8
 -1.000000000000000   0.000000000000000   0.000000000000000
  0.000000000000000   1.000000000000000   0.000000000000000
  0.000000000000000   0.000000000000000  -1.000000000000000
  0.000000000000000   0.500000000000000   0.500000000000000
%ENDBLOCK SYMMETRY_OPS
```

E.2.2 ACh Chloride

```
%BLOCK LATTICE_CART
ang    # angstrom units
   6.307800000000000   0.000000000000000   0.000000000000000
   0.000000000000000   9.901899999999999   0.000000000000000
   0.000000000000000   0.000000000000000  15.317100000000002
%ENDBLOCK LATTICE_CART

%BLOCK POSITIONS_FRAC
Cl   0.763320000000000   0.653540000000000   0.834900000000000
Cl   0.263320000000000   0.846460000000000   0.165100000000000
Cl   0.736680000000000   0.346460000000000   0.334900000000000
Cl   0.236680000000000   0.153540000000000   0.665100000000000
O    0.407800000000000   0.539010000000000   0.507140000000000
O    0.907800000000000   0.960990000000000   0.492860000000000
O    0.092200000000000   0.460990000000000   0.007140000000000
O    0.592200000000000   0.039010000000000   0.992860000000000
O    0.506900000000000   0.727350000000000   0.436160000000000
O    0.006900000000000   0.772650000000000   0.563840000000000
O    0.993100000000000   0.272650000000000   0.936160000000000
O    0.493100000000000   0.227350000000000   0.063840000000000
N    0.729300000000000   0.393650000000000   0.643720000000000
N    0.229300000000000   0.106350000000000   0.356280000000000
N    0.770700000000000   0.606350000000000   0.143720000000000
N    0.270700000000000   0.893650000000000   0.856280000000000
C    0.409200000000000   0.622450000000000   0.437180000000000
C    0.909200000000000   0.877550000000000   0.562820000000000
C    0.090800000000000   0.377550000000000   0.937180000000000
C    0.590800000000000   0.122450000000000   0.062820000000000
C    0.931500000000000   0.471600000000000   0.635490000000000
C    0.431500000000000   0.028400000000000   0.364510000000000
C    0.568500000000000   0.528400000000000   0.135490000000000
C    0.068500000000000   0.971600000000000   0.864510000000000
C    0.708700000000000   0.299420000000000   0.567400000000000
C    0.208700000000000   0.200580000000000   0.432600000000000
C    0.791300000000000   0.700580000000000   0.067400000000000
C    0.291300000000000   0.799420000000000   0.932600000000000
C    0.538600000000000   0.485610000000000   0.652100000000000
C    0.038600000000000   0.014390000000000   0.347900000000000
C    0.961400000000000   0.514390000000000   0.152100000000000
C    0.461400000000000   0.985610000000000   0.847900000000000
C    0.513100000000000   0.593130000000000   0.583220000000000
C    0.013100000000000   0.906870000000000   0.416780000000000
C    0.986900000000000   0.406870000000000   0.083220000000000
C    0.486900000000000   0.093130000000000   0.916780000000000
C    0.277900000000000   0.568420000000000   0.363960000000000
C    0.777900000000000   0.931580000000000   0.636040000000000
C    0.222100000000000   0.431580000000000   0.863960000000000
C    0.722100000000000   0.068420000000000   0.136040000000000
C    0.739200000000000   0.312070000000000   0.726720000000000
C    0.239200000000000   0.187930000000000   0.273280000000000
C    0.760800000000000   0.687930000000000   0.226720000000000
C    0.260800000000000   0.812070000000000   0.773280000000000
H    0.049712000000000   0.411054000000000   0.640618000000000
H    0.549712000000000   0.088946000000000   0.359382000000000
H    0.450288000000000   0.588946000000000   0.140618000000000
H    0.950288000000000   0.911054000000000   0.859382000000000
H    0.938614000000000   0.538211000000000   0.680926000000000
H    0.438614000000000   0.961789000000000   0.319074000000000
```

```
H    0.561386000000000   0.461789000000000   0.180926000000000
H    0.061386000000000   0.038211000000000   0.819074000000000
H    0.935867000000000   0.515502000000000   0.579643000000000
H    0.435867000000000   0.984498000000000   0.420357000000000
H    0.564133000000000   0.484498000000000   0.079643000000000
H    0.064133000000000   0.015502000000000   0.920357000000000
H    0.703697000000000   0.350800000000000   0.514288000000000
H    0.203697000000000   0.149200000000000   0.485712000000000
H    0.796303000000000   0.649200000000000   0.014288000000000
H    0.296303000000000   0.850800000000000   0.985712000000000
H    0.580758000000000   0.247638000000000   0.573147000000000
H    0.080758000000000   0.252362000000000   0.426853000000000
H    0.919242000000000   0.752362000000000   0.073147000000000
H    0.419242000000000   0.747638000000000   0.926853000000000
H    0.828351000000000   0.239578000000000   0.565962000000000
H    0.328351000000000   0.260422000000000   0.434038000000000
H    0.671649000000000   0.760422000000000   0.065962000000000
H    0.171649000000000   0.739578000000000   0.934038000000000
H    0.412154000000000   0.429882000000000   0.651820000000000
H    0.912154000000000   0.070118000000000   0.348180000000000
H    0.087846000000000   0.570118000000000   0.151820000000000
H    0.587846000000000   0.929882000000000   0.848180000000000
H    0.545557000000000   0.529741000000000   0.708571000000000
H    0.045557000000000   0.970259000000000   0.291429000000000
H    0.954443000000000   0.470259000000000   0.208571000000000
H    0.454443000000000   0.029741000000000   0.791429000000000
H    0.430753000000000   0.667503000000000   0.606659000000000
H    0.930753000000000   0.832497000000000   0.393341000000000
H    0.069247000000000   0.332497000000000   0.106659000000000
H    0.569247000000000   0.167503000000000   0.893341000000000
H    0.651369000000000   0.627605000000000   0.566763000000000
H    0.151369000000000   0.872395000000000   0.433237000000000
H    0.848631000000000   0.372395000000000   0.066763000000000
H    0.348631000000000   0.127605000000000   0.933237000000000
H    0.346190000000000   0.490536000000000   0.339412000000000
H    0.846190000000000   0.009464000000000   0.660588000000000
H    0.153810000000000   0.509464000000000   0.839412000000000
H    0.653810000000000   0.990536000000000   0.160588000000000
H    0.262624000000000   0.636519000000000   0.319801000000000
H    0.762624000000000   0.863481000000000   0.680199000000000
H    0.237376000000000   0.363481000000000   0.819801000000000
H    0.737376000000000   0.136519000000000   0.180199000000000
H    0.140574000000000   0.543470000000000   0.385608000000000
H    0.640574000000000   0.956530000000000   0.614392000000000
H    0.359426000000000   0.456530000000000   0.885608000000000
H    0.859426000000000   0.043470000000000   0.114392000000000
H    0.859724000000000   0.252982000000000   0.724792000000000
H    0.359724000000000   0.247018000000000   0.275208000000000
H    0.640276000000000   0.747018000000000   0.224792000000000
H    0.140276000000000   0.752982000000000   0.775208000000000
H    0.612098000000000   0.259444000000000   0.732444000000000
H    0.112098000000000   0.240556000000000   0.267556000000000
H    0.887902000000000   0.740556000000000   0.232444000000000
H    0.387902000000000   0.759444000000000   0.767556000000000
H    0.751942000000000   0.371844000000000   0.775789000000000
H    0.251942000000000   0.128156000000000   0.224211000000000
H    0.748058000000000   0.628156000000000   0.275789000000000
H    0.248058000000000   0.871844000000000   0.724211000000000
%ENDBLOCK POSITIONS_FRAC
```

```
# Commented out pseudopotential block for easy editing
#%BLOCK SPECIES_POT
# H   H_00.usp
# C   C_00.usp
# N   N_00.usp
# O   O_00.usp
# Cl  Cl_00.usp
#%ENDBLOCK SPECIES_POT

%BLOCK SYMMETRY_OPS
# Symm. op. 1
  1.000000000000000   0.000000000000000   0.000000000000000
  0.000000000000000   1.000000000000000   0.000000000000000
  0.000000000000000   0.000000000000000   1.000000000000000
  0.000000000000000   0.000000000000000   0.000000000000000
# Symm. op. 2
  1.000000000000000   0.000000000000000   0.000000000000000
  0.000000000000000  -1.000000000000000   0.000000000000000
  0.000000000000000   0.000000000000000  -1.000000000000000
  0.500000000000000   0.500000000000000   0.000000000000000
# Symm. op. 3
 -1.000000000000000   0.000000000000000   0.000000000000000
  0.000000000000000  -1.000000000000000   0.000000000000000
  0.000000000000000   0.000000000000000   1.000000000000000
  0.500000000000000   0.000000000000000   0.500000000000000
# Symm. op. 4
 -1.000000000000000   0.000000000000000   0.000000000000000
  0.000000000000000   1.000000000000000   0.000000000000000
  0.000000000000000   0.000000000000000  -1.000000000000000
  0.000000000000000   0.500000000000000   0.500000000000000
%ENDBLOCK SYMMETRY_OPS
```

E.2.3 ACh Bromide

```
%BLOCK LATTICE_CART
ang    # angstrom units
   7.072200000000000   0.000000000000000   0.000000000000000
   0.000000000000000  13.449500000000000   0.000000000000000
  -3.509820048770950   0.000000000000000  10.374682574192111
%ENDBLOCK LATTICE_CART


%BLOCK POSITIONS_FRAC
Br   0.641050000000000   0.616030000000000   0.285140000000000
Br   0.358950000000000   0.383970000000000   0.714860000000000
Br   0.858950000000000   0.116030000000000   0.214860000000000
Br   0.141050000000000   0.883970000000000   0.785140000000000
O    0.439900000000000   0.868060000000000   0.492540000000000
O    0.560100000000000   0.131940000000000   0.507460000000000
O    0.060100000000000   0.368060000000000   0.007460000000000
O    0.939900000000000   0.631940000000000   0.992540000000000
O    0.392000000000000   0.900010000000000   0.282900000000000
O    0.608000000000000   0.099990000000000   0.717100000000000
O    0.108000000000000   0.400010000000000   0.217100000000000
O    0.892000000000000   0.599990000000000   0.782900000000000
N    0.243600000000000   0.653980000000000   0.495450000000000
N    0.756400000000000   0.346020000000000   0.504550000000000
N    0.256400000000000   0.153980000000000   0.004550000000000
N    0.743600000000000   0.846020000000000   0.995450000000000
C    0.503400000000000   0.892490000000000   0.391700000000000
C    0.496600000000000   0.107510000000000   0.608300000000000
C    0.996600000000000   0.392490000000000   0.108300000000000
C    0.003400000000000   0.607510000000000   0.891700000000000
C    0.207400000000000   0.560250000000000   0.416540000000000
C    0.792600000000000   0.439750000000000   0.583460000000000
C    0.292600000000000   0.060250000000000   0.083460000000000
C    0.707400000000000   0.939750000000000   0.916540000000000
C    0.458700000000000   0.657010000000000   0.577210000000000
C    0.541300000000000   0.342990000000000   0.422790000000000
C    0.041300000000000   0.157010000000000   0.922790000000000
C    0.958700000000000   0.842990000000000   0.077210000000000
C    0.113800000000000   0.652570000000000   0.580410000000000
C    0.886200000000000   0.347430000000000   0.419590000000000
C    0.386200000000000   0.152570000000000   0.919590000000000
C    0.613800000000000   0.847430000000000   0.080410000000000
C    0.725700000000000   0.903170000000000   0.433400000000000
C    0.274300000000000   0.096830000000000   0.566600000000000
C    0.774300000000000   0.403170000000000   0.066600000000000
C    0.225700000000000   0.596830000000000   0.933400000000000
C    0.230000000000000   0.842840000000000   0.458700000000000
C    0.770000000000000   0.157160000000000   0.541300000000000
C    0.270000000000000   0.342840000000000   0.041300000000000
C    0.730000000000000   0.657160000000000   0.958700000000000
C    0.188600000000000   0.739590000000000   0.401020000000000
C    0.811400000000000   0.260410000000000   0.598980000000000
C    0.311400000000000   0.239590000000000   0.098980000000000
C    0.688600000000000   0.760410000000000   0.901020000000000
H    0.292713000000000   0.559304000000000   0.363764000000000
H    0.707287000000000   0.440696000000000   0.636236000000000
H    0.207287000000000   0.059304000000000   0.136236000000000
H    0.792713000000000   0.940696000000000   0.863764000000000
H    0.070463000000000   0.557941000000000   0.362545000000000
```

```
H    0.929537000000000   0.442059000000000   0.637455000000000
H    0.429537000000000   0.057941000000000   0.137455000000000
H    0.570463000000000   0.942059000000000   0.862545000000000
H    0.235977000000000   0.503640000000000   0.472900000000000
H    0.764023000000000   0.496360000000000   0.527100000000000
H    0.264023000000000   0.003640000000000   0.027100000000000
H    0.735977000000000   0.996360000000000   0.972900000000000
H    0.489442000000000   0.599323000000000   0.631643000000000
H    0.510558000000000   0.400677000000000   0.368357000000000
H    0.010558000000000   0.099323000000000   0.868357000000000
H    0.989442000000000   0.900677000000000   0.131643000000000
H    0.483163000000000   0.715839000000000   0.629600000000000
H    0.516837000000000   0.284161000000000   0.370400000000000
H    0.016837000000000   0.215839000000000   0.870400000000000
H    0.983163000000000   0.784161000000000   0.129600000000000
H    0.541447000000000   0.657813000000000   0.522751000000000
H    0.458553000000000   0.342187000000000   0.477249000000000
H    0.958553000000000   0.157813000000000   0.977249000000000
H    0.041447000000000   0.842187000000000   0.022751000000000
H    0.976125000000000   0.649923000000000   0.527914000000000
H    0.023875000000000   0.350077000000000   0.472086000000000
H    0.523875000000000   0.149923000000000   0.972086000000000
H    0.476125000000000   0.850077000000000   0.027914000000000
H    0.137061000000000   0.711689000000000   0.632243000000000
H    0.862939000000000   0.288311000000000   0.367757000000000
H    0.362939000000000   0.211689000000000   0.867757000000000
H    0.637061000000000   0.788311000000000   0.132243000000000
H    0.145428000000000   0.595209000000000   0.635402000000000
H    0.854572000000000   0.404791000000000   0.364598000000000
H    0.354572000000000   0.095209000000000   0.864598000000000
H    0.645428000000000   0.904791000000000   0.135402000000000
H    0.774756000000000   0.918996000000000   0.523627000000000
H    0.225244000000000   0.081004000000000   0.476373000000000
H    0.725244000000000   0.418996000000000   0.976373000000000
H    0.274756000000000   0.581004000000000   0.023627000000000
H    0.760798000000000   0.955504000000000   0.385073000000000
H    0.239202000000000   0.044496000000000   0.614927000000000
H    0.739202000000000   0.455504000000000   0.114927000000000
H    0.260798000000000   0.544496000000000   0.885073000000000
H    0.784259000000000   0.841877000000000   0.418422000000000
H    0.215741000000000   0.158123000000000   0.581578000000000
H    0.715741000000000   0.341877000000000   0.081578000000000
H    0.284259000000000   0.658123000000000   0.918422000000000
H    0.151674000000000   0.890972000000000   0.397143000000000
H    0.848326000000000   0.109028000000000   0.602857000000000
H    0.348326000000000   0.390972000000000   0.102857000000000
H    0.651674000000000   0.609028000000000   0.897143000000000
H    0.189314000000000   0.846137000000000   0.535192000000000
H    0.810686000000000   0.153863000000000   0.464808000000000
H    0.310686000000000   0.346137000000000   0.964808000000000
H    0.689314000000000   0.653863000000000   0.035192000000000
H    0.047371000000000   0.734841000000000   0.353197000000000
H    0.952629000000000   0.265159000000000   0.646803000000000
H    0.452629000000000   0.234841000000000   0.146803000000000
H    0.547371000000000   0.765159000000000   0.853197000000000
H    0.260827000000000   0.731792000000000   0.339800000000000
H    0.739173000000000   0.268208000000000   0.660200000000000
H    0.239173000000000   0.231792000000000   0.160200000000000
H    0.760827000000000   0.768208000000000   0.839800000000000
```

```
%ENDBLOCK POSITIONS_FRAC

# Commented out pseudopotential block for easy editing
#%BLOCK SPECIES_POT
# H   H_00.usp
# C   C_00.usp
# O   O_00.usp
# Br  Br_00.usp
# N   N_00.usp
#%ENDBLOCK SPECIES_POT




%BLOCK SYMMETRY_OPS
# Symm. op. 1
  1.000000000000000   0.000000000000000   0.000000000000000
  0.000000000000000   1.000000000000000   0.000000000000000
  0.000000000000000  -0.000000000000000   1.000000000000000
  0.000000000000000   0.000000000000000   0.000000000000000
# Symm. op. 2
 -1.000000000000000   0.000000000000000   0.000000000000000
  0.000000000000000  -1.000000000000000   0.000000000000000
  0.000000000000000   0.000000000000000  -1.000000000000000
  0.000000000000000   0.000000000000000   0.000000000000000
# Symm. op. 3
 -1.000000000000000   0.000000000000000   0.000000000000000
  0.000000000000000   1.000000000000000   0.000000000000000
  0.000000000000000  -0.000000000000000  -1.000000000000000
  0.500000000000000   0.500000000000000   0.500000000000000
# Symm. op. 4
  1.000000000000000   0.000000000000000   0.000000000000000
 -0.000000000000000  -1.000000000000000   0.000000000000000
  0.000000000000000   0.000000000000000   1.000000000000000
  0.500000000000000   0.500000000000000   0.500000000000000
%ENDBLOCK SYMMETRY_OPS
```

E.2.4 ACh Iodide

```
%BLOCK LATTICE_CART
ang    # angstrom units
  31.306000000000001   0.000000000000000   0.000000000000000
   0.000000000000000  11.499010000000000   0.000000000000000
   0.000000000000000   0.000000000000000  11.492530000000000
%ENDBLOCK LATTICE_CART


%BLOCK POSITIONS_FRAC
I    0.599350000000000   0.750000000000000   0.250000000000000
I    0.900650000000000   0.250000000000000   0.250000000000000
I    0.400650000000000   0.250000000000000   0.750000000000000
I    0.099350000000000   0.750000000000000   0.750000000000000
I    0.592010000000000   0.250000000000000   0.750000000000000
I    0.907990000000000   0.750000000000000   0.750000000000000
I    0.407990000000000   0.750000000000000   0.250000000000000
I    0.092010000000000   0.250000000000000   0.250000000000000
I    0.766710000000000   0.250000000000000   0.750000000000000
I    0.733290000000000   0.750000000000000   0.750000000000000
I    0.233290000000000   0.750000000000000   0.250000000000000
I    0.266710000000000   0.250000000000000   0.250000000000000
I    0.730620000000000   0.250000000000000   0.250000000000000
I    0.769380000000000   0.750000000000000   0.250000000000000
I    0.269380000000000   0.750000000000000   0.750000000000000
I    0.230620000000000   0.250000000000000   0.750000000000000
O    0.440360000000000   0.419130000000000   0.075380000000000
O    0.059640000000000   0.919130000000000   0.424620000000000
O    0.559640000000000   0.580870000000000   0.924620000000000
O    0.059640000000000   0.580870000000000   0.075380000000000
O    0.440360000000000   0.080870000000000   0.424620000000000
O    0.940360000000000   0.080870000000000   0.575380000000000
O    0.940360000000000   0.419130000000000   0.924620000000000
O    0.559640000000000   0.919130000000000   0.575380000000000
O    0.558970000000000   0.075390000000000   0.080500000000000
O    0.941030000000000   0.575390000000000   0.419500000000000
O    0.441030000000000   0.924610000000000   0.919500000000000
O    0.941030000000000   0.924610000000000   0.080500000000000
O    0.558970000000000   0.424610000000000   0.419500000000000
O    0.058970000000000   0.424610000000000   0.580500000000000
O    0.058970000000000   0.075390000000000   0.919500000000000
O    0.441030000000000   0.575390000000000   0.580500000000000
O    0.553950000000000   0.098500000000000   0.274550000000000
O    0.946050000000000   0.598500000000000   0.225450000000000
O    0.446050000000000   0.901500000000000   0.725450000000000
O    0.946050000000000   0.901500000000000   0.274550000000000
O    0.553950000000000   0.401500000000000   0.225450000000000
O    0.053950000000000   0.401500000000000   0.774550000000000
O    0.053950000000000   0.098500000000000   0.725450000000000
O    0.446050000000000   0.598500000000000   0.774550000000000
O    0.445940000000000   0.225530000000000   0.099380000000000
O    0.054060000000000   0.725530000000000   0.400620000000000
O    0.554060000000000   0.774470000000000   0.900620000000000
O    0.054060000000000   0.774470000000000   0.099380000000000
O    0.445940000000000   0.274470000000000   0.400620000000000
O    0.945940000000000   0.274470000000000   0.599380000000000
O    0.945940000000000   0.225530000000000   0.900620000000000
O    0.554060000000000   0.725530000000000   0.599380000000000
N    0.340490000000000   0.478880000000000   0.011330000000000
```

```
N    0.159510000000000   0.978880000000000   0.488670000000000
N    0.659510000000000   0.521120000000000   0.988670000000000
N    0.159510000000000   0.521120000000000   0.011330000000000
N    0.340490000000000   0.021120000000000   0.488670000000000
N    0.840490000000000   0.021120000000000   0.511330000000000
N    0.840490000000000   0.478880000000000   0.988670000000000
N    0.659510000000000   0.978880000000000   0.511330000000000
N    0.659070000000000   0.010420000000000   0.020720000000000
N    0.840930000000000   0.510420000000000   0.479280000000000
N    0.340930000000000   0.989580000000000   0.979280000000000
N    0.840930000000000   0.989580000000000   0.020720000000000
N    0.659070000000000   0.489580000000000   0.479280000000000
N    0.159070000000000   0.489580000000000   0.520720000000000
N    0.159070000000000   0.010420000000000   0.979280000000000
N    0.340930000000000   0.510420000000000   0.520720000000000
C    0.690990000000000   0.929170000000000   0.074500000000000
C    0.809010000000000   0.429170000000000   0.425500000000000
C    0.309010000000000   0.070830000000000   0.925500000000000
C    0.809010000000000   0.070830000000000   0.074500000000000
C    0.690990000000000   0.570830000000000   0.425500000000000
C    0.190990000000000   0.570830000000000   0.574500000000000
C    0.190990000000000   0.929170000000000   0.925500000000000
C    0.309010000000000   0.429170000000000   0.574500000000000
C    0.682790000000000   0.095790000000000   0.946220000000000
C    0.817210000000000   0.595790000000000   0.553780000000000
C    0.317210000000000   0.904210000000000   0.053780000000000
C    0.817210000000000   0.904210000000000   0.946220000000000
C    0.682790000000000   0.404210000000000   0.553780000000000
C    0.182790000000000   0.404210000000000   0.446220000000000
C    0.182790000000000   0.095790000000000   0.053780000000000
C    0.317210000000000   0.595790000000000   0.446220000000000
C    0.308350000000000   0.425380000000000   0.929950000000000
C    0.191650000000000   0.925380000000000   0.570050000000000
C    0.691650000000000   0.574620000000000   0.070050000000000
C    0.191650000000000   0.574620000000000   0.929950000000000
C    0.308350000000000   0.074620000000000   0.570050000000000
C    0.808350000000000   0.074620000000000   0.429950000000000
C    0.808350000000000   0.425380000000000   0.070050000000000
C    0.691650000000000   0.925380000000000   0.429950000000000
C    0.501040000000000   0.984300000000000   0.173800000000000
C    0.998960000000000   0.484300000000000   0.326200000000000
C    0.498960000000000   0.015700000000000   0.826200000000000
C    0.998960000000000   0.015700000000000   0.173800000000000
C    0.501040000000000   0.515700000000000   0.326200000000000
C    0.001040000000000   0.515700000000000   0.673800000000000
C    0.001040000000000   0.984300000000000   0.826200000000000
C    0.498960000000000   0.484300000000000   0.673800000000000
C    0.498570000000000   0.326900000000000   0.984400000000000
C    0.001430000000000   0.826900000000000   0.515600000000000
C    0.501430000000000   0.673100000000000   0.015600000000000
C    0.001430000000000   0.673100000000000   0.984400000000000
C    0.498570000000000   0.173100000000000   0.515600000000000
C    0.998570000000000   0.173100000000000   0.484400000000000
C    0.998570000000000   0.326900000000000   0.015600000000000
C    0.501430000000000   0.826900000000000   0.484400000000000
C    0.459740000000000   0.314520000000000   0.058890000000000
C    0.040260000000000   0.814520000000000   0.441110000000000
C    0.540260000000000   0.685480000000000   0.941110000000000
C    0.040260000000000   0.685480000000000   0.058890000000000
```

```
C    0.459740000000000   0.185480000000000   0.441110000000000
C    0.959740000000000   0.185480000000000   0.558890000000000
C    0.959740000000000   0.314520000000000   0.941110000000000
C    0.540260000000000   0.814520000000000   0.558890000000000
C    0.363540000000000   0.380680000000000   0.072510000000000
C    0.136460000000000   0.880680000000000   0.427490000000000
C    0.636460000000000   0.619320000000000   0.927490000000000
C    0.136460000000000   0.619320000000000   0.072510000000000
C    0.363540000000000   0.119320000000000   0.427490000000000
C    0.863540000000000   0.119320000000000   0.572510000000000
C    0.863540000000000   0.380680000000000   0.927490000000000
C    0.636460000000000   0.880680000000000   0.572510000000000
C    0.597660000000000   0.143730000000000   0.083440000000000
C    0.902340000000000   0.643730000000000   0.416560000000000
C    0.402340000000000   0.856270000000000   0.916560000000000
C    0.902340000000000   0.856270000000000   0.083440000000000
C    0.597660000000000   0.356270000000000   0.416560000000000
C    0.097660000000000   0.356270000000000   0.583440000000000
C    0.097660000000000   0.143730000000000   0.916560000000000
C    0.402340000000000   0.643730000000000   0.583440000000000
C    0.401920000000000   0.416060000000000   0.144520000000000
C    0.098080000000000   0.916060000000000   0.355480000000000
C    0.598080000000000   0.583940000000000   0.855480000000000
C    0.098080000000000   0.583940000000000   0.144520000000000
C    0.401920000000000   0.083940000000000   0.355480000000000
C    0.901920000000000   0.083940000000000   0.644520000000000
C    0.901920000000000   0.416060000000000   0.855480000000000
C    0.598080000000000   0.916060000000000   0.644520000000000
C    0.635780000000000   0.071250000000000   0.119040000000000
C    0.864220000000000   0.571250000000000   0.380960000000000
C    0.364220000000000   0.928750000000000   0.880960000000000
C    0.864220000000000   0.928750000000000   0.119040000000000
C    0.635780000000000   0.428750000000000   0.380960000000000
C    0.135780000000000   0.428750000000000   0.619040000000000
C    0.135780000000000   0.071250000000000   0.880960000000000
C    0.364220000000000   0.571250000000000   0.619040000000000
C    0.539800000000000   0.058400000000000   0.185790000000000
C    0.960200000000000   0.558400000000000   0.314210000000000
C    0.460200000000000   0.941600000000000   0.814210000000000
C    0.960200000000000   0.941600000000000   0.185790000000000
C    0.539800000000000   0.441600000000000   0.314210000000000
C    0.039800000000000   0.441600000000000   0.685790000000000
C    0.039800000000000   0.058400000000000   0.814210000000000
C    0.460200000000000   0.558400000000000   0.685790000000000
C    0.316860000000000   0.554180000000000   0.096290000000000
C    0.183140000000000   0.054180000000000   0.403710000000000
C    0.683140000000000   0.445820000000000   0.903710000000000
C    0.183140000000000   0.445820000000000   0.096290000000000
C    0.316860000000000   0.945820000000000   0.403710000000000
C    0.816860000000000   0.945820000000000   0.596290000000000
C    0.816860000000000   0.554180000000000   0.903710000000000
C    0.683140000000000   0.054180000000000   0.596290000000000
C    0.371190000000000   0.550970000000000   0.942350000000000
C    0.128810000000000   0.050970000000000   0.557650000000000
C    0.628810000000000   0.449030000000000   0.057650000000000
C    0.128810000000000   0.449030000000000   0.942350000000000
C    0.371190000000000   0.949030000000000   0.557650000000000
C    0.871190000000000   0.949030000000000   0.442350000000000
C    0.871190000000000   0.550970000000000   0.057650000000000
```

```
C    0.628810000000000   0.050970000000000   0.442350000000000
C    0.628470000000000   0.942070000000000   0.947590000000000
C    0.871530000000000   0.442070000000000   0.552410000000000
C    0.371530000000000   0.057930000000000   0.052410000000000
C    0.871530000000000   0.057930000000000   0.947590000000000
C    0.628470000000000   0.557930000000000   0.552410000000000
C    0.128470000000000   0.557930000000000   0.447590000000000
C    0.128470000000000   0.942070000000000   0.052410000000000
C    0.371530000000000   0.442070000000000   0.447590000000000
H    0.707631000000000   0.891308000000000   0.013029000000000
H    0.792369000000000   0.391308000000000   0.486971000000000
H    0.292369000000000   0.108692000000000   0.986971000000000
H    0.792369000000000   0.108692000000000   0.013029000000000
H    0.707631000000000   0.608692000000000   0.486971000000000
H    0.207631000000000   0.608692000000000   0.513029000000000
H    0.207631000000000   0.891308000000000   0.986971000000000
H    0.292369000000000   0.391308000000000   0.513029000000000
H    0.675960000000000   0.869991000000000   0.120232000000000
H    0.824040000000000   0.369991000000000   0.379768000000000
H    0.324040000000000   0.130009000000000   0.879768000000000
H    0.824040000000000   0.130009000000000   0.120232000000000
H    0.675960000000000   0.630009000000000   0.379768000000000
H    0.175960000000000   0.630009000000000   0.620232000000000
H    0.175960000000000   0.869991000000000   0.879768000000000
H    0.324040000000000   0.369991000000000   0.620232000000000
H    0.710214000000000   0.973167000000000   0.125424000000000
H    0.789786000000000   0.473167000000000   0.374576000000000
H    0.289786000000000   0.026833000000000   0.874576000000000
H    0.789786000000000   0.026833000000000   0.125424000000000
H    0.710214000000000   0.526833000000000   0.374576000000000
H    0.210214000000000   0.526833000000000   0.625424000000000
H    0.210214000000000   0.973167000000000   0.874576000000000
H    0.289786000000000   0.473167000000000   0.625424000000000
H    0.702357000000000   0.141245000000000   0.994814000000000
H    0.797643000000000   0.641245000000000   0.505186000000000
H    0.297643000000000   0.858755000000000   0.005186000000000
H    0.797643000000000   0.858755000000000   0.994814000000000
H    0.702357000000000   0.358755000000000   0.505186000000000
H    0.202357000000000   0.358755000000000   0.494814000000000
H    0.202357000000000   0.141245000000000   0.005186000000000
H    0.297643000000000   0.641245000000000   0.494814000000000
H    0.662383000000000   0.148146000000000   0.908295000000000
H    0.837617000000000   0.648146000000000   0.591705000000000
H    0.337617000000000   0.851854000000000   0.091705000000000
H    0.837617000000000   0.851854000000000   0.908295000000000
H    0.662383000000000   0.351854000000000   0.591705000000000
H    0.162383000000000   0.351854000000000   0.408295000000000
H    0.162383000000000   0.148146000000000   0.091705000000000
H    0.337617000000000   0.648146000000000   0.408295000000000
H    0.699126000000000   0.053790000000000   0.886851000000000
H    0.800874000000000   0.553790000000000   0.613149000000000
H    0.300874000000000   0.946210000000000   0.113149000000000
H    0.800874000000000   0.946210000000000   0.886851000000000
H    0.699126000000000   0.446210000000000   0.613149000000000
H    0.199126000000000   0.446210000000000   0.386851000000000
H    0.199126000000000   0.053790000000000   0.113149000000000
H    0.300874000000000   0.553790000000000   0.386851000000000
H    0.323224000000000   0.377862000000000   0.871902000000000
H    0.176776000000000   0.877862000000000   0.628098000000000
```

```
H    0.676776000000000   0.622138000000000   0.128098000000000
H    0.176776000000000   0.622138000000000   0.871902000000000
H    0.323224000000000   0.122138000000000   0.628098000000000
H    0.823224000000000   0.122138000000000   0.371902000000000
H    0.823224000000000   0.377862000000000   0.128098000000000
H    0.676776000000000   0.877862000000000   0.371902000000000
H    0.292304000000000   0.487098000000000   0.890614000000000
H    0.207696000000000   0.987098000000000   0.609386000000000
H    0.707696000000000   0.512902000000000   0.109386000000000
H    0.207696000000000   0.512902000000000   0.890614000000000
H    0.292304000000000   0.012902000000000   0.609386000000000
H    0.792304000000000   0.012902000000000   0.390614000000000
H    0.792304000000000   0.487098000000000   0.109386000000000
H    0.707696000000000   0.987098000000000   0.390614000000000
H    0.288602000000000   0.376351000000000   0.974341000000000
H    0.211398000000000   0.876351000000000   0.525659000000000
H    0.711398000000000   0.623649000000000   0.025659000000000
H    0.211398000000000   0.623649000000000   0.974341000000000
H    0.288602000000000   0.123649000000000   0.525659000000000
H    0.788602000000000   0.123649000000000   0.474341000000000
H    0.788602000000000   0.376351000000000   0.025659000000000
H    0.711398000000000   0.876351000000000   0.474341000000000
H    0.483588000000000   0.012740000000000   0.108995000000000
H    0.016412000000000   0.512740000000000   0.391005000000000
H    0.516412000000000   0.987260000000000   0.891005000000000
H    0.016412000000000   0.987260000000000   0.108995000000000
H    0.483588000000000   0.487260000000000   0.391005000000000
H    0.983588000000000   0.487260000000000   0.608995000000000
H    0.983588000000000   0.012740000000000   0.891005000000000
H    0.516412000000000   0.512740000000000   0.608995000000000
H    0.484380000000000   0.987558000000000   0.245929000000000
H    0.015620000000000   0.487558000000000   0.254071000000000
H    0.515620000000000   0.012442000000000   0.754071000000000
H    0.015620000000000   0.012442000000000   0.245929000000000
H    0.484380000000000   0.512442000000000   0.254071000000000
H    0.984380000000000   0.512442000000000   0.745929000000000
H    0.984380000000000   0.987558000000000   0.754071000000000
H    0.515620000000000   0.487558000000000   0.745929000000000
H    0.509639000000000   0.903748000000000   0.158611000000000
H    0.990361000000000   0.403748000000000   0.341389000000000
H    0.490361000000000   0.096252000000000   0.841389000000000
H    0.990361000000000   0.096252000000000   0.158611000000000
H    0.509639000000000   0.596252000000000   0.341389000000000
H    0.009639000000000   0.596252000000000   0.658611000000000
H    0.009639000000000   0.903748000000000   0.841389000000000
H    0.490361000000000   0.403748000000000   0.658611000000000
H    0.489925000000000   0.343799000000000   0.904172000000000
H    0.010075000000000   0.843799000000000   0.595828000000000
H    0.510075000000000   0.656201000000000   0.095828000000000
H    0.010075000000000   0.656201000000000   0.904172000000000
H    0.489925000000000   0.156201000000000   0.595828000000000
H    0.989925000000000   0.156201000000000   0.404172000000000
H    0.989925000000000   0.343799000000000   0.095828000000000
H    0.510075000000000   0.843799000000000   0.404172000000000
H    0.514972000000000   0.254308000000000   0.986132000000000
H    0.985028000000000   0.754308000000000   0.513868000000000
H    0.485028000000000   0.745692000000000   0.013868000000000
H    0.985028000000000   0.745692000000000   0.986132000000000
H    0.514972000000000   0.245692000000000   0.513868000000000
```

```
H    0.014972000000000   0.245692000000000   0.486132000000000
H    0.014972000000000   0.254308000000000   0.013868000000000
H    0.485028000000000   0.754308000000000   0.486132000000000
H    0.516292000000000   0.390642000000000   0.013875000000000
H    0.983708000000000   0.890642000000000   0.486125000000000
H    0.483708000000000   0.609358000000000   0.986125000000000
H    0.983708000000000   0.609358000000000   0.013875000000000
H    0.516292000000000   0.109358000000000   0.486125000000000
H    0.016292000000000   0.109358000000000   0.513875000000000
H    0.016292000000000   0.390642000000000   0.986125000000000
H    0.483708000000000   0.890642000000000   0.513875000000000
H    0.373030000000000   0.323875000000000   0.013162000000000
H    0.126970000000000   0.823875000000000   0.486838000000000
H    0.626970000000000   0.676125000000000   0.986838000000000
H    0.126970000000000   0.676125000000000   0.013162000000000
H    0.373030000000000   0.176125000000000   0.486838000000000
H    0.873030000000000   0.176125000000000   0.513162000000000
H    0.873030000000000   0.323875000000000   0.986838000000000
H    0.626970000000000   0.823875000000000   0.513162000000000
H    0.342931000000000   0.340507000000000   0.124033000000000
H    0.157069000000000   0.840507000000000   0.375967000000000
H    0.657069000000000   0.659493000000000   0.875967000000000
H    0.157069000000000   0.659493000000000   0.124033000000000
H    0.342931000000000   0.159493000000000   0.375967000000000
H    0.842931000000000   0.159493000000000   0.624033000000000
H    0.842931000000000   0.340507000000000   0.875967000000000
H    0.657069000000000   0.840507000000000   0.624033000000000
H    0.594067000000000   0.208690000000000   0.139127000000000
H    0.905933000000000   0.708690000000000   0.360873000000000
H    0.405933000000000   0.791310000000000   0.860873000000000
H    0.905933000000000   0.791310000000000   0.139127000000000
H    0.594067000000000   0.291310000000000   0.360873000000000
H    0.094067000000000   0.291310000000000   0.639127000000000
H    0.094067000000000   0.208690000000000   0.860873000000000
H    0.405933000000000   0.708690000000000   0.639127000000000
H    0.602877000000000   0.177463000000000   0.005470000000000
H    0.897123000000000   0.677463000000000   0.494530000000000
H    0.397123000000000   0.822537000000000   0.994530000000000
H    0.897123000000000   0.822537000000000   0.005470000000000
H    0.602877000000000   0.322537000000000   0.494530000000000
H    0.102877000000000   0.322537000000000   0.505470000000000
H    0.102877000000000   0.177463000000000   0.994530000000000
H    0.397123000000000   0.677463000000000   0.505470000000000
H    0.396811000000000   0.493889000000000   0.178613000000000
H    0.103189000000000   0.993889000000000   0.321387000000000
H    0.603189000000000   0.506111000000000   0.821387000000000
H    0.103189000000000   0.506111000000000   0.178613000000000
H    0.396811000000000   0.006111000000000   0.321387000000000
H    0.896811000000000   0.006111000000000   0.678613000000000
H    0.896811000000000   0.493889000000000   0.821387000000000
H    0.603189000000000   0.993889000000000   0.678613000000000
H    0.405687000000000   0.360194000000000   0.209264000000000
H    0.094313000000000   0.860194000000000   0.290736000000000
H    0.594313000000000   0.639806000000000   0.790736000000000
H    0.094313000000000   0.639806000000000   0.209264000000000
H    0.405687000000000   0.139806000000000   0.290736000000000
H    0.905687000000000   0.139806000000000   0.709264000000000
H    0.905687000000000   0.360194000000000   0.790736000000000
H    0.594313000000000   0.860194000000000   0.709264000000000
```

```
H    0.626046000000000   0.011663000000000   0.175277000000000
H    0.873954000000000   0.511663000000000   0.324723000000000
H    0.373954000000000   0.988337000000000   0.824723000000000
H    0.873954000000000   0.988337000000000   0.175277000000000
H    0.626046000000000   0.488337000000000   0.324723000000000
H    0.126046000000000   0.488337000000000   0.675277000000000
H    0.126046000000000   0.011663000000000   0.824723000000000
H    0.373954000000000   0.511663000000000   0.675277000000000
H    0.656338000000000   0.122270000000000   0.160009000000000
H    0.843662000000000   0.622270000000000   0.339991000000000
H    0.343662000000000   0.877730000000000   0.839991000000000
H    0.843662000000000   0.877730000000000   0.160009000000000
H    0.656338000000000   0.377730000000000   0.339991000000000
H    0.156338000000000   0.377730000000000   0.660009000000000
H    0.156338000000000   0.122270000000000   0.839991000000000
H    0.343662000000000   0.622270000000000   0.660009000000000
H    0.300667000000000   0.613530000000000   0.053876000000000
H    0.199333000000000   0.113530000000000   0.446124000000000
H    0.699333000000000   0.386470000000000   0.946124000000000
H    0.199333000000000   0.386470000000000   0.053876000000000
H    0.300667000000000   0.886470000000000   0.446124000000000
H    0.800667000000000   0.886470000000000   0.553876000000000
H    0.800667000000000   0.613530000000000   0.946124000000000
H    0.699333000000000   0.113530000000000   0.553876000000000
H    0.337313000000000   0.592050000000000   0.148552000000000
H    0.162687000000000   0.092050000000000   0.351448000000000
H    0.662687000000000   0.407950000000000   0.851448000000000
H    0.162687000000000   0.407950000000000   0.148552000000000
H    0.337313000000000   0.907950000000000   0.351448000000000
H    0.837313000000000   0.907950000000000   0.648552000000000
H    0.837313000000000   0.592050000000000   0.851448000000000
H    0.662687000000000   0.092050000000000   0.648552000000000
H    0.297168000000000   0.506146000000000   0.141940000000000
H    0.202832000000000   0.006146000000000   0.358060000000000
H    0.702832000000000   0.493854000000000   0.858060000000000
H    0.202832000000000   0.493854000000000   0.141940000000000
H    0.297168000000000   0.993854000000000   0.358060000000000
H    0.797168000000000   0.993854000000000   0.641940000000000
H    0.797168000000000   0.506146000000000   0.858060000000000
H    0.702832000000000   0.006146000000000   0.641940000000000
H    0.387212000000000   0.500746000000000   0.889054000000000
H    0.112788000000000   0.000746000000000   0.610946000000000
H    0.612788000000000   0.499254000000000   0.110946000000000
H    0.112788000000000   0.499254000000000   0.889054000000000
H    0.387212000000000   0.999254000000000   0.610946000000000
H    0.887212000000000   0.999254000000000   0.389054000000000
H    0.887212000000000   0.500746000000000   0.110946000000000
H    0.612788000000000   0.000746000000000   0.389054000000000
H    0.391078000000000   0.590086000000000   0.995303000000000
H    0.108922000000000   0.090086000000000   0.504697000000000
H    0.608922000000000   0.409914000000000   0.004697000000000
H    0.108922000000000   0.409914000000000   0.995303000000000
H    0.391078000000000   0.909914000000000   0.504697000000000
H    0.891078000000000   0.909914000000000   0.495303000000000
H    0.891078000000000   0.590086000000000   0.004697000000000
H    0.608922000000000   0.090086000000000   0.495303000000000
H    0.355378000000000   0.609307000000000   0.897512000000000
H    0.144622000000000   0.109307000000000   0.602488000000000
H    0.644622000000000   0.390693000000000   0.102488000000000
```

```
H    0.144622000000000   0.390693000000000   0.897512000000000
H    0.355378000000000   0.890693000000000   0.602488000000000
H    0.855378000000000   0.890693000000000   0.397512000000000
H    0.855378000000000   0.609307000000000   0.102488000000000
H    0.644622000000000   0.109307000000000   0.397512000000000
H    0.644391000000000   0.897058000000000   0.889612000000000
H    0.855609000000000   0.397058000000000   0.610388000000000
H    0.355609000000000   0.102942000000000   0.110388000000000
H    0.855609000000000   0.102942000000000   0.889612000000000
H    0.644391000000000   0.602942000000000   0.610388000000000
H    0.144391000000000   0.602942000000000   0.389612000000000
H    0.144391000000000   0.897058000000000   0.110388000000000
H    0.355609000000000   0.397058000000000   0.389612000000000
H    0.608849000000000   0.995390000000000   0.907966000000000
H    0.891151000000000   0.495390000000000   0.592034000000000
H    0.391151000000000   0.004610000000000   0.092034000000000
H    0.891151000000000   0.004610000000000   0.907966000000000
H    0.608849000000000   0.504610000000000   0.592034000000000
H    0.108849000000000   0.504610000000000   0.407966000000000
H    0.108849000000000   0.995390000000000   0.092034000000000
H    0.391151000000000   0.495390000000000   0.407966000000000
H    0.612126000000000   0.889022000000000   0.997318000000000
H    0.887874000000000   0.389022000000000   0.502682000000000
H    0.387874000000000   0.110978000000000   0.002682000000000
H    0.887874000000000   0.110978000000000   0.997318000000000
H    0.612126000000000   0.610978000000000   0.502682000000000
H    0.112126000000000   0.610978000000000   0.497318000000000
H    0.112126000000000   0.889022000000000   0.002682000000000
H    0.387874000000000   0.389022000000000   0.497318000000000
%ENDBLOCK POSITIONS_FRAC

# Commented out pseudopotential block for easy editing
#%BLOCK SPECIES_POT
# I   I_00.usp
# H   H_00.usp
# C   C_00.usp
# O   O_00.usp
# N   N_00.usp
#%ENDBLOCK SPECIES_POT


%BLOCK SYMMETRY_OPS
# Symm. op. 1
  1.000000000000000   0.000000000000000   0.000000000000000
  0.000000000000000   1.000000000000000   0.000000000000000
  0.000000000000000   0.000000000000000   1.000000000000000
  0.000000000000000   0.000000000000000   0.000000000000000
# Symm. op. 2
 -1.000000000000000   0.000000000000000   0.000000000000000
  0.000000000000000  -1.000000000000000   0.000000000000000
  0.000000000000000   0.000000000000000  -1.000000000000000
  0.000000000000000   0.000000000000000   0.000000000000000
# Symm. op. 3
 -1.000000000000000   0.000000000000000   0.000000000000000
  0.000000000000000  -1.000000000000000   0.000000000000000
  0.000000000000000   0.000000000000000   1.000000000000000
  0.500000000000000   0.000000000000000   0.000000000000000
# Symm. op. 4
  1.000000000000000   0.000000000000000   0.000000000000000
```

```
  0.000000000000000   1.000000000000000   0.000000000000000
  0.000000000000000   0.000000000000000  -1.000000000000000
  0.500000000000000   0.000000000000000   0.000000000000000
# Symm. op. 5
  1.000000000000000   0.000000000000000   0.000000000000000
  0.000000000000000  -1.000000000000000   0.000000000000000
  0.000000000000000   0.000000000000000  -1.000000000000000
  0.000000000000000   0.500000000000000   0.500000000000000
# Symm. op. 6
 -1.000000000000000   0.000000000000000   0.000000000000000
  0.000000000000000   1.000000000000000   0.000000000000000
  0.000000000000000   0.000000000000000   1.000000000000000
  0.000000000000000   0.500000000000000   0.500000000000000
# Symm. op. 7
 -1.000000000000000   0.000000000000000   0.000000000000000
  0.000000000000000   1.000000000000000   0.000000000000000
  0.000000000000000   0.000000000000000  -1.000000000000000
  0.500000000000000   0.500000000000000   0.500000000000000
# Symm. op. 8
  1.000000000000000   0.000000000000000   0.000000000000000
  0.000000000000000  -1.000000000000000   0.000000000000000
  0.000000000000000   0.000000000000000   1.000000000000000
  0.500000000000000   0.500000000000000   0.500000000000000
%ENDBLOCK SYMMETRY_OPS
```

E.3 *CASTEP* Simulation Parameter Code

```
! Tell CASTEP that we want to do a single SCF electronic
  minimisation

TASK : MagRes
MAGRES_TASK : NMR

! Using the GGA exchange-correlation functional PBE.
XC_FUNCTIONAL : PBE

! The basis set should contain plane-waves up to this value
CUT_OFF_ENERGY : 1000 eV

WRITE_CELL_STRUCTURE : true

IPRINT : 2

! Speed up the calculation by not worrying about spin
  polarisation
  SPIN_POLARIZED : true

! Allow the occupancies of the state to change k-point
  per k-point and not just be 0 or 1. WARNING: for the
  NMR calculations later you MUST set this to TRUE as
  GIPAW-NMR will not work with metals
  FIX_OCCUPANCY : true

! Stop if no convergence at this number of SCF loops
  MAX_SCF_CYCLES : 100

! These are here to keep the simulation fast. If you want
  to know more about them. Use the CASTEP help system
 write_bib : false
 opt_strategy : speed
 page_wvfns : 0
 num_dump_cycles : 0
 backup_interval : 0
 finite_basis_corr : 0
```

E.4 *CASTEP* Simulation Job File

```
#!/bin/bash
#SBATCH --ntasks=40     # Number of processor cores (i.e. tasks)
#SBATCH --nodes=1     # Number of nodes requested
#SBATCH --ntasks-per-node=40     # Tasks per node
#SBATCH --cpus-per-task=1     # Threads per task
#SBATCH --time=48:00:00   # walltime

cd $SLURM_SUBMIT_DIR

# set basename for calculation
seed=achBr

# setup directory for temporary files
export TMPDIR=/scratch/jb3e16/CASTEP-Â{seed}_$$
mkdir -p $TMPDIR

# setup software environment
module load openmpi/3.0.0
module load CASTEP

# run calculation
mpirun CASTEP $seed
rm -fr $TMPDIR
```

E.5 Nitrogen-14 MAS Simulation Code for ACh Chloride

```
% Simulate 14N MAS lineshape for ACh chloride

function static_powder_nqi_Cl()
% Clear up windows
close all;

% System specification
sys.magnet=14.1; % Magnetic field
sys.isotopes={'14N'}; % Isotope

% Input Cq and eta values - for ACh chloride
% Obtained from CASTEP simulations
inter.coupling.matrix{1,1}=eeqq2nqi(145700,0.2477,1,[0 0 0]);

% Basis set
bas.formalism='sphten-liouv';
bas.approximation='none';

% SPINACH housekeeping
spin_system=create(sys,inter);
spin_system=basis(spin_system,bas);

% Sequence parameters
parameters.rate=10000; % Spin rate Hz
parameters.axis=[1 1 1]; % MAS axis
parameters.max_rank=35;
parameters.spins={'14N'};
parameters.decouple={};
parameters.offset=0;
parameters.sweep=2.5e5*3; % sweep width
parameters.npoints=512;
parameters.zerofill=2048; % zerofill
parameters.axis_units='Hz'; % units
parameters.invert_axis=1;
parameters.grid='icos_2ang_163842pts'; % number of pts
parameters.rho0=state(spin_system,'L+','14N','cheap');
parameters.coil=state(spin_system,'L+','14N','cheap');
parameters.verbose=0;

% Simulation
fid=floquet(spin_system,@acquire,parameters,'nmr');

% Apodization
fid=apodization(fid,'exp-1d',1);
save('chloride_fid.mat')

% Fourier transform
spectrum=fftshift(fft(fid,parameters.zerofill));

% Plot Spectrum
figure(); plot_1d(spin_system,real(spectrum),parameters);

end
```

E.6 Nitrogen-14 T_1 Relaxation Curve Fitting Script

```
% Clear windows and workspace
close all; clear all;

% Delays for T1 recovery, obtained from NMR parameters file.
x=[3 3.6377433125 4.4110587875 5.348766525 6.4858132125
7.8645745375...
   9.53643445 11.5637002 14.0219243375 17.0027204625 20.617177525
24.99999985];

% Load experimental data
load ACh_chloride_40deg_T1_sept.mat

% Sum over all sidebands (sb) - calls function, with data, sb
width (pts),
% The number of sb, and the position of the central peak (pts).
% Assumes data acquired at 10 kHz with 500 kHz spectra width.

% y=sum(sum_sidebands(data,sb width,number of sb,centre of
spectrum)
y=sum(sum_sidebands(ACh_cloride_40deg_T1_sept,13,10,2052));
fit_t1(x,y);

function sbints=sum_sidebands(spectra,width,nosbs,centre)
% spectra : matNMR data set
% width : width of your peak in pts
% nosbs : no of sidebands on each side
% centre : postion of centre line in pts

sbints=zeros(((nosbs*2)+1),size(spectra.Spectrum,1));
counter=1;
       for j=(-1*nosbs):1:nosbs
           startint=round(centre+((j*82)-width/2));
           endint=round(centre+((j*82)+width/2));

sbints(counter,:)=real(sum(spectra.Spectrum(:,startint:endint),2))
;
           counter=counter+1;
       end
end

function cfa1_=fit_t1(x,y)

% Normalise the data;
y=y./max(y)
% Plot intensities vs time
plot(x,y,'ro')
hold on

% Define fitting function and fit using non linear least squares
% disp(['The T1 for the region ',num2str(data.AxisTD2(xlim1)),'
ppm to...
% ',num2str(data.AxisTD2(xlim2)),' ppm is:'])
fo1_ = fitoptions('method','NonlinearLeastSquares','StartPoint',[1
1 1],...
       'Lower',[0 0 0],'Upper',[100 100 100],'MaxFunEvals',1000);
```

```
ft1_ = fittype('A1*(1-A2*exp(-1.0*x/T1))',...
    'dependent',{'y'},'independent',{'x'},...
    'coefficients',{'A1','A2','T1'});

% Output results of fit and plot fit on experimental data
cfa1_ = fit(x',y',ft1_,fo1_)
T1_curve=plot(cfa1_,'fit',0.95);
ylim ([0 1.1]);
xlim ([0 25]);
set(T1_curve,'Color','k');
ylabel ('intensity');
xlabel ('time (sec)');
hLeg=legend('boxoff');
set(hLeg,'visible','off');
end
```

E.7 Herzfeld-Berger Analysis

```
clear all; close all;

% Test data sbdata.mat (sideband file) calculated assuming
delta=54000 Hz, eta=0.0
% Load test data

load sbdata_ach20C.mat

% Format for fitting (Lazy)
x=data(:,1)
y=data(:,2)

% Setup simulation paramaters
qu=14           % Number of powder points
omegar=10000    % Spinning speed in Hz

% Setup function to be fitted
fun=@(deltaeta,x)
Herzfeld_Berger(x,deltaeta(1),deltaeta(2),qu,omegar);
% Enter initial guess (delta, eta)
guess=[54,0];
% Fix display options
opts=statset('Display','iter');
% Fit data to model
mdl=fitnlm(x,y,fun,guess,'Options',opts,'CoefficientName',{'delta'
,'eta'})

% Generate output with fitted data and residuals
figure(1)
subplot(2,1,1)
y(:,2)=mdl.Fitted;
bar(x,y);
title('Fitted Sideband Intensity')
subplot(2,1,2)
bar(x,mdl.Residuals.Raw);
title('Residuals')

function y=Herzfeld_Berger(x,delta,eta,qu,omegar)
%% Herzfeld Berger Analysis Based on J Chem Phys 1980 (73) 6021
% Input paramaters
% x      : array containing the number of sidebands
% delta  : anisotropy
% eta    : asymmetry parameter
% qu     : Number of powder points
% omegar : Spinning speed in Hz

y=zeros(size(x));

% Setup Chen averaging
value1 = [2, 50, 100, 144, 200, 300, 538, 1154, 1500, 2000, 2500,
10000, 50000, 100000];
value2 = [1,  7,  27,  11,  29,  37,  55,  107,  139,  297,  363,
3189,  9027,  27205];
value3 = [1, 11,  41,  53,  79,  61, 229,  271,  621,  479,  917,
4713, 14857,  38057];
```

```
% Input parameters - most now passed to function - but convert to
right
% units
omegar=omegar*2*pi;         % Spinning speed (converted to
rad/sec)
delta=delta*2*pi*1000;      % anisotropy (converted to rad/sec)
gammah0=1.0;                % For CSA (for quadrupolar can leave)
counter=0;          % Book keeping counter for number of sidebands

parfor i=1:1:length(x)
    counter=counter+1;      % Keep track of which sideband
    intn=0.0;               % Zero sideband intensity
    N=x(i);                 % Get sideband to calculate from x

    for count=1:1:value1(qu)

      % Generate powder angles
      % Convert to radians and change modular arithmatic
      beta=(pi*count/value1(qu));
      alpha=2*pi*mod((value2(qu)*count),value1(qu))/value1(qu);
      gamma=2*pi*mod((value3(qu)*count),value1(qu))/value1(qu);

      % Calculate F for a given orientation beta

      F=complex(0.0,0.0);

      for theta=0:(pi/180):2*pi
            tauplus=(1.0/24.0)*(cos(2.0*beta)-
1.0)*sin(2*theta)+(sqrt(2.0)/6.0)*sin(2.0*beta)*sin(theta);

tauminus=(1.0/24.0)*cos(2*alpha)*(3+cos(2*beta))*sin(2*theta)-
(1/6)*sin(2*alpha)*cos(beta)*cos(2*theta)+...
               (sqrt(2)/6)*cos(2*alpha)*sin(2*beta)*sin(theta)-
...
               (sqrt(2)/3)*sin(2*alpha)*sin(beta)*cos(theta);
            deltaplus=-1.0*(gammah0*delta*3.0)/omegar;
            deltaminus=-1.0*(gammah0*delta*eta)/omegar;
            ntheta=theta*N;
            temp=(deltaminus*tauminus)+(deltaplus*tauplus)-ntheta;
            temp2=complex(0,temp);
            Ftheta=exp(temp2);
            F=F+Ftheta;
      end
      % Take magnitude and weight for powder (sin(beta)
      intnbeta=real(F)*real(F);
      intn=intn+(intnbeta*sin(beta));
  end
    y(i)=intn;
end

% Symmetrize data to obtain quadrupolar pattern
 y=y+flip(y);

% Normalize to maximum intensity
y=y./max(y);
end
```

Bibliography

1. Williamson, P.; A. Watts, J.; Addona, G.; W. Miller, K.; Watts, A., *Dynamics and orientation of N1(CD3)3- bromoacetylcholine bound to its binding site on the nicotinic acetylcholine receptor*. 2001; Vol. 98.

2. Ma, J. C.; Dougherty, D. A., The Cation−π Interaction. *Chemical Reviews* **1997,** *97* (5), 1303-1324.

3. Dutta, A.; Saxena, K.; Schwalbe, H.; Klein-Seetharaman, J., Isotope labeling in mammalian cells. *Methods Mol Biol* **2012,** *831*, 55-69.

4. Levitt, M. H., *Spin Dynamics: Basics of Nuclear Magnetic Resonance*. Wiley: 2008.

5. Duer, M., Solid-State NMR Spectroscopy Principles and Applications. 2007; pp 73-110.

6. Seelig, J., Deuterium magnetic resonance: theory and application to lipid membranes. *Quarterly Reviews of Biophysics* **1977,** *10* (3), 353-418.

7. Mehring, M., *High Resolution NMR Spectroscopy in Solids*. Springer: 1976.

8. Beckmann, P. A., Spectral densities and nuclear spin relaxation in solids. *Physics Reports* **1988,** *171* (3), 85-128.

9. O'Dell, L. A.; Ratcliffe, C. I., Quadrupolar NMR to Investigate Dynamics in Solid Materials. In *eMagRes*, pp 1-16.

10. Hahn, E. L., Spin Echoes. *Physical Review* **1950,** *80* (4), 580-594.

11. Levitt, M., *Spin dynamics*. 2015

12. Ariza-Castolo, A., Beyond excitation NMR relaxation. *Concepts in Magnetic Resonance Part A* **2008,** *32A* (3), 168-182.

13. Lewandowski, J. R., Advances in Solid-State Relaxation Methodology for Probing Site-Specific Protein Dynamics. *Accounts of Chemical Research* **2013,** *46* (9), 2018-2027.

14. Lewandowski, J. R.; Sass, H. J.; Grzesiek, S.; Blackledge, M.; Emsley, L., Site-Specific Measurement of Slow Motions in Proteins. *Journal of the American Chemical Society* **2011,** *133* (42), 16762-16765.

15. Ernst, M.; Meier, B. H.; Tomaselli, M.; Pines, A., Time reversal of cross-polarization in solid-state NMR. *Molecular Physics* **1998,** *95* (5), 849-858.

16. Bain, A. D., Chemical Exchange Effects in NMR☆. In *Encyclopedia of Spectroscopy and Spectrometry (Third Edition)*, Lindon, J. C.; Tranter, G. E.; Koppenaal, D. W., Eds. Academic Press: Oxford, 2017; pp 180-187.

17. Vold, R. L.; Hoatson, G. L., Effects of jump dynamics on solid state nuclear magnetic resonance line shapes and spin relaxation times. *Journal of Magnetic Resonance* **2009,** *198* (1), 57-72.

18. Hazendonk, P.; Bain, A. D.; Grondey, H.; Harrison, P. H. M.; Dumont, R. S., Simulations of Chemical Exchange Lineshapes in CP/MAS Spectra Using Floquet Theory and Sparse Matrix Methods. *Journal of Magnetic Resonance* **2000,** *146* (1), 33-42.

19. Hogben, H. J.; Krzystyniak, M.; Charnock, G. T. P.; Hore, P. J.; Kuprov, I., Spinach – A software library for simulation of spin dynamics in large spin systems. *J. Magn. Reson.* **2011,** *208* (2), 179-194.

20. Edwards, L. J.; Savostyanov, D. V.; Nevzorov, A. A.; Concistrè, M.; Pileio, G.; Kuprov, I., Grid-free powder averages: On the applications of the Fokker–Planck equation to solid state NMR. *Journal of Magnetic Resonance* **2013,** *235*, 121-129.

21. Kleckner, I. R.; Foster, M. P., An introduction to NMR-based approaches for measuring protein dynamics. *Biochim Biophys Acta* **2011,** *1814* (8), 942-968.

22. Schanda, P.; Ernst, M., Studying dynamics by magic-angle spinning solid-state NMR spectroscopy: Principles and applications to biomolecules. *Progress in Nuclear Magnetic Resonance Spectroscopy* **2016,** *96*, 1-46.

23. Krushelnitsky, A.; Gauto, D.; Rodriguez Camargo, D. C.; Schanda, P.; Saalwächter, K., Microsecond motions probed by near-rotary-resonance R1ρ 15N MAS NMR experiments: the model case of protein overall-rocking in crystals. *Journal of Biomolecular NMR* **2018,** *71* (1), 53-67.

24. Duer, M. J., The Basics of Solid-State NMR. In *Solid-State NMR Spectroscopy Principles and Applications*, 2007.

25. Mahajan, V.; Sass, R. L., Crystal structure of acetylcholine perchlorate. *Journal of Crystal and Molecular Structure* **1974,** *4* (1), 15-21.

26. Duer, M. J., *Introduction to Solid-State NMR Spectroscopy*. Wiley: 2005.

27. Jarvis, J. A.; Haies, I. M.; Williamson, P. T. F.; Carravetta, M., An efficient NMR method for the characterisation of 14N sites through indirect 13C detection. *Phys. Chem. Chem. Phys.* **2013,** *15* (20), 7613-7620.

28. Williamson, P. T. F., Solid-state NMR for the analysis of high-affinity ligand/receptor interactions. *Concepts in Magnetic Resonance Part A* **2009,** *34A* (3), 144-172.

29. Scholz, I.; Hodgkinson, P.; Meier, B. H.; Ernst, M., Understanding two-pulse phase-modulated decoupling in solid-state NMR. *The Journal of Chemical Physics* **2009,** *130* (11), 114510.

30. Detken, A.; Hardy, E. H.; Ernst, M.; Meier, B. H., Simple and efficient decoupling in magic-angle spinning solid-state NMR: the XiX scheme. *Chemical Physics Letters* **2002,** *356* (3), 298-304.

31. Fung, B. M.; Khitrin, A. K.; Ermolaev, K., An Improved Broadband Decoupling Sequence for Liquid Crystals and Solids. *Journal of Magnetic Resonance* **2000,** *142* (1), 97-101.

32. Leary, G. J.; Newman, R. H., Cross Polarization/Magic Angle Spinning Nuclear Magnetic Resonance (CP/MAS NMR) Spectroscopy. In *Methods in Lignin Chemistry*, Lin, S. Y.; Dence, C. W., Eds. Springer Berlin Heidelberg: Berlin, Heidelberg, 1992; pp 146-161.

33. O'Dell, L. A., Direct detection of nitrogen-14 in solid-state NMR spectroscopy. *Prog. Nucl. Magn. Reson. Spectrosc.* **2011,** *59* (4), 295-318.

34. Clark, S. J.; Segall, M. D.; Pickard, C. J.; Hasnip, P. J.; Probert, M. I. J.; Refson, K.; Payne, M. C., First principles methods using CASTEP. *Zeitschrift für Kristallographie - Crystalline Materials* **2005,** *220* (5-6), 567.

35. Datta, S.; Grant, D. J. W., Crystal structures of drugs: advances in determination, prediction and engineering. *Nature Reviews Drug Discovery* **2004,** *3* (1), 42-57.

36. Smyth, M. S.; Martin, J. H., x ray crystallography. *Mol Pathol* **2000,** *53* (1), 8-14.

37. Krissinel, E.; Henrick, K., Inference of Macromolecular Assemblies from Crystalline State. *Journal of Molecular Biology* **2007,** *372* (3), 774-797.

38. Hook, J. R.; Hall, H. E., *Solid State Physics*. Wiley: 2013.

39. Guinier, A., *X-ray diffraction in crystals, imperfect crystals, and amorphous bodies*. W.H. Freeman: San Francisco, 1963.

40. Myers, H. P., Introductory solid state physics. **2014**.

41. Coppens, P., Electron Density from X-Ray Diffraction. *Annual Review of Physical Chemistry* **1992,** *43* (1), 663-692.

42. Qi, S.-Y.; Tian, Y.; Zou, W.-B.; Hu, C.-Q., Characterization of Solid-State Drug Polymorphs and Real-Time Evaluation of Crystallization Process Consistency by Near-Infrared Spectroscopy. *Frontiers in Chemistry* **2018,** *6* (506).

43. Rustichelli, C.; Gamberini, G.; Ferioli, V.; Gamberini, M. C.; Ficarra, R.; Tommasini, S., Solid-state study of polymorphic drugs: carbamazepine. *Journal of Pharmaceutical and Biomedical Analysis* **2000,** *23* (1), 41-54.

44. Karpinski, P. H., Polymorphism of Active Pharmaceutical Ingredients. *Chemical Engineering & Technology* **2006,** *29* (2), 233-237.

45. Milman, V.; Refson, K.; Clark, S. J.; Pickard, C. J.; Yates, J. R.; Gao, S. P.; Hasnip, P. J.; Probert, M. I. J.; Perlov, A.; Segall, M. D., Electron and vibrational spectroscopies using DFT, plane waves and pseudopotentials: CASTEP implementation. *Journal of Molecular Structure: THEOCHEM* **2010,** *954* (1), 22-35.

46. Yates, J. R.; Pickard, C. J., Computations of Magnetic Resonance Parameters for Crystalline Systems: Principles. In *eMagRes*, 2008.

47. Payne, M. C.; Teter, M. P.; Allan, D. C.; Arias, T. A.; Joannopoulos, J. D., Iterative minimization techniques for ab initio total-energy calculations: molecular dynamics and conjugate gradients. *Reviews of Modern Physics* **1992,** *64* (4), 1045-1097.

48. Bernard, G. M.; Wasylishen, R. E., A 13C Solid-State NMR Investigation of the Alkynyl Carbon Chemical Shift Tensors for 2-Butyne-1,4-diol. *Solid State Nuclear Magnetic Resonance* **2002,** *21* (1), 86-104.

49. Sturniolo, S.; Green, T. F. G.; Hanson, R. M.; Zilka, M.; Refson, K.; Hodgkinson, P.; Brown, S. P.; Yates, J. R., Visualization and processing of computed solid-state NMR parameters: MagresView and MagresPython. *Solid State Nuclear Magnetic Resonance* **2016,** *78*, 64-70.

50. Casanovas, J.; Illas, F.; Pacchioni, G., Ab initio calculations of 29Si solid state NMR chemical shifts of silane and silanol groups in silica. *Chemical Physics Letters* **2000,** *326* (5), 523-529.

51. Dickson, R. M.; Ziegler, T., NMR Spin−Spin Coupling Constants from Density Functional Theory with Slater-Type Basis Functions. *The Journal of Physical Chemistry* **1996,** *100* (13), 5286-5290.

52. Jagner, S.; Jensen, B., The crystal structure of acetylcholine iodide. *Acta Crystallographica Section B* **1977,** *33* (9), 2757-2762.

53. Pullman, B.; CourriÉRe, P., Further Molecular Orbital Studies on the Conformation of Acetylcholine and Its Derivatives. *Molecular Pharmacology* **1972,** *8* (6), 612.

54. Rigaku, V. b. CrysAlisPro Software System, Rigaku Oxford Diffraction.

55. Sheldrick, G., SHELXT - Integrated space-group and crystal-structure determination. *Acta Crystallographica Section A* **2015,** *71* (1), 3-8.

56. Sheldrick, G., Crystal structure refinement with SHELXL. *Acta Crystallographica Section C* **2015,** *71* (1), 3-8.

57. Bourhis, L. J.; Dolomanov, O. V.; Gildea, R. J.; Howard, J. A. K.; Puschmann, H., The anatomy of a comprehensive constrained, restrained refinement program for the modern computing environment - Olex2 dissected. *Acta Crystallographica Section A* **2015,** *71* (1), 59-75.

58. Björkman, T., CIF2Cell: Generating geometries for electronic structure programs. *Computer Physics Communications* **2011,** *182* (5), 1183-1186.

59. Rankin, A. G. M.; Trébosc, J.; Paluch, P.; Lafon, O.; Amoureux, J.-P., Evaluation of excitation schemes for indirect detection of 14N via solid-state HMQC NMR experiments. *Journal of Magnetic Resonance* **2019,** *303*, 28-41.

60. Maelicke, A.; Albuquerque, E. X., Allosteric modulation of nicotinic acetylcholine receptors as a treatment strategy for Alzheimer's disease. *European Journal of Pharmacology* **2000,** *393* (1), 165-170.

61. Gotti, C.; Zoli, M.; Clementi, F., Brain nicotinic acetylcholine receptors: native subtypes and their relevance. *Trends in Pharmacological Sciences* **2006,** *27* (9), 482-491.

62. Fujita, M.; Ichise, M.; Zoghbi, S. S.; Liow, J.-S.; Ghose, S.; Vines, D. C.; Sangare, J.; Lu, J.-Q.; Cropley, V. L.; Iida, H.; Kim, K. M.; Cohen, R. M.; Bara-Jimenez, W.; Ravina, B.; Innis, R. B., Widespread decrease of nicotinic acetylcholine receptors in Parkinson's disease. *Annals of Neurology* **2006,** *59* (1), 174-177.

63. Lindstrom, J., Nicotinic acetylcholine receptors in health and disease. *Molecular Neurobiology* **1997,** *15* (2), 193-222.

64. Ko, C. P., Neuromuscular System. In *International Encyclopedia of the Social & Behavioral Sciences*, Smelser, N. J.; Baltes, P. B., Eds. Pergamon: Oxford, 2001; pp 10595-10600.

65. Pierce, K. L.; Premont, R. T.; Lefkowitz, R. J., Seven-transmembrane receptors. *Nature reviews. Molecular cell biology* **2002,** *3* (9), 639-50.

66. Williamson, P.; Meier, B.; Watts, A., Structural and functional studies of the nicotinic acetylcholine receptor by solid-state NMR. *European biophysics journal : EBJ* **2004,** *33*, 247-54.

67. Seo, M.-H.; Park, J.; Kim, E.; Hohng, S.; Kim, H.-S., Protein conformational dynamics dictate the binding affinity for a ligand. *Nature Communications* **2014,** *5*, 3724.

68. Atreya, H. S., Structures of biomolecules by NMR spectroscopy. *Resonance* **2015,** *20* (11), 1033-1039.

69. Williamson, P. T. F.; Zandomeneghi, G.; Barrantes, F. J.; Watts, A.; Meier, B. H., Structural and dynamic studies of the γ-M4 trans-membrane domain of the nicotinic acetylcholine receptor. *Molecular Membrane Biology* **2005,** *22* (6), 485-496.

70. Mallikarjunaiah, K. J.; Damle, R.; Ramesh, K. P., Study of molecular dynamics and cross relaxation in tetramethylammonium hexafluorophosphate (CH3)4NPF6 by 1H and 19F NMR. *Solid State Nuclear Magnetic Resonance* **2008,** *34* (3), 180-185.

71. Merwin, L. H.; Ross, S. D., Solid-state 13C and 1H NMR study of anomalous acid salts of dibasic carboxylic acids. *Magnetic Resonance in Chemistry* **1992,** *30* (5), 440-448.

72. Wasyluk, L.; Peplinska, B.; Klinowski, J.; Jurga, S., NMR studies of the molecular dynamics of tert-butyl chloride confined in the mesoporous molecular sieve MCM-41. *Physical Chemistry Chemical Physics* **2002,** *4* (11), 2392-2397.

73. Ratcliffe, C. I.; Ripmeester, J. A., 2H nuclear magnetic resonance studies of motions in tetramethylammonium salts: the question of methyl reorientation. *Canadian Journal of Chemistry* **1986,** *64* (7), 1298-1304.

74. Duer, M. J., Solid-State NMR Studies of Molecular Motion. In *Annual Reports on NMR Spectroscopy*, Webb, G. A., Ed. Academic Press: 2006; Vol. 59, pp 41-116.

75. Herzfeld, J.; Berger, A. E., Sideband intensities in NMR spectra of samples spinning at the magic angle. *The Journal of Chemical Physics* **1980,** *73* (12), 6021-6030.

76. Lindström, F.; Williamson, P. T. F.; Gröbner, G., Molecular Insight into the Electrostatic Membrane Surface Potential by 14N/31P MAS NMR Spectroscopy: Nociceptin−Lipid Association. *Journal of the American Chemical Society* **2005,** *127* (18), 6610-6616.

77. Carper, W. R.; Wahlbeck, P. G.; Dölle, A., 13C NMR Relaxation Rates: Separation of Dipolar and Chemical Shift Anisotropy Effects. *The Journal of Physical Chemistry A* **2004,** *108* (29), 6096-6099.

78. Cheng, V. B.; Jr., H. H. S.; Wolfsberg, M., Investigations of a nonrandom numerical method for multidimensional integration. *The Journal of Chemical Physics* **1973,** *59* (8), 3992-3999.

79. Wu, X.; Juban, E. A.; Butler, L. G., 15 T, 4.2 K field-swept 27Al NMR spectroscopy. *Chemical Physics Letters* **1994,** *221* (1), 65-67.

80. Hill, E. A.; Yesinowski, J. P., A slow-turning method for measuring large anisotropic interactions in inhomogeneously broadened nuclear magnetic resonance spectra. *The Journal of Chemical Physics* **1997,** *106* (21), 8650-8659.

81. Olivieri, A. C., Solid state NMR sideband shape simulations for any spinning angle and speed. First order calculation of residual dipolar coupling to quadrupolar nuclei. *Solid State Nuclear Magnetic Resonance* **1997,** *10* (1), 19-24.

82. Berendt, R. T.; Sperger, D. M.; Munson, E. J.; Isbester, P. K., Solid-state NMR spectroscopy in pharmaceutical research and analysis. *TrAC Trends in Analytical Chemistry* **2006,** *25* (10), 977-984.

83. Agrawal, S.; Ashokraj, Y.; Bharatam, P. V.; Pillai, O.; Panchagnula, R., Solid-state characterization of rifampicin samples and its biopharmaceutic relevance. *European Journal of Pharmaceutical Sciences* **2004,** *22* (2), 127-144.

84. Tishmack, P. A.; Bugay, D. E.; Byrn, S. R., Solid-State Nuclear Magnetic Resonance Spectroscopy-Pharmaceutical Applications. *Journal of Pharmaceutical Sciences* **2003,** *92* (3), 441-474.

85. Geppi, M.; Mollica, G.; Borsacchi, S.; Veracini, C. A., Solid-State NMR Studies of Pharmaceutical Systems. *Applied Spectroscopy Reviews* **2008,** *43* (3), 202-302.

86. Rovó, P.; Smith, C. A.; Gauto, D.; de Groot, B. L.; Schanda, P.; Linser, R., Mechanistic Insights into Microsecond Time-Scale Motion of Solid Proteins Using Complementary 15N and 1H Relaxation Dispersion Techniques. *Journal of the American Chemical Society* **2019,** *141* (2), 858-869.

87. G. Riddell, F.; Rogerson, M., Further studies of intramolecular motions in crystalline ammonium bromides by CP/MAS NMR. *Journal of the Chemical Society, Perkin Transactions 2* **1997,** (2), 249-256.

88. Ratcliffe, C. I.; Garg, S. K.; Davidson, D. W., NMR studies of molecular motion in tetramethylammonium hydroxide pentahydrate. *Journal of inclusion phenomena and molecular recognition in chemistry* **1990,** *8* (1), 159-175.

89. Pettersen, E. F.; Goddard, T. D.; Huang, C. C.; Couch, G. S.; Greenblatt, D. M.; Meng, E. C.; Ferrin, T. E., UCSF Chimera—A visualization system for exploratory research and analysis. *Journal of Computational Chemistry* **2004,** *25* (13), 1605-1612.

90. Williamson, P. T. F.; Gröbner, G.; Spooner, P. J. R.; Miller, K. W.; Watts, A., Probing the Agonist Binding Pocket in the Nicotinic Acetylcholine Receptor: A High-Resolution Solid-State NMR Approach. *Biochemistry* **1998,** *37* (30), 10854-10859.

91. Remis, J. P.; Wei, D.; Gorur, A.; Zemla, M.; Haraga, J.; Allen, S.; Witkowska, H. E.; Costerton, J. W.; Berleman, J. E.; Auer, M., Bacterial social networks: structure and composition of Myxococcus xanthus outer membrane vesicle chains. *Environmental Microbiology* **2014,** *16* (2), 598-610.

92. Kim, H. J.; Howell, S. C.; Van Horn, W. D.; Jeon, Y. H.; Sanders, C. R., Recent Advances in the Application of Solution NMR Spectroscopy to Multi-Span Integral Membrane Proteins. *Progress in nuclear magnetic resonance spectroscopy* **2009,** *55* (4), 335-360.

93. Bennett, W. F. D.; MacCallum, J. L.; Tieleman, D. P., Thermodynamic Analysis of the Effect of Cholesterol on Dipalmitoylphosphatidylcholine Lipid Membranes. *Journal of the American Chemical Society* **2009,** *131* (5), 1972-1978.

94. Bartke, N.; Hannun, Y. A., Bioactive sphingolipids: metabolism and function. *Journal of Lipid Research* **2009,** *50*, S91-S96.

95. Curatolo, W., The physical properties of glycolipids. *Biochimica et Biophysica Acta (BBA) - Reviews on Biomembranes* **1987,** *906* (2), 111-136.

96. Castro, V.; Dvinskikh, S. V.; Widmalm, G.; Sandström, D.; Maliniak, A., NMR studies of membranes composed of glycolipids and phospholipids. *Biochimica et Biophysica Acta (BBA) - Biomembranes* **2007,** *1768* (10), 2432-2437.

97. Marsh, D., Electron spin resonance in membrane research: protein–lipid interactions from challenging beginnings to state of the art. *European Biophysics Journal* **2010,** *39* (4), 513-525.

98. Marsh, D., Protein modulation of lipids, and vice-versa, in membranes. *Biochimica et Biophysica Acta (BBA) - Biomembranes* **2008,** *1778* (7), 1545-1575.

99. Marsh, D.; Horváth, L. I., Structure, dynamics and composition of the lipid-protein interface. Perspectives from spin-labelling. *Biochimica et Biophysica Acta (BBA) - Reviews on Biomembranes* **1998,** *1376* (3), 267-296.

100. de Planque, M. R. R.; Kruijtzer, J. A. W.; Liskamp, R. M. J.; Marsh, D.; Greathouse, D. V.; Koeppe, R. E.; de Kruijff, B.; Killian, J. A., Different Membrane Anchoring Positions of Tryptophan and Lysine in Synthetic Transmembrane α-Helical Peptides*. *Journal of Biological Chemistry* **1999,** *274* (30), 20839-20846.

101. Sankaram, M. B.; Marsh, D., Chapter 6 Protein-lipid interactions with peripheral membrane proteins. In *New Comprehensive Biochemistry*, Watts, A., Ed. Elsevier: 1993; Vol. 25, pp 127-162.

102. Weingarth, M.; Prokofyev, A.; van der Cruijsen, E. A. W.; Nand, D.; Bonvin, A. M. J. J.; Pongs, O.; Baldus, M., Structural Determinants of Specific Lipid Binding to Potassium Channels. *Journal of the American Chemical Society* **2013,** *135* (10), 3983-3988.

103. Marius, P.; Zagnoni, M.; Sandison, M. E.; East, J. M.; Morgan, H.; Lee, A. G., Binding of Anionic Lipids to at Least Three Nonannular Sites on the Potassium Channel KcsA is Required for Channel Opening. *Biophysical Journal* **2008,** *94* (5), 1689-1698.

104. Marius, P.; de Planque, M. R. R.; Williamson, P. T. F., Probing the interaction of lipids with the non-annular binding sites of the potassium channel KcsA by magic-angle spinning NMR. *Biochimica et Biophysica Acta (BBA) - Biomembranes* **2012,** *1818* (1), 90-96.

105. Mollinedo, F.; Gajate, C., Lipid rafts as major platforms for signaling regulation in cancer. *Advances in Biological Regulation* **2015,** *57*, 130-146.

106. Helms, J. B.; Zurzolo, C., Lipids as Targeting Signals: Lipid Rafts and Intracellular Trafficking. *Traffic* **2004,** *5* (4), 247-254.

107. Kumar, A.; Kodidela, S.; Tadrous, E.; Cory, T. J.; Walker, C. M.; Smith, A. M.; Mukherjee, A.; Kumar, S., Extracellular Vesicles in Viral Replication and Pathogenesis and Their Potential Role in Therapeutic Intervention. *Viruses* **2020,** *12* (8), 887.

108. Francesconi, A.; Kumari, R.; Zukin, R. S., Regulation of Group I Metabotropic Glutamate Receptor Trafficking and Signaling by the Caveolar/Lipid Raft Pathway. *The Journal of Neuroscience* **2009,** *29* (11), 3590.

109. Marius, P.; Wright, J. N.; Findlow, I. S.; Williamson, P. T. F., Expression and purification of the transmembrane domain of Fukutin-I for biophysical studies. *Protein Expression and Purification* **2010,** *72* (1), 107-112.

110. Matsumoto, H.; Noguchi, S.; Sugie, K.; Ogawa, M.; Murayama, K.; Hayashi, Y. K.; Nishino, I., Subcellular Localization of Fukutin and Fukutin-Related Protein in Muscle Cells. *The Journal of Biochemistry* **2004,** *135* (6), 709-712.

111. Xiong, H.; Kobayashi, K.; Tachikawa, M.; Manya, H.; Takeda, S.; Chiyonobu, T.; Fujikake, N.; Wang, F.; Nishimoto, A.; Morris, G. E.; Nagai, Y.; Kanagawa, M.; Endo, T.; Toda, T., Molecular interaction between fukutin and POMGnT1 in the glycosylation pathway of α-dystroglycan. *Biochemical and Biophysical Research Communications* **2006,** *350* (4), 935-941.

112. Coskun, Ü.; Simons, K., Cell Membranes: The Lipid Perspective. *Structure* **2011,** *19* (11), 1543-1548.

113. Banfield, D. K., Mechanisms of protein retention in the Golgi. *Cold Spring Harb Perspect Biol* **2011,** *3* (8), a005264-a005264.

114. Drew, D. L.; Butcher, B.; Sahu, I. D.; Ahammad, T.; Dixit, G.; Lorigan, G. A., Active S2168 and inactive S21IRS pinholin interact differently with the lipid bilayer: A 31P and 2H solid state NMR study. *Biochimica et Biophysica Acta (BBA) - Biomembranes* **2020,** *1862* (7), 183257.

115. Schmidt, M. L.; Davis, J. H., Liquid Disordered–Liquid Ordered Phase Coexistence in Lipid/Cholesterol Mixtures: A Deuterium 2D NMR Exchange Study. *Langmuir* **2017,** *33* (8), 1881-1890.

116. Boulanger, Y.; Schreier, S.; Smith, I. C. P., Molecular details of anesthetic-lipid interaction as seen by deuterium and phosphorus-31 nuclear magnetic resonance. *Biochemistry* **1981,** *20* (24), 6824-6830.

117. Jolly, M. M.; Jarvis, J. A.; Carravetta, M.; Levitt, M. H.; Williamson, P. T. F., Bidirectional band-selective magnetization transfer along the protein backbone doubles the information content of solid-state NMR correlation experiments. *Journal of Biomolecular NMR* **2017,** *69* (4), 197-205.

118. Liang, B.; Tamm, L. K., NMR as a tool to investigate the structure, dynamics and function of membrane proteins. *Nat Struct Mol Biol* **2016,** *23* (6), 468-474.

119. Watts, A., NMR of Lipids. In *Encyclopedia of Biophysics*, Roberts, G. C. K., Ed. Springer Berlin Heidelberg: Berlin, Heidelberg, 2013; pp 1727-1738.

120. Ulrich, A. S.; Watts, A., Molecular response of the lipid headgroup to bilayer hydration monitored by 2H-NMR. *Biophysical Journal* **1994,** *66* (5), 1441-1449.

121. Oxenoid, K.; Chou, J. J., A functional NMR for membrane proteins: dynamics, ligand binding, and allosteric modulation. *Protein Sci* **2016,** *25* (5), 959-973.

122. Salnikov, E. S.; Aisenbrey, C.; Pokrandt, B.; Brügger, B.; Bechinger, B., Structure, Topology, and Dynamics of Membrane-Inserted Polypeptides and Lipids by Solid-State NMR Spectroscopy: Investigations of the Transmembrane Domains of the DQ Beta-1 Subunit of the MHC II Receptor and of the COP I Protein p24. *Frontiers in Molecular Biosciences* **2019,** *6* (83).

123. Dave, P. C.; Tiburu, E. K.; Damodaran, K.; Lorigan, G. A., Investigating structural changes in the lipid bilayer upon insertion of the transmembrane domain of the membrane-bound protein phospholamban utilizing 31P and 2H solid-state NMR spectroscopy. *Biophysical journal* **2004,** *86* (3), 1564-1573.

124. van Meer, G.; Holthuis, J. C. M., Sphingolipid transport in eukaryotic cells. *Biochimica et Biophysica Acta (BBA) - Molecular and Cell Biology of Lipids* **2000,** *1486* (1), 145-170.

125. Rappolt, M.; Vidal, M.; Kriechbaum, M.; Steinhart, M.; Amenitsch, H.; Bernstorff, S.; Laggner, P., Structural, dynamic and mechanical properties of POPC at low cholesterol concentration studied in pressure/temperature space. *European Biophysics Journal* **2003,** *31* (8), 575-585.

126. Seelig, A.; Seelig, J., Dynamic structure of fatty acyl chains in a phospholipid bilayer measured by deuterium magnetic resonance. *Biochemistry* **1974,** *13* (23), 4839-4845.

127. Seelig, J.; Niederberger, W., Deuterium-labeled lipids as structural probes in liquid crystalline bilayers. Deuterium magnetic resonance study. *Journal of the American Chemical Society* **1974,** *96* (7), 2069-2072.

128. Latanowicz, L., Spin-lattice NMR relaxation and second moment of NMR line in solids containing CH3 groups. *Concepts in Magnetic Resonance Part A* **2015,** *44* (4), 214-225.